Max-Planck-Institut für Plasmaphysik
Garching bei München

Shakedown Analysis of Fiber-Reinforced Metal Matrix Composite under Fusion-Relevant Thermomechanical Loading

Byoung Yoon Kim

Vollständiger Abdruck der von der Fakultät für Maschinenwesen der Technischen Universität München zur Erlangung des akademischen Grades eines

Doktor-Ingenieurs

genehmigten Dissertation.

Vorsitzender:	Univ.-Prof. Dr.-Ing. H. Baier
Prüfer der Dissertation:	1. Hon.-Prof. Dr.-Ing., Dr.-Eng. (Japan) H. H. Bolt
	2. Univ.-Prof. Dr. mont. habil. E. Werner

Die Dissertation wurde am 16. 12. 2004 bei der Technischen Universität München eingereicht und durch die Fakultät für Maschinenwesen am 10. 03. 2005 angenommen.

Abstract

The aim of thermonuclear fusion research is to confine a hot deuterium-tritium (D-T) plasma long enough so that fusion reactions between hydrogen isotope ions occur, leading to a commercial power generation. The successful operation of fusion devices depends on the development of plasma facing components (PFCs) which can withstand the surface heat loads of up to 20 MW/m^2 under quasi-stationary conditions. Copper alloys have been considered as a structural material for the heat sink substrate of a PFC due to their excellent thermal conductivity. However, insufficient high temperature strength and large thermal expansion set the limitations to structural applications.

Fiber-reinforced metal matrix composites (FRMMCs) can be a candidate for a structural material for the future PFCs due to the excellent high temperature strength. Since the FRMMCs of the PFCs are exposed to thermal and mechanical loads, the resulting stress fields in mesoscopic level is highly heterogeneous and often exceed the yield limit of the matrix. The shakedown limit was investigated as the safety criterion of the FRMMCs considering the fusion-relevant thermomechanical loads.

In principle, it is possible to determine the macro- and mesoscopic stress states by means of finite element method (FEM), in which the real FRMMC architecture is modeled by direct meshing. Surely, this is not a practical approach since it requires a high computational cost. In this case, shakedown analysis can be an appropriate tool to estimate structural safety. The shakedown theorems were formulated by several researchers. Further, these could be combined with FEM and the large-scale nonlinear optimization program and applied to complex system.

In this work, the shakedown formulation was extended to three-dimensional models. The developed computational algorithm was verified by comparing with literature results. The shakedown limits were determined for both lamina and laminate of FRMMC composite system. The results showed that shakedown limits were dependent on geometrical factor (fiber architecture and fiber volume fraction), loading direction, thermal loading, and hardening effect. They were discussed based on the maximum value and the distribution of von Mises stress.

The stress and temperature loading paths of FRMMC components were determined in the fusion-relevant loading. The thermomechanical loading paths obtained were compared with the shakedown limits. The results showed that the loading paths in the real operation situation were only partly covered by the area of shakedown limit. It was interpreted that the FRMMC layers may undergo low cycle fatigue.

Kurzfassung

Das Ziel der thermonuklearen Fusionsforschung ist es, ein heißes Deuterium-Tritium (D-T) Plasma lange genug einzuschließen, so dass Fusionsreaktionen zwischen Wasserstoffisotopen stattfinden, so dass eine kommerzielle Elektrizitätserzeugung ermöglicht wird. Der erfolgreiche Betrieb von Fusionsanlagen hängt von der Entwicklung plasmabelasteter Komponenten (PFCs) ab, die einer Wärmelast von bis zu 20 MW/m² auf ihrer Oberfläche unter quasistationären Bedingungen standhalten können. Als Strukturmaterial für die Wärmesenkenträger einer PFC werden Kupferlegierungen wegen ihrer exzellenten thermischen Leitfähigkeit in Betracht gezogen. Ungenügende Hochtemperaturfestigkeit und starke Wärmeausdehnung setzen jedoch Grenzen in der Strukturanwendung.

Faserverstärkte Metallmatrix-Kompositmaterialien (FRMMCs) können wegen ihrer hervorragenden Hochtemperaturfestigkeit als Strukturmaterialien für künftige PFCs in Frage kommen. Da die FRMMCs der PFCs mit ihrer heterogenen Mikrostruktur thermischen und mechanischen Lasten ausgesetzt sind, sind die resultierenden Spannungsfelder auf mesoskopischer Ebene stark heterogen und überschreiten oft die Fließgrenze der Matrix. In dieser Arbeit wurden die Einspielgrenzen als Sicherheitskriterien der FRMMCs unter Berücksichtigung fusionsrelevanter thermomechanischer Lasten untersucht.

Es ist prinzipiell möglich die makroskopischen und mesoskopischen Spannungszustände mit der Finite-Elemente-Methode (FEM) zu ermitteln, wenn der tatsächliche FRMMC-Aufbau durch direkte Vernetzung modelliert ist. Das ist natürlich keine praktische Näherung, da sie hohe Rechnerleistung erfordert. Alternativ kann eine Einspielanalyse ein geeignetes Werkzeug zur Abschätzung der strukturellen Sicherheit sein. Die Einspieltheoreme wurden von mehreren Forschern formuliert. Ferner können sie mit FEM und großskaligen nichtlinearen Optimierungsprogrammen kombiniert und auf komplexe Systeme angewandt werden.

In dieser Arbeit wurde die Einspielformulierung auf dreidimensionale Modelle erweitert. Der entwickelte Rechenalgorithmus wurde durch den Vergleich mit Literaturergebnissen überprüft. Die Einspielgrenzen wurden sowohl für Einzelschichten als auch für Laminate von FRMMC-Kompositsystemen ermittelt. Die Ergebnisse zeigten, dass die Einspielgrenzen von geometrischen Faktoren (Faseraufbau und Faservolumenanteil), Belastungsrichtung, thermischer Last und Aufhärtungseffekten abhängen. Sie wurden unter Berücksichtigung der maximalen von-Mises-Spannungen und ihrer Verteilungen interpretiert.

Spannungs- und Temperaturlastkurven der FRMMC-Komponenten wurden für fusionsrelevante Bedingungen bestimmt. Die gewonnenen thermomechanischen Lastkurven wurden mit den Einspielgrenzen verglichen. Die Lastkurven decken im realen Betrieb nur teilweise den Bereich der Einspielgrenzen ab. Dies lässt sich mit plastischer zyklischer Ermüdung der FRMMC-Schichten interpretieren.

Contents

List of Symbols

[b]	-	independent residual stress of discretized body
B^e	-	elastic reference body
[B]	-	matrix for derivative of shape function
[C]	-	equilibrium matrix
d	m	diameter of fiber
$\dot{D}^p$	1/s	plastic damage rate
E	N/m2	Young's modulus
f^*	N	external body force
F	N	force
F^ϑ	N	thermal load
$\{F\}$	N	the vector of nodal force
F_K	N	nodal force at each element
F	-	Melan's condition
G	N/m^2	shear modulus
$[J_j]$	m	Jacobian matrix of j^{th} element
[K]	N/m	stiffness matrix
l	m	length of component
l_i		lower bounds
L	-	load domain
L	-	Lagrangian function
∇L	-	gradient of Lagrangian function
L	N/m^2	elasticity tensor
[L]	N/m^2	elasticity matrix
n_j	-	unit vector
[N]	-	matrix for shape function
p	N/m^2	pressure
p_x	N/m^2	x-directional pressure
p_y	N/m^2	y-directional pressure
p^*	N/m^2	surface traction
P	N/m^2	macroscopic stress
P		projection operator
P_j	N/m^2	j^{th} loading corner
s_{ii}	-	component of constraint scaling factor
S	-	area of body
[S]	-	diagonal matrix of constraint scaling factor
t	s	time
T	K, °C	temperature
T_{ref}	K, °C	reference temperature
u^e	m	displacement vector
u_i		upper bounds
δu	m	arbitrary displacement vector
$\{u_K^e\}$	-	nodal displacement at each element

$\{\delta u^e\}$	m	vector of virtual displacement field
δU_{int}	J	internal virtual energy
V	mm^3	volume of body
V_f	vol %	fiber volume fraction
W	J	positive definite quadratic function
$\dot{W}$	W	time derivative of W
w_i	-	weighting factor
w_p	J/mm^3	specific plastic energy dissipation
W_p	J/mm^3	plastic energy dissipation
δW_{ext}	J	external virtual work
x	-	x-directional coordinate
X	-	arbitrary vector for optimization
y	-	y-directional coordinate
z	-	z-directional coordinate

Greek Symbols

α	-	shakedown safety factor
α^{SD}	-	shakedown safety factor ($\alpha^{SD} = \max_{\bar{\rho}} \alpha$)
α^e	-	elastic safety factor
α_ϑ	1/K	coefficient of thermal expansion
γ	-	shear strain
ε	-	strain
ε_c, ε_l	-	convergence tolerance in optimization
ε^e	-	elastic strain
$\tilde{\varepsilon}^e$	-	strain for elastic reference body
ε^p	-	plastic strain
ε^ϑ	-	thermal strain
$\dot{\varepsilon}^e$	1/s	elastic strain rate
$\dot{\tilde{\varepsilon}}^e$	1/s	strain rate for elastic reference body
$\dot{\varepsilon}^p$	1/s	plastic strain rate
$\dot{\varepsilon}_{ij}^r$	1/s	strain rate of ratecheting
$\{\delta\varepsilon^e\}$	-	vector of virtual strain field
$\Delta\varepsilon_{ij}^{AP}$	-	alternating plastic strain during a cycle time τ
$\Delta\varepsilon_{ij}^r$	-	ratcheting strain during a cycle time τ
Φ	-	augmented Lagrangian function
η	-	η component in natural coordinate
$\eta^{(k)}$	-	tolerance for approximate minimizer
κ	-	kinematic hardening variable
$\dot{\kappa}$	1/s	rate of kinematic hardening variable
λ	-	Lagrangian multiplier estimate
$\dot{\Lambda}$	-	monotonic function
μ	-	penalty parameter
μ_j	-	scalar multiplier

μ_j^+	-	maximum scalar multiplier
μ_j^-	-	minimum scalar multiplier
ϑ	K, °C	temperature difference (T-T_{ref})
ν	-	Poisson's ratio
$\overline{\pi}$	N/m^2	time-independent back stress field
ρ_m	kg/m^3	mass density
ρ	N/m^2	actual residual stress field
$\overline{\rho}$	N/m^2	time-independent residual stress field
$\dot{\rho}$	N/m^2s	rate of ρ
$\dot{\overline{\rho}}$	N/m^2s	rate of $\overline{\rho}$
σ	N/m^2	stress
σ_v	N/m^2	von Mises stress
$\sigma^{(a)}$	N/m^2	admissible stress state
σ^{AP}	N/m^2	alternating plastic stress
σ^e	N/m^2	elastic stress
$\tilde{\sigma}^e$	N/m^2	stress for elastic reference body
σ^p	N/m^2	instantaneous plastic stress
σ^r	N/m^2	incremental plastic (or ratcheting) stress
$\sigma^{(s)}$	N/m^2	safe stress state
σ^{SD}	N/m^2	shakedown stress
σ_Y	N/m^2	yield stress
σ_L	N/m^2	limit stress
$\dot{\tilde{\sigma}}^e$	N/m^2s	time derivative of $\tilde{\sigma}^e$
Σ	N/m^2	macroscopic stress
τ	N/m^2	shear stress
τ_{max}	N/m^2	maximum shear stress
ξ	-	ξ component in natural coordinate
$\boldsymbol{\xi}$	-	position vector in natural coordinate
Ψ	J/kg	thermodynamic potential
Ψ^e	J/kg	elastic thermodynamic potential
Ψ^p	J/kg	plastic thermodynamic potential
ζ	-	ζ component in natural coordinate
$\omega^{(k)}$	-	tolerance for approximate minimizer

Abbreviations

AP	Alternating Plasticity
CFC	Carbon-Fiber Reinforced Carbon
CT	Cooling Temperature
CTE	Coefficient of Thermal Expansion
CVD	Chemical Vapor Deposition
D-T	Deuterium-Tritium
DS	Dispersion Strengthened
EIP	Elastic-Ideal (Perfectly) Plastic
ET	Effectively Stress-free Temperature
FEA	Finite Element Analysis
FEM	Finite Element Method
FRMMCs	Fiber-Reinforced Metal Matrix Composites
HHF	High Heat Flux
HIP	Hot Isostatic Pressing
ISS	International Space Station
ITER	International Thermonuclear Experimental Reactor
JT	Joining Temperature
LCF	Low Cycle Fatigue
LKH	Limited Kinematic Hardening
MMCs	Metal Matrix Composites
NBC	Number of Constrained Boundary Conditions
NE	Number of Elements
NF	Number of Degree of Freedom of Displacements
NG	Number of Total Gaussian Points
NGE	Number of Gaussian Points at Element
NK	Number of Total Nodes
NKE	Number of Nodes at Element
NSK	Number of Dimensions of Stress Vectors
NV	Number of Loading Corners
ODS	Oxide Dispersion Strengthened
PF	Poloidal Field
PFCs	Plasma Facing Components
PFMs	Plasma Facing Materials
PH	Precipitation Hardened
PMI	Plasma-Material Interaction
RAMS	Reduced Activation Martensitic Steel
RF	Radio Frequency
RT	Room Temperature
SD	Shakedown
SiC	Silicon Carbide
SIF	Standard Input File
TF	Toroidal Field
TiC	Titanium Carbide
TMF	Thermomechanical Fatigue
ULKH	Unlimited Kinematic Hardening

1. Introduction

In the introductory section, the motivation of the work is presented. Firstly, the structural components for fusion application are briefly explained. Secondly, the potential merits of fiber-reinforced metal matrix composites (FRMMCs) are presented as the candidate of the structural component for fusion application. Thirdly, the structural behavior of FRMMCs is discussed and the need for safety analysis of FRMMCs is proposed. Finally, previous literature studies about safety analysis are surveyed and the structure of this thesis is outlined.

1.1. Structural components for fusion application

1.1.1. Fusion reactor and the role of plasma facing components (PFCs)

The main worldwide consumption of energy is currently made of fossil fuels such as oil, coal and gas. During the last decades, their exploitation has been rising strongly because of the process of industrialization and the increasing world population. The burning of these fuels carries out grave climatic changes due to massive CO_2 emission into the atmosphere, furthermore, these resources are restricted, insufficient and more expensive. For these reasons, substitutes for fossil fuels should urgently be developed. Nuclear fusion is being investigated in this framework as an alternative energy concept. Although its performance presents difficulties from an engineering point of view, nuclear fusion has substantial advantages over current energy supplies, for example, a nearly inexhaustible fuel supply and a low environmental impact. In this respect nuclear fusion has significant potential.

The aim of thermonuclear fusion research is to confine a hot deuterium-tritium (D-T) plasma long enough such that fusion reactions between hydrogen ions occur leading to a commercial power generation[1]. The operation of fusion power reactors will impose very demanding operation conditions on the plasma facing components (PFCs). The PFCs will be operated in an extreme environment caused by incident particles and heat flux from the fusion plasma[2]. The surface of the plasma facing material (PFM) is subjected to erosion by energetic ions and neutral atoms escaping from the plasma. In a next generation fusion reactor, surface heat loads which have to be removed by the PFCs will reach up to 20 MW/m^2 under quasi-stationary conditions. In addition, high transient heat loads during strong edge localized mode (ELM)[3] activity of the plasma and off-normal events like disruptions can cause ablation at the heated surface. Tritium is absorbed by the PFMs or it can also be chemically bonded to redeposited material. Therefore the successful operation of fusion devices depends on the development of PFCs for withstanding the high heat flux loads and the particle and neutron fluxes from the fusion plasma [1-4].

---

[1] Nuclear fusion is the fusing of light atomic nuclei to form heavier nuclei. Of all pairs of light atomic nuclei capable of fusing it is the reaction between the two heavy hydrogen isotopes, deuterium and tritium, that affords the greatest energy yield at the lowest temperature. One deuterium and one tritium nucleus fuse here to form a helium nucleus. A fast neutron is then released that carries eighty per cent of the energy gained (17.5 MeV).

[2] Plasma is the “fourth aggregate state of matter”, largely composed of ionized atoms or molecules and their free electrons. Fusion-oriented high-temperature plasma physics is concerned with ionized hydrogen.

[3] Edge localized mode (ELM) is an instability which occurs in short periodic bursts during the high confinement mode (H-mode) in divertor tokamaks. It causes transient heat and particle loss into the divertor which can be damaging.

PFC components are located in the inner vessel of the fusion device. The cut-away view of the inner vessel of ITER (International Thermonuclear Experimental Reactor)[4] is represented in Figure 1.1. ITER will be the first fusion device to produce thermal energy at the level of an electricity-generating power station. It will provide the next major step for the advancement of fusion science and technology, and is the key element in the strategy to reach the following stage, a demonstration electrical power plant (DEMO), in a single experimental step. ITER is based on the tokamak concept[5] - a toroidal (doughnut-shaped) magnetic configuration in which to create and maintain the conditions for controlled fusion reactions. The overall ITER plant is comprised of the tokamak, its auxiliaries, and supporting plant facilities. The components of ITER are the superconductive coils, the blanket, the neutron shield, and a toroidally structured wall with PFC components. The details of ITER are represented in appendix A.

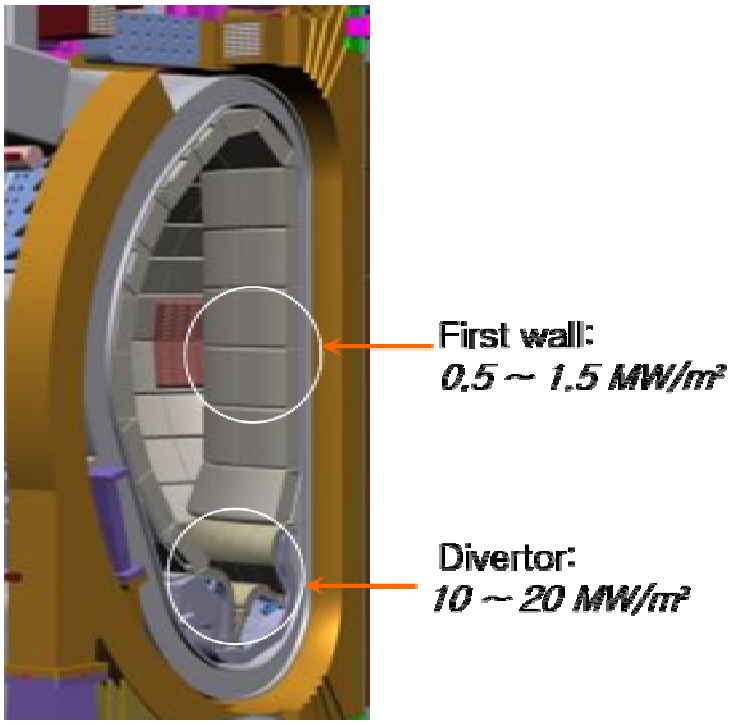

Figure 1.1. Cut-away view of vaccum chamber of ITER reactor: first wall and divertor.

[4] The International Thermonuclear Experimental Reactor (ITER) is the next major step for the development of commercial fusion device. Scientists and engineers from Europe, Canada, Japan, Russia, Korea, China and USA are working in an unprecedented international collaboration on this reactor, which is the second world's largest international co-operative research and development project after the International Space Station (ISS) (see appendix A).

[5] Tokamak is the most investigated and furthest advanced configuration for the magnetic cage of a fusion plasma. In a tokamak the plasma is confined by two superposed magnetic fields: firstly by a toroidal field produced by external coils and secondly by the field of a ring current flowing in the plasma. The field lines in the combined field are then helical. In addition, the tokamak requires a third, vertical field that fixes the position of the current in the plasma vessel and shapes the plasma edge. The plasma is normally induced by a transformer coil in the plasma. A tokamak therefore does not operate continuously, but in pulsed mode like the transformer. Pulse times of a few hours are anticipated in a future power plant. For technical reasons, however, a power plant has to operate in continuous mode and so methods of producing a continuous current are being investigated.

The inner vessel of ITER is composed of the plasma facing components, i.e. first wall and divertor. The first wall is the first element encountered by the plasma heat load. The function of the first wall is to absorb particles and radioactive heat fluxes from the plasma and thus protect the other components from the fusion plasma. Divertor components are used in order to achieve clean plasmas by impurity control. In a tokamak, the outer magnetic field lines are diverted to a location far from the plasma by means of a specially shaped magnetic field. Here the field lines contact the vessel wall on specially equipped divertor plates. The main function of the divertor system is to exhaust the major part of the alpha particle power as well as helium and impurities from the plasma. It must tolerate high heat flux loads and remove these heat loads reliably under quasi-stationary conditions.

The PFC component in the divertor region is composed of plasma facing material (PFM) and metallic heat sink furnished with cooling tubes (Figure 1.2). Since the PFC component receives severe localized and cyclic heat loads during fusion operation, it requires high thermal conductivity, excellent thermal shock resistance, low erosion by plasma particles and a good connection with the heat sink material for active cooling. Tungsten has been studied as the armor materials for the divertor component, because in this area the key issue is the erosion lifetime. Tungsten has a lower erosion rate due to its low sputtering yield and its higher sputtering threshold energy, as compared with other PFMs, such as beryllium and carbon. Another advantage of tungsten is its low tritium retention. Therefore tungsten is expected to be the PFM in the next generation fusion device[6].

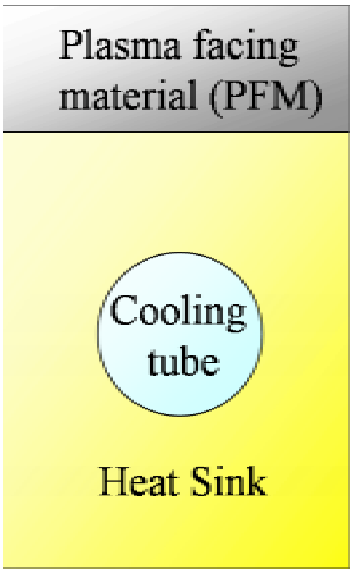

Figure 1.2. A geometry of possible plasma facing component (PFC) in the divertor region.

The heat sink materials have to exhibit a high thermal conductivity, needed for achieving an efficient heat transfer into the cooling system. In addition to thermal conductivity, other properties such as tensile strength and ductility, fracture toughness, fatigue at high temperature and irradiation resistance have to be taken into consideration. Copper alloys

[6] The plasma compatibility of tungsten is an issue, because a small amount of tungsten in the confined plasma region could lead to a very large power loss form the plasma. Therefore, in some PFC areas exposed to high thermal fluxes during normal operation and large energy excursions during plasma instabilities, other armor material, e.g. CFC, is selected.

(CuCrZr) have been considered as a structural material for the heat sink substrate due to their excellent thermal conductivity [5-6]. However, insufficient high temperature strength and large thermal expansion of copper based materials are the main limitation from a structure-mechanical viewpoint. Even with metallurgical hardening techniques, copper alloys have not been able to fully meet the high temperature strength requirement for the next generation fusion device [7]. Therefore, the development of new class of PFCs, such as metal matrix composite (MMC) materials, has been an important subject of investigations.

1.1.2. Fiber-reinforced metal matrix composites (FRMMCs) for PFC application

Many of our modern technologies require materials with unusual combinations of properties that cannot be met by the conventional metal alloys, ceramics, and polymeric materials. This is especially the case for materials in aerospace, underwater, and transportation applications. In this area, material property combinations and ranges have been extended by the development of composite materials. Most composites have been developed to improve combinations of mechanical characteristics such as stiffness, toughness, and high temperature strength [8-12].

Many composite materials are usually composed of two phases, i.e. matrix and reinforcement. In MMCs, the high strength, stiffness and creep resistance of ceramic reinforcements are combined with the toughness of a ductile metallic matrix. The major advantages and disadvantages are summarized in Table 1.1 [13]. Fiber-reinforced metal matrix composites (FRMMCs) have been developed since the 1960s. Their major advantages are high specific stiffness, strength, and tailorable properties. These advantageous properties of FRMMCs made a wide application range in many structural components in defense, aerospace, and leisure industries [14-15].

Table 1.1. Advantages and disadvantages of MMCs compared with other materials.

MMCs compared with:	**MMCs' advantages**	**MMCs Disadvantages**
Unreinforced materials	-higher specific strength -higher specific stiffness -improved high temperature creep resistance -improved wear resistance	-lower toughness and ductility -more complicated and expensive production methods
Polymer matrix composites [16]	-higher transverse strength -higher toughness -better damage tolerance -improved environmental resistance -higher thermal and electrical conductivity -higher temperature capability	-less developed technology -smaller data base of properties -higher cost
Ceramic matrix composites [17]	-higher toughness and ductility -ease of fabrication -lower cost -high thermal conductivity	-inferior high temperature capability

For the future PFC application, FRMMCs might be used as the interlayer of divertor component, as shown in Figure 1.3. SiC fiber reinforced Cu alloy (CuCrZr)) metal matrix composite may provide a highly creep resistant alternative for operation at higher temperatures. The SiC fibers of the reinforcement provide the necessary high temperature strength, whereas the Cu matrix mainly provides high thermal conductivity. Therefore, SiC fiber reinforced Cu alloy metal matrix can have a much higher ultimate strength, work-hardening rate and creep resistance than conventional materials at high temperature. The elastic stiffness as well as the coefficient of thermal expansion (CTE) can be tailored to wider ranges, which is especially advantageous for the application to bond-joint-type plasma facing components to reduce the thermal mismatch stress at the bonded interface of dissimilar materials. Therefore the permanent dimensional change by plastic ratcheting can be effectively suppressed. In addition, FRMMC can be introduced locally into the mostly highly loaded regions of the PFCs [18-20].

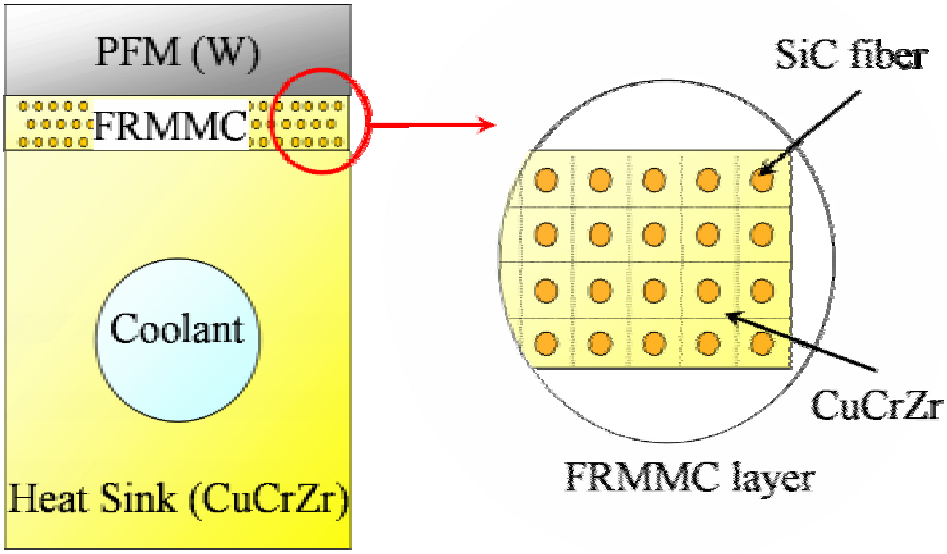

Figure 1.3. Plasma Facing Component with MMC layer

1.2. Why safety analysis of FRMMCs for fusion application?

1.2.1. Structural problem of FRMMCs

As mentioned in the previous section, the global properties of FRMMC are often increased by the existence of fiber reinforcement. However, there are some limitations to use FRMMC-based PFC in a tokamak-type fusion device, since the fusion device does not operate continuously, but in pulsed mode like the transformer. Therefore, FRMMC-based PFC will be subjected to the cyclic heat flux loading during fusion operation. This type of loading condition so called thermomechanical fatigue (TMF) loading has been extensively studied in the structural area [21-23]. Cyclic TMF loading is considered as one of the most severe loading conditions in FRMMC structure.

The possible thermal history of PFCs during fusion operation is schematically drawn

including the manufacturing process, as shown in Figure 1.4. In the manufacturing state, PFM, FRMMC layer, and heat sink will be assembled at the high joining temperature. The manufacturing stage is assumed to be a stress free state during the whole procedure. The assembled PFC is cooled down to room temperature in order to install in the vacuum chamber of the fusion device. Next the PFC is subjected to repeated high heat flux loading due to the pulsed fusion plasma operation.

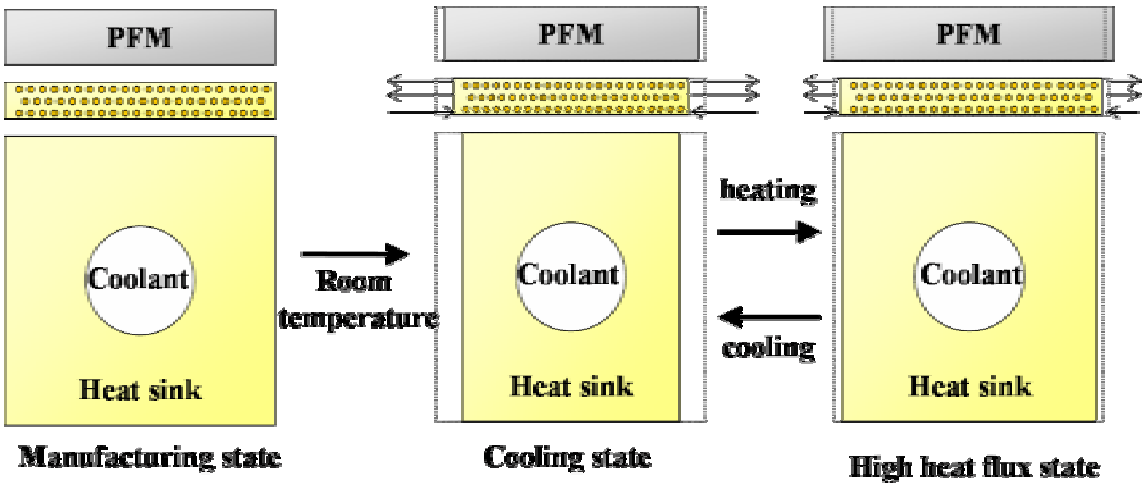

Figure 1.4. Thermal history of PFC during fusion operation including manufacturing process.

This thermal loading history generates two kinds of stresses in the FRMMC layer in the PFC. Firstly, the mechanical stress is generated due to the difference the difference of the CTE between tungsten PFM armor tile (3.9×10^{-6}/K at room temperature) and CuCrZr heat sink substrate (15.7×10^{-6}/K at room temperature). This causes so-called mismatch stress especially in the region near the bond interfaces between FRMMC layer and other components. This mismatch thermal stress is controlled mainly by the change of temperature at the bond interface, provided that steep thermal gradients are not the cause of any further significant stress contribution. Such a mismatch stress can already be generated during the manufacturing process resulting in residual stresses within the components. Additional stress from the subsequent thermal load is superposed on this residual stress field. Under this circumstance, the temperature difference between the stress free state (joining temperature) and the current state (high heat flux loading) is the controlling parameter. Secondly, the internal thermal stress is generated due to the CTE mismatch between SiC fiber reinforcement (5.7×10^{-6}/K at room temperature) and CuCrZr metal matrix (15.7×10^{-6}/K at room temperature). Internal stresses are common in most composite materials which are inhomogeneous. Such a misfit stress arises from a temperature change [24-26].

The internal stress of FRMMC can be easily understood by the finite element analysis (FEA). Thermo-elastic FEA was carried out for SiC fiber Cu-based metal matrix composite. The considered geometry was the two-dimensional square unit cell. The instantaneous thermal loading, i.e. 100 ^{o}C of temperature increase, was considered in this case. The von Mises stress field[7] was represented, as shown in Figure 1.5. The resulting stresses of FRMMC were visualized by different colors. From FEA result, it has been noticed that the resulting von

[7] Von Mises Stress is one of the most commonly used yield criteria. It is discussed in the section 6.5. For detail understanding, see references [25, 26].

Mises stress fields of the matrix were highly heterogeneous at a mesoscopic[8] level and exceeded the yield limit of the matrix. Von Mises stress of Cu matrix at the interface between fiber and matrix was higher than the other area of matrix [27-28].

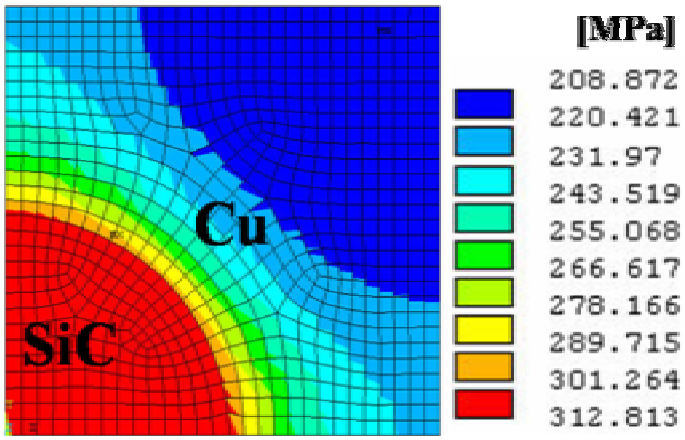

Figure 1.5. Von Mises stress profile with possible thermal loading.

Normally, the structure with instantaneous thermal loading is found to be safe, as far as homogeneous materials with ductile properties are concerned, even if the resulting thermal stresses exceed the yield stress of the material. Also fatigue is not found to occur before the thermal cycling is accompanied by repeated plastic deformation. However, in this work, FRMMC in the PFC is subjected to the cyclic heat flux loading with progressive plastic deformation. The density of dislocations produced during cyclic thermomechanical loading is often higher than during monotonic loading. Finally, the FRMMC will undergo the irreversible deformation and failure mechanisms. This cyclic thermal loading combined with mechanical loading will reduce the serviceability of FRMMC and result in its plastic collapse such as low cycle fatigue. Therefore, the FRMMC layer has to be investigated with the serviceability viewpoint to avoid the structural failure in the fusion relevant loading condition [29].

1.2.2. Structural safety assessment under cyclic loading

To avoid structural failure of FRMMC layer in the cyclic loading, it is very important to estimate safety limit of the structure using design-by-analysis (DBA). DBA is necessary to address the requirements for new constructions of structure while providing reasonable assurance of reliable operation. A significant ground rule for the DBA procedures was to permit the application of elastic stress analysis techniques. However, practically all of the criteria were developed based on consideration of elastic-plastic failure modes, i.e. plastic shakedown, ratcheting, shakedown, etc.

If the *elastic* limit is chosen as the safety criterion, the structure will be in strictly safe state since no plastic deformation occurs. However, the load carrying potential of the structure is not fully surveyed. In *plastic shakedown,* the structure experiences reverse or alternating plasticity over each cycle, that is, finite positive plastic strain in the first half of the load cycle

[8] The mesoscopic scale is the scale at which the constitutive equations for mechanics analysis are written. It will be discussed in the next chapter.

followed by equal magnitude negative plastic strain in the second half. Structures exhibiting plastic shakedown will fail after a number of load cycles due to low cycle fatigue. If the structure undergoes net increments of plastic strain with each load cycle, the strain will accumulate until gross plastic deformation and eventually incremental plastic collapse of the structure occurs. This failure mode is known as *ratcheting*. In *shakedown* limit, the structure experiences finite plastic deformations in the first few cycles, which give rise to residual stress in the structure such that in subsequent load cycles only elastic deformation of the structure occurs. Therefore, the shakedown limit might be the relevant safety criterion in this work since it has less stringent rules without occurring progressive plastic failure, such as low cycle fatigue. The details of structural behaviors are discussed in the following chapter.

The main objective of this work is to describe the shakedown safety criterion of the FRMMC layer. The shakedown safety limits can be obtained for the cyclic thermomechanical loading. The shakedown limit is schematically represented in the thermal and mechanical loading space, as shown in Figure 1.6. Here, *x*-directional axis and *y*-directional axis indicate the mechanically applied stress and the thermal stress, respectively. The ellipsoidal plane with grey color indicates the shakedown safety limit. If the loading paths are in the shakedown safety limit, FRMMC is in a safe state. To the contrary, if the loading paths are outside of this safety limit, the FRMMC layer might be unserviceable due to progressive plastic deformation. Therefore, the serviceability of FRMMC can be discussed with the shakedown limits and the realistic loading paths of the structure.

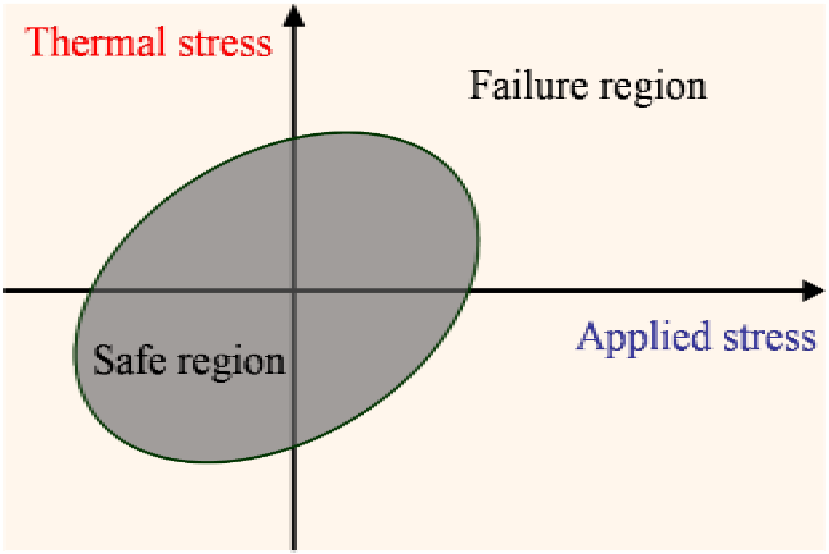

Figure 1.6. Schematic shakedown safety criterion for cyclic thermomechanical loading.

1.2.3. Overview of shakedown analysis

There are several systematic methods to obtain shakedown safety limit, that is, experimental method, incremental FEM analysis, and direct method with the optimization tool so called shakedown analysis. In situ *experimental investigations* have been rarely performed due to their prohibitive cost [30]. The most classical approach for the structural safety assessment consists as a detailed study of its stress, strain and displacement fields, so called *incremental analysis* (step-by-step finite element analysis). Under the action of variable repeated

mechanical and thermal loading the successive stages must be examined in which time-dependent stress and strain states develop. It requires an excessive computational cost and a cumbersome identification process associated with each type of material. In addition, the existing constitutive equations also present some difficulties in the description of the phenomenon of incremental plastic collapse. Therefore the increment analysis is not a practical approach [31].

Shakedown analysis is based on shakedown theory, which generalized the limit analysis theory to the case of cyclic loads. The shakedown theory was founded in the 1930s. The computational shakedown analysis has been recently implemented with the finite element method (FEM) and the nonlinear constrained optimization program. The FEM-based shakedown analysis, that is, direct method rests on the direct computations and does not need any information about the loading path. Therefore, if the history of loads during the lifetime of the considered mechanical elements is not precisely known, shakedown analysis is an appropriate tool to determine shakedown safety limits.

The computational methods between incremental FEM analysis and shakedown analysis are schematically compared in Figure 1.7. In the step-by-step incremental analysis, computational calculation has to be performed for the whole loading path since it is path-dependent. Therefore, the shakedown safety limits determined by incremental analysis are dependent on the considered loading path. If the loading path is changed (Path 1 to Path 2), the computational analysis has to be carried out for the changed loading path. It means that the incremental analysis may be an impractical approach for the structural safety assessment. However shakedown analysis does not necessarily require the full information of the loading path. It needs only the elastic information at the corners of the considered loading space. Although the loading path is changed, the computational analysis is not required since it is path-independent. Therefore shakedown analysis is usually less laborious and more effective to determine shakedown safety limit from a computational standpoint. In this work, the FEM-based shakedown analysis will be used to obtain shakedown safety limit of the FRMMCs for general thermomechanical loading.

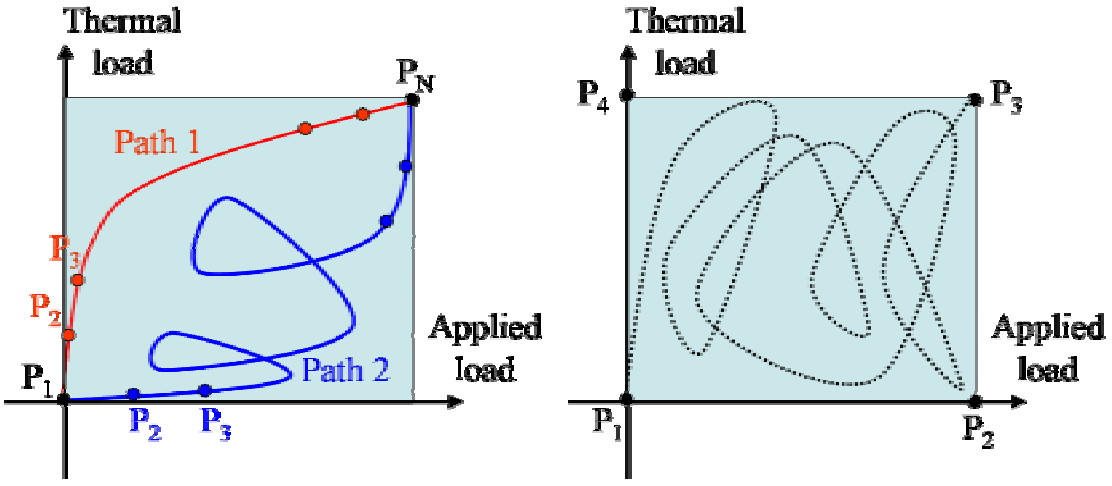

Figure 1.7. Schematic of computational methods to determine shakedown safety limit: (a) incremental FEM analysis and (b) FEM-based shakedown analysis.

1.3. Literature reviews

In this section, the extensive literature studies to determine shakedown safety limit are reviewed, that is, experimental approach, incremental FEM analysis, and FEM-based shakedown analysis. Since the safety assessment of composite materials is the main theme of this work, the literatures are investigated with a focus on the composite materials at each method. For the FEM-based shakedown analysis, the extensive reviews are performed from classical theorems to various application fields.

1.3.1. Conventional methods

Experimental approach

To date, there are not many experimental results for the shakedown limits because of experimental difficulties. Two-bar experiments using copper at ambient temperature were described by Ponter et al [32], in which the thermal strains are simulated by means of electrical signal. The elastic shakedown limits and ratcheting limits under tension-torsion loadings were determined by Heitzer et al [33]. The cyclic plastic deformation tests were carried out to verify FEM-based shakedown analyses by Lang et al [34]. The experiment comprised a water-cooled internal tube, and three insulated heatable outer test bars and the system was subjected to alternating axial forces, superimposed with alternating temperature. The elastic-plastic behavior of a fibrous boron-aluminum composite was investigated by Dvorak et al [35]. They described well the results of an experimental investigation of initial and subsequent yield surfaces and of plastic strains of a MMC under many plane stress loading programs. The behavior of the composite when subjected to mechanical and thermal loading was investigated by Jansson and Leckie. Shakedown limits were determined by cyclic thermomechanical test and compared with the values which obtained by step-by-step numerical method [36-37].

Incremental FEM analysis

Many numerical analyses have been carried out using a unit cell micromechanical model to compute the mechanical or thermomechanical behavior of composite materials reinforced by continuous fibers and short discontinuous fibers. Gunawardena et al. have developed constitutive laws for both strongly and weakly bonded composites, with emphasis on the role of the interface between the fibers and the matrix and the residual stresses incurred during the fabrication [38]. Zahl et al. investigated the transverse behavior of metal matrix composites with a strongly bonded interface using a cell model, with emphasis on the influence of the fiber arrangement, volume fraction and loading direction on the transverse strength [39]. Du and McMeeking et al. [40] studied the influence of a thin, well bonded ductile interphase between the fibers and the matrix on both the longitudinal and transverse composite strength. To date, only a few researchers have examined the properties of multi-directionally reinforced MMCs, i.e. laminate structure. There were several attempts to focus on a cross-ply laminate whose numerical investigation necessitates a three-dimensional model. Biglow calculated thermal residual stresses in a SiC/Ti [0/90] laminate [41]. For the same material, Nicholas et al. analyzed the influence of a thermo-mechanical cyclic loading on the fatigue behavior of the composite [42]. Sherwood and Quimby used viscoplastic constitutive equations based on the theory of Bodner and Partom to investigate the damage growth in titanium-based metal matrix composite [43]. Ismar et al. focused on the thermo-mechanical behavior of aluminum bi-directionally reinforced with SiC fibers [44-45].

1.3.2. FEM-based shakedown analysis

Classical shakedown theorem

The classical field of application of shakedown theory is the assessment of mechanical structures of structural elements exposed to variable thermo- and/or mechanical loads. It addresses basically failure (non-shakedown) caused by unlimited growth of plastic dissipation during the loading process, leading to incremental collapse or alternating plasticity. Limit analysis covers the particular case of the instantaneous collapse under a monotonous loading. The foundations of shakedown theory have been laid by Melan [46] and Koiter [47], who derived sufficient criteria for shakedown and non-shakedown, respectively, for elastic-perfectly plastic structures in the framework of geometrically linearized continuum mechanics. Due to the evident practical importance, their classical theorems have been extended to larger classes of problems and widely applied to structural analysis. Reviews and overviews of such studies can be found e.g. in Gokhfeld and Cherniavsky [48], König [49], Mróz et al. [50], Weichert and Maier [51], Staat and Heitzer [52].

Material hardening effect

Material hardening has been addressed in the pioneering work by Melan, where unlimited linear kinematic hardening was taken into account in the framework of continuum mechanics [53]. On the basis of this concept further results have been obtained by Neal [54], Ponter [55], Zarka and Casier [56]. For discretized structures and piecewise linear yield function, Maier investigated linear hardening and softening effects [57], and König and Siemaszko considered the effects of strain hardening in shakedown process [58]. With the help of generalized standard material model introduced by Halphen and Nguyen [59], Mandel [60] gives a simple and pertinent formulation of Melan's theorem for hardening materials. By imposing limits to the evolution of the internal parameters in this model, Weichert and Gross-Weege interpreted it as a simplified two-surface material allowing for limited kinematic hardening and applied it numerically [61]. The concept of internal variables for the representation of the hardening material behavior was in the sequel also applied by Comi and Corigliano [62] and Polizzotto *et al.* [63]. More general nonlinear hardening has been investigated in the context of discrete systems by Maier [64] and using overlay model by Stein *et al*. [65]. Other applications of internal parameters representation of changes of material properties can be found in Corigliano et al. [66] and Pycko and Maier [67].

Geometrically nonlinear effect

The geometrically nonlinear problem has been studied firstly by Maier, who introduced a new class of shakedown problems for pre-stressed discrete structures and extended Melan's and Koiter's theorems as to include so called second order geometric effects by using piecewise linear yield conditions [68]. Siemaszko and König showed the influence of geometrical effects on the stability of the deformation process for particular structures under certain assumptions on the deformation modes [69]. Weichert investigated the problem of geometrical effects in several papers within the frame-work of continuum mechanics and gave an extension of Melan's theorems which is practically applicable to situations where information about the expected deformation pattern is available [70-71]. He assumed an additive strains decomposition and applied it to shell-like structures undergoing moderate rotations at small strains [72]. The same decomposition of total strain has been used by Gross-Weege [73]. He gives unified formulation of Melan's theorem for structures subjected to a constant load, responsible for large displacements, and to small additional variable loads causing small additional displacement. The same concept was used by Pycko and König [74]. Recently, Polizzotto and Borino give an extension of Melan's and Koiter's shakedown theorem in the framework of large displacements [75]. They studied the asymptotic response

of the structure subjected to periodically variable loads in order to show the conditions under which there may exist a stabilized long term response. In order to overcome the restrictions of an additive decomposition of total strains, the multiplicative strain decomposition rule was used by Saczuk and Stumpf [76], Tritsch and Weichert [77] and Stumpf [78]. An extension of the Gross-Weege's shakedown formulation [73] to more general nonlinear problems is proposed in Saczuk and Stumpf [76]. In Tritsch and Weichert a sufficient Melan-type statement for shakedown and a comparative study with previous works are given [77]. Stumpf employed the multiplicative decomposition of total strains and attempted to reformulate shakedown theorems stating that shakedown occurs if there exists some real self-equilibrated residual state, which is dependent on the loading and unloading paths [78]. More recently, Saczuk proposed a criterion of adaptation process, accounting for the influence of deformation path on the material properties based on the continuum model within the theory of differential inequalities [79].

Three-dimensional modeling

The studied structures were often only two-dimensional structures, and only few researchers have been working on the development of methods for three-dimensional shakedown and limit analyses. Feng and Liu have studied shakedown of kinematic strain-hardening three-dimensional structures [80]. Chen and Ponter have developed a method to evaluate shakedown limits of three-dimensional structures, which is based on linear matching method [81]. Khalij *et al.* have considered three-dimensional structures submitted to cyclic loading [82].

Application to composite material

Although the application of shakedown theory by means of structural mechanics is nowadays well established, the use of shakedown analysis to assess and to design composite materials is rather new. The first attempts had been undertaken in a pioneering work by Tarn et al. for the determination of safe loading domains of unidirectional composites under an axi-symmetric loading [83]. Ponter and Leckie investigated the shakedown behavior of an aluminum/ alumina system under fluctuating temperatures by means of the homogenization technique, focusing on the application of the upper bound theorem [84]. Making use of the finite-element analysis, Carvelli et al. applied the upper bound theorem of the shakedown theory to two-dimensional problems [85]. Weichert et al. calculated the admissible loading domains for composites by using the lower bound theorem [86-87]. Maier et al. used finite element analysis and the kinematic approach of shakedown coupled with periodic homogenization to investigate two-dimensional perforated sheets [88]. Dvorak et al., who have widely reported on theoretical and experimental micromechanics of heterogeneous media, studied the shakedown of metal matrix composites [89]. Weichert and Hachemi coupled the periodic homogenization and shakedown theories to study the strength of periodic composites [90]. Schwabe has extensively studied periodic composites using two-dimensional shakedown analysis [91].

Application to nuclear technology

The importance of nuclear power and the necessity for ensuring continued satisfactory operation has been investigated for several decades. One of the primary factors that could affect the continued operation and development of nuclear power relates to aging of the plants and its potential impact on performance. Nuclear power plants are designed, built, and operated to standards that aim to reduce the releases of radioactive materials to levels as low as reasonably achievable. Nuclear power plants, however, involve complex engineering structures and components operating in demanding environments that potentially can challenge the high level of safety (i.e. safety margin) required throughout the operating life of

the plant. It is necessary that safety issues related to plant aging and continuing the service of the nuclear plants be resolved through development of sound scientific and engineering understanding. To secure the structural safety of nuclear component, the integrity or reliability investigation of the pressure boundary components is essential. An extensive piping research program has been conducted to demonstrate the safety and reliability of piping system of nuclear component. In order to evaluate the fatigue crack growth behavior in piping structure, the shakedown analysis is carried out [34,92-96].

1.4. Scope of the thesis

From the introductory discussions and literature reviews, the following contents were summarized.

FRMMCs will be exposed to significant cyclic heat flux loading in the fusion device, and the resulting stress fields at mesoscopic level would be highly heterogeneous and often exceed the elastic limit of the matrix. The cyclic thermo-mechanical loads together with macroscopic local strain gradient can lead to a progressive accumulation of plastic deformation and finally to structural failure. Therefore, it is important to predict the safety assessment against structural failure. For the structural safety assessment of FRMMC, the shakedown safety limit was expected to be the relevant safety criterion since it had less stringent rules without occurring progressive plastic failure such as low cycle fatigue.

Although there have been two conventional approaches to determine shakedown limit, that is, experimental and incremental approaches, they have some limitations. Firstly, the experimental approach required a very high cost and then cannot be automatically used except for certain validation cases. Secondly, the incremental FEM analysis calls for an excessive computational cost and a cumbersome parameter identification process with each type of material. In addition, the existing constitutive equations also present some difficulties in the description of the ratcheting phenomenon. Also it requires detailed knowledge of load history and material law, neither of which can be guaranteed to be available to the required extent in practice. By contrast, shakedown analysis is expected to be less laborious and more effective to determine shakedown safety limits from a computational standpoint.

Classical shakedown theorem is very well defined and extended to consider material hardening effect and geometrically nonlinear effect by several authors. However, FEM-based shakedown analysis has been recently studied, since this approach led to a large-scale nonlinear constrained optimization problem. Therefore, the application study of shakedown analysis has not been extensively carried out for a realistic situation. The primary purpose of this work is to obtain safety shakedown limits for three-dimensional fiber-reinforced metal matrix composite material under fusion relevant cyclic thermomechanical loading condition. The obtained shakedown limits are compared with the realistic loading paths obtained by incremental analysis. For this, the following studies are mainly performed in this work.

(i) FEM-based shakedown analysis tool is developed with nonlinear optimization program and extended to three-dimensional model.

(ii) The shakedown analysis is performed for the complex three-dimensional FRMMC (lamina and laminate) considering thermomechanical loading.

(iii) For the comparison with the results of the shakedown analysis, thermomechanical loading path is obtained using incremental analysis in fusion-relevant loading.

This dissertation is structured in eight chapters. At the end of the thesis, five appendices with more detailed information including fusion basics, computational codes, and additional graphical results are attached.

Chapter 2. Theoretical Backgrounds

This chapter is devoted to the description of the structural behaviors and the formulation of the static shakedown theorem in the framework of continuum mechanics. The adopted constitutive equations and general assumptions will be reviewed by considering an evolution of a three-dimensional elastic-plastic body. The proof of static shakedown theorem is represented using thermodynamic concept. Finally the shakedown theorem is extended into the thermal loading case. The unlimited kinematic hardening effect and the limited kinematic hardening effect are also considered in the shakedown theorem.

Chapter 3. FEM-based Shakedown Formulation

In this chapter, the computational formulation of shakedown theory is carried out with finite element discretization. Firstly, the brief introduction to FEM is represented. Next the computational details for FEM-based shakedown formulation are represented with the nonlinear large-scale mathematical optimization programming.

Chapter 4. Verification Tests

The developed computational tool of FEM-based shakedown analysis is extensively verified with the conventional models. The used examples are two-dimensional plate with a hole and Al_2O_3 fiber reinforced Al metal matrix composite. The results of shakedown analysis are compared with the previous shakedown results, analytical results, and experimental results.

Chapter 5. Description of Problem

In this chapter, the details of the problem are represented since the fusion loading history is not easily understood. Analysis objective, material properties, model geometry, and loading history are explained for FRMMC-based PFC. Finally the methodology of structural safety assessment is described using shakedown analysis and incremental analysis.

Chapter 6. Results of Shakedown Analysis

Three-dimensional lamina and laminate composites are investigated to obtain shakedown limits in the biaxial loading space with temperature change. The results of shakedown limits are numerically illustrated and compared with elastic limits. The influences of geometrical effect, fiber volume fraction, loading direction, hardening effect are extensively investigated. In the last section, the results are discussed with von Mises stress distribution.

Chapter 7. Application of Shakedown Analysis

Several parametric studies are performed by considering typical fusion loading condition. The loading paths are obtained using thermo-elasto-plastic incremental analysis. The obtained paths are illustrated and compared with shakedown limits in three-dimensional loading space. From these comparison results, the structural safety of FRMMC-based PFC component is discussed using the shakedown viewpoint.

Chapter 8. Summary
Finally, the conclusions and contributions of this thesis are summarized.

APPENDIX

Appendix A. Thermonuclear Fusion
This chapter contains some basic notions about nuclear fusion and main structural components, an introduction to the next major steps in fusion research, ITER, PFC, and the related material questions.

Appendix B. CMat3D: Fortran Code for C-Matrix
For the FEM-based shakedown formulation in chapter 3, the equilibrium [C] matrix is used as constraints of the formulation. This procedure is performed similar to FEM discretization. In this appendix, Fortran code of the formulation of the equilibrium [C] matrix for three-dimensional model is represented.

Appendix C. An Example of SIF (Standard Input File)
In this work, the FEM-based shakedown analysis is carried out by using an advanced optimization code LANCELOT which is based on an augmented Lagrangian method. LANCELOT needs a special input format the so called standard input file (SIF). This file has to include all the information of shakedown analysis, that is, elastic stress, equilibrium [C] matrix, shakedown inequality constraints, etc. In this appendix, an example of SIF file is represented for the simple two-dimensional model with two elements and six nodes.

Appendix D. Shakedown Limits in Cooling
In chapter 6, the results of shakedown limits are represented for the positive thermal loading (heating). Since the manufacturing temperature of FRMMC is normally higher than its operation temperature, FRMMC undergoes negative thermal loading in the manufacturing process. Therefore, the results of the shakedown limits for the negative thermal loading (cooling) are represented.

Appendix E. Shakedown Limits and Loading Paths
Since there are some ambiguous regions in the figures of the shakedown limits with real loading paths, represented in three-dimensional loading spaces (chapter 7), the additional diagrams are represented as two-dimensional viewpoints.

2. Theoretical Backgrounds

In this chapter, several theoretical backgrounds are represented. In the first section, several structural behaviors subjected to variable repeated loading are investigated including shakedown behavior. Secondly, previous investigations about shakedown theory are reviewed. Finally, the shakedown analysis is extended into the complex system combined with thermal loading and hardening effects.

2.1. Shakedown, one of structural behaviors

The development of numerical methods for assessment of the long-time behavior, the usability and safety against failure of structures subjected to variable repeated loading is of great importance in mechanical and civil engineering. The behavior of the structure subjected to cyclic loading can be classified into elasticity, instantaneous plastic collapse, incremental plastic collapse, and shakedown. In the following sections, the details of structural behavior are investigated.

2.1.1. Elasticity

All materials are composed of atoms, which are held together by bonds resulting from the interaction of electromagnetic fields. Elasticity is directly related to the relative movement of atoms. The physical study of the properties of an atomic lattice leads to the theory of elasticity, but a much easier way is to write the mathematical constitutive equations directly at the mesoscale[1] level using the property of reversibility of strain, which implies a one-to-one relationship, and eventually incorporate the properties of linearity and isotropy. Elastic deformation is not permanent, which means that when the applied load is released, the piece returns to its original shape. As shown in the stress-strain plot (Figure 2.1), application of the load corresponds to moving from the origin up and along the straight line. Upon release of the load, the line is traversed in the opposite direction, back to the origin.

2.1.2. Instantaneous plasticity

As the material is deformed sufficiently high beyond the elastic limit, the instantaneous load-carrying capacity of the structure becomes exhausted and unconstrained plastic flow and damage occur. In this loading, the stress is no loner proportional to strain, and permanent, nonrecoverable, or instantaneous plastic deformation, as shown in Figure 2.2.

From an atomic perspective, plastic deformation corresponds to the breaking of bonds with original atom neighbors and then reforming bonds with new neighbors as large numbers of atoms or molecules move relative to one another. Therefore, upon removal of the stress, they

[1] Continuum mechanics deals with quantities defined at a mathematical point. From the physical point of view, these quantities represent averages on a certain volume. The “representative volume element (RVE)” must be small enough to avoid smoothing of high gradients but large enough to represent an average of the microprocesses. There are three scales concerning the phenomenon and damage. The microscale is the scale of the mechanisms used to consider strains and damage. The mesoscale is the scale at which the constitutive equations for mechanics analysis are written. The macroscale is the scale of engineering structures.

do not return to their original positions.

There are two types of plastic flow: perfectly plastic flow and plastic flow with hardening. Perfectly plastic flow without hardening corresponds to the case in which the stress remains constant during the flow; this is exhibited by e.g. mild steel in the flat (plateau) zone. If the stress still increases, the hardening effect should be considered. The hardening effect on the shakedown theory will be discussed in the section 2.3.

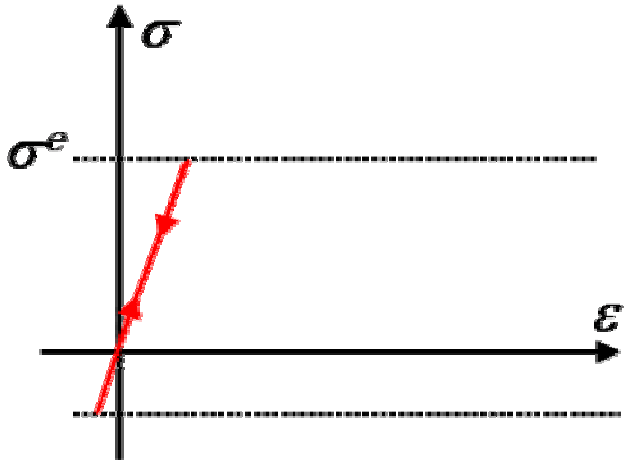

Figure 2.1. Schematic stress-strain diagram showing linear elastic deformation.

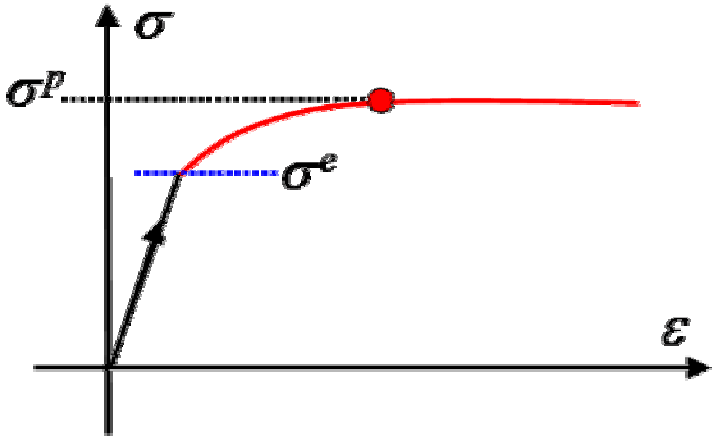

Figure 2.2. Schematic stress-strain diagram showing instantaneous plastic flow.

2.1.3. Incremental plasticity (ratcheting)

If the plastic strain increments in each load cycle are of the same sign then, after a sufficient number of cycles, the total strains (and therefore displacements) become so large that the structure departs from its original form and becomes unserviceable as shown in Figure 2.3. This phenomenon is called “incremental plasticity” or “ratcheting.” In this case, the structure experiences net increments of plastic strain with each load cycle. The resulting strain will accumulate until gross plastic deformation and eventually incremental plastic collapse of the structure occurs as follows.

$$\Delta\varepsilon_{ij}^{r} = \int_{\tau} \dot{\varepsilon}_{ij}^{r} dt \neq 0, \qquad \dot{\varepsilon}_{ij}^{r} \neq 0 \tag{2.1}$$

$$\dot{\varepsilon}_{ij}^{r} = \dot{\Lambda}(t)\Delta\varepsilon_{ij}^{r} \tag{2.2}$$

$\Delta\varepsilon_{ij}^{r}$ indicates the ratcheting strain due to plastic strain accumulation during one cycle time period τ. Here, $\dot{\Lambda}(t)$ is monotonic function.

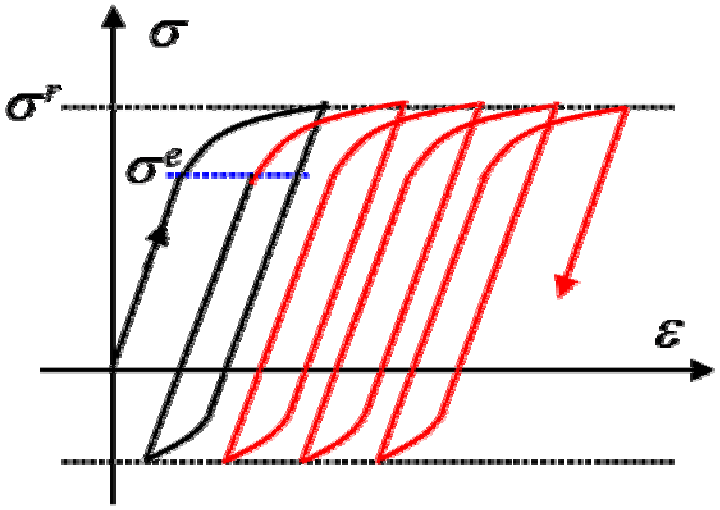

Figure 2.3. Schematic stress-strain diagram showing incremental plastic collapse (ratcheting).

2.1.4. Alternating plasticity (plastic shakedown)

If the strain increments change sign in every cycle, they tend to cancel each other and total deformations remain small leading to "alternating plasticity (AP)", as shown in Figure 2.4. In this case, the structure experiences reverse of alternating plasticity over each cycle; that is, finite positive plastic strain in the first half of the load cycle followed by equal magnitude negative plastic strain in the second half (such that the net plastic strain $\Delta\varepsilon_{ij}^{AP}$ over the cycle time period τ is zero), as represented in the following equation.

$$\Delta\varepsilon_{ij}^{AP} = \int_{\tau} \dot{\varepsilon}_{ij}^{AP} dt = 0, \qquad \dot{\varepsilon}_{ij}^{AP} \neq 0 \tag{2.3}$$

This is sometimes called plastic shakedown, because the structure shakes down or settles to a steady state of non-cumulative cyclic plastic straining. Structures exhibiting plastic shakedown will fail after a finite number of load cycles due to low cycle fatigue. However in some practical cases, very local alternating plasticity is permitted in engineering design. By consequence a small plastic cell is surrounded by a large elastic body. This is called overall shakedown. For example, through a local thickness of a shell, the alternating plasticity should be restricted to less than 20 % of the section for safety assessment [52].

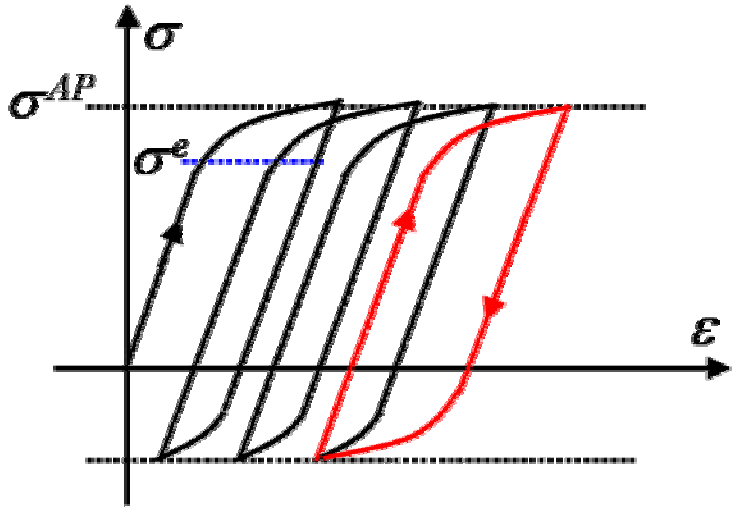

Figure 2.4. Schematic stress-strain diagram showing alternating plasticity.

2.1.5. Shakedown

If neither alternating plasticity nor ratcheting occur when the structure is cyclically loaded between the first elastic yield limit and plastic collapse load, the structure is said to exhibit shakedown (SD). In shakedown, the structure experiences finite plastic deformations in the first few cycles. After some cyclic loads, plastic flow and damage cease to develop further and the accumulated dissipated energy in the whole structure remains bounded such that the structure responds purely elastically to the applied loads, as shown in Figure 2.5. This phenomenon is sometimes referred to as elastic shakedown, to make it clear that after the initial elastic-plastic response the structure shakes down to wholly elastic behavior.

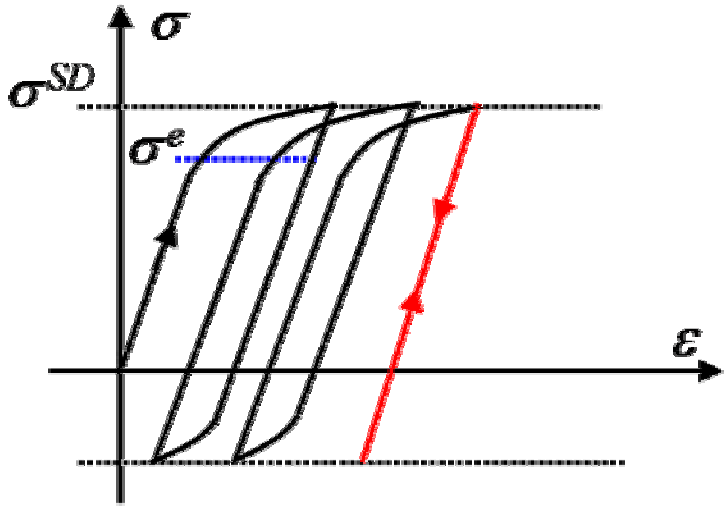

Figure 2.5. Schematic stress-strain diagram showing shakedown.

2.2. Review of static shakedown theorem

Shakedown theory is based on the fundamental theorems formulated for the case of a three-dimensional elastic-ideal (perfectly) plastic (EIP) body. The theorems enable us to determine the conditions for shakedown together with the conditions for the occurrence of limit states such as alternating plasticity or incremental plastic collapse (ratcheting), without the need to carry out the calculations of the development of deformation in the process of stabilization of a stress cycle. Before the details of computational procedures are described, it is worthwhile to briefly discuss some useful theory of ideal plasticity and the fundamental shakedown theory.

2.2.1. Prerequisites from mechanics of elastic-ideal plastic solids

The condition of equilibrium requires that $\sigma_{ij} = \sigma_{ji}$ which means the stress tensor is symmetric. The strain tensor components at small displacements have the following form, called compatibility condition, where u is the displacement vector.

$$\varepsilon = \frac{1}{2}\left(\nabla(u) + \nabla(u)^T\right) \tag{2.4}$$

In the theory of EIP solids considered here, the total strain tensor ε is assumed to be composed of its elastic part ε^e and its plastic part ε^p. The elastic part is related to the stress tensor by means of Hook's law. Plastic deformation can develop when the stress components satisfy a yield condition.

So far as the EIP model is concerned, the yield surface remains unaltered over the deformation process. The end of the stress vector can either lie inside the yield surface (elastic domain) and then the plastic strain rates are equal to zero or can touch the yield surface thus generating non-vanishing plastic strain rates. The situation in which the stress vector would 'pierce' the yield surface to lie partly outside is impossible in the case of ideal plasticity. In the stress space, loading occurs when the stress point is on the yield surface and remains there. If the stress point moves to the inside of the yield surface, it causes unloading (Figure 2.6). Here, the direction of vector $\partial f / \partial \sigma$ is in the direction of outer normal n to the yield surface.

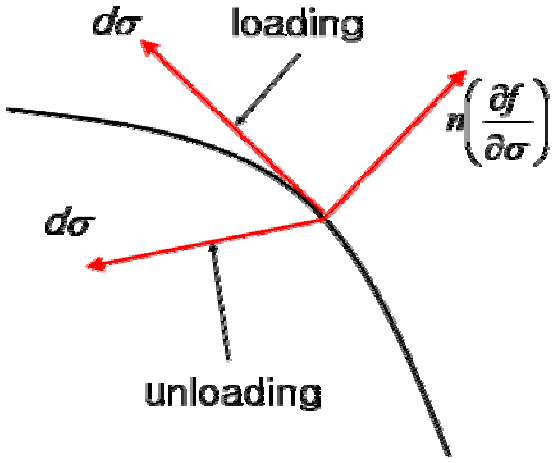

Figure 2.6. Loading and unloading for ideal plastic materials.

The stress state corresponding to a stress point lying inside the yield surface is usually termed a safe stress state and denoted by $\sigma_{ij}^{(s)}$, whereas the stress states corresponding to positions of the stress point including those on the yield surface are termed admissible stress states $\sigma_{ij}^{(a)}$. The equation of a yield surface may be written down in the following forms.

$$F(\sigma_{ij}^{(s)}) < 0, \quad F(\sigma_{ij}^{(a)}) \leq 0 \tag{2.5}$$

The yield surface is always convex. In the tree-dimensional space an arbitrary plane intersection of a convex surface gives a convex curve, i.e. a curve that can be intersected by a straight lime in two points only. The assumption of convexity, i.e. Drucker's stability postulate, is of primary importance in the theory of plasticity. In the Drucker's postulation, the following assumption is considered [97-98].

> There exists a yield surface that separates the plastic region from the elastic region. The change of the stress state within or along the surface will cause only elastic deformation, and change of the stress state from the yield surface toward its interior will cause elastic unloading. Plastic loading will occur only if the increment of the stress is directed toward the outside of the yield surface. The relationship between the infinitesimal increments of the stress and the plastic strain is linear.

When an EIP element under a certain stress state is subjected to a slow loading and unloading process[2], Drucker's postulate asserts that if a material is stable (Figure 2.7). Then the following inequality condition must be satisfied. Here σ_{ij} is the yield surface stress state generating the plastic strain $\dot{\varepsilon}_{ij}^{p}$.

$$[\sigma_{ij} - \sigma_{ij}^{(s)}]\dot{\varepsilon}_{ij}^{p} > 0 \tag{2.6}$$

$$[\sigma_{ij} - \sigma_{ij}^{(a)}]\dot{\varepsilon}_{ij}^{p} \geq 0 \tag{2.7}$$

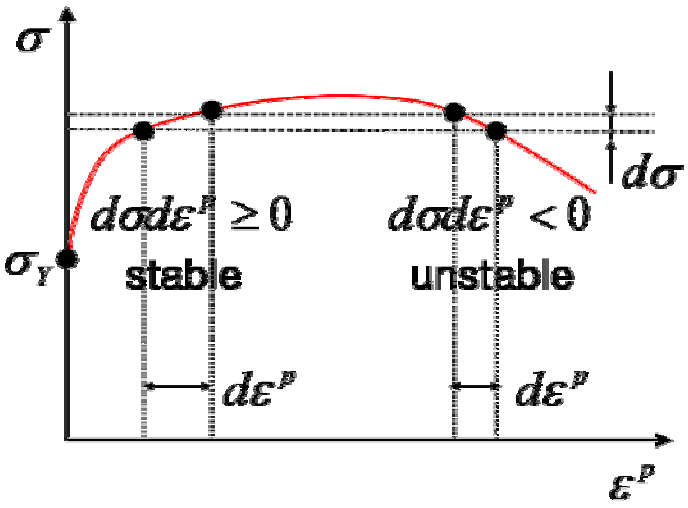

Figure 2.7. Stable and unstable material behavior.

[2] In other words, a quasi-static isothermal loading process is assumed.

For smooth convex yield surfaces, the above formulated postulate leads to the following statement. If the plastic strain rates are represented in the stress space, the plastic strain rate tensor is directed along the outer normal to the yield surface. This statement is the well-known associated flow rule or normality rule in the theory of plasticity since it relates the plastic region at a point in the body with the location of the stress point on the yield surface.

The plastic strain rate is determined by the flow rule associated with the yield condition within a certain common factor $d\lambda$, as follows.

$$d\varepsilon_{ij}^{p} = \frac{\partial F(\sigma_{kl})}{\partial \sigma_{ij}} d\lambda \tag{2.8}$$

Since the stress state in an ideal plastic medium is bounded by an appropriate yield condition, the external loads supported by a body in agreement with equilibrium requirements must also be bounded by certain limiting condition. Application of the limit load brings about the plastic collapse which manifests itself by unlimited increase in deformation under steady load. Such a concept of plastic collapse is applied in shakedown theory.

In order to formulate the fundamental theorem of the shakedown theory, the following principle of virtual work is employed.

$$\delta U_{\text{int}} = \delta W_{ext} \tag{2.9}$$

$$\int_V \{\sigma\}\{\delta\varepsilon\} dV = \int_S \{p^*\}\{\delta u\} dS + \int_V \{f^*\}\{\delta u\} dV \tag{2.10}$$

These equations are a generalization of the equilibrium conditions and they remain valid for an arbitrary system of external body forces f^* and surface traction p^* supported by the stress state and for an arbitrary displacement field δu compatible with a kinematically admissible strain distribution $\delta\varepsilon$. The work done by a self-equilibrated stress system on a kinematically admissible strain field is null from the equation (2.10).

2.2.2. Static shakedown theorem

The static approach to the analysis of shakedown condition in the presence of repeated loading is based on the static theorem formulated by Melan, who derived sufficient criterion for shakedown of EIP model (Figure 2.8). The static shakedown theorem is composed of the following statement.

The structure will shake down to the variable repeated loading, i.e. its behavior after a number of initial loading cycles will become purely elastic, if there exists a time-independent distribution of residual stresses $\overline{\rho}(\mathrm{x})$ such that its superposition with elastic stresses $\tilde{\sigma}^{e}(\mathrm{x},t)$ results in a safe stress state $\sigma^{(s)}(\mathrm{x},t)$ at any point of the structure under any combination of loads inside prescribed limits.

$$\sigma_{ij}^{(s)} = \tilde{\sigma}_{ij}^{e} + \overline{\rho}_{ij} \ \wedge \ \sigma_{ij}^{s} \in C^{i} \tag{2.11}$$

$$\bar{\rho}_{ij,j} = 0_i \;\; in\, V \;\wedge\; n_j \bar{\rho}_{ij} = 0_i \;\; on \;\; S_F \tag{2.12}$$

Then, the static (Melan's) theorem of shakedown can be expresses as follows.

> If there exists a safety factor $\alpha^{SD} > 1$ and a time-independent residual stress $\bar{\rho}(\mathrm{x})$, such that
>
> $$F(\alpha^{SD}\tilde{\sigma}^e(\mathrm{x},t) + \bar{\rho}(\mathrm{x}), \sigma_Y(\mathrm{x})) < 0 \quad \forall \mathrm{x} \in V \;\wedge\; \forall P(t) \in L \tag{2.13}$$
>
> is satisfied for all load domain $P(t)$ in L and for all x in V, then the body will shake down under the given load domain L.

An essential part of this statement is the assertion that, if shakedown is at all possible under a given repeated loading, then it will certainly take place. The shakedown will be caused by plastic deformations during the first cycles which are followed by a certain steady, independent of a further loading program, distribution of residual stresses. On the other hand, shakedown never takes place unless a time-independent distribution of residual stresses can be found such that under all the possible load combinations the sum of the residual and elastic stresses proves to be an admissible stress state [48].

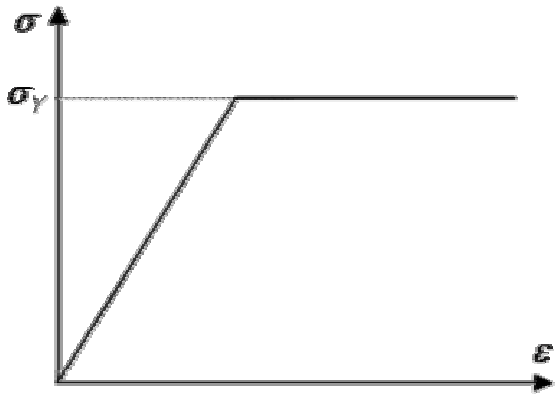

Figure 2.8. Stress-strain curve for elastic-ideal plastic (EIP) structure.

Proof

For the proof of the static shakedown theorem, a positive definite quadratic function $W(t)$, i.e. elastic strain energy, is considered as follows.

$$W(t) = \frac{1}{2}\int_{(V)} (\rho_{ij} - \bar{\rho}_{ij}) L^{-1}_{ijkl} (\rho_{kl} - \bar{\rho}_{kl}) dV \geq 0 \tag{2.14}$$

$$\rho_{ij} = \sigma_{ij} - \tilde{\sigma}^e_{ij} \tag{2.15}$$

In this equation, $\rho(\mathrm{x},t)$ denotes the current magnitude of actual residual stress field and $\bar{\rho}(\mathrm{x})$ indicates the time-independent residual stress field satisfying shakedown condition

(2.11) at a given loading cycle. σ_{ij} denotes the current stresses in a considered cycle reaching the yield surface at an instant at which the plastic strain rates at appropriate points of the body cease to be equal to zero. L^{-1}_{ijkl} is the component of the inverse elasticity tensor [L].

From the symmetry of the tensor L^{-1}_{ijkl}, it follows that the time derivative of elastic strain energy $\dot{W}(t)$ is expressed as follows.

$$\dot{W}(t) = \int_{(V)} (\rho_{ij} - \overline{\rho}_{ij}) L^{-1}_{ijkl} \dot{\rho}_{kl} dV = \int_{(V)} (\rho_{ij} - \overline{\rho}_{ij}) \dot{\varepsilon}^{r}_{ij} dV \tag{2.16}$$

Here $\dot{\varepsilon}^{r}_{ij}$ is the elastic strain rate corresponding to the residual stress state that result form the plastic deformation. Since the distribution of the total residual strain rate is composed of the elastic component $\dot{\varepsilon}^{e}(x,t)$ and the plastic component $\dot{\varepsilon}^{p}(x,t)$, $\dot{\varepsilon}^{r}_{ij}$ can be expressed as follows.

$$\begin{aligned} \dot{\varepsilon} &= \dot{\varepsilon}^{e}_{ij} + \dot{\varepsilon}^{p}_{ij} \\ &= L^{-1}_{ijkl} \dot{\sigma}_{kl} + \dot{\varepsilon}^{p}_{ij} \\ &= L^{-1}_{ijkl} (\dot{\tilde{\sigma}}^{e}_{kl} + \dot{\rho}_{kl}) + \dot{\varepsilon}^{p}_{ij} \\ &= \dot{\tilde{\varepsilon}}^{e}_{ij} + \dot{\varepsilon}^{r}_{ij} + \dot{\varepsilon}^{p}_{ij} \end{aligned} \tag{2.17}$$

$$\Rightarrow \quad \dot{\varepsilon}^{r}_{ij} = L^{-1}_{ijkl} \dot{\rho}_{kl} = \dot{\varepsilon}_{ij} - \dot{\tilde{\varepsilon}}^{e}_{ij} - \dot{\varepsilon}^{p}_{ij} \tag{2.18}$$

From equations (2.11), (2.15), (2.18), the time derivative of elastic strain energy $\dot{W}(t)$ is restated as follows.

$$\begin{aligned} \dot{W}(t) &= \int_{(V)} (\sigma_{ij} - \tilde{\sigma}^{e}_{ij} - \sigma^{(s)}_{ij} + \tilde{\sigma}^{e}_{ij})(\dot{\varepsilon}_{ij} - \dot{\tilde{\varepsilon}}^{e}_{ij} - \dot{\varepsilon}^{p}_{ij}) dV \\ &= \int_{(V)} (\sigma_{ij} - \sigma^{(s)}_{ij})(\dot{\varepsilon}_{ij} - \dot{\tilde{\varepsilon}}^{e}_{ij}) dV - \int_{(V)} (\sigma_{ij} - \tilde{\sigma}^{(s)}_{ij}) \dot{\varepsilon}^{p}_{ij} dV \end{aligned} \tag{2.19}$$

According to the definition of strain rate tensor, the first term of equation (2.19) can be represented denoting the displacement velocity vector by $v_{i,j}$.

$$\int_{(V)} (\sigma_{ij} - \tilde{\sigma}^{(s)}_{ij})(\dot{\varepsilon}_{ij} - \dot{\tilde{\varepsilon}}^{e}_{ij}) dV = \int_{(V)} (\sigma_{ij} - \tilde{\sigma}^{(s)}_{ij})(\dot{u}_{i,j} - \dot{\tilde{u}}^{e}_{i,j}) dV = \int_{(V)} (\sigma_{ij} - \tilde{\sigma}^{(s)}_{ij})(v_{i,j} - \tilde{v}^{e}_{i,j}) dV \tag{2.20}$$

Since the distribution of the total residual strain rate is kinematically admissible, i.e. satisfying the continuity requirements, the principle of virtual work can be employed with Gauss theorem (divergence theorem) [99], as follows.

$$\begin{aligned} &\int_{(V)} (\sigma_{ij} - \tilde{\sigma}^{(s)}_{ij})(v_{i,j} - \tilde{v}^{e}_{i,j}) dV \\ &= \int_{(S_F \cup S_K)} n_j (\sigma_{ij} - \tilde{\sigma}^{(s)}_{ij})(v_i - \tilde{v}^{e}_{i}) dS - \int_{(V)} (\sigma_{ij,j} - \tilde{\sigma}^{(s)}_{ij,j})(v_i - \tilde{v}^{e}_{i}) dS = 0 \end{aligned} \tag{2.21}$$

Now we have the condensed time derivative of elastic strain energy instead of the equation (2.16).

$$\dot{W}(t) = -\int_{(V)} (\sigma_{ij} - \tilde{\sigma}_{ij}^{(s)}) \dot{\varepsilon}_{ij}^{p} dV \leq 0 \tag{2.22}$$

According to Drucker's postulate (2.6), the integrand in (2.22) is positive only when σ_{ij} is the yield surface stress state. Hence it follows that the derivative (2.22) is negative at those instants of time at which, under the actual loading program, non-vanishing plastic strain rates are appearing at any point of the body whereas these rates vanish at other instants of time. Since the elastic strain energy cannot be negative, the plastic yielding under repeated loading cannot go on unlimitedly. Then the total deformation of the structure must be bounded (Figure 2.9). Termination of yielding will mean that the shakedown is about to take place. Therefore the statement of static shakedown theorem is proved. The details were well investigated in [48-49,91].

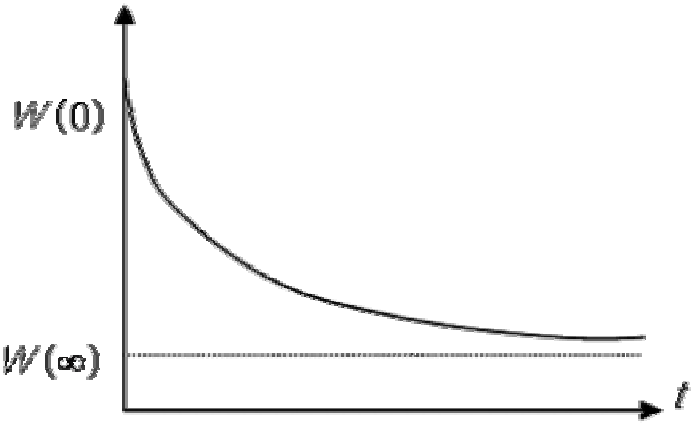

Figure 2.9. The possible behavior of plastic energy dissipation with time.

2.3. Extension of static shakedown theorem

2.3.1. Shakedown theorem with thermal loading

In previous considerations of the shakedown theory an idealized model of structural material has been employed. In the realistic system, however, the temperature dependent effects cannot be neglected. Material constants such as the yield stress, Young's modulus, Poisson's ratio, the coefficient of thermal expansion (CTE), etc. vary in fact with temperature. Thus the shakedown theorem considering the thermal loading system can be formulated as follows.

> If there exists a safety factor $\alpha > 1$ and a time-independent residual stress $\bar{\rho}(\mathrm{x})$, such that

$$F(\alpha^{SD}\tilde{\sigma}^{e}(\mathrm{x},\vartheta,t)+\bar{\rho}(\mathrm{x}),\sigma_{Y}(\mathrm{x},\vartheta))<0 \quad \forall \mathrm{x}\in V \ \wedge \ \forall P(t)\in L \tag{2.23}$$

then the body will shakedown under the given load domain L.

Here, ϑ is the thermal loading due to the difference between actual temperature and reference temperature (T-T_{ref}). The details of the proof are well investigated by Gokhfeld and Cherniavsky [48] or König [49].

2.3.2. Shakedown theorem with unlimited kinematic hardening (ULKH) model

Most of the results in shakedown theory have been obtained for the perfect plastic model. In the real application of shakedown method, the influence of the hardening effect should be considered. The unlimited kinematic hardening (ULKH) effect is considered in shakedown theorem as shown in the Figure 2.10.

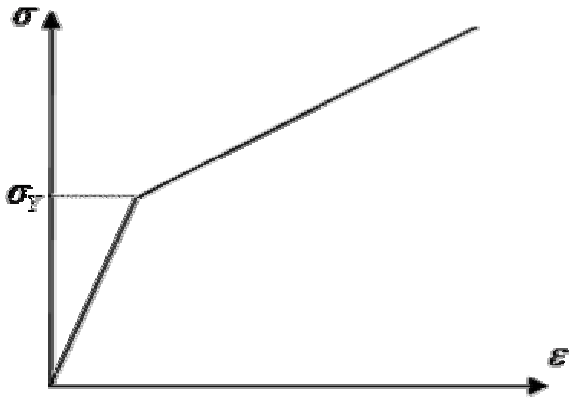

Figure 2.10. Stress-strain curve for unlimited kinematic hardening (ULKH) behavior.

The shakedown theorem with UKLM model can be formulated as follows.

If there exists a safety factor $\alpha>1$, a time-independent of residual stress $\bar{\rho}(\mathrm{x})$, and time-independent back-stress $\bar{\pi}(\mathrm{x})$, such that

$$F(\alpha^{SD}\tilde{\sigma}^{e}(x,t)+\bar{\rho}(x)-\bar{\pi}(x),\sigma_{Y}(x))<0 \quad \forall x\in V \ \wedge \ \forall P(t)\in L \tag{2.24}$$

then the body will shakedown under the given load domain L.

Here, $\bar{\pi}(\mathrm{x})$ denotes the time-independent back stress field. The details of the proof are well investigated in [46].

2.3.3. Shakedown theorem with limited kinematic hardening (LKH) model

When shakedown theorem for unlimited kinematic hardening model is used, the safety limit can be overestimated because it does not have the limited yield stress. To overcome its

disadvantage, two surface yield criteria can be employed as shown in the Figure 2.11. Here σ_y and σ_L indicate the initial yield stress and the limit stress, respectively. Therefore shakedown theorem for limited kinematic hardening (LKH) model is formulated, as follows.

If there exists a safety factor $\alpha > 1$, a time-independent of residual stress $\bar{\rho}(\mathrm{x})$, and time-independent back-stress $\bar{\pi}(\mathrm{x})$, such that

$$F(\alpha^{SD}\sigma^{e}(x,t) + \rho(x) - \pi(x), \sigma_Y(x)) < 0 \tag{2.25}$$

$$F(\alpha^{SD}\sigma^{e}(x,t) + \rho(x), \sigma_L(x)) < 0 \quad \forall x \in V \ \wedge \ \forall P(t) \in L \tag{2.26}$$

then the body will shakedown under the given load domain L.

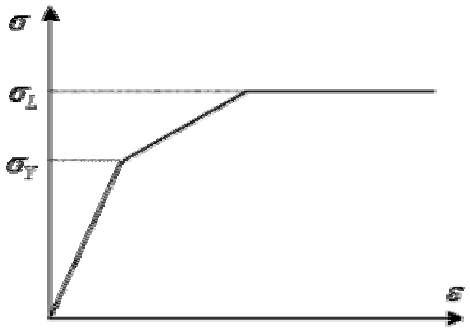

Figure 2.11. Stress-strain curve for limited kinematic behavior.

For the EIP model ($\sigma_Y = \sigma_L$), the back-stresses π are identical zero due to the second inequality. For ULKH model, it can be also deduced from the previous formulation if $\sigma_L \to \infty$. Then the second inequality is not relevant anymore and the back-stresses $\bar{\pi}(\mathrm{x})$ are free variables. The details were well investigated in [61].

2.4. Review of kinematic shakedown theorem

The kinematic shakedown theorem was established in 1950s by Koiter [47], who used the analogy between the theorems of limit analysis and those of shakedown. In this work, the kinematic theorem is not included but the brief introduction is represented in this section. The detail description and proof of the kinematic shakedown theorem can be found in [48-49].

The kinematic theorem is based on the fundamental concept of an admissible cycle of plastic strain rates $\dot{\varepsilon}_{ij}^{p}$. In accordance with the definition of the admissible strain rate cycle, the plastic strain increment represents a following kinematically admissible strain distribution over a certain time interval. This is derived from compatibility condition (2.28) and from the increments of residual displacements (2.29) that satisfy the kinematic boundary condition.

$$\Delta\varepsilon_{ij}^{p} = \int_{\tau} \dot{\varepsilon}_{ij}^{p} dt \tag{2.27}$$

$$\dot{\varepsilon}_{ij}^{c} = \frac{1}{2}\left(u_{i,j}^{c} + u_{j,i}^{c}\right) \tag{2.28}$$

$$\Delta u_{i}^{c} = \int_{0}^{T^{c}} \dot{u}_{i}^{c} dt \tag{2.29}$$

Since the plastic deformation increments per cycle of period T^c are kinematically admissible, they generate no changes in the elastic strains and stresses. This means that the residual stresses at an instant of time $\tau = T^c$ assume again their initial values at $\tau = 0$. Thus the elastic strain increments per cycle are equal to zero as follows.

$$\int_{0}^{T^{c}} \dot{\varepsilon}_{ij}^{e} dt = 0 \tag{2.30}$$

Now the kinematic shakedown theorem will be formulated in the following form of two statements:

(i) Shakedown never takes place, i.e. a body will eventually collapse as a result of cyclic plastic deformation, if there can be found an admissible cycle of plastic strain rates $\dot{\varepsilon}_{ij}^{p}$ such that the following inequality condition is satisfied under the stresses determined by external actions p*(x, *t*) and f*(x, *t*) that vary inside prescribed loading limits.

$$\int_{0}^{T}\int_{(V)} f_{i}^{*}\dot{u}_{i}^{c} dV dt + \int_{0}^{T}\int_{(S_F)} p_{i}^{*}\dot{u}_{i}^{c} dS dt > \int_{0}^{T}\int_{(V)} \sigma_{ij}\dot{\varepsilon}_{ij}^{p} dV dt \tag{2.31}$$

(ii) A body will shakedown if the following inequality holds true and the factor $\alpha > 1$ can be found during arbitrary admissible cycles of non-vanishing plastic strain rates $\dot{\varepsilon}_{ij}^{p}$ at stresses generated by external actions p^{*}(x, *t*) and f^{*}(x, *t*) which vary inside prescribed loading limits.

$$\alpha\left(\int_{0}^{T}\int_{(V)} f_{i}^{*}\dot{u}_{i}^{c} dV dt + \int_{0}^{T}\int_{(S_F)} p_{i}^{*}\dot{u}_{i}^{c} dS dt\right) \leq \int_{0}^{T}\int_{(V)} \sigma_{ij}\dot{\varepsilon}_{ij}^{p} dV dt \tag{2.32}$$

3. FEM-based Shakedown Formulation

A discrete formulation of shakedown theorem for large-scale problem is presented. It is based on the finite element method (FEM) [100-106]. This formulation is called a direct method to compute the safety factor against failure, which leads to a problem of nonlinear mathematical programming.

3.1. Introduction to FEM

In this section, basic concepts for FEM analysis are explained. They will be used in FEM-based shakedown formulation. Firstly, stress is defined as the intensity of the load per unit area. The component of the stress normal to the surface is called the normal stress σ and the stress parallel to the surface is called the shear stress τ. Although nine different stresses act at a point in the three-dimensional body, there are only six independent stresses by equilibrium of moments of the infinitesimal cube. The knowledge of deformations is specified in terms of strains, that is, the relative change in the size and shape of the body. The strain at a point is also defined in an infinitesimal cube similar to stress. Here ε and γ denote the normal strain and the shear strain, respectively. The components of stress and strain for three-dimensional structure are expressed in the following equation.

$$\left\{\sigma^e\right\}=\begin{Bmatrix}\sigma_x^e\\ \sigma_y^e\\ \sigma_z^e\\ \tau_{xy}^e\\ \tau_{yz}^e\\ \tau_{xz}^e\end{Bmatrix},\ \left\{\varepsilon^e\right\}=\begin{Bmatrix}\varepsilon_x^e\\ \varepsilon_y^e\\ \varepsilon_z^e\\ \gamma_{xy}^e\\ \gamma_{yz}^e\\ \gamma_{xz}^e\end{Bmatrix} \tag{3.1}$$

The vector of nodal forces and displacement vector at each element are expressed as follows, when *NK* denote the number of total nodes.

$$\left\{F_K\right\}=\begin{Bmatrix}F_{1x}\\ F_{1y}\\ F_{1z}\\ \vdots\\ F_{NKx}\\ F_{NKy}\\ F_{NKz}\end{Bmatrix},\ \left\{u_K^e\right\}=\begin{Bmatrix}u_{1x}^e\\ u_{1y}^e\\ u_{1z}^e\\ \vdots\\ u_{NKx}^e\\ u_{NKy}^e\\ u_{NKz}^e\end{Bmatrix} \tag{3.2}$$

For a body which is linearly elastic and has small deformations, stresses and strains at a point are related through six simultaneous linear equations called Hook's law. [L] denotes a contracted version of elasticity tensor so-called stiffness matrix. If there are no directional preferences at all, the material is assumed to be isotropic and is described by the following tensor form (E: Elastic modulus, ν: Poisson's ratio).

$$[\mathrm{L}]=\frac{E}{1+\nu}\begin{bmatrix} \frac{1-\nu}{1-2\nu} & \frac{\nu}{1-2\nu} & \frac{\nu}{1-2\nu} & 0 & 0 & 0 \\ \frac{\nu}{1-2\nu} & \frac{1-\nu}{1-2\nu} & \frac{\nu}{1-2\nu} & 0 & 0 & 0 \\ \frac{\nu}{1-2\nu} & \frac{\nu}{1-2\nu} & \frac{1-\nu}{1-2\nu} & 0 & 0 & 0 \\ 0 & 0 & 0 & \frac{1}{2} & 0 & 0 \\ 0 & 0 & 0 & 0 & \frac{1}{2} & 0 \\ 0 & 0 & 0 & 0 & 0 & \frac{1}{2} \end{bmatrix} \tag{3.3}$$

For the discretization of the domain into a set of finite elements, the shape function has to be defined on each finite element. The matrix [N] includes shape functions corresponding to the corner nodes of one finite element, when *NKE* is the number of nodes at each element and y(*x*, *y*, *z*) is the global coordinate of the system. The matrix [B] is called B matrix in FEM formulation. It is composed of the components of the derivative of shape functions.

$$\left[\mathrm{N(y)}\right]=\begin{bmatrix} N_1(\mathrm{y}) & 0 & 0 & \cdots & N_{NKE}(\mathrm{y}) & 0 & 0 \\ 0 & N_1(\mathrm{y}) & 0 & \cdots & 0 & N_{NKE}(\mathrm{y}) & 0 \\ 0 & 0 & N_1(\mathrm{y}) & \cdots & 0 & 0 & N_{NKE}(\mathrm{y}) \end{bmatrix} \tag{3.4}$$

$$\left[\mathrm{B(y)}\right]=\begin{bmatrix} \frac{\partial N_1(\mathrm{y})}{\partial x} & 0 & 0 & \cdots & 0 \\ 0 & \frac{\partial N_1(\mathrm{y})}{\partial y} & 0 & \cdots & 0 \\ 0 & 0 & \frac{\partial N_1(\mathrm{y})}{\partial z} & \cdots & \frac{\partial N_{NKE}(\mathrm{y})}{\partial z} \\ \frac{\partial N_1(\mathrm{y})}{\partial y} & \frac{\partial N_1(\mathrm{y})}{\partial x} & 0 & \cdots & 0 \\ 0 & \frac{\partial N_1(\mathrm{y})}{\partial z} & \frac{\partial N_1(\mathrm{y})}{\partial y} & \cdots & \frac{\partial N_{NKE}(\mathrm{y})}{\partial y} \\ \frac{\partial N_1(\mathrm{y})}{\partial z} & 0 & \frac{\partial N_1(\mathrm{y})}{\partial x} & \cdots & \frac{\partial N_{NKE}(\mathrm{y})}{\partial x} \end{bmatrix} \tag{3.5}$$

Exact evaluation of the integrals appearing in element stiffness matrices and force vectors is not always possible because of the algebraic complexity. In such cases, it is necessary to seek numerical evaluation of these integral expressions. Numerical evaluation of integrals is called numerical integration or numerical quadrature. Of all quadrature formulae, Gauss-Legendre technique is the most commonly used. The details of the computational and mathematical methods are represented in [107]. The Gauss-Legendre technique requires the transformation of the global coordinate $\mathrm{y}(x, y, z)$ to the natural coordinate $\boldsymbol{\xi}(\xi, \eta, \zeta)$. For the coordinate transformation, the following Jacobian matrix $[J_j(\boldsymbol{\xi})]$ is needed.

$$[J_j(\xi)] = \begin{bmatrix} \sum_{i=1}^{NKE} \frac{\partial N_i(\xi)}{\partial \xi} x_i^j & \sum_{i=1}^{NKE} \frac{\partial N_i(\xi)}{\partial \xi} y_i^j & \sum_{i=1}^{NKE} \frac{\partial N_i(\xi)}{\partial \xi} z_i^j \\ \sum_{i=1}^{NKE} \frac{\partial N_i(\xi)}{\partial \eta} x_i^j & \sum_{i=1}^{NKE} \frac{\partial N_i(\xi)}{\partial \eta} y_i^j & \sum_{i=1}^{NKE} \frac{\partial N_i(\xi)}{\partial \eta} z_i^j \\ \sum_{i=1}^{NKE} \frac{\partial N_i(\xi)}{\partial \zeta} x_i^j & \sum_{i=1}^{NKE} \frac{\partial N_i(\xi)}{\partial \zeta} y_i^j & \sum_{i=1}^{NKE} \frac{\partial N_i(\xi)}{\partial \zeta} z_i^j \end{bmatrix} \tag{3.6}$$

By taking the inverse of the relationship (3.6), the first derivatives of the shape functions with respect to the global coordinates are obtained as follows.

$$\begin{Bmatrix} \frac{\partial N_i(y)}{\partial x} \\ \frac{\partial N_i(y)}{\partial y} \\ \frac{\partial N_i(y)}{\partial z} \end{Bmatrix} = \left[J_j(\xi)\right]^{-1} \begin{Bmatrix} \frac{\partial N_i(\xi)}{\partial \xi} \\ \frac{\partial N_i(\xi)}{\partial \eta} \\ \frac{\partial N_i(\xi)}{\partial \zeta} \end{Bmatrix} \tag{3.7}$$

For the evaluation of the volume change in the transformation process, the determinant of Jacobian matrix $\det[J_j(\xi)]$ can be obtained, as follows.

$$dV = dx\,dy\,dz = \det[J_j(\xi)]\,d\xi\,d\eta\,d\zeta \tag{3.8}$$

3.2. Procedure of FEM-based shakedown formulation

This section deals with the discretization technique using finite element method and nonlinear optimization program in order to obtain shakedown safety limit in the considered loading domain. Firstly, the discretization techniques of initial loading space, fictitious elastic stresses, residual stress field will be explained. Finally, the FEM-based shakedown formulation technique will be represented using the nonlinear optimization program [108].

3.2.1. Discretization of initial loading space

A shakedown limit can be obtained in the specific loading case. However, for multi-dimensional loadings (e.g. biaxial loading or thermomechanical loading), the macroscopic admissible domain, that is, a set of shakedown limits can be determined by carrying out several shakedown analyses. These domains are here called macroscopic admissible domains of loads or macroscopic strength domains and are expressed in terms of macroscopic stress Σ.

To perform FEM-shakedown analysis in the specific loading domain, an initial loading domain has to be discretized. Next, the maximum admissible domain can be obtained from the initial loading space using shakedown analysis. For this searching process, the initial loading paths are assumed to be included in an initial loading space, that is, a convex polyhedron L. It can be defined as a linear combination of *n*-independent loads, as follows.

$$L = \left\{ \Sigma \middle| \Sigma(x,t) = \sum_{j=1}^{n} \mu_j(t)\Sigma_j(x), \quad \mu_j \in \left[\mu_j^-, \mu_j^+\right] \right\} \tag{3.9}$$

Here, Σ is a state of macroscopic stresses (or thermal stresses), and t denotes a loading parameter denoting the time. μ_j are scalar multipliers with upper and lower bounds μ_j^+ and μ_j^-, respectively. Σ_j represents n fixed and independent macroscopic stresses. The corners of the polyhedron (load domain L) are numbered by the index j, such that $j = 1, \ldots, NV$, where NV denotes the total number of loading corners. There is a simple rule between number of independent loadings and number of loading corners, that is, $NV = 2^n$ (n is the number of independent loading). For example, when two-independent loadings, i.e. Σ_1 and Σ_2, are considered in a loading domain L, four loading corners (P_1 - P_4) are obtained, as shown in Figure 3.1.

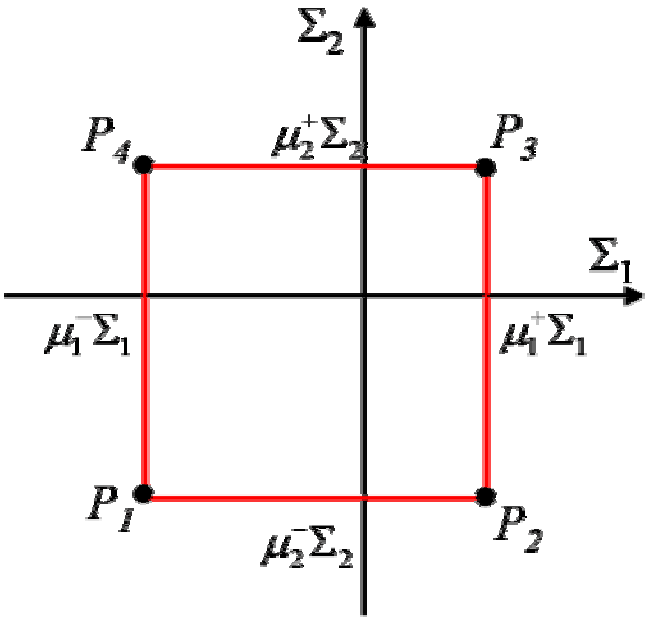

Figure 3.1. Loading domain L for two independent loadings and four obtained loading corners.

3.2.2. Discretization of elastic stresses

To calculate the elastic stresses σ^e in reference body, the principle of virtual work combined with the finite element discretization and test functions for the displacement fields are used. The elastic stresses σ^e are in equilibrium with body force f^* and surface traction p^* if the following equality holds for any virtual displacement δu^e and any virtual strains $\delta\varepsilon^e$ satisfying the compatibility condition[1].

$$\delta U_{\text{int}} = \delta W_{ext} \tag{3.10}$$

[1] $\varepsilon^e = \frac{1}{2}\left(\nabla(u^e) + \nabla(u^e)^T\right)$

$$\int_V \{\sigma^e\}\{\delta\varepsilon^e\}dV = \int_S \{p^*\}\{\delta u^e\}dS + \int_V \{f^*\}\{\delta u^e\}dV \tag{3.11}$$

The virtual displacement field δu^e of each element *e* is approximately according to the following equation, when *NK* denotes the number of nodes at each element.

$$\{\delta u^e\} = \sum_{k=1}^{NK} N_k \delta u_k^e \tag{3.12}$$

Here N_k and δu_k^e denote the k^{th} shape function matrix and the vector of virtual displacements of the k^{th} node of the element *e*, respectively. The virtual strain field $\delta\varepsilon^e(x)$ is derived by substitution of equation (3.12) into the compatibility condition.

$$\{\delta\varepsilon^e(x)\} = \sum_{k=1}^{NK} B_k(x)\delta u_k^e \tag{3.13}$$

Here [B] is the compatibility matrix depending on the coordinates. The integration of equation (3.12) has to be carried out over all Gaussian points *NG* with their weighting factors w_i in the considered element *e*, where the index *i* refers to i^{th} Gaussian point. The corresponding coordinate vector shall be denoted by x_i, as follows, where {F} denotes the vector of nodal forces and [K] denotes the stiffness matrix.

$$\begin{aligned}\int_V \{\delta\varepsilon^e(x)\}^T\{\sigma^e(x)\}dV &= \{\delta u^e\}^T\left\{\sum_{k=1}^{NGE} w_i \det[J_j(\xi)][\mathrm{B}(x_i)]^T[\mathrm{L}][\mathrm{B}(x_i)]\right\}\{u^e\} \\ &= \{\delta u^e\}^T[\mathrm{K}^*]\{u^e\}\end{aligned} \tag{3.14}$$

By summation of the contribution of all elements and by variation of the virtual node displacements with regard to the boundary conditions, the linear system of finite element equation can be obtained as follows.

$$[\mathrm{K}]\{u^e\} = \{\mathrm{F}\} \tag{3.15}$$

3.2.3. Discretization of residual stress field

In shakedown theorem, the residual stress field $\bar{\rho}$ should satisfy the homogenous static self-equilibrium and boundary conditions represented in equations (2.5) and (2.6). Therefore, the field of residual stress can be formulated as follows.

$$\int_V \{\bar{\rho}\}\{\delta\varepsilon\}dV = 0 \tag{3.16}$$

By introducing a vector form for the strain tensor ε, the corresponding virtual strains $\delta\varepsilon$ are represented in each element *e* as follows.

$$\left\{\delta\varepsilon^{e}\right\}=\sum_{k=1}^{NK}B_{k}\delta u_{k}^{e} \tag{3.17}$$

Using the relation (3.17) and introducing the unknown residual stress vector $\{\overline{\rho}_i\}$ at each Gaussian point *i*, the equilibrium condition (3.16), is integrated numerically by using the well-known Gauss-Legendre technique. Denoting the weighting factor for numerical integration for the i^{th} Gaussian point by w_i, the numerical integration over all Gaussian points *NG* can be carried out as follows.

$$\int_{V^e}\{\overline{\rho}(x)\}\{\delta\varepsilon(x)\}dV=\sum_{i=1}^{NG}w_i\{\det[J_i(\xi)]\}\left[\sum_{k=1}^{NK}B_k\delta u_k^e\right]\overline{\rho}_i=[\mathrm{C}^*]\{\overline{\rho}\} \tag{3.18}$$

[C*] is a constant equilibrium matrix, uniquely defined by the discretized system and the boundary conditions and $\{\overline{\rho}\}$ is the global residual stress vector of the discretized reference body B^e [86,108-110]. According to (3.16), the virtual work of the time-independent residual stress field $\{\overline{\rho}\}$ must be null. Substituting (3.18) into (3.16) and performing the variation of node displacement with regard to the kinematic boundary condition, one obtains a system of linear equation.

$$\sum_{i=1}^{NG}C_i\overline{\rho}_i=[\mathrm{C}]\{\overline{\rho}\}=\{0\} \tag{3.19}$$

The kinematic boundary conditions are included through the fact that the rows in the matrix [C*] should be erased, which would be multiplied by null virtual displacement according to (3.18). Since the matrix [C] has more rows than columns, the system of (3.19) cannot be used to obtain time-independent residual stress field $\{\overline{\rho}\}$ in the integration points directly. The Fortran code for the generation of the matrix [C] is attached in Appendix B.

3.2.4. FEM discretization of shakedown formulation

In view of the convexity of the yield function and due to above assumption on the load domain *L* it can be shown that

$$F(\alpha\tilde{\sigma}^{e}(x,t)+\overline{\rho}(x))\le\sigma_Y \tag{3.20}$$

is fulfilled at any time *t*, if

$$F(\alpha\tilde{\sigma}_i^{e}(P_j)+\overline{\rho}_i)\le\sigma_Y \tag{3.21}$$

holds for all $j\in[1,NV]$ and for all $i\in[1,NG]$, when *NV* and *NG* indicate total number of loading corners and total number of Gaussian points.

The final form of the discretized formulation of the static shakedown theorem for the determination of the shakedown loading factor is given by the following conditions (3.22)-(3.24).

$$\alpha^{SD} = \max_{\bar{\rho}} \alpha \tag{3.22}$$

with the subsidiary conditions

$$F(\alpha\tilde{\sigma}_i^e(P_j) + \bar{\rho}_i) \le \sigma_Y \quad \forall i \in [1, NG] \; and \; \forall j \in [1, NV] \tag{3.23}$$

$$[C]\{\bar{\rho}\} = \{0\} \tag{3.24}$$

As mentioned, the unknown variables of the optimization problem are shakedown factor α and the residual stress field $\{\bar{\rho}\}$. Therefore, the number of total unknown variables is $N = 1 + NG \times NSK$, where *NSK* is the dimension of the stress vector at each Gaussian point (two-dimensional model: *NSK* = 3, three-dimensional model *NSK* = 6). The shakedown criterion (3.23) has to be fulfilled at total Gaussian points $i \in [1, NG]$ and in each loading corner $j \in [1, NV]$, where $NV = 2^n$ (*n* is the number of independent loading). The number of inequality constraints from the shakedown criterion (3.23) is $NV \times NG$. The number of equality constraints from the [C] matrix (3.24) is *NF*, that is, the degrees of freedom of displacements of the discretized body. Therefore, the number of total constraints is $NV \times NG + NF$.

For the understanding about the number of known variables and constraints, the simple two-dimensional plane with four-node quadrilateral element (*NE*: 100 elements, *NK*: 121 nodes) is considered, as represented in Figure 3.2. Two-independent biaxial loading is considered (i.e. $4(NV) = 2^{2(n)}$). The number of constrained boundary conditions (*NBC*) is 22. Each element is composed of four Gaussian points, that is, the number of total Gaussian points (*NG*) is 400. Therefore the number of resulting unknown variables will be $1201 = 1 + 400(NG) \times 3(NSK)$. The number of inequality constraints (3.23) is $1600 = 4(NV) \times 400(NG)$ and the number of equality constraints (3.24) is $222(NF) = 121(NK) \times 2 - 22(NBC)$.

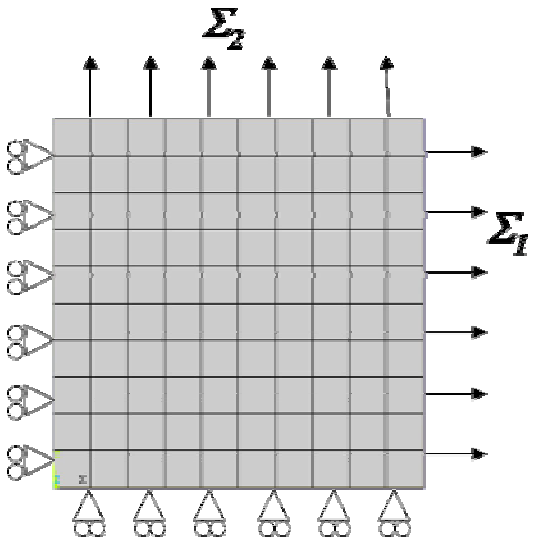

Figure 3.2. Two-dimensional plane with finite element discretization.

The direct approach presented above of shakedown analysis leads to a problem of mathematical programming, which requires a large amount of computer memory, because the numbers of unknown variables and constraints are very high. Furthermore, for the implementation of the nonlinear yield conditions (e.g. von Mises criterion), the solution technique of the respective nonlinear optimization problem is required with highly iterative procedures. Therefore, this problem can be solved by large-scale nonlinear optimization program.

3.3. Procedure of large-scale nonlinear optimization

3.3.1. Description of large-scale nonlinear optimization problem

The resolution of large-scale nonlinear optimization problems can be carried out by using advanced code LANCELOT [111]. LANCELOT, an acronym for Large And Nonlinear Constrained Extended Lagrangian Optimization Technique, is a package of standard Fortran subroutines and utilities. It has been designed for problems where the objective function is a smooth function of many real variables and where the value of these variables may be restricted by a finite set of smooth constraints. LANCELOT considers the problem of minimizing or maximizing an objective function of the problem. In this shakedown application, the minimization problem is considered since the objective function is chosen as the negative value of shakedown safety factor.

$$f(X) = \alpha \tag{3.25}$$

The general equality and inequality constraint functions are represented as follows.

$$b_p(X) = C_{pq}\rho_q \quad p = 1,..., NF; q = 1,..., NG \times NSK \tag{3.26}$$

$$b_r(X) = F(\alpha\sigma_r^e + \rho_r) \le \sigma_Y \quad r = NF + 1,..., NG \times NV \tag{3.27}$$

There is no loss in assuming that all the general constraints are equations, as inequality constraints may easily be transformed to equations by addiction of extra slack or surplus variables. LANCELOT automatically transforms inequality constraints (3.27) into equations. This technique is extensively used in simplex-like methods for large-scale linear and nonlinear programs [112]. The objective function and generalized constraints can be combined into a composite function, that is, the augmented Lagrangian function Φ.

$$\Phi(X, \lambda, s, \mu) = f(X) + \sum_{i=1}^{m} \lambda_i b_i(X) + \frac{1}{2\mu} \sum_{i=1}^{m} s_{ii} b_i(X)^2 \tag{3.28}$$

Here the components λ_i of the vector λ are known as Lagrange multiplier estimates. The entries s_{ii} of the diagonal matrix [S] are constraint scaling factors, and μ indicates the penalty parameter. The constrained maximization problem (3.25)-(3.27) can be solved by finding approximate minimizers of the augmented Lagrangian function for a carefully constructed sequence of Lagrange multiplier estimates, constraint scaling factors and penalty parameters.

3.3.2. Optimization technique using augmented Lagrangian method

The iteration steps for the optimization are composed of two main steps, as follows.

(i) Minimize the augmented Lagrangian function.
(ii) Find an approximate minimizer

3.3.2.1. Minimize the augmented Lagrangian function

The first order necessary conditions for a feasible point $X^* = \left(\alpha^*, \{\overline{\rho}\}^*\right)$ to solve the problem (3.25)-(3.27) require that there are Lagrangian multipliers λ^*, for which the projected gradient of the Lagrangian function at X^* and λ^* and the general constraints (3.25)-(3.27) at X^* vanish. Here, the Lagrangian function is expressed as the following function.

$$L(X,\lambda) = f(X) + \sum_{i=1}^{m} \lambda_i b_i(X) \tag{3.29}$$

The projected gradient of *f* is replaced by the gradient of Lagrangian function, $\nabla_X L(X,\lambda)$. One may then assess the convergence of the augmented Lagrangian method by the size of the projected gradient and constraints at $X^{(k)}$ and $\lambda^{(k)}$. The optimization will be terminated if the following conditions hold for some appropriate small convergence tolerances ε_l and ε_c.

$$\left\| X^{(k)} - P(X^{(k)} - \nabla_X L(X^{(k)}, \lambda^{(k)}), l, u) \right\| \le \varepsilon_l \tag{3.30}$$

$$\left\| b(X^{(k)}) \right\| \le \varepsilon_c \tag{3.31}$$

Here, $P(X, l, u)$ denotes the projection operator defined by the following equation, when *l* and *u* are lower bounds and upper bounds, respectively.

$$P(X,l,u) = \begin{cases} l_i & \text{if} \quad X_i < l_i \\ u_i & \text{if} \quad X_i > u_i \\ X_i & \text{otherwise} \end{cases} \tag{3.32}$$

3.3.2.2. Find approximate minimizer

The convergence of augmented Lagrangian method is guaranteed, under very weak assumptions, if the penalty parameter is gradually reduced to zero, almost regardless of the values of the Lagrange multiplier estimates. The Lagrange multiplier estimates may even diverge provided that $\mu^{(k)}\left\|\lambda^{(k)}\right\|$ converges to zero. However, it becomes more difficult to minimize (3.28) when $\mu^{(k)}$ is small. Fortunately, a judicious choice of Lagrange multipliedr estimates also ensures convergence for fixed μ provided $X^{(k)}$ is close to X^*. Thus $\mu^{(k)}$ is allowed to decrease until we are sure that we are in a neighborhood of X^* from which point $\mu^{(k)}$ is left unchanged but the Lagrange multipliers adjusted to ensure ultimate convergence. We can gauge whether we are in such a neighborhood by monitoring the expected decrease $\left\|b(X^{(k+1)})\right\|$. At each iteration, we exit the iteration loop when the following condition is

satisfied for some tolerance $\omega^{(k)}$.

$$\left\| X^{(k+1)} - P(X^{(k+1)} - \nabla_x \Phi(X^{(k+1)}, \lambda^{(k)}, s^{(k)}, \mu^{(k)}), l, u) \right\| \le \omega^{(k)} \tag{3.33}$$

Then the function can be tested for some other tolerance $\eta^{(k)}$, as follows.

$$\left\| b(X^{(k+1)}) \right\| \le \eta^{(k)} \tag{3.34}$$

If (3.34) is satisfied, we leave the penalty parameter unchanged but update the Lagrange multiplier estimates. Otherwise, we reduce the penalty parameter while leaving the Lagrange multiplier estimates as they are.

3.3.2.3. Application to FEM-based shakedown formulation

It turns out that the elements of $\{\bar{\rho}\}$ are not independent of each other and so a Gauss-Jordan elimination procedure [113] can be applied to the matrix [C] to eliminate the equality constraints (3.26) and to reduce the size of the problem. Then, we obtain the matrix [b] with the following property

$$[C][b] = 0 \tag{3.35}$$

By this means, an arbitrary vector *X* with $NX = NG \times NSK - NF$ components yields with the relation

$$\{\bar{\rho}\} = [b]\{X\} \tag{3.36}$$

a residual stress vector $\{\bar{\rho}\}$, satisfying equation (3.26) for any vector $\{X\}$. The column vectors of [b] represent linearly independent residual stress states of the discretized body. Then, the following optimization problem is obtained.

$$\alpha^{SD} = \max_X \alpha \tag{3.37}$$

$$F(\alpha\sigma_r^e(P_j) + [b_i]\{X\}) \le \sigma_Y \quad \forall i \in [1, NG], \ \forall j \in [1, NV] \tag{3.38}$$

3.4. Summary of FEM-based shakedown formulation

In this work, the computational program for FEM-based shakedown analysis was developed using a software package LANCELOT for solving large-scale nonlinear optimization problems. The computational algorithm is represented in Figure 3.3.

The program is composed of two main parts, that is, FEM process (section 3.2) and optimizations process (section 3.3). In FEM process, the elastic stresses at each loading corner are determined using conventional FEM analysis (section 3.2.1-2). The equilibrium [C] matrix has to be obtained using special program for [C] matrix formulation (section 3.3.3). Next the shakedown formulation has to be performed (section 3.3.4).

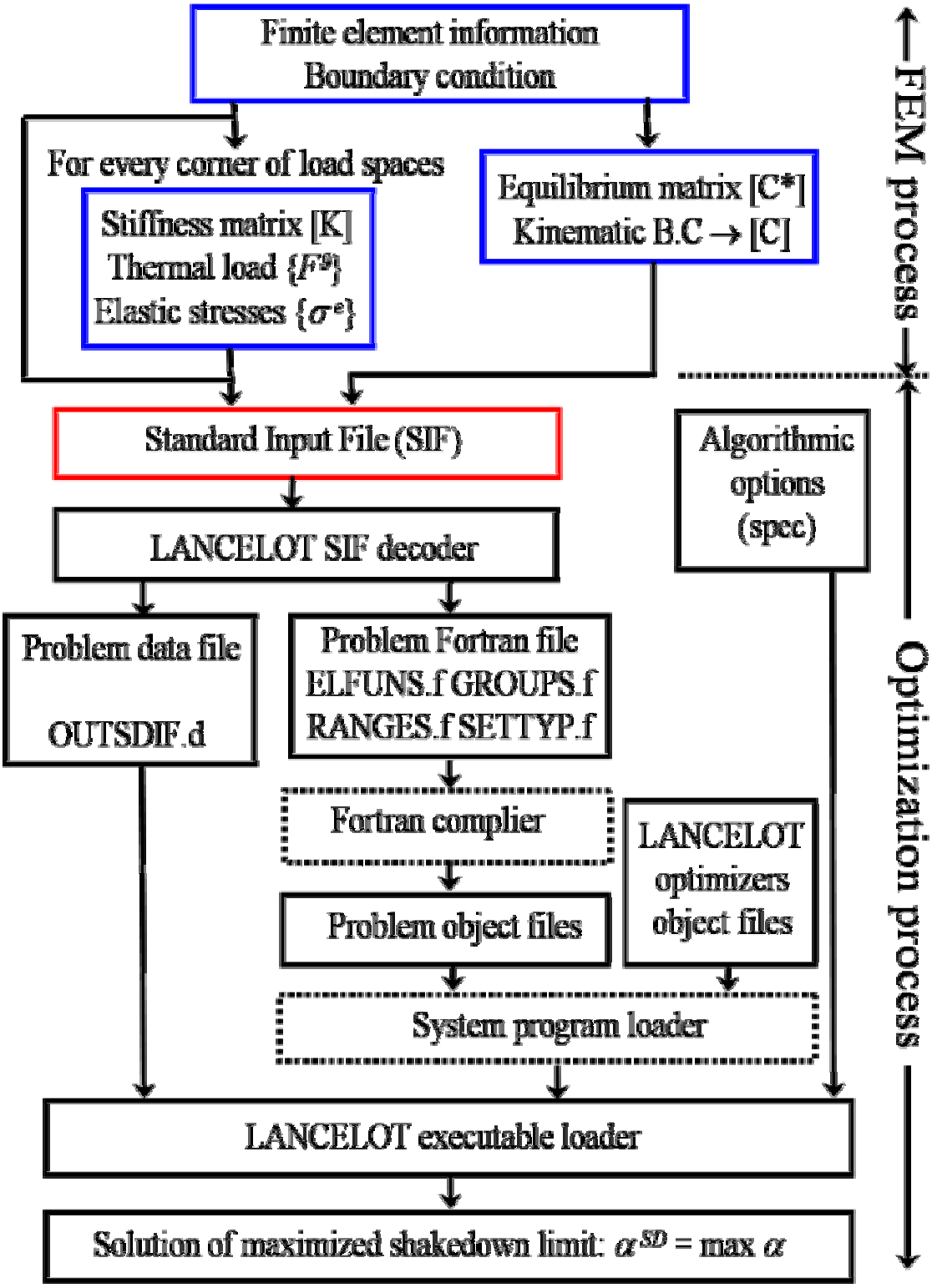

Figure 3.3. Flowchart of FEM-based shakedown formulation using LANCELOT optimization program.

The obtained results from FEM process are used as unknown and known variables in optimization process. They may be several hundred thousands of variables including equality and inequality constraints. The input of the problem data will be extremely time-consuming and prone to error. Therefore, the simplified process of specifying variables is required. This can be performed with standard input file (SIF) format. The SIF / LANCELOT interface produces Fortran subroutines that are subsequently used by LANCELOT optimizers. These routines contain variables that are named within the SIF problem specification. The typical example of SIF file for FEM-based shakedown analysis is attached in appendix C.

If the SIF file is prepared, the optimization process is performed with LANCELOT program. In the first step of optimization process, LANCELOT SIF decoder module reads a description of the problem from a SIF file. This module interprets the statements found in the file and produces four Fortran subroutines (ELFUNS.f, GROUPS.f, RANGES.f, SETTYP.f) and a data file (OUTSDIF.d). Four Fortran subroutine files are compiled at the next step of the process. The resulting object modules are then loaded with the LANCELOT “optimization object module”. This step simply uses the system-provided Fortran compiler and program loader. Then the LANCELOF module is executed with OUTSDIF.d and algorithmic options in the specification file (SPEC.spc). Finally the numerical solution to the optimization problem is found, that is, the maximized shakedown factor in this problem. The details of LANCELOT program description including SIF file format were represented in [111].

4. Verification Tests

The developed computational tool for shakedown analysis is validated with previous literature result. The accuracy and the effectiveness of the computational algorithm of shakedown analysis tool are discussed.

4.1. Two-dimensional plate with a hole

Two-dimensional plate with a hole problem was chosen to verify the developed computational algorithm. The chosen geometry was used as one of the most conventional models for structural analysis including shakedown analysis [91]. In this geometry, the chosen ratio between diameter of the inner hole and the length of the plate (d/l) was fixed to be 0.2. The finite element meshes and the boundary conditions for the chosen model were represented in Figure 4.1. Since this model was symmetric to x-axis and y-axis, only a quarter plane was used to carry out FE analysis for computational efficiency. The four node quadrilateral elements were used in FE analysis. The plane stress was assumed since the chose plate was thin enough[1]. The number of total elements and the number of total nodes were 574 and 626, respectively. Young's modulus and Poisson's ratio were E = 210 000 MPa and v = 0.3, respectively. The plate was subjected to biaxial uniform loads p_x (x-directional pressure) and p_y (y-directional pressure).

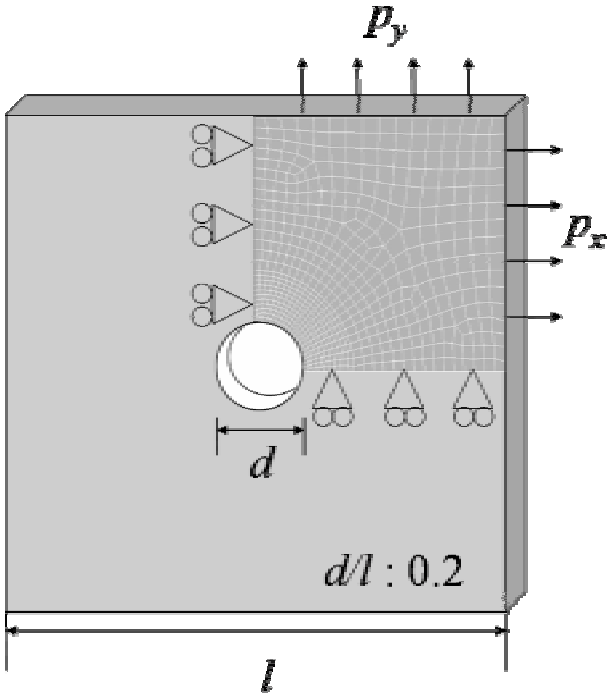

Figure 4.1. A plate with a hole and its finite element mesh.

[1] If a thin plate is loaded by forces applied at the boundary, parallel to the plane of the plate and distributed uniformly over the thickness, the stress components σ_z, τ_{xz}, τ_{yz} are zero on both faces of the plate, and it may be assumed , tentatively, that they are zero also within the plate. The state of stress is then specified by σ_x, σ_y, τ_{xy} only, and is called plane stress [119].

For FEM-based shakedown analysis, the loading parameters have to be defined for the arbitrarily chosen initial loading space. With regard to the number of loading parameters, shakedown analysis is categorized into one-parameter case and two-parameter case, as follows.

(i) Shakedown limit (one-parameter loading): α_{SD_1}

$$p_x = \alpha_{SD_1} \mu \, p_1^*, \qquad p_y = \alpha_{SD_1} \mu \, p_y^* \;\; (0 \le \mu \le 1) \tag{4.1}$$

(ii) Shakedown limit (two-parameter loading): α_{SD_2}

$$p_x = \alpha_{SD_2} \mu_1 \, p_1^*, \qquad p_y = \alpha_{SD_2} \mu_2 \, p_y^* \;\; (0 \le \mu_1 \le 1 \;\; and \;\; 0 \le \mu_2 \le 1) \tag{4.1}$$

In one-parameter loading p_x and p_y vary simultaneously proportionally with the same factor of proportionality since there exists only one variable, μ. If the loading source of the component is limited as one-parameter, the one-parameter approach can be used for shakedown analysis. However, in two-parameter loading, p_x and p_y vary independently, since there exist two independent variables, μ_1 and μ_2. If two more independent loadings are considered in the structure, multi-parameter loading can be used. The number of boundary of loading space (m) was also dependent on the number of loading parameters (n), i.e. $m = 2^n$. For example, two loading boundaries (P_1, P_2) are expected in one-parameter loading while four loading boundaries (P_1-P_4) are expected in two-parameter loading.

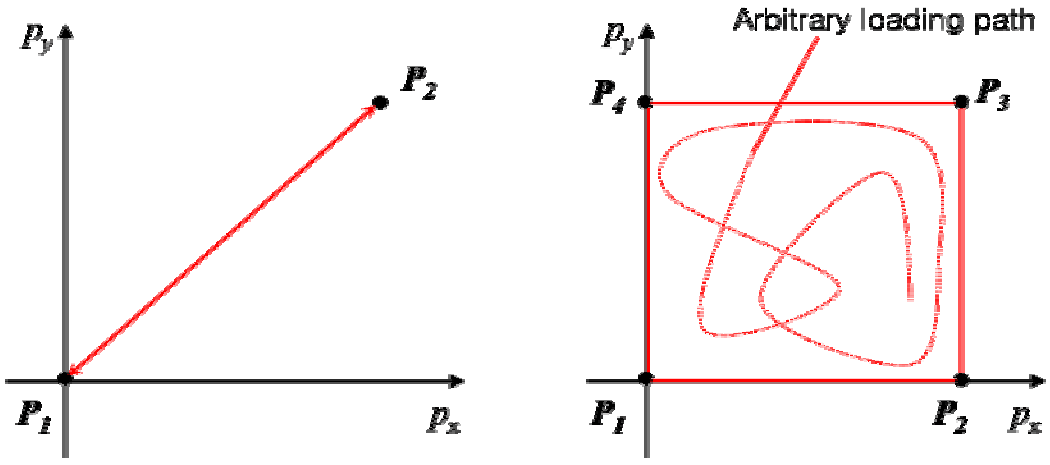

Figure 4.2. The initial loading space for shakedown analysis: (a) one-parameter loading and (b) two-parameter loading.

One-parameter and two-parameter shakedown analyses were performed for the chosen geometry. The obtained shakedown limits were represented in in-plane biaxial loading space, as shown in Figure 4.3. For the graphical representation of the results, the values of x-directional and y-directional pressures were normalized by the yield stress of material. In the Figure 4.3, shakedown limit for one-parameter loading was denoted by cross symbol with red solid line and shakedown limit for two-parameter loading was denoted by square symbol with blue solid line. For the comparison, the yield limit was shown as dark grey line in the loading space. As expected, shakedown limits were larger than elastic limits. One-parameter

shakedown limits have more gain than two-parameter shakedown limits in the first and the third quarter loading planes, while they were same in the second and the fourth quarter loading planes.

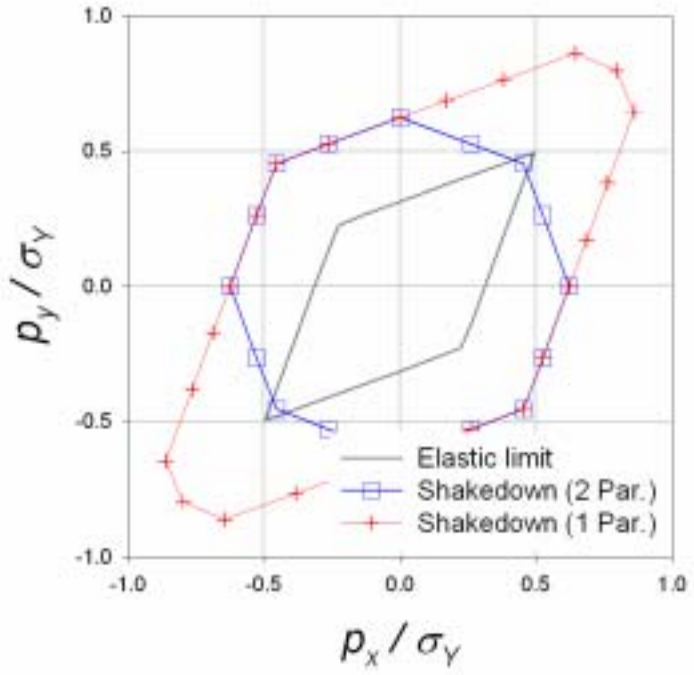

Figure 4.3. Shakedown limits in two-dimensional loading space.

The present results will now be compared with other literature values for three special load combinations. The compared shakedown limits were for two-parameter loading. The available results were summarized in Table 4.1. The literature results were based on different approaches concerning both discretization of the problem and the numerical solution technique. The computational methods used in literature were remarked as follows.

(i) Belytschko [114] used pure equilibrium triangular elements with second-order shape functions for the stresses.

(ii) Nguyen Dang Hung and Palgen [115] developed quadrilateral equilibrium elements based on the static shakedown theorem and a so-called yield criterion of the mean.

(iii) Corradi and Zavelani [116] replaced the original discretized problem by its dual after a linearization of the yield condition.

(iv) Genna [117] used isoparametric eight node displacement elements and Melan's static formulation with the von Mises yield condition. Moreover a numerical scheme for the direct determination of the safety factor was developed.

(v) Zhang [109] used the static shakedown theorem and the von Mises yield criterion in combination with finite element discretization based on classical four node displacement elements. The solution of optimization problem has been obtained with the reduced basis technique.

(vi) Gross-Weege [110] used four node plane stress quadrilateral elements with an iterative solution method using a reduced basis technique.

(vii) Schwabe [91] used the static shakedown theorem and the von Mises yield criterion in combination with finite element discretization based on classical six node displacement elements. The large-scale nonlinear optimization process was used for the computational formulation.

The obtained shakedown limits (0.622 in uniaxial loading, 0.453 in biaxial loading) were represented in in-plane biaxial loading space and compared with other literature values (0557-0.654 in uniaxial loading, 0.430-0.504 in biaxial loading) as shown in Table 4.1. The present results were generally very close to the available exact analytical values and other shakedown limit values.

Table 4.1. Comparison of different numerical solutions for shakedown analysis.

Authors	Shakedown results (Two-parameter)		
	$p_x = p_y$	$p_y = p_x / 2$	$p_y = 0$
Belytschko [114]	0.431	0.501	0.571
Nguyen Dang Hung and Palgen [115]	0.431	0.514	0.557
Corradi and Zavelani [116]	0.504	0.579	0.654
Genna [117]	0.478	0.566	0.653
Zhang [109]	0.453	0.539	0.624
Gross-Weege [110]	0.446	0.524	0.614
Schwabe [91]	0.430	0.505	0.595
Analytical solution [110]	0.431	0.514	0.596
Present result	0.453	0.538	0.622

4.2. Two-dimensional model of FRMMC

The developed computational tool is verified with composite structure. Recently, shakedown analysis for two-dimensional FRMMC structure has been studied by Schwabe [91]. The main study was focused on the periodical composite structure such as Al_2O_3 fiber and Al metal matrix. Here FRMMC was assumed to be perfect bonding between fiber reinforcement and matrix. The material properties of matrix and fiber were shown in Table 4.2. Since the fiber was assumed to be infinitely long, the plane strain assumption was possibly used for this geometry[2].

[2] A simplification is possible at the extreme when the dimension of the body in the z direction is very large. If a long cylinder body is loaded by forces that are perpendicular to the longitudinal elements and do not vary along the length, it may be assumed that all cross sections are in the same condition. It is simplest to suppose at first that the end sections are confined between fixed smooth rigid planes, so that displacement in the axial direction

Table 4.2. Material properties of Aluminum and Al_2O_3 fiber (at room temperature) [91].

Material Properties	Aluminum	Al_2O_3 fiber
Young's modulus, E (GPa)	70	370
Poisson's ratio, ν	0.3	0.3
Yield stress, σ_Y (MPa)	80	2000

The heterogeneous materials with a periodic microstructure, e.g. FRMMC, were obtained by the periodic translation of a regular pattern, usually called RVE (Representative Volume Element) or unit cell. Figure 4.4 shows the transverse cross-section of the so-called square edge packing of fibers where the red line represents the unit cell[3]. The symmetry condition can be used for x- and y-axis for the chosen unit cell in order to reduce computational time as shown in Figure 4.5. The fiber volume fraction was chosen as 20 %. The four node plane strain quadrilateral elements were used for the FEA calculation. The number of elements and the number of nodes were 744 and 801, respectively. The macroscopic stresses were imposed to in-plane biaxial direction. Here Σ_x and Σ_y indicate the x-directional macroscopic stress and y-directional macroscopic stress, respectively.

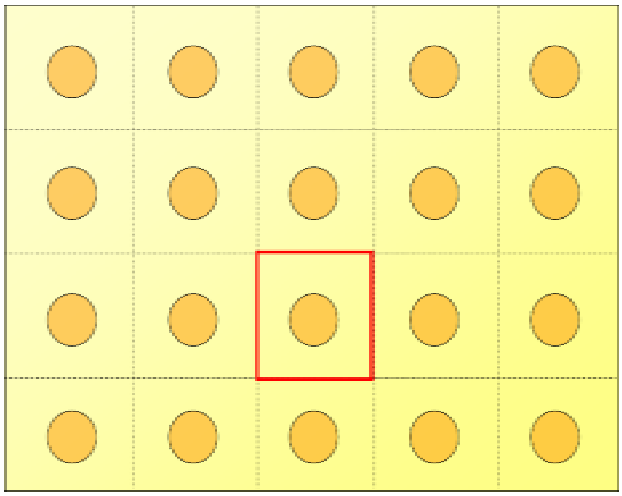

Figure 4.4. A transverse cross-section of the square packing of the fibers.

The shakedown analyses in in-plane loading plane (Σ_x, Σ_y) were performed as shown in Figure 4.6. They were normalized by the yield stress of matrix, σ_Y. For the comparison, the shakedown limits of literature and analytical results were shown. The red solid line indicates

is prevented. Since there is no axial displacement at the ends and, by symmetry, at the midsection, it may be assumed that the same holds at every cross-section. Since the longitudinal displacement is zero and the longitudinal normal stress can be found in terms of σ_x and σ_y, the plan strain problem reduces to the determination of σ_x, σ_y, τ_{xy} as functions of x and y only [118].

[3] Conventionally, there are three unit cell methods for periodic arrangement: square unit cell with edge packing, square unit cell with diagonal packing, and periodic hexagonal array. For details, see reference [119].

the present result and the blue solid line indicates the shakedown result obtained by Schwabe [91]. Circle and triangle indicate analytical results which were determined by Du et al. [120] and Ponter et al. [121], respectively. The comparison result shows the shakedown limits by present approach have a good correspondence with the previous studies. Therefore the developed computational tool for shakedown analysis can be used for determination of shakedown safety limits of FRMMC composite.

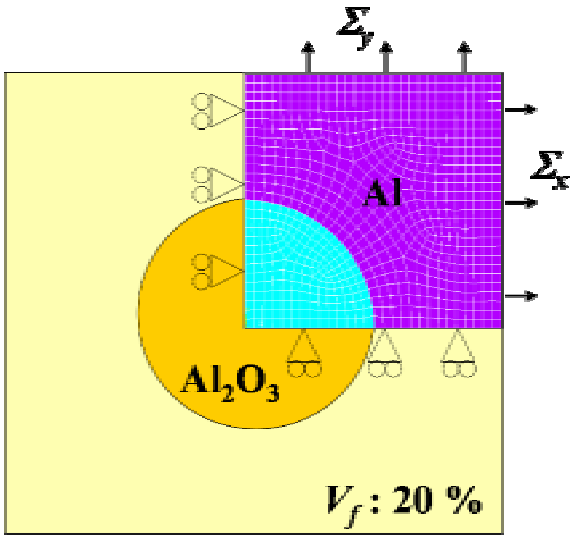

Figure 4.5. A square unit cell (from Figure 4.3) with finite element mesh and boundary condition.

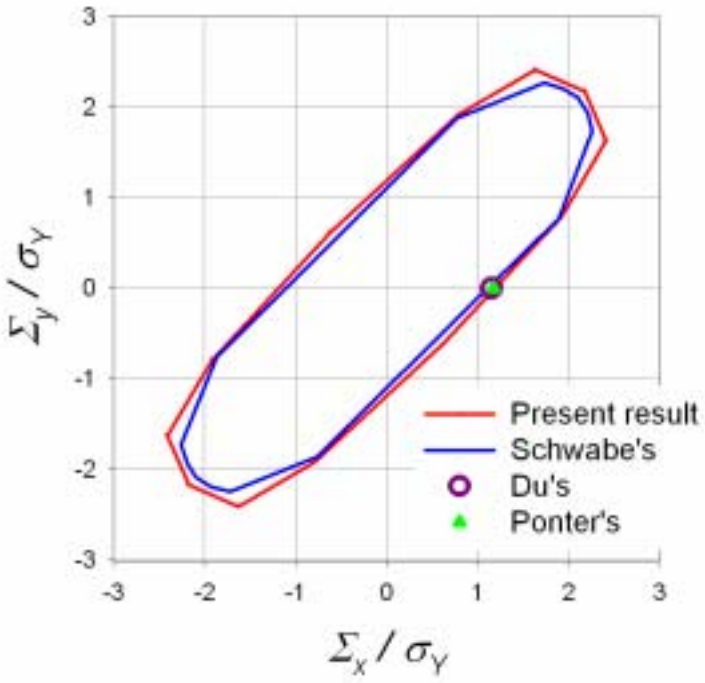

Figure 4.6. Shakedown limits of FRMMC in in-plane biaxial loading space.

4.3. Experimental result of FRMMC

The present results are verified with experimental results. The thermomechanical fatigue (TMF) experiment of lamina-type FRMMC composite was performed by Leckie and Jansson [36]. The used materials were Al_2O_3 long fiber and Al metal matrix composite. Shakedown limits were determined by cyclic thermomechanical test and compared with the values which were obtained by step-by-step numerical method. The materials properties used in computations were represented in Table 4.3. For the experiment, the fiber consists of 99 % polycrystalline α-alumina (Al_2O_3) coated with silica that improves the strength of the fiber and aids the wetting by the molten metal. The fiber has a diameter of approximately 20 μm, and an elastic modulus of 345-380 GPa.

Table 4.3. Material properties used in computations [36].

Material Properties	Aluminum	Al_2O_3 fiber
Young's modulus, E (GPa)	70	345
Poisson's ratio, ν	0.32	0.26
Coefficient of thermal expansion, α_g (10^{-6} /K)	8.6	0.26
Yield stress, σ_Y (MPa)	95	-

In the computational analysis, the fibers were assumed to be long parallel cylinders and the thermomechanical loading was considered. The chosen unit cell was hexagonal array. Since the shakedown limits were dependent on the geometry, the two geometries were chosen in this study [91]. Figure 4.7 shows the transverse cross-section of the packing of fibers and two kinds of hexagonal unit cell with finite element mesh. The fiber volume fraction was determined to be 55 %. The four node plane strain quadrilateral elements were used. The number of elements and the number of nodes used in FEA calculation were 419 and 471 for geom. 1 and 470 and 514 for geom. 2.

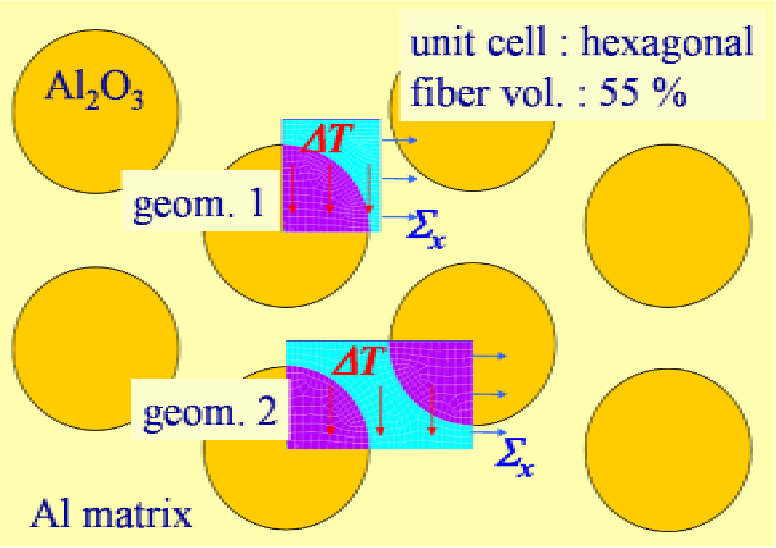

Figure 4.7. A hexagonal unit cell with finite element mesh and boundary condition.

The shakedown limits for thermomechanical loading case were represented in Figure 4.8. The x-directional macroscopic stress and thermal loading were considered. Thermal loading (ΔT) and macroscopic stress (Σ_x) were normalized by the yield stress of the Al matrix. For the comparison, elastic limits were denoted by blue dashed line for geom. 1 and red dashed line for geom. 2. Also shakedown limits obtained by the incremental analysis were shown in the same loading plane as grey solid line.

Shakedown limits as well as elastic limits were dependent on the chosen geometry (geom. 1 and geom. 2). This effect was because the transverse strength was sensitive to the fiber arrangements and loading directions, with a square arrangement of fibers loaded in the 0^o direction being the strongest (geom. 1), a square arrangement loaded in the 45^o or a hexagonal arrangement in the 0^o being the weakest (geom. 2) [120]. From the results, the shakedown limits of the experimental method were higher than shakedown limits of the shakedown analysis. This discrepancy of shakedown limits between shakedown analysis and experimental method can be explained by the fact that there exists the influence of strain hardening in the metal matrix from cycle to cycle. Also, the difference of shakedown limits between incremental analysis and experimental analysis was investigated in the literature work [36]. However, shakedown limits obtained from the experimental investigation were in a fairly good agreement with those obtained by the developed tool.

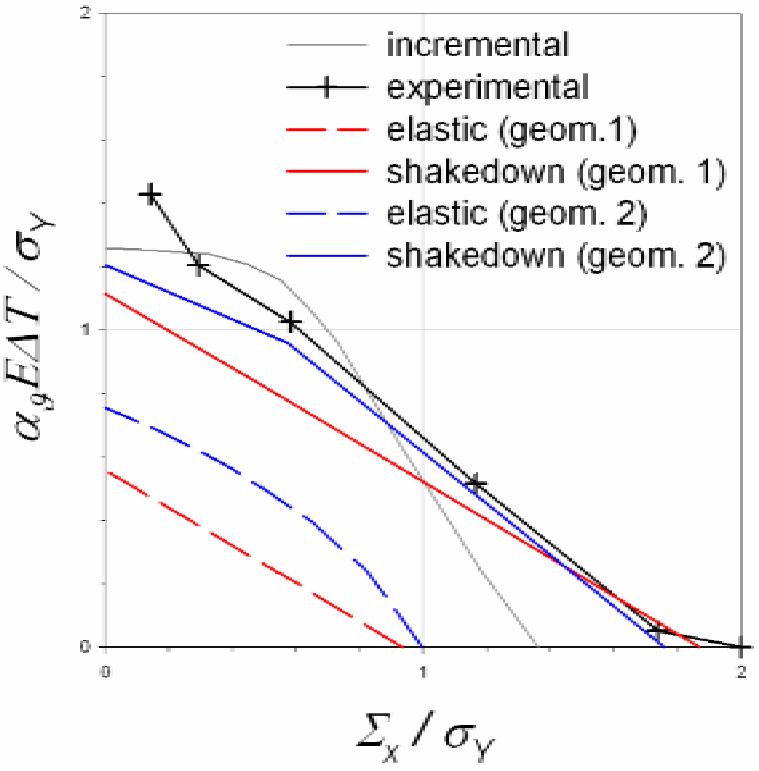

Figure 4.8. Shakedown limits of FRMMC in thermomechanical loading space.

5. Description of Problem

In this work, the shakedown analysis of FRMMC is performed for the structural safety assessment for fusion application. The application of shakedown analysis for the plasma facing component (PFC) was not simple due to the complexity in the loading history of the cyclic heat flux loading combined with the manufacturing process. Therefore, in this chapter, the systematic methods were represented with analysis objective, materials and computational methods.

5.1. Analysis objective

Firstly, we apply the shakedown analysis into FRMMC layers to investigate shakedown safety limits for the fusion application. The model for analysis is shown in Figure 5.1. The FEM-based shakedown analysis is performed for the unit cell of FRMMC layer. The chosen unit cells are lamina and laminate, as shown in Figure 5.1 (b) and (c). Secondly, the incremental FEM (thermo-elasto-plastic) analysis is carried out for the whole PFC (Figure 5.1 (a)) in order to obtain the realistic loading path. The details of analysis were shown in the following sections.

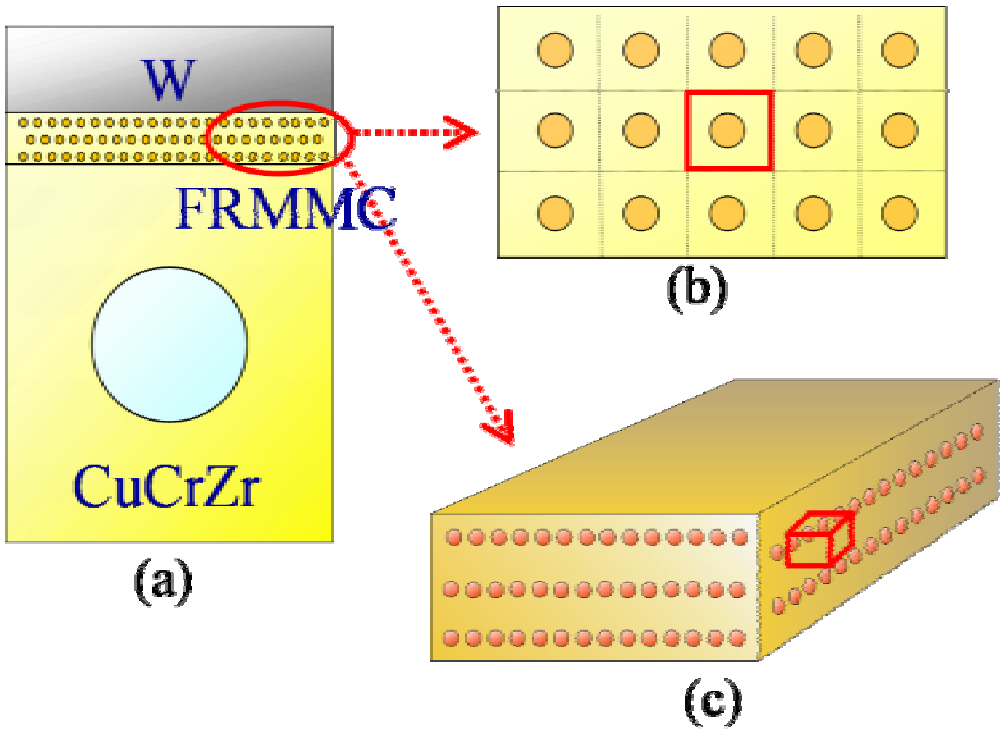

Figure 5.1. The schematic view of PFC component and typical FRMMC layers: (a) FRMMC layer included PFC component, (b) lamina type FRMMC layer and its unit cell, and (c) laminate type FRMMC layer and its unit cell.

5.2. Material properties for analyses

5.2.1. FRMMC for shakedown analysis

As mentioned, shakedown analyses are performed for unit cells of FRMMC layer. In this work, SiC long fiber and Cu alloy (CuCrZr) are used. SiC long fibers can provide high temperature strength. The Cu alloy mainly provides high thermal conductivity. The material properties of the matrix and the fiber are represented in Table 5.1.

For FEM-based shakedown analysis, the SiC long fiber was assumed to be linear elastic whereas the metal for the matrix was considered to be elastic-ideal (perfectly) plastic (EIP). The arrangements of fiber in the matrix were based on the some geometrical assumptions as follows.

- The interface of fiber and matrix is perfectly bonded.
- Fibers of straight cylinders are formed with circular cross-sections of the diameter.
- All fibers possess identical geometry and they are homogeneous.
- Fibers are infinitely long, i.e. the ratio of the diameter to length is very small.
- Fibers are arranged in parallel and unidirectionally in one ply with a same distance between neighboring fiber centerlines.

Since the copper alloy was hardened with deformation, the hardening effect cannot be ignored. In this shakedown analysis, both limited kinematic hardening (LKH) effect and unlimited kinematic hardening (ULKH) effect are considered. For LKH model, the hardening factor has to be determined by the experimental data [122].

Table 5.1. Properties of matrix and fiber at room temperature.

Materials	CuCrZr [123]	SiC long fiber
Young's modulus, E (GPa)	128	380
Poisson's ratio, ν	0.34	0.17
Coefficient of thermal expansion, α_g (10^{-6}/K)	15.7	5.7
Yield stress, σ_Y (MPa)	297	∞
Hardening effect	$1.2\sigma_Y$ (LKH), ∞ (ULKH)	-

* LKH: limited kinematic hardening model, ULKH: unlimited kinematic hardening model.

5.2.2. PFC related materials for incremental analysis

The thermo-elasto-plastic analysis is performed for the whole PFC using commercial FEM code, ANSYS. For this, the used PFC related materials are tungsten for plasma facing material (PFM), FRMMC (SiC fiber and CuCrZr) for interlayer, and CuCrZr for heat sink. For the incremental analysis, extensive temperature-dependent thermomechanical properties

of these materials are necessary, e.g. Young's modulus, Poisson's ratio, coefficient of thermal expansion, stress-strain curve, thermal conductivity, density, heat capacity, etc. Some important mechanical properties (at room temperature and joining temperature) were listed in Table 5.2.

The properties of tungsten and CuCrZr can be available from the ITER materials handbook [123]. Since the FRMMC for the incremental analysis is homogenized, the material properties for the whole FRMMC layer are necessary. However, the FRMMC (SiC fiber and CuCrZr matrix) is under developing stage and they are not successfully made up to now. Therefore, the mechanical properties of FRMMCs cannot be obtained experimentally but be obtained by FEM calculation. For the FEM computation, the laminate FRMMC is considered and its fiber volume fraction is fixed to 20 %. The laminate structure is orthotropic, and the resulting material properties are dependent on the directions for FRMMC. In the Table 5.2, *la* indicates in-plane (laminate) direction and *tr* indicates out-of-plane (transverse) direction.

Table 5.2. Properties of tungsten, FRMMC, and CuCrZr.

Materials	Tungsten [123]		FRMMC (20 %)		CuCrZr [123]	
	20 °C	700 °C	20 °C	700 °C	20 °C	700 °C
Young's modulus, E (GPa)	398	383	170 (*la*) 160 (*tr*)	128 (*la*) 111 (*tr*)	128	85
Poisson's ratio, ν	0.28	0.29	0.29 (*la*) 0.27 (*tr*)	0.36 (*la*) 0.38 (*tr*)	0.34	0.34
Coefficient of thermal expansion, α_g (10^{-6} /K)	3.9	4.3	12.5 (*la*) 14.0 (*tr*)	16.6 (*la*) 20.1 (*tr*)	15.7	19.3
Yield stress, σ_Y (MPa)	656	155	-	-	297	128
Thermal conductivity (W/mK)	0.17	0.12	0.28 (*la*) 0.26 (*tr*)	0.28 (*la*) 0.26 (*tr*)	0.38	0.37

5.3. Scope of shakedown analysis

To perform FEM-based shakedown analysis for the composite materials, unit cell concept of the fiber arrangement is introduced by considering the periodicity of the fiber arrangement. In this work, two types of fiber arrangements are considered, i.e. lamina and laminate. For lamina structure, square unit cell is used, as described in Figure 5.2. A quarter part of unit cell is chosen for mesh generation in order to reduce the computational cost. Two different fiber volume fractions (20 % and 40 %) are considered to investigate the effect of fiber volume fraction on the shakedown limits. Although three-dimensional shakedown analysis is the main object in this work, two-dimensional shakedown analysis is performed for lamina structure. From this comparative study, the difference between two-dimension analysis and three-dimensional analysis is investigated. The finite element meshes of each unit cell and their boundary conditions are represented in Figure 5.2. Here Σ_x, Σ_y, and Σ_z indicate x-, y-, and z-directional macroscopic stress and ΔT indicates the thermal loading from the difference between current temperature and stress free temperature, respectively.

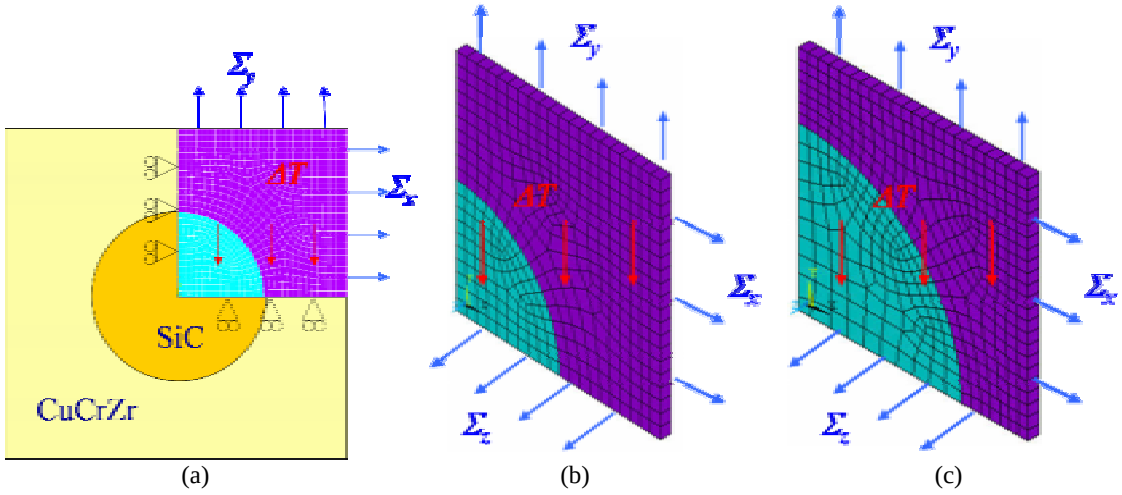

Figure 5.2. Finite element meshes for the lamina (square unit cell) with fiber volume fraction of (a) 20 % (2D analysis), (b) 20 % (3D analysis), and (c) 40 % (3D analysis).

For laminate structure, an anti-symmetric cross-ply laminate with the stacking sequence [0/90] is considered (left figure of Figure 5.3). The fiber arrangement and the resulting unit cell are represented in Figure 5.3. Two different fiber volume fractions (20 % and 40 %) are considered to investigate the effect of fiber volume fraction.

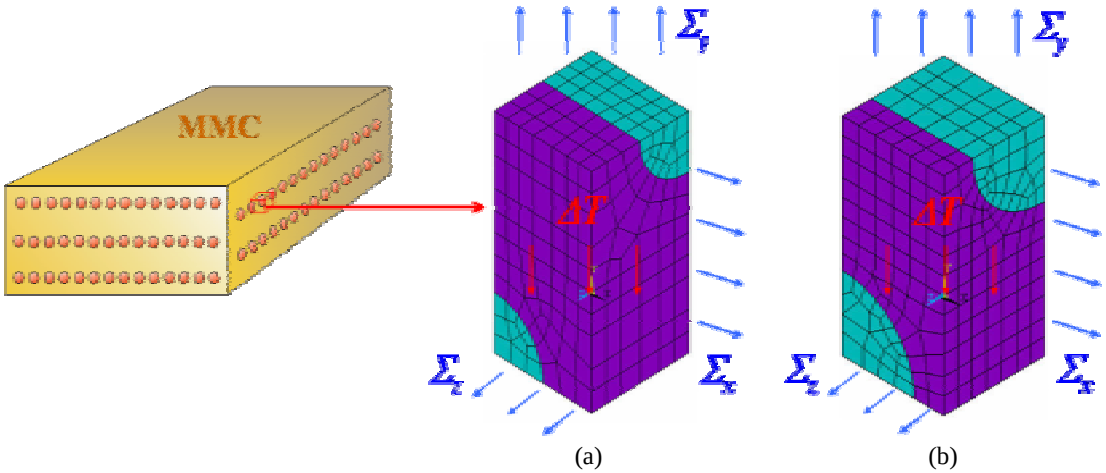

Figure 5.3. Finite element meshes for the laminate with fiber volume fraction of (a) 20 % and (b) 40 %.

As a whole, five unit cells are made for the analysis, that is, lamina with 20 % of volume fraction (2D analysis), lamina with 20 % of volume fraction (3D analysis), lamina with 40 % of volume fraction (3D analysis), laminate with 20 % of volume fraction (3D analysis), and laminate with 20 % of volume fraction (3D analysis). Number of elements, number of nodes and the number of variables of each unit cell are summarized in Table 5.3. From the element and node information, the numbers of known variables (elastic stress field, yield stress, limit stress) and unknown variables (shakedown safety factor, residual stress field) are determined. The shakedown parameters have very strong dependence with the number of elements and nodes.

Table 5.3. Elemental information in FEM and shakedown variables.

	Lamina (2D analysis)	Lamina (3D analysis)		Laminate (3D analysis)	
(Fiber volume fraction)	(20 %)	(20 %)	(40 %)	(20 %)	(40 %)
Number of elements	744	402	402	525	657
Number of nodes	801	886	884	745	905
Number of known variables	35,127	154,368	154,368	201,600	252,288
Number of unknown variables	8,929	19,297	19,297	25,201	41,137

5.4. Scope of incremental analysis

5.4.1. Thermal loading history and geometry of PFCs

The thermal loading history of PFC is investigated including manufacturing process. The thermal history can be separated into two main processes, i.e. manufacturing process and fusion operation process. During fusion operation, the cyclic high heat flux loading causes the thermal stresses in the PFC. In the normal operation of fusion reactor, 10,000 cycles of the repeated HHF loads were expected [124]. In the incremental FEM analysis, two cycles of fusion operation are considered with a manufacturing step. The loading history is made up of uniform cooling process from the joining stage, residual state, pre-heating, 1^{st} high heat flux (HHF) cycle, and 2^{nd} HHF cycle. A schematic of the thermal loading history of a PFC used in the incremental analysis is represented in Figure 5.4.

Firstly, the thermal history during the manufacturing process is explained. The parts of PFC, that is, plasma facing material (PFM), FRMMC layer, and heat sink, are joined at high temperature. The joining process is considered as the stress free state. The assembled PFC is cooled down to the room temperature in order to install in the inner vessel of the fusion reactor. During the cooling process, the PFC component is subjected to significant residual stress due to the difference of the coefficient of thermal expansion between PFM, FRMMC layer, and heat sink. Next, the pre-heating procedure is performed and the uniform temperature of PFC reaches to coolant temperature before the real fusion operation. Since the temperature of component is changed slowly, temperature is assumed to be uniform in the whole PFC. In this figure, the black solid line indicates the uniform temperature evolution from joining process to pre-heating process.

Secondly, the thermal history during the fusion operation process is investigated. As mentioned, the two cycles of heat flux loading are concerned with the incremental analysis. During the heat flux loading, PFC undergoes the cyclic thermomechanical loads due to the

different material properties between PFM and heat sink. In Figure 5.4, the red solid line indicates temperature evolution of the first wall, the green solid line indicates the temperature evolution of the interface between PFM and FRMMC layer, and the blue solid line indicated the temperature evolution of the interface between FRMMC layer and heat sink.

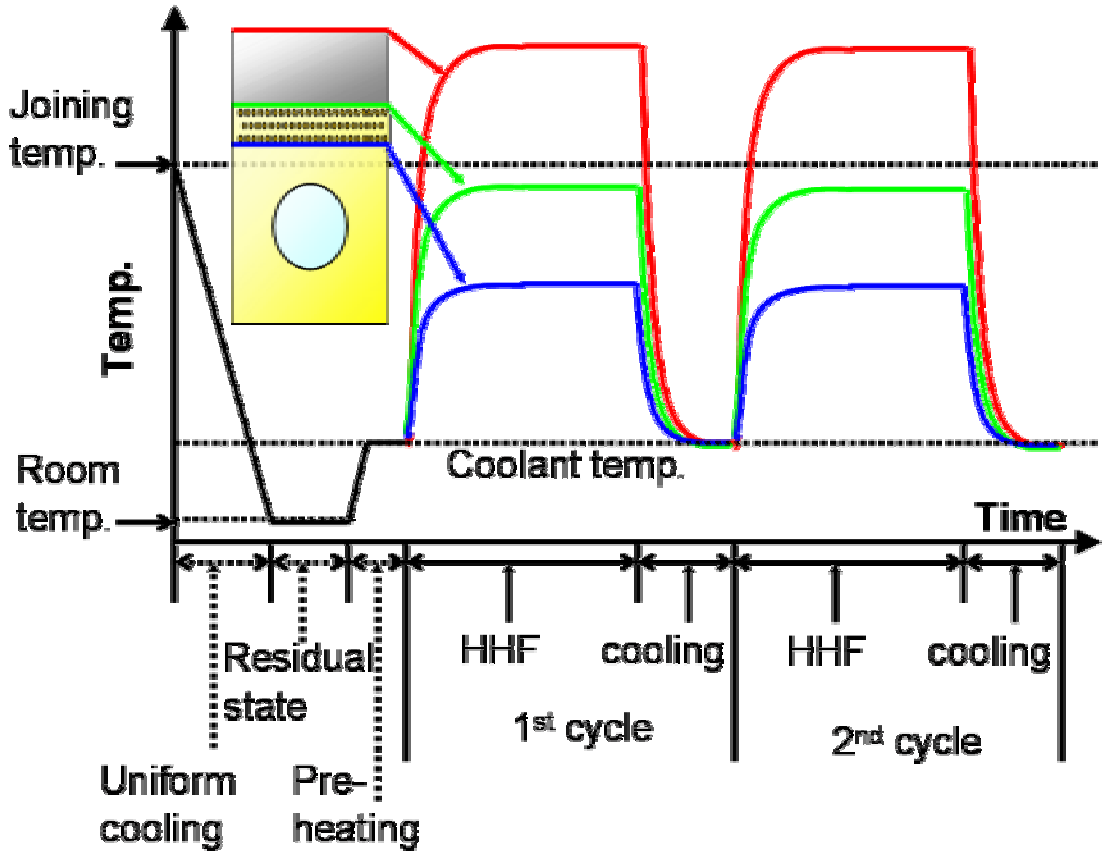

Figure 5.4. Schematic of the temperature development in a PFC under typical fusion operation condition [125].

This thermal loading history generates thermomechanical stresses in the PFC. The stress is generated due to the difference of CTE between tungsten PFM armor tile and CuCrZr heat sink substrate. This causes mismatch stress in the region near the interfaces between FRMMC layer and the other components. Such a mismatch stress can be generated already during the manufacturing process resulting in residual stresses within the components.

The incremental analysis is performed using three-dimensional finite element analysis (FEA). The geometry and the finite element meshes are shown in Figure 5.5. Due to symmetry of the PFC, the half geometry is considered. A linear rectangular brick element with eight nodes is used for the FEA. In the model, the number of total elements and the number of total nodes are 1852 and 3009, respectively.

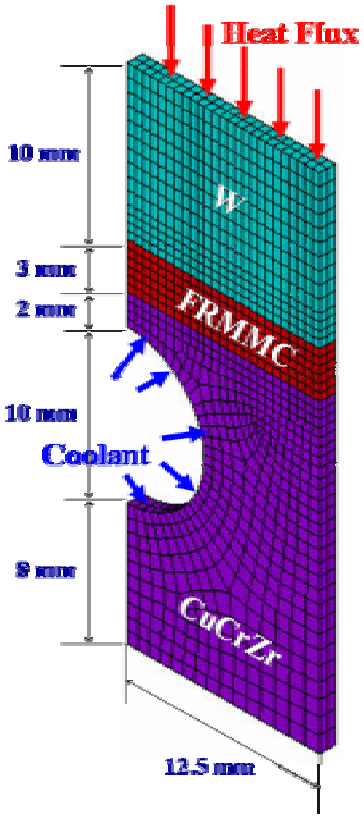

Figure 5.5. The geometry of candidate PFC component and its finite element mesh [126].

5.4.2. Methodology of incremental analysis

The complete procedure of this work is represented in Figure 5.6. For shakedown analysis, the unit cell of FRMMC layer is used (Figure 5.6 (a)). Then the shakedown limits are obtained with temperature change (Figure 5.6(b)) in a two-dimensional loading space. They can be redrawn with additional thermal axis in a three-dimensional loading space (Figure 5.6 (c)). In chapter 6, the details of shakedown limits are represented and discussed.

PFC and the loading condition are chosen to implement in thermo-elasto-plastic FEM. Four typical locations are selected to represent the loading paths of the FRMMC layer (Figure 5.6 (d)). Firstly the thermal analysis is performed for the given loading conditions. Then the temperature evolutions are obtained. Using the observed thermal information, the structural analysis is carried out. Then the stress evolutions are obtained (Figure 5.6 (e)). Using the components of temperature and stresses, the thermomechanical loading paths are obtained in a three-dimensional loading space (Figure 5.6 (f)).

Finally, the shakedown limits and the thermomechanical loading paths can be drawn in a three-dimensional loading space, as shown in Figure 5.6 (g). From the results of a comparison between the shakedown limits and the loading paths, the structural loading paths are investigated with several loading combinations. The results will be discussed with safety assessment of the PFC can be discussed. In chapter 7, the thermomechanical shakedown limits.

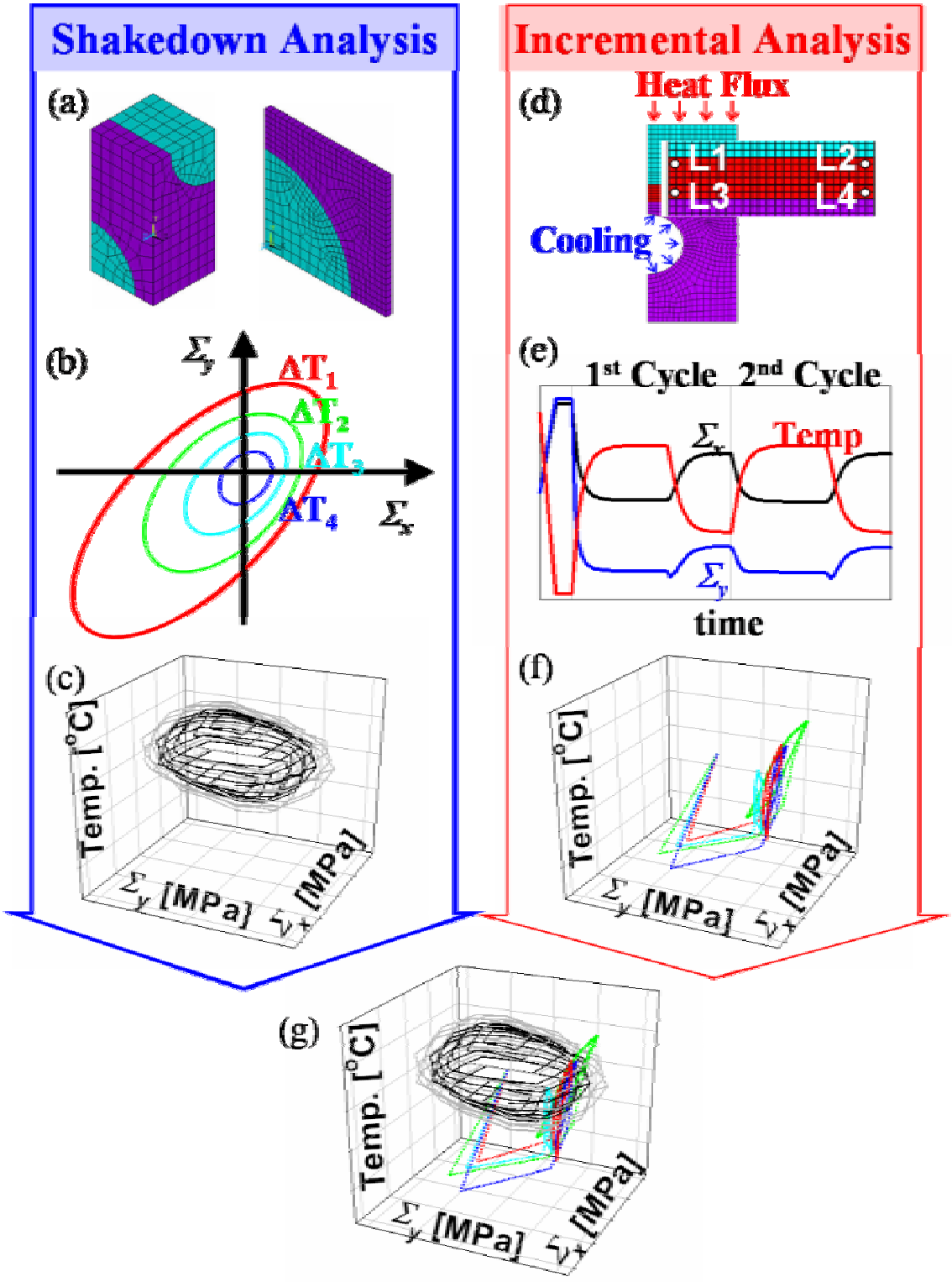

Figure 5.6. The procedure of shakedown analysis and incremental analysis: (a) model for shakedown analysis, (b) shakedown limits with temperature, (c) shakedown limits in three-dimensional space, (d) model for incremental analysis, (e) stress and temperature evolution path, (f) thermomechanical loading paths in three-dimensional space, and (g) shakedown limits with thermomechanical loading paths in three-dimensional space.

6. Results of Shakedown Analysis

The three-dimensional analysis of composites is performed to obtain shakedown limits in two-dimensional loading spaces including temperature changes. The results of shakedown limits will be discussed with geometrical influences, increase of fiber volume fraction, loading direction and hardening effect, as shown in Table 6.1.

Table 6.1. Loading condition and geometry in shakedown analysis.

	Lamina with 2D analysis (**6.2**)	Lamina with 3D analysis (**6.1**)	Laminate with 3D analysis (**6.3**)
Loading effect	In-plane only	In-plane (**6.1.1**), out-of-plane (**6.1.2**)	In-plane (**6.3.1**), out-of-plane (**6.3.2**)
Hardening effect	No	No	LKH, ULKH (**6.4**)

6.1. Shakedown analysis of FRMMC lamina

The lamina structure is considered to obtain the shakedown limits. Three-dimensional shakedown analysis is carried out and the results are represented in two-dimensional loading spaces (Σ_x, Σ_y) and (Σ_x, Σ_z), i.e. in-plane bi-axial loading and out-of-plane bi-axial loading, with temperature change.

6.1.1. Shakedown analysis of FRMMC lamina for in-plane loading

In this section, shakedown limits were obtained for three-dimensional lamina geometry and represented in in-plane loading plane (Σ_x, Σ_y). 20 % and 40 % of fiber volume fraction were considered to investigate the effect of fiber volume fraction, as shown in Figures 6.1 and 6.2. For the comparison, elastic limits were shown as dashed lines. Here Σ_x and Σ_y indicate x-directional macroscopic stress and y-directional macroscopic stress, respectively, and they were normalized by the yield stress of matrix. To consider the effect of thermal loading, four reference temperature differences, i.e. 0 ^{o}C, 10 ^{o}C, 50 ^{o}C, and 100 ^{o}C, were investigated. The results were illustrated with different colors (0 ^{o}C: red, 10 ^{o}C: green, 50 ^{o}C: bright blue, 100 ^{o}C: blue). The following contents were observed from the graphical views of shakedown limits.

(i) The values of shakedown limits were higher than those of the elastic limits in every reference temperature difference. The sizes of shakedown limits and elastic limits had very strong dependence on temperature increase.

(ii) Both shakedown spaces and elastic spaces had longish shapes along the first and the third quarter planes.

(iii) The margins from shakedown limits in the first quarter and the third quarter planes were bigger than those in the second and the fourth quarter planes.

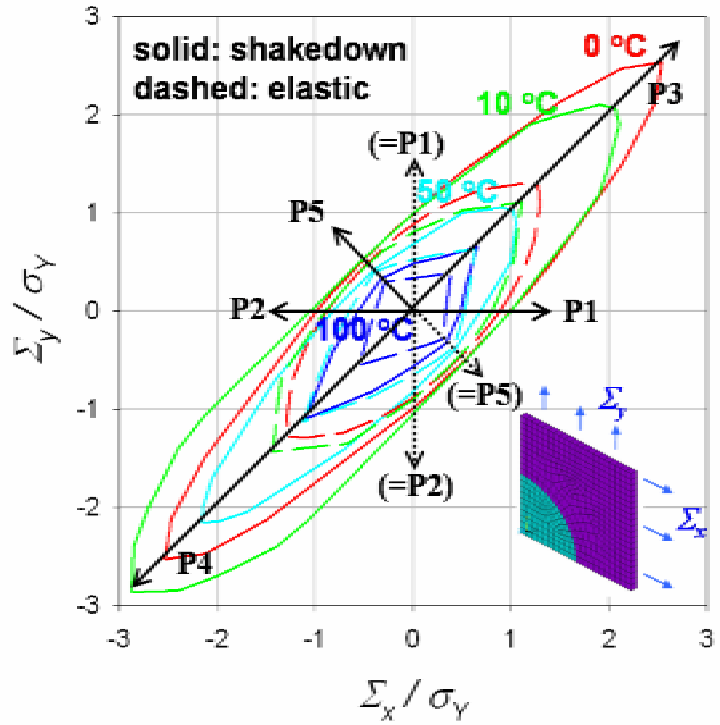

Figure 6.1. Elastic limits and shakedown limits of lamina with 20 % of fiber volume fraction in in-plane biaxial loading space (3D analysis): P1-P5 are loading directions and 10, 50 and 100 °C indicate the magnitude of reference temperature increase (heating).

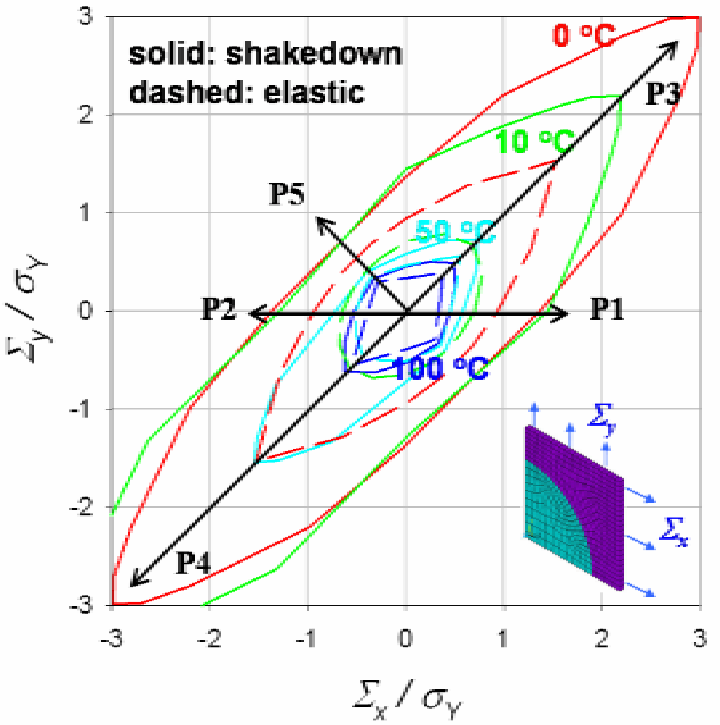

Figure 6.2. Elastic limits and shakedown limits of lamina with 40 % of fiber volume fraction in in-plane biaxial loading space (3D analysis): P1-P5 are loading directions and 10, 50, and 100 °C indicate the magnitude of reference temperature increase (heating).

(iv) The results showed the sensitivity of shakedown limits and elastic limits to prescribed thermal loads. They were shifted to the compression loading direction with increase of temperature difference.

(v) The fiber volume fraction of the composite gives an influence to both shakedown limits and elastic limits. At small temperature change, the size of shakedown limits with 40 % of fiber volume fraction was bigger than that of 20 % of fiber volume fraction. However, at larger temperature change, the tendency was reversed.

For detail understanding of previously observed effects, the elastic limits, the shakedown limits, and the margins are listed in Table 6.2. The considered loading conditions were uniaxial tension loading (P1), uniaxial compression loading (P2), biaxial tension loading (P3), biaxial compression loading (P4), and biaxial tension-compression combined loading (P5).

Effect of thermal loading

As shown in Table 6.2, in case of a 20 % of fiber volume fraction without thermal loading, elastic limit and shakedown limit for uniaxial tension loading (P1) were 0.885 and 0.987, respectively. For the uniaxial compression loading (P2), they had the same values with the uniaxial tension loading (P1). They had a symmetric shape for tension and compression loading when the thermal loading was not considered. When the thermal loading was considered, the symmetric tendency was not shown any more. For example, in case of 100 ^{o}C of thermal loading for uniaxial tension loading (P1), elastic limit and shakedown limit were 0.336 and 0.484, respectively. For uniaxial compression loading (P2), elastic limit and shakedown limit were 0.389 and 0.566, respectively.

Effect of loading direction

The asymmetric effect was more clearly observed in the elastic and shakedown limits in the biaxial loading (P3 and P4) than those in the uniaxial loading (P1 and P2). For example, in the case of 100 ^{o}C of thermal loading for biaxial tension loading (P3), the elastic limit and shakedown limit were 0.382 and 0.651, while for biaxial compression loading (P4), the elastic limit and shakedown limit were 0.550 and 1.100. From this observation, shakedown limits and elastic limits were shifted to the biaxial compression loading plane due to an asymmetric effect from positive thermal loadings. Since the structural deformation state from temperature increase was similar with that from applied biaxial tension loading, positive thermal loading combined with biaxial tension loading causes decreases in the elastic limits and the shakedown limits.

Effect of loading direction (margin)

The magnitude of margin represents the relative gain of shakedown limits over elastic limits. The margins are obtained by the following equation and represented in Table 6.1. Here, α^{SD} and α^{e} indicate the shakedown limit and the elastic limit, respectively.

$$\text{margin}\,[\%] = \frac{\alpha^{SD} - \alpha^{e}}{\alpha^{e}} \tag{6.1}$$

The margins in the first quarter and the third quarter loading planes (P3 and P4) were larger than those of other loading planes (P1, P2, and P5). For example, in case of 0 ^{o}C with 20 % of fiber volume fraction, the obtained margins were 11.5 % in uniaxial loading (P1 and P2), 97.9 % in biaxial loading (P3 and P4), and 8.0 % in tension-compression combined loading (P5). In tension-compression combined loading, the margins were significantly decreased.

Table 6.2. Elastic limits and shakedown limits of lamina (3D analysis) and their margins in in-plane loading (from Figures 6.1 and 6.2). .

Geometry (fiber fraction)		**P1** ($\Sigma_x = P$, $\Sigma_y = 0$)			**P2** ($\Sigma_x = -P$, $\Sigma_y = 0$)			**P3** ($\Sigma_x = \Sigma_y = P$)			**P4** ($\Sigma_x = \Sigma_y = -P$)			**P5** ($\Sigma_x = -\Sigma_y = -P$)		
		$\alpha^e P/\sigma_Y$	$\alpha^{SD} P/\sigma_Y$	margin (%)	$\alpha^e P/\sigma_Y$	$\alpha^{SD} P/\sigma_Y$	margin (%)	$\alpha^e P/\sigma_Y$	$\alpha^{SD} P/\sigma_Y$	margin (%)	$\alpha^e P/\sigma_Y$	$\alpha^{SD} P/\sigma_Y$	margin (%)	$\alpha^e P/\sigma_Y$	$\alpha^{SD} P/\sigma_Y$	margin (%)
3d-lamina (20 %)	0 °C	0.885	0.987	11.5	0.885	0.987	11.5	1.279	2.531	97.9	1.279	2.531	97.9	0.476	0.514	8.0
	10 °C	0.804	1.000	24.4	0.897	1.083	20.7	1.108	2.063	86.2	1.437	2.868	99.6	0.468	0.520	11.1
	50 °C	0.527	0.686	30.2	0.653	0.818	25.3	0.633	1.021	61.3	1.128	2.156	91.1	0.393	0.410	4.3
	100 °C	0.336	0.484	44.0	0.389	0.566	45.5	0.382	0.651	70.4	0.550	1.100	100.0	0.292	0.329	12.7
3d-lamina (40 %)	0 °C	0.939	1.366	45.5	0.939	1.366	45.5	1.531	2.986	95.0	1.531	2.986	95.0	0.524	0.683	30.3
	10 °C	0.706	1.448	105.1	0.649	1.292	99.1	0.678	2.188	222.7	0.579	3.880	570.1	0.406	0.685	68.7
	50 °C	0.458	0.586	27.9	0.513	0.725	41.3	0.557	0.729	30.9	0.443	1.548	249.4	0.350	0.398	13.7
	100 °C	0.336	0.454	35.1	0.390	0.531	36.2	0.382	0.488	27.7	0.550	0.621	12.9	0.292	0.330	13.0

(i) P indicates the positive applied loading. The value was fixed to 100 MPa. For example, P5 loading indicates Σ_x = -100 MPa, Σ_y = 100 MPa.
(ii) α^e and α^{SD} indicate elastic safety factor and shakedown safety factor. $\alpha^e P/\sigma_Y$ and $\alpha^{SD} P/\sigma_Y$ indicate normalized macroscopic stresses.
(iii) Margin indicates the relative gain shakedown limits over elastic limits.

From theses results, it is expected that the margins are basically increased in the symmetric loading condition (P3 and P4). In the last section, the reason for these expected increases will be investigated considering the distribution and localization of stress field.

Effect of thermal loading (margin)
When the thermal loadings (10 ^{o}C, 50 ^{o}C, 100 ^{o}C) were investigated, the tendency of margin showed asymmetric effect with the loading sign, i.e. tension or compression. There was a difference in margins between uniaxial tension loading and uniaxial compression loading. For example, in case of 100 ^{o}C of thermal loading, margin for uniaxial tension loading (P1) was 44 %, while margin for uniaxial compression loading (P2) was 45.5%. When the biaxial loading was considered, the asymmetry effect of margin was more clearly represented. For example, in case of 100 ^{o}C of thermal loading, margin for biaxial tension loading (P3) was 70.4 %, while margin for biaxial compression loading (P4) was 100 %. From the observation of margin, there might be dependence between loading state and the gain of margin.

Effect of fiber volume fraction
For the investigation of the effect of fiber volume fraction, FRMMC with different fiber volume fraction (40 %) was considered. The general tendency was similar to the results of 20 % of fiber volume fraction. The asymmetry of elastic limits, shakedown limits, and their margins were also observed with the increase of temperature difference.

The asymmetry of margins in 40 % of fiber volume fraction was significantly increased in the smaller thermal loading. For example, in case of 10 ^{o}C of thermal loading, margins for 20 % of fiber volume fraction were 86.2 % (P3) and 99.6 % (P4), while margins for 40 % of fiber volume fraction were 222.7 % (P3) and 570.1 % (P4). On the contrary, the tendency was reversed in the larger thermal loading. For example, in case of 100 ^{o}C of thermal loading, margins for 20 % of fiber volume fraction were 70.4 % (P3) and 100 % (P4), while margins for 40 % of fiber volume fraction were 27.7 % (P3) and 12.9 % (P4). The increase of margins is correlated with increase of the shakedown safety limits. From a shakedown viewpoint, the serviceability is improved with the increase of fiber volume fraction in the smaller thermal loading, while it is decreased with increase of fiber volume fraction in the higher thermal loading.

6.1.2. Shakedown analysis of FRMMC lamina for out-of-plane loading

The shakedown limits were represented in out-of-plane bi-axial loading plane (Σ_x, Σ_z). Here Σ_x and Σ_z denote x-directional macroscopic stress and z-directional (fiber-axis) macroscopic stress, respectively, and they were normalized by the yield stress of matrix. To consider the effect of thermal loading, the same thermal loading with in-plane loading (section 6.1.1) was investigated. Several conclusions were drawn from the Figures 6.3 and 6.4, as follows.

(i) Elastic limits and shakedown limits in an out-of-loading plane had very strong dependence with thermal loading.

(ii) Both shakedown spaces and elastic spaces had longish shape along the fiber-axis direction (P1 and P2 in Figures 6.3 and 6.4).

(iii) The margins from shakedown limits in the axial loading (P1 and P2) were larger than those in the other loading.

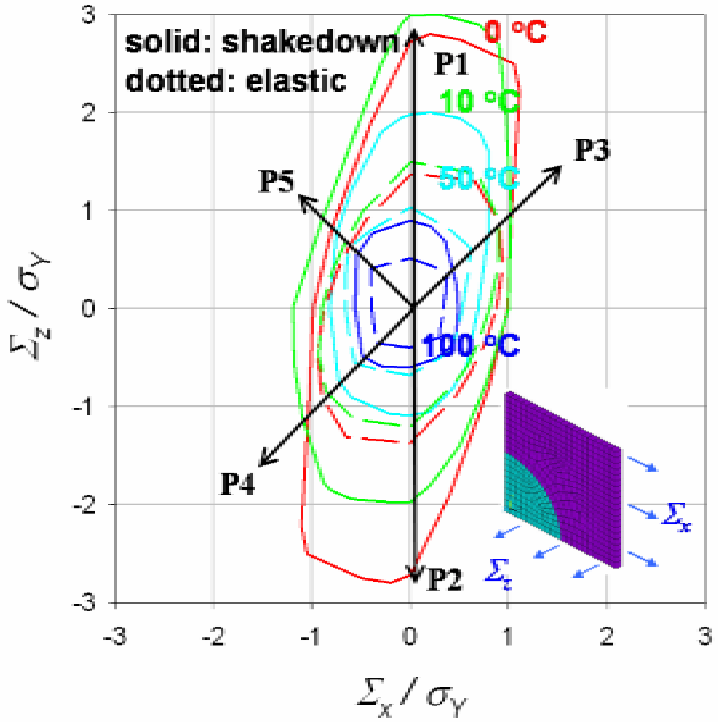

Figure 6.3. Elastic limits and shakedown limits of lamina with 20 % of fiber volume fraction in out-of-plane biaxial loading space (3D analysis): P1-P5 are loading directions and 10 50, and 100 °C indicate the magnitude of reference temperature increase (heating).

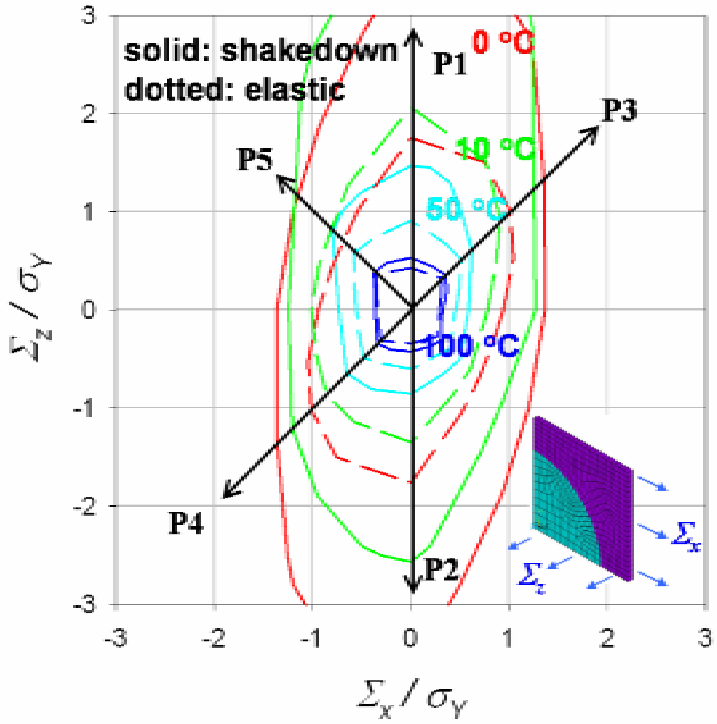

Figure 6.4. Elastic limits and shakedown limits of lamina with 20 % of fiber volume fraction in out-of-plane biaxial loading space (3D analysis): P1-P5 are loading directions and 10 50, and 100 °C indicate the magnitude of reference temperature increase (heating).

(iv) Both shakedown limits and elastic limits were shifted to axial (fiber-axis) tension loading direction (P3) with an increase of reference temperature.

(v) At a smaller temperature change, the size of shakedown limits in 40 % of fiber volume fraction was bigger than that of 20 % of fiber volume fraction. However, at a larger temperature change, this tendency was reversed

Elastic limits, shakedown limits, and margins for out-of-plane loading are represented in Table 6.3. The chosen loading conditions were uniaxial (fiber direction) tension loading (P1), uniaxial (fiber direction) compression loading (P2), biaxial tension loading (P3), biaxial compression loading (P4), and biaxial tension-compression combined loading (P5).

Effect of thermal loading

In case of 20 % of fiber volume fraction without thermal loading, the elastic limits and the shakedown limits for uniaxial tension loading (P1) were 1.375 and 2.72 (margin: 97.8 %), respectively. For uniaxial compression loading (P2), they had same values with uniaxial tension loading (P1). They had symmetric shape for tension and compression loading without thermal loading. When the thermal loading was considered, the symmetric tendency was not shown any more. For example, in the case of 50 ^{o}C of thermal loading for uniaxial tension loading (P1), elastic limit and shakedown limit were 1.033 and 1.978, respectively. For uniaxial compression loading (P2), elastic limit and shakedown limit were 0.678 and 1.083, respectively. From this observation, shakedown limits and elastic limits were shifted to the uniaxial tension loading plane (P1) with heating temperature increase.

Comparison between in-plane loading and out-of-plane loading

The asymmetric effect in the biaxial loading (P3 and P4) was less observed than that in the uniaxial loading (P1 and P2). For example, in the case of 50 ^{o}C of thermal loading for biaxial tension loading (P3), the elastic limit and shakedown limit were 0.678 and 1.083, respectively while for biaxial compression loading (P4), the elastic limit and shakedown limit were 0.550 and 1.100, respectively. In the case of in-plane loading, the longish shape of shakedown limits and larger margin were observed in the biaxial loading direction (P3 and P4 in Figures 6.1 and 6.2). However, in case of out-of-plane loading, they were clearly observed in the axial loading direction along the fiber arrangement (P1 and P2 in Figures 6.3 and 6.4). The von Mises stresses of in-plane biaxial loading (Σ_x, Σ_y) in the case of in-plane loading and axial loading (Σ_z) in the case of out-of-plane loading were represented as follows.

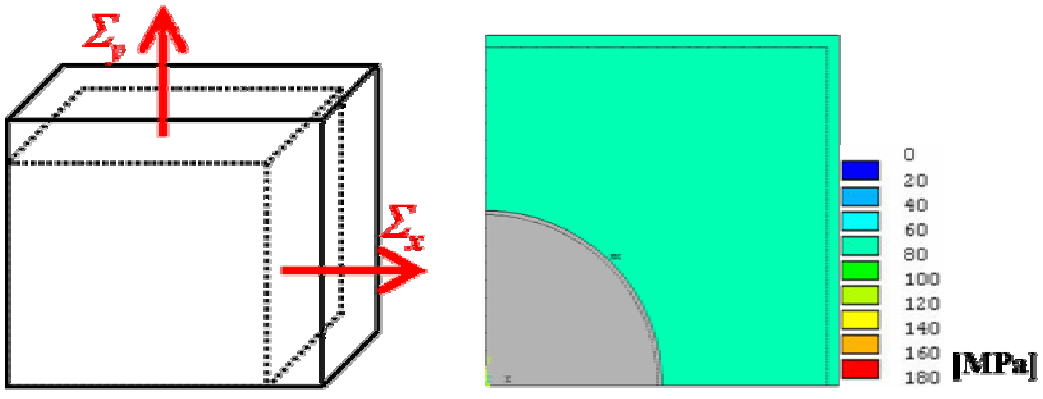

Figure 6.5. Biaxial tension loading ($\Sigma_x = \Sigma_y$ = 100 MPa) and the resulting von Mises stress (≅70 MPa in matrix): Dotted line and solid line indicate undeformed state and deformed state, respectively.

Table 6.3. Elastic limits and shakedown limits of lamina (3D analysis) and their margins in out-of-plane loading (from Figures 6.3 and 6.4).

Geometry (fiber fraction)		**P1** ($\Sigma_x = 0$, $\Sigma_z = P$)			**P2** ($\Sigma_x = 0$, $\Sigma_z = -P$)			**P3** ($\Sigma_x = \Sigma_z = P$)			**P4** ($\Sigma_x = \Sigma_z = -P$)			**P5** ($\Sigma_x = -\Sigma_z = -P$)		
		$\alpha^{el}P/\sigma_Y$	$\alpha^{SD}P/\sigma_Y$	margin (%)	$\alpha^{el}P/\sigma_Y$	$\alpha^{SD}P/\sigma_Y$	margin (%)	$\alpha^{el}P/\sigma_Y$	$\alpha^{SD}P/\sigma_Y$	margin (%)	$\alpha^{el}P/\sigma_Y$	$\alpha^{SD}P/\sigma_Y$	margin (%)	$\alpha^{el}P/\sigma_Y$	$\alpha^{SD}P/\sigma_Y$	margin (%)
3d-lamina (20 %)	0 °C	1.375	2.720	97.8	1.375	2.720	97.8	0.894	1.033	15.5	0.894	1.033	28.9	0.626	0.800	35.5
	10 °C	1.499	2.991	99.5	1.206	1.975	63.8	0.894	1.025	14.7	0.852	1.098	29.8	0.664	0.900	20.5
	50 °C	1.033	1.978	91.5	0.678	1.083	59.7	0.616	0.800	29.9	0.560	0.727	39.3	0.623	0.751	34.2
	100 °C	0.519	0.899	73.2	0.399	0.600	50.4	0.373	0.419	12.3	0.349	0.486	34.7	0.407	0.546	44.3
3d-lamina (40 %)	0 °C	0.939	3.471	269.6	0.939	3.471	269.6	1.010	1.360	34.7	1.010	1.360	41.0	0.693	1.000	37.9
	10 °C	0.778	4.057	421.5	1.008	2.568	154.8	0.912	1.253	37.4	0.857	1.208	33.5	0.810	1.117	38.1
	50 °C	0.458	1.475	222.1	0.551	0.850	54.3	0.518	0.619	19.5	0.486	0.649	10.5	0.578	0.798	5.9
	100 °C	0.293	0.532	81.6	0.335	0.417	24.5	0.320	0.358	11.9	0.306	0.338	28.9	0.358	0.379	35.5

(i) P indicates the positive applied loading. The value was fixed to 100 MPa. For example, P5 loading indicates Σ_x = -100 MPa, Σ_z = 100 MPa.
(ii) α^e and α^{SD} indicate elastic safety factor and shakedown safety factor. α^eP/σ_Y and $\alpha^{SD}P/\sigma_Y$ indicate normalized macroscopic stresses.
(iii) Margin indicates the relative gain shakedown limits over elastic limits using equation (6.1).

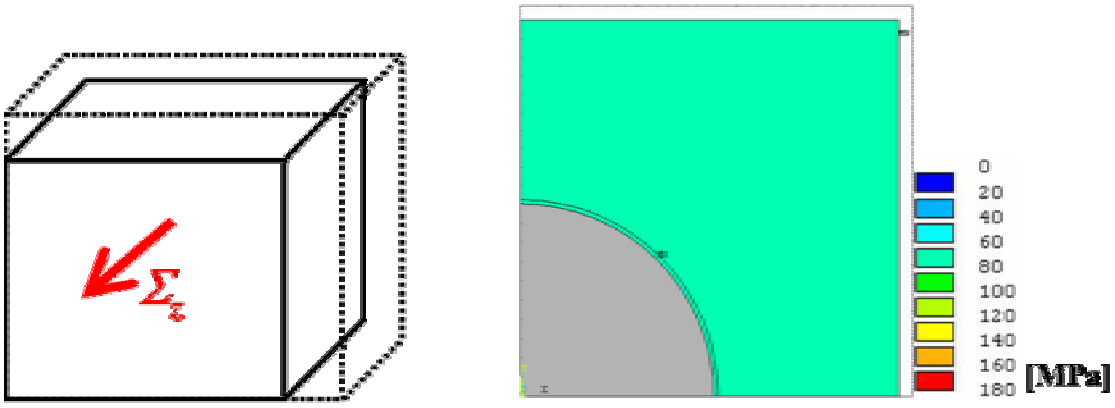

Figure 6.6 Axial tension loading (Σ_z = 100 MPa) and the resulting von Mises stress (≅70 MPa in matrix): Dotted line and solid line indicate undeformed state and deformed state, respectively.

In Figures 6.5 and 6.6, the loading state is described in the left figures. Dotted lines and solid lines indicate the undeformed state and the deformed state, respectively. There were only the in-plane components of stress (Σ_x, Σ_y) in the biaxial loading, while the axial stress component (Σ_z) remained in the axial loading. Although their stress states were totally different, their maximum values and distributions of von Mises stresses were similar.

Effect of thermal loading (margin)

In case of 20 % of fiber volume fraction without thermal loading, the obtained margins were 97.8 % in uniaxial (fiber direction) loading (P1 and P2) and 15.5 % in biaxial loading (P3 and P4). The tendency of margin in out-of-plane loading was totally reversed with in-plane loading. When the thermal loading was considered, the margins had similar trends without thermal loading. There was less difference of margins between biaxial tension loading and biaxial compression loading (e.g. 29.9% in P3 and 39.3 % in P4, 50 ^{o}C) than between uniaxial tension loading and uniaxial compression loading to the fiber direction (e.g. 91.5 % in P1 and 59.7% in P2, 50 ^{o}C). Marginal result showed the similar effect for loading direction as investigated in the previous section.

Effect of fiber volume fraction

FRMMC with different fiber volume fraction (40 %) was considered in out-of-plane loading to investigate the effect with the fiber volume fraction. The trend was similarly observed with the results of 20 % of fiber volume fraction. In the case of 40 % of fiber volume fraction, the asymmetric trend of elastic limits and shakedown limits was clearly represented with the increase of temperature difference. The general marginal effect of 40 % of fiber volume fraction had similar trend with that of 20 % of fiber volume fraction. However, the magnitude of asymmetry and marginal effect of 40 % of the fiber volume fraction was increased in 10 ^{o}C and 50 ^{o}C of thermal loading. For example, the margins of axial tension loading (P1) were dramatically increased to 421.5 % (10 ^{o}C of temperature increase) and 222.1 % (50 ^{o}C of temperature increase) in the case of 40 % of the fiber volume fraction, while they were 99.5 % (10 ^{o}C of temperature increase) and 91.5 % (50 ^{o}C of temperature increase) in case of 20 % of fiber volume fraction. To the contrary, the tendency of magnitude of margins was reversed in the larger thermal loading (100 ^{o}C). The effect of fiber volume fraction was similarly shown in case of in-plane loading and out-of-plane loading. The gains of margin were influenced by the fiber volume fraction.

6.2. Comparison between 2D analysis and 3D analysis

Shakedown limits were obtained for two-dimensional lamina model and represented in in-plane loading plane (Σ_x, Σ_y), as shown in Figure 6.7. 20 % of fiber volume fraction was considered. For the comparison, elastic limits were shown as dashed lines. Here Σ_x and Σ_y indicate *x*-directional macroscopic stress and *y*-directional macroscopic stress, respectively, and they were normalized by the yield stress of matrix. Four reference temperature differences were considered to investigate the effect of thermal loading. For the comparison between a two-dimensional shakedown analysis and a three-dimensional shakedown analysis, the results obtained by two approaches were simultaneously represented in a two-dimensional loading diagram, as shown in Figure 6.8. The solid lines indicate shakedown limits obtained by a three-dimensional analysis and the dashed lines indicate those obtained by a two-dimensional analysis. From these results, several differences between the two-dimensional analysis and the three-dimensional analysis were observed.

(i) The space of both shakedown limits and elastic limits by the three-dimensional analysis were smaller than that of the two-dimensional analysis for all reference temperature differences.

(ii) Shakedown limits by the three-dimensional analysis were shifted more to the third quarter loading plane (biaxial compression loading direction) by temperature increase than those by the two-dimensional analysis.

(iii) For the smaller thermal loading, the sizes of shakedown limits by the two-dimensional analysis were larger than those of the three-dimensional analysis. However, at a larger thermal loading, the tendency was reversed.

The elastic limits, the shakedown limits, and their margins obtained by two- and three-dimensional analysis are compared in Table 6.4. The considered loading conditions were uniaxial tension loading (P1), uniaxial compression loading (P2), biaxial tension loading (P3), biaxial compression loading (P4), and biaxial tension-compression combined loading (P5).

Effect of loading direction

As shown in Table 6.4, in the two-dimensional shakedown analysis without thermal loading, the elastic limit and the shakedown limit for uniaxial loading (P1) were 0.916 and 1.635 (margin: 78.5 %), respectively. However, in the three-dimensional shakedown analysis without thermal loading, they were decreased to 0.885 and 0.987 (margin: 11.5 %), respectively. When biaxial loading was concerned, the difference of the shakedown limits between the two-dimensional analysis and the three-dimensional analysis was significantly increased. In two-dimensional analysis without thermal loading, the elastic limit and the shakedown limit for biaxial loading were 2.873 and 5.711 (margin 98.8 %), respectively. In the three-dimensional analysis without thermal loading, they were 1.279 and 2.531 (margin 97.9 %), respectively. For tension-compression combined loading (P5) in the two-dimensional analysis, elastic limit and shakedown limit were 0.465 and 0.818 (margin 75.9 %), respectively. In the three-dimensional analysis, they were also decreased to 0.476 and 0.514 (margin 8.0 %), respectively.

Effect of *z*-directional stress field

From this comparison, shakedown limits and elastic limits were significantly influenced due to dimensional change. For a detail investigation of this difference between the two-dimensional analysis and the three-dimensional analysis, *z*-directional stress (σ_z) fields were

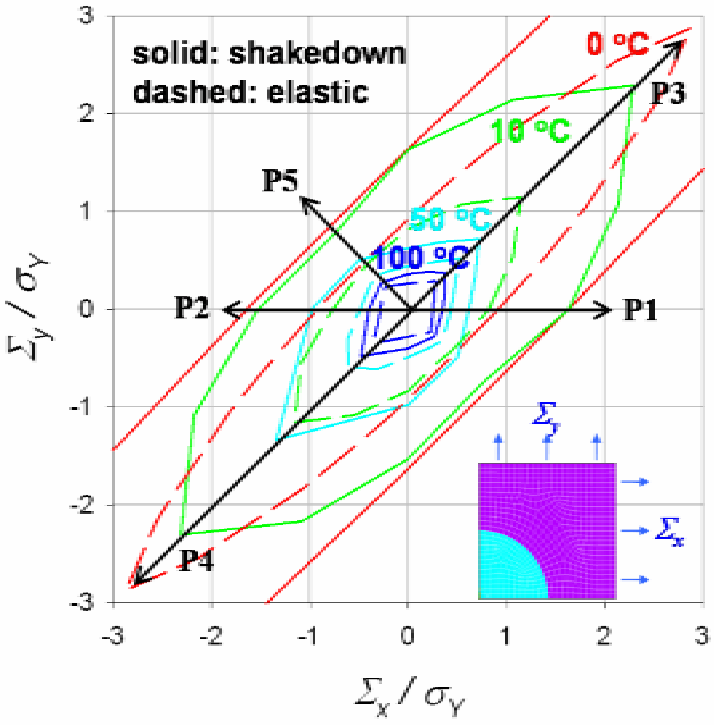

Figure 6.7. Elastic limits and shakedown limits of lamina with 20 % of fiber volume fraction in in-plane biaxial loading space (2D analysis): P1-P5 are loading directions and 10, 50 and 100 °C indicate the magnitude of reference temperature increase (heating).

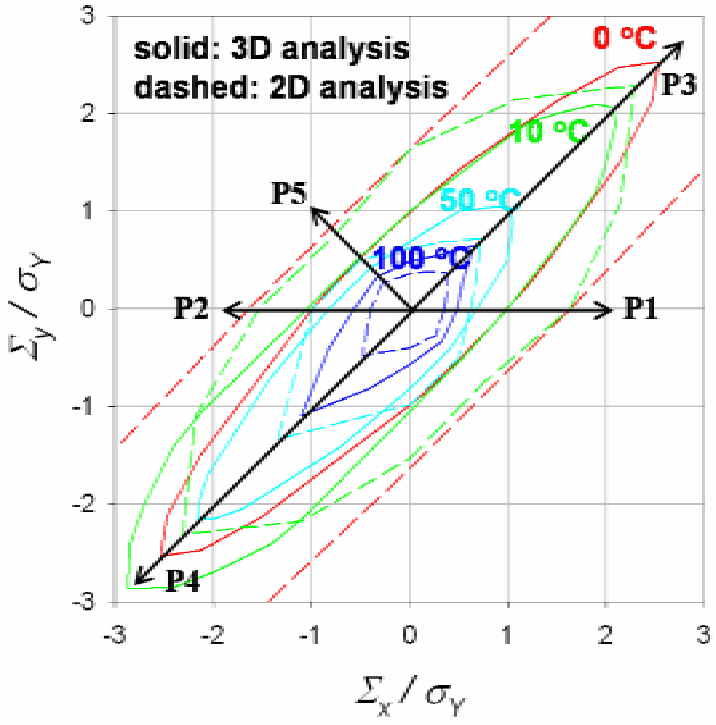

Figure 6.8. Shakedown limits of lamina with 20 % of fiber volume fraction in in-plane biaxial loading space (2D and 3D analyses): P1-P5 are loading directions and 10, 50, and 100 °C indicate the magnitude of reference temperature increase (heating).

obtained using FEM analysis, as drawn in Figure 6.9. In this case, the biaxial loading without thermal loading was considered as a boundary condition.

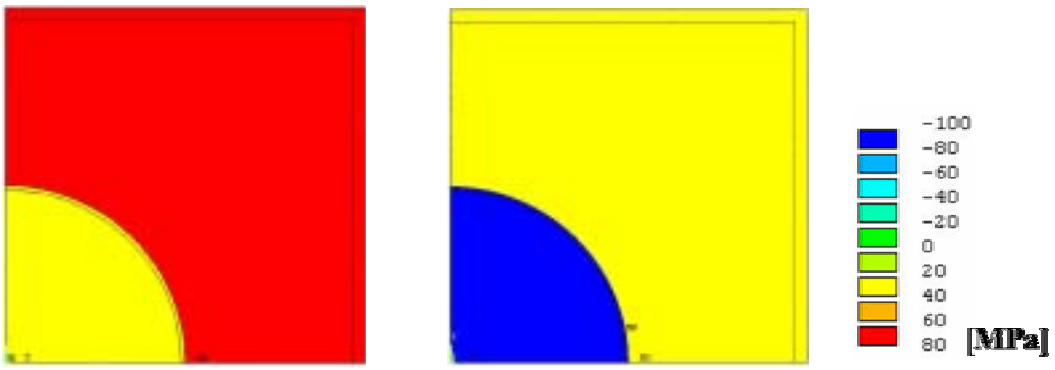

(a) (b)

Figure 6.9. *Z*-directional (axial) stress fields: (a) two-dimensional analysis, (b) three-dimensional analysis. The considered loading is biaxial tension ($\Sigma_x = \Sigma_y$ = 100 MPa).

When a two-dimensional analysis is performed for the long fiber structure, the plane strain assumption is used. Then the components of *z*-directional stress (Σ_z) of fiber and matrix without thermal loading are calculated from the *x*-directional stress and *y*-directional stress, as follows.

$$\Sigma_z = \nu(\Sigma_x + \Sigma_y) \tag{6.2}$$

In case of the biaxial tension loading using two-dimensional analysis (Figure 6.9 (a)), *z*-directional stress (Σ_z) of the fiber and the matrix had to be positive values, since *x*-directional stress (Σ_x) and *y*-directional stress (Σ_y) were positive values.

When a three-dimensional model is considered, the boundary plane of composite has to be coupled to conserve the parallel plane for the deformation. When in-plane biaxial tension loading is considered in a three-dimensional model, the structure will be contracted to *z*-directional axis as the magnitude of Poisson's ratio of fiber and matrix. Since Poisson's ratios are different between fiber (ν = 0.17) and matrix (ν = 0.34), the magnitude of the contraction will also be different. The stress misfit is generated between fiber and matrix to keep the boundary condition of the plane. As a result, the fiber was subjected to negative axial stress while the matrix was subjected to positive axial stress, as represented in Figure 6.9 (b). The difference of the axial stress fields between a two-dimensional analysis and a three-dimensional analysis create a difference between shakedown limits and yield limits.

Effect of thermal loading

When the thermal loading was investigated, the difference of the shakedown limits and the elastic limits was more clearly observed. For example, shakedown limits of biaxial compression loading (P4) in the two-dimensional analysis were 5.711 (0 ^{o}C), 2.289 (10 ^{o}C), 0.72 (50 ^{o}C), and 0.372 (100 ^{o}C) while shakedown limits in the three-dimensional analysis were 2.531 (0 ^{o}C), 2.063 (10 ^{o}C), 1.021 (50 ^{o}C), and 0.651 (100 ^{o}C). Elastic limits and shakedown limits were decreased in the two-dimensional analysis with the temperature increase. Therefore, in the smaller thermal loading, shakedown limits in the two-dimensional analysis were higher than those in the three-dimensional analysis, while the tendency was reversed in the larger thermal loading.

Table 6.4. Elastic limits and shakedown limits of lamina (2D and 3D analyses) in in-plane loading space (from Figures 6.1 and 6.7).

Geometry (fiber fraction)		**P1** (Σ_x = P, Σ_y = 0)			**P2** (Σ_x = -P, Σ_y = 0)			**P3** (Σ_x = Σ_y = P)			**P4** (Σ_x = Σ_y = -P)			**P5** (Σ_x = -Σ_y = P)		
		$\alpha^{el}P/\sigma_Y$	$\alpha^{SD}P/\sigma_Y$	margin (%)	$\alpha^{el}P/\sigma_Y$	$\alpha^{SD}P/\sigma_Y$	margin (%)	$\alpha^{el}P/\sigma_Y$	$\alpha^{SD}P/\sigma_Y$	margin (%)	$\alpha^{el}P/\sigma_Y$	$\alpha^{SD}P/\sigma_Y$	margin (%)	$\alpha^{el}P/\sigma_Y$	$\alpha^{SD}P/\sigma_Y$	margin (%)
2d-lamina (20 %)	0 °C	0.916	1.635	78.5	0.916	1.635	78.5	2.873	5.711	98.8	2.873	5.711	98.8	0.465	0.818	75.9
	10 °C	0.816	1.633	100.1	0.833	1.530	83.7	1.145	2.289	99.9	1.155	2.309	99.9	0.437	0.756	73.0
	50 °C	0.433	0.622	43.6	0.490	0.981	100.2	0.521	0.720	38.2	0.602	1.340	122.6	0.335	0.501	49.6
	100 °C	0.257	0.355	38.1	0.280	0.400	42.9	0.285	0.372	30.5	0.351	0.478	36.2	0.232	0.270	16.4
3d-lamina (20 %)	0 °C	0.885	0.987	11.5	0.885	0.987	11.5	1.279	2.531	97.9	1.279	2.531	97.9	0.476	0.514	8.0
	10 °C	0.804	1.000	24.4	0.897	1.083	20.7	1.108	2.063	86.2	1.437	2.868	99.6	0.468	0.520	11.1
	50 °C	0.527	0.686	30.2	0.653	0.818	25.3	0.633	1.021	61.3	1.128	2.156	91.1	0.393	0.410	4.3
	100 °C	0.336	0.484	44.0	0.389	0.566	45.5	0.382	0.651	70.4	0.550	1.100	100.0	0.292	0.329	12.7

(i) *P* indicates the positive applied loading. The value was fixed to 100 MPa. For example, P5 loading indicates Σ_x = -100 MPa, Σ_y = 100 MPa.
(ii) α^e and α^{SD} indicate elastic safety factor and shakedown safety factor. α^eP/σ_Y and $\alpha^{SD}P/\sigma_Y$ indicate normalized macroscopic stresses.
(iii) Margin indicates the relative gain shakedown limits over elastic limits using equation (6.1).

6.3. Shakedown analysis of FRMMC laminate

In this section, three-dimensional laminate structure is investigated to obtain elastic limits and shakedown limits. Shakedown analyses with a three-dimensional model are performed with the thermal loading. The two-dimensional loading spaces considered here are in-plane bi-axial loading (Σ_x, Σ_y) and out-of-plane bi-axial loading (Σ_x, Σ_z), Finally, the results of laminate structure were compared with those of the three-dimensional lamina structure.

6.3.1. Shakedown analysis of FRMMC laminate for in-plane loading

Shakedown limits were obtained for the three-dimensional laminate. 20 % and 40 % of fiber volume fraction were chosen to investigate the influence of fiber volume fraction, as represented in Figure 6.10 and 6.11. For the comparison, the elastic limits were drawn with shakedown limits in the same loading space. The dashed lines indicate elastic limit and the solid lines indicate shakedown limits. The considered loading was in-plane bi-axial loading (Σ_x, Σ_y). Σ_x and Σ_y indicate *x*-directional macroscopic stress and *y*-directional macroscopic stress, respectively. They were normalized by the yield stress of the matrix. Four reference temperature differences were considered to investigate the effect of thermal loading. The following points were drawn from these graphical results.

(i) The area of the shakedown limits had a strong dependence on temperature change.

(ii) The margins between the shakedown limits and the elastic limits of the laminate structure were narrower than those of lamina structure.

(iii) Although both the shakedown spaces and the elastic spaces had longish shapes along the first and the third quarter loading plane, the extent of locus of laminate structure was less than that of lamina structure.

(iv) There was no significant difference in the shape of the elastic limits and the shakedown limits with the increase of fiber volume fraction.

Elastic limits, shakedown limits, and their margins are represented in Table 6.5. The chosen loading conditions were uniaxial (in-plane direction) tension loading (P1), uniaxial compression loading (P2), biaxial tension loading (P3), biaxial compression loading (P4), and biaxial tension-compression combined loading (P5).

Effect of loading direction

In the case of laminate with 20 % of fiber volume fraction without thermal loading, the elastic limit and the shakedown limit for uniaxial loading (P1 and P2) were 0.932 and 1.142 (margin: 22.5 %), respectively. They had a symmetric image for tension and compression loading when the thermal loading was not included. For biaxial loading (P3), they were 0.948 and 1.034 (margin 9.1 %), respectively. For tension-compression combined loading (P5), they were 0.634 and 0.636 (margin 0.3 %), respectively.

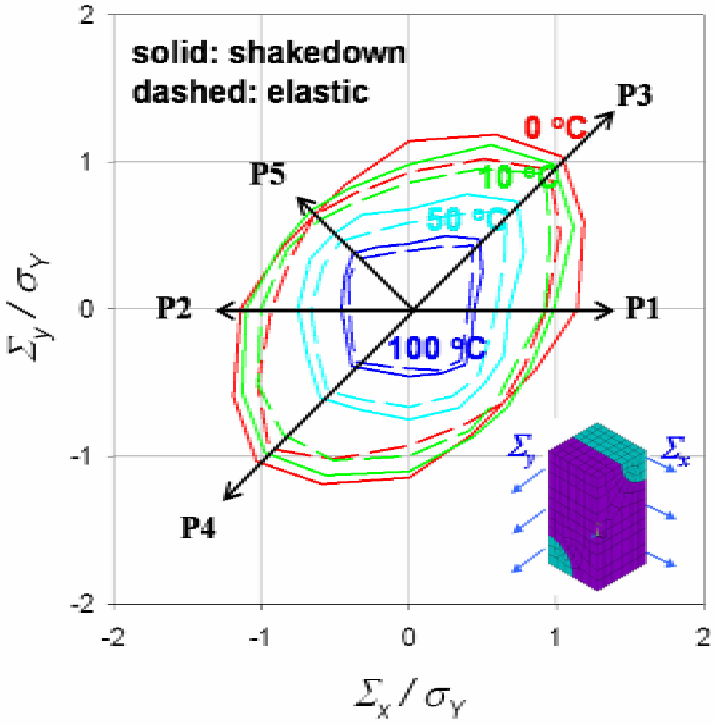

Figure 6.10. Elastic limits and shakedown limits of laminate with 20 % of fiber volume fraction in in-plane biaxial loading space (3D analysis): P1-P5 are loading directions and 10, 50, and 100 °C indicate the magnitude of reference temperature increase (heating).

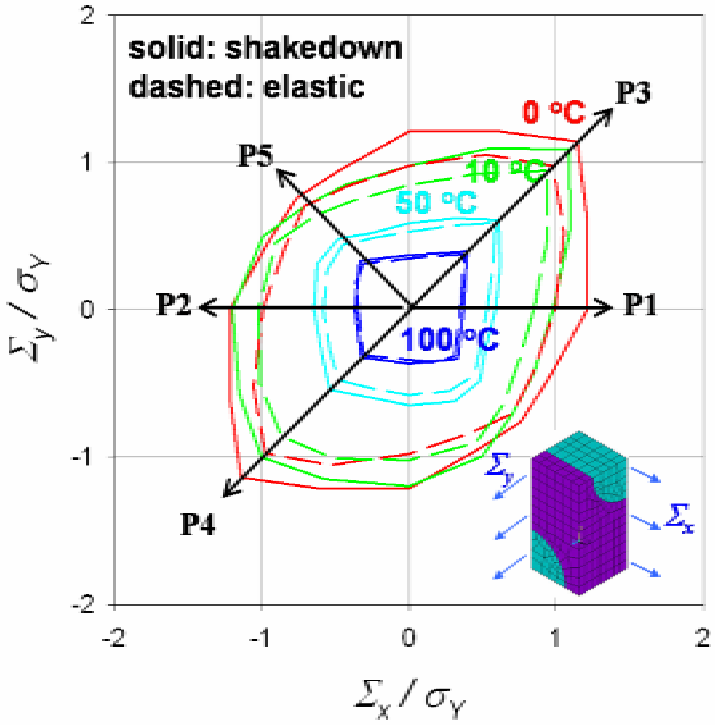

Figure 6.11. Elastic limits and shakedown limits of laminate with 40 % of fiber volume fraction in in-plane biaxial loading space (3D analysis): P1-P5 are loading directions and 10, 50, and 100 °C indicate the magnitude of reference temperature increase (heating).

Table 6.5. Elastic limits and shakedown limits of laminate (3D analysis) in in-plane loading space (from Figures 6.10 and 6.11).

Geometry (fiber fraction)		**P1** (Σ_x = P, Σ_y = 0)			**P2** (Σ_x = -P, Σ_y = 0)			**P3** (Σ_x = Σ_y = P)			**P4** (Σ_x = Σ_y = -P)			**P5** (Σ_x = -Σ_y = P)		
		$\alpha^{el}P/\sigma_Y$	$\alpha^{SD}P/\sigma_Y$	margin (%)	$\alpha^{el}P/\sigma_Y$	$\alpha^{SD}P/\sigma_Y$	margin (%)	$\alpha^{el}P/\sigma_Y$	$\alpha^{SD}P/\sigma_Y$	margin (%)	$\alpha^{el}P/\sigma_Y$	$\alpha^{SD}P/\sigma_Y$	margin (%)	$\alpha^{el}P/\sigma_Y$	$\alpha^{SD}P/\sigma_Y$	margin (%)
3d-laminate (20 %)	0 °C	0.932	1.142	22.5	0.932	1.142	22.5	0.948	1.034	9.1	0.948	1.034	9.1	0.634	0.636	0.3
	10 °C	0.866	0.986	13.9	1.002	1.100	9.8	0.924	0.983	6.4	0.852	0.975	14.4	0.604	0.666	10.3
	50 °C	0.592	0.679	14.7	0.664	0.752	13.3	0.666	0.733	10.1	0.553	0.602	8.9	0.465	0.509	9.5
	100 °C	0.404	0.444	9.9	0.405	0.455	12.3	0.434	0.476	9.7	0.361	0.389	7.8	0.348	0.379	8.9
3d-laminate (40 %)	0 °C	0.993	1.213	22.2	0.993	1.213	22.2	0.976	1.141	16.9	0.976	1.141	16.9	0.706	0.760	7.6
	10 °C	0.849	0.979	15.3	1.021	1.200	17.5	0.944	1.087	15.1	0.862	1.001	16.1	0.640	0.703	9.8
	50 °C	0.530	0.586	10.6	0.582	0.646	11.0	0.594	0.612	3.0	0.479	0.540	12.7	0.444	0.482	8.6
	100 °C	0.346	0.372	7.5	0.342	0.364	6.4	0.378	0.398	5.3	0.305	0.322	5.6	0.310	0.333	7.4

(i) P indicates the positive applied loading. The value was fixed to 100 MPa. For example, P5 loading indicates Σ_x = -100 MPa, Σ_y = 100 MPa.
(ii) α^e and α^{SD} indicate elastic safety factor and shakedown safety factor. α^eP/σ_Y and $\alpha^{SD}P/\sigma_Y$ indicate normalized macroscopic stresses.
(iii) Margin indicates the relative gain shakedown limits over elastic limits using equation (6.1).

Comparison between lamina and laminate

The magnitude of margins of laminate was compared with those of lamina. Shakedown limits and their margins of laminate in the biaxial loading (P3 and P4) were significantly decreased over those of lamina. However, the similar tendency between laminate and lamina was shown in the uniaxial loading (P1 and P2) and the tension-compression combined loading (P5). The shakedown limit and the margin in uniaxial tension loading (P1) without thermal loading were 0.987 and 11.5 % in lamina (Table 6.2), while they were 1.142 and 22.5 % in laminate (Table 6.5). In the tension-compression combined loading (P5), the shakedown limit and the margin were 0.514 and 8 % in lamina while they were 0.636 and 0.3 % in laminate. To the contrary, in the biaxial loading, the shakedown limit and the margin were 2.531 and 97.9 % in lamina while they were decreased to 1.034 and 9.1 % in laminate. This tendency can be explained by the stress localization and distribution due to the influence of the geometrical complexity and the loading direction. It will be discussed in the final remark of this chapter with the graphical view of von-Mises stress profile.

Effect of thermal loading

When the thermal loading was considered, elastic limits and shakedown limits were decreased with the temperature increase. For example, in biaxial tension loading (P3), shakedown limits were 0.983 (10 ^{o}C), 0.733 (50 ^{o}C), and 0.476 (100 ^{o}C). The asymmetry of shakedown limits was also observed when the thermal loading was concerned. Therefore, shakedown limits in biaxial compression loading (P4) were less than them in biaxial tension loading (P3). The resulting shakedown limits were 0.975 (10 ^{o}C), 0.602 (50 ^{o}C), and 0.389 (100 ^{o}C). The decreasing extent as well as the asymmetric effect in laminate was not significantly observed in the case of lamina.

Effect of fiber volume fraction

In 40 % of fiber volume fraction, the asymmetries of elastic and shakedown limits were also observed with the increase of the temperature difference. The marginal effect of 40 % of fiber volume fraction had similar tendencies as 20 % of fiber volume fraction. On the contrary with the lamina model, the shakedown limits and their margins were not significantly influenced by the increase of the fiber volume fraction in laminate model. In other words, the increase of the fiber volume fraction in the laminate structure did not increase the serviceability of the structure in relation to the shakedown viewpoint.

6.3.2. Shakedown analysis of FRMMC laminate for out-of-plane loading

The shakedown analyses of laminate were performed in out-of-plane loading. 20 % and 40 % of the fiber volume fraction were chosen to explain the effect of the fiber volume fraction, as represented in Figure 6.12 and 6.13. For the comparison, the elastic limits were shown with shakedown limits in a same out-of-plane loading space. Σ_x (x-directional macroscopic stress) and Σ_z (z-directional macroscopic stress) were normalized by the yield stress of the matrix, respectively. For out-of-plane loading of laminate, several remarks were obtained and compared with its in-plane loading case. Also the results of laminate structure were compared with those of the three-dimensional lamina structure.

(i) The area of shakedown limits had a strong dependency on temperature change.

(ii) The margins between the shakedown limits and the elastic limits in the out-of-plane loading were as small as those in the in-plane loading.

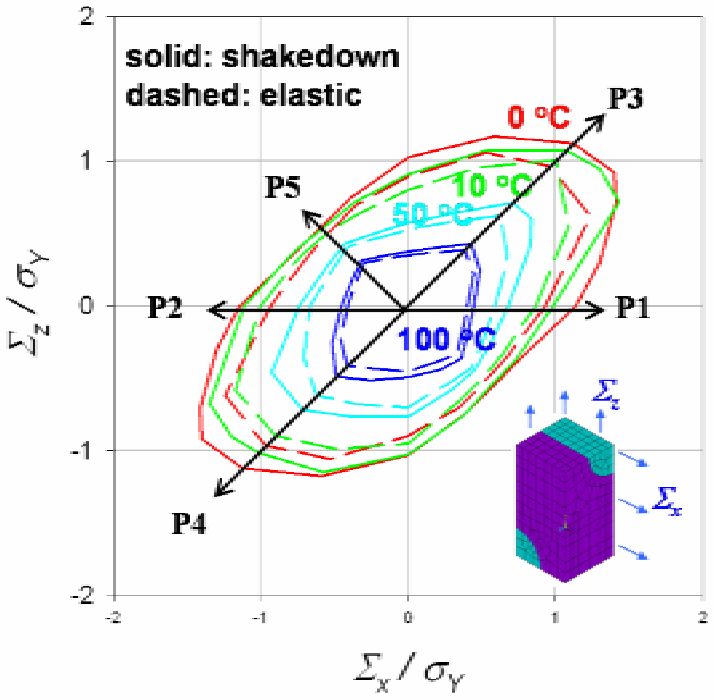

Figure 6.12. Elastic limits and shakedown limits of laminate with 20 % of fiber volume fraction in out-of-plane biaxial loading space (3D analysis): P1-P5 are loading directions and 10, 50, and 100 °C indicate the magnitude of reference temperature increase (heating).

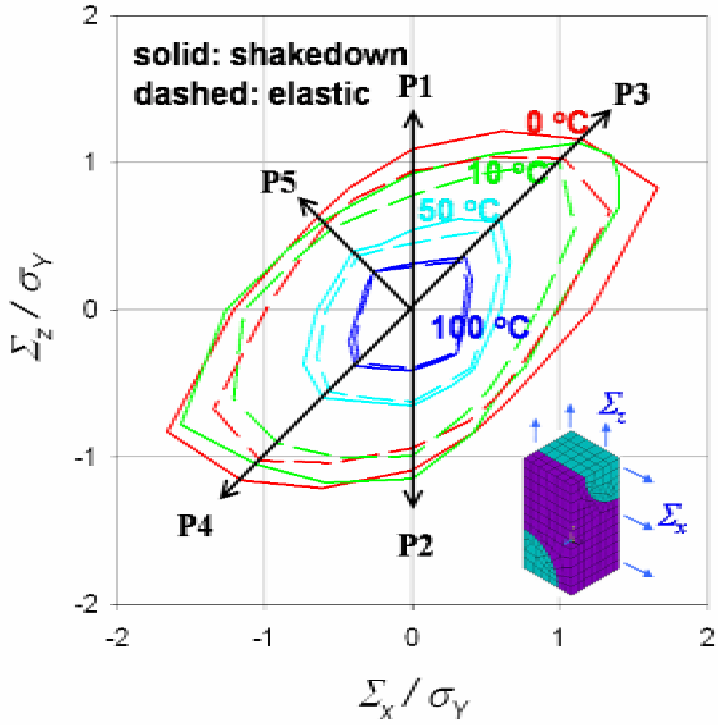

Figure 6.13. Elastic limits and shakedown limits of laminate with 40 % of fiber volume fraction in out-of-plane biaxial loading space (3D analysis): P1-P5 are loading directions and 10, 50, and 100 °C indicate the magnitude of reference temperature increase (heating).

(iii) The longish extent of shakedown limits and elastic limits along the first and the third quarter loading plane in the out-of-plane loading was as small as those in the in-plane loading.

(iv) There was no significant difference in the shape of the elastic limits and the shakedown limits with the increase of fiber volume fraction for both in-plane and out-of-plane loading.

Elastic limits, shakedown limits, and their margins are available in Table 6.6. The considered loading conditions in the table were uniaxial (out-of-plane direction) tension loading (P1), uniaxial compression loading (P2), biaxial tension loading (P3), biaxial compression loading (P4), and biaxial tension-compression combined loading (P5).

Effect of loading direction

In case of laminate with 20 % of fiber volume fraction without considering thermal loading, the elastic limit and the shakedown limit for uniaxial loading (P1) were 0.895 and 1.029 (margin: 15 %), respectively. For biaxial loading (P3), they were 0.964 and 1.121 (margin 16.3 %), respectively. For tension-compression combined loading (P5), they were 0.522 and 0.567 (margin 8.6 %). Like the preceding results of laminate (in-plane loading space), shakedown limits and margins in the biaxial loading (P3 and P4) were significantly decreased over those of laminate model, while they had a similar tendency in the uniaxial loading (P1 and P2) and the tension-compression combined loading (P5) for both lamina and laminate.

Effect of thermal loading

When the thermal loading was considered, elastic limits and shakedown limits were decreased with the temperature increase. For example, in biaxial tension loading (P3), shakedown limits were 1.073 (10 ^{o}C of thermal loading), 0.711 (50 ^{o}C), and 0.431 (100 ^{o}C). In biaxial compression loading (P4), the shakedown limits were 1.012 (10 ^{o}C), 0.716 (50 ^{o}C), and 0.489 (100 ^{o}C). The asymmetry of shakedown limits was observed where thermal loading was concerned. However, the extent of the asymmetric effect in laminate structure was significantly decreased over that in lamina structure.

Effect of fiber volume fraction

In case of out-of-plane loading with 40 % of fiber volume fraction, the asymmetric trends of elastic and shakedown limits were similarly observed like those of the 20 % of fiber volume fraction. The marginal effect of 40 % of fiber volume fraction had a similar tendency as the 20 % of fiber volume fraction. As investigated in the in-plane loading of laminate structure, the shakedown limits and their margins were not significantly influenced by the increase of fiber volume fraction in out-of-plane loading. In the shakedown viewpoint, the serviceability of the structure is not strongly related with the increase of fiber volume fraction in the laminate structure.

From the investigation of the laminate structure for the in-plane loading and out-of-plane loading, their elastic limits and shakedown limits had very similar tendencies. In other words, when the laminate structure was investigated in shakedown analysis, there were no significant marginal gains between elastic limits and shakedown limits in any loading combination. Since the laminate structure was difficult to have the distributed stress state in the matrix region, the shakedown limits and their margins were dissimilar with the lamina structure.

Table 6.6. Elastic limits and shakedown limits of laminate (3D analysis) in out-of-plane loading space (from Figures 6.12 and 6.13).

Geometry (fiber fraction)		**P1** (Σ_x = 0, Σ_z = P)			**P2** (Σ_x = 0, Σ_z = -P)			**P3** (Σ_x = Σ_z = P)			**P4** (Σ_x = Σ_z = -P)			**P5** (Σ_x = -Σ_z = P)		
		$\alpha^{el}P/\sigma_Y$	$\alpha^{SD}P/\sigma_Y$	margin (%)	$\alpha^{el}P/\sigma_Y$	$\alpha^{SD}P/\sigma_Y$	margin (%)	$\alpha^{el}P/\sigma_Y$	$\alpha^{SD}P/\sigma_Y$	margin (%)	$\alpha^{el}P/\sigma_Y$	$\alpha^{SD}P/\sigma_Y$	margin (%)	$\alpha^{el}P/\sigma_Y$	$\alpha^{SD}P/\sigma_Y$	margin (%)
3d-laminate (20 %)	0 °C	0.895	1.029	15.0	0.895	1.029	15.0	0.964	1.121	16.3	0.964	1.121	16.3	0.522	0.567	8.6
	10 °C	0.803	0.908	13.1	0.949	1.026	8.1	1.006	1.073	6.7	0.899	1.012	12.6	0.526	0.555	5.5
	50 °C	0.525	0.572	9.0	0.701	0.765	9.1	0.624	0.711	13.9	0.619	0.716	15.7	0.408	0.429	5.1
	100 °C	0.348	0.374	7.5	0.451	0.493	9.3	0.388	0.431	11.1	0.412	0.489	18.7	0.299	0.316	5.7
3d-laminate (40 %)	0 °C	0.939	1.090	16.1	0.939	1.090	16.1	1.028	1.156	12.5	1.028	1.156	12.5	0.582	0.638	9.6
	10 °C	0.778	0.928	19.3	0.994	1.148	15.5	1.001	1.133	13.2	0.909	1.050	15.5	0.548	0.602	9.9
	50 °C	0.452	0.540	19.5	0.627	0.654	4.3	0.539	0.595	10.4	0.558	0.601	7.7	0.367	0.400	9.0
	100 °C	0.293	0.315	7.5	0.394	0.410	4.1	0.326	0.356	9.2	0.361	0.383	6.1	0.259	0.261	0.8

(i) P indicates the positive applied loading. The value was fixed to 100 MPa. For example, P5 loading indicates Σ_x = -100 MPa, Σ_z = 100 MPa.
(ii) α^e and α^{SD} indicate elastic safety factor and shakedown safety factor. α^eP/σ_Y and $\alpha^{SD}P/\sigma_Y$ indicate normalized macroscopic stresses.
(iii) Margin indicates the relative gain shakedown limits over elastic limits using equation (6.1).

6.4. Shakedown analyses with hardening effect

Up to now, the results of the shakedown limits were obtained for the elastic-ideal plastic (EIP) model. In the real structural application, the influence of the hardening effect should be considered. In this section, the hardening effect was integrated in shakedown analysis. To investigate the hardening effect, two different hardening behaviors were assumed in the shakedown formulation.

(i) Shakedown with limited kinematic hardening (LKH) model ($\sigma_L = 1.2 \times \sigma_Y$): To simulate the nonlinear strain-hardening effect several subelements with different yield stresses can be introduced. The weakest of these yield stresses had the initial yield stress, σ_Y. The limit stress σ_L in the macroscale was fixed to be the value $1.2 \times \sigma_Y$ (see Figure 2.11).

(ii) Shakedown with unlimited kinematic hardening (ULKH) model ($\sigma_L = +\infty$): By assuming the same model as in case (ii) but with an infinite limit stress, the limit case can be analyzed (see Figure 2.10).

The laminate structure with 20 % of fiber volume fraction was considered. Shakedown limits were obtained considering hardening effect, as shown in Figures 6.14 (in-plane loading space) and 6.15 (out-of-plane loading space). The thermal loading was not considered. The red line indicates shakedown limits with EIP model, the green line indicates shakedown limits with LKH model, and the light blue line indicates shakedown limits with ULKH model. For the comparison, elastic limits were shown as blue line. Following conclusions were drawn from these results.

(i) When the hardening behavior was employed for the matrix material of the laminate structure, shakedown safety limits were increased due to the presence of hardening.

(ii) Shakedown limits of ULKH model increased significantly.

(iii) Shakedown limits of LKH model did not significantly increase in comparison with those of EIP model.

Elastic limits, shakedown limits, and their margins for in-plane loading are listed in Table 6.7. The loading conditions considered here were uniaxial tension loading (P1), biaxial tension loading (P2), and tension-compression combined loading (P3).

In EIP model, shakedown limits were already discussed in the previous section. In ULKH model, shakedown limits in the uniaxial loading (P1) and its margin were 1.865 and 100 %, respectively. In the biaxial loading (P2), they were 1.896 and 100 %. In the tension-compression combined loading (P3), they were 1.268 and 100 %. Shakedown limits of ULKH model were doubled in comparison with elastic limits. However, the shakedown limits of the ULKH model were overestimated, since LKH model was used in the matrix material [122].

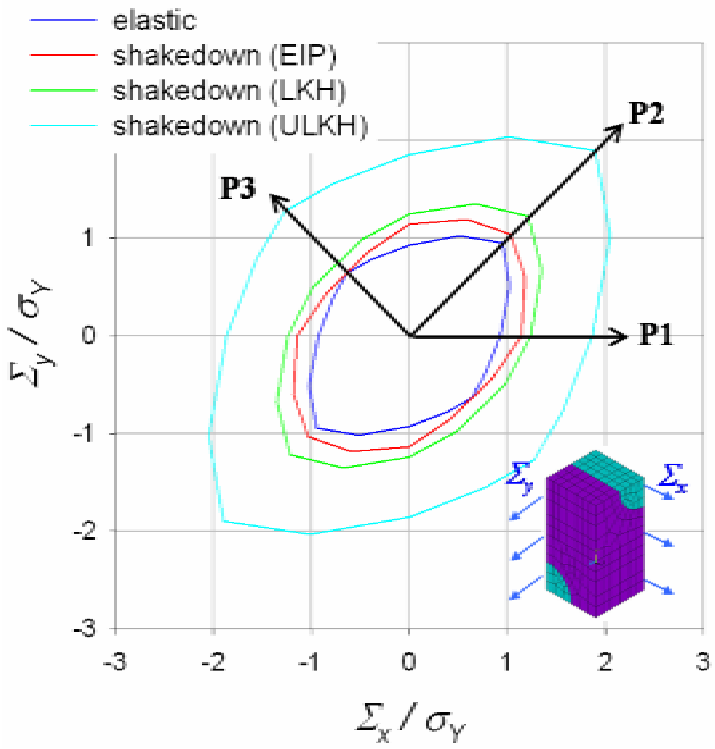

Figure 6.14. Elastic limits and shakedown of laminate with 20 % of fiber volume fraction in out-of-plane biaxial loading space (3D analysis): EIP (Elastic Ideal-Plastic) model, LKH (Limited Kinematic Hardening) model, and ULKH (Unlimited Kinematic Hardening) model

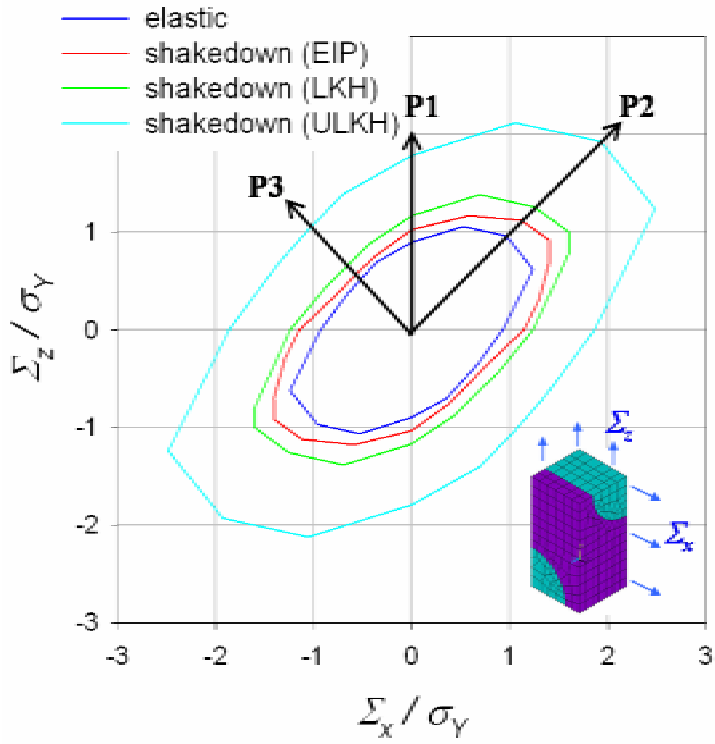

Figure 6.15. Elastic limits and shakedown of laminate with 20 % of fiber volume fraction in in-plane biaxial loading space (3D analysis): EIP (Elastic Ideal-Plastic) model, LKH (Limited Kinematic Hardening) model, and ULKH (Unlimited Kinematic Hardening) model.

In the LKH model, the margins from the shakedown limits of EIP model were 8.7 % in uniaxial tension loading (P1), 17.8 % in biaxial tension loading (P2), and 15.7 % in tension-compression combined loading (P3). Although the assumed hardening was 20 % (limit stress was 1.2 times higher than initial yield stress), the margins were less than 20 % in all loading combination. When the LKH model was used, the gains were not significantly increased even though the hardening degree is one of the important factors for the shakedown limits.

Table 6.7. Elastic limits and shakedown limits of laminate (3D analysis) in in-plane loading space with considering hardening effect (from Figure 6.14).

	P1 ($\Sigma_x = P$, $\Sigma_y = 0$)			**P2** ($\Sigma_x = \Sigma_y = P$)			**P3** ($\Sigma_x = -\Sigma_y = P$)		
	$\alpha^{el}P/\sigma_Y$	$\alpha^{SD}P/\sigma_Y$	margin (%)	$\alpha^{el}P/\sigma_Y$	$\alpha^{SD}P/\sigma_Y$	margin (%)	$\alpha^{el}P/\sigma_Y$	$\alpha^{SD}P/\sigma_Y$	margin (%)
EIP		1.142	22.5		1.034	9.1		0.636	0.3
LKH	0.932	1.241	33.2 (8.7)[1]	0.948	1.218	28.5 (17.8)	0.634	0.736	16.1 (15.7)
ULKH		1.865	100		1.896	100		1.268	100

When the out-of-plane loading space was considered, elastic limits, shakedown limits, and their margins are represented in Table 6.8. The chosen loading conditions were uniaxial tension loading (P1), biaxial tension loading (P2), and tension-compression combined loading (P3). As discussed in the case of in-plane loading, the overall tendency was similarly represented in this loading space. Shakedown limits of ULKH model were also twice as high as the elastic limits in all the loading combinations. In the LKH model, the margins were slightly increased in comparison with the shakedown limits with the EIP model. The difference of shakedown limits between the EIP model and the hardening material (ULKH and LKH) of the out-of-plane loading space was obtained in a similar way to that of the in-plane loading space.

Table 6.8. Elastic limits and shakedown limits of laminate (3D analysis) in out-of-plane loading space with considering hardening effect (from Figure 6.15).

	P1 ($\Sigma_x = 0$, $\Sigma_z = $ P)			**P2** ($\Sigma_x = \Sigma_z = $ P)			**P3** ($\Sigma_x = -\Sigma_z = $ P)		
	$\alpha^{el}P/\sigma_Y$	$\alpha^{SD}P/\sigma_Y$	margin (%)	$\alpha^{el}P/\sigma_Y$	$\alpha^{SD}P/\sigma_Y$	margin (%)	$\alpha^{el}P/\sigma_Y$	$\alpha^{SD}P/\sigma_Y$	margin (%)
EIP		1.029	15.0		1.121	16.3		0.567	8.6
LKH	0.895	1.169	30.6 (13.6)	0.964	1.257	30.4 (12.1)	0.522	0.658	26.1 (16.0)
ULKH		1.790	100		1.928	100		1.044	100

[1] Normally, margins are the gain of shakedown limits against elastic limits. However, in LKH material, the margins are also obtained by the gain from shakedown limits in EIP material. This margin is shown with parenthesis.

6.5. Remarks of shakedown results

The three-dimensional composites of lamina and laminate were investigated to obtain shakedown limits. The results of the shakedown limits were discussed with geometrical influences, increase of fiber volume fraction, loading direction, and hardening effect. In this section, the following will be discussed additionally with von Mises stress field.

(i) Both shakedown spaces and elastic spaces had longish shape along the first quarter plane and the third quarter plane.

(ii) The margins from the shakedown limits along the first quarter plane and the third quarter plane were larger than those along the second quarter plane and the fourth quarter plane.

(iii) The margins along the first quarter plane and the third quarter plane of the laminate structure were narrower than those of lamina structure. For the second quarter plane and the fourth quarter plane, there were no significant margins in the case of both lamina structure and laminate structure.

The effect of symmetric loading can be understood in views of stress distribution. Von Mises stress distribution can give a clearer explanation to the effect of stress localization and to the shape of the shakedown limits. According to von Mises criterion, the plasticity threshold was linked to the elastic shear energy. The expanded expressions of the von Mises yield criterion were as follows

$$\sigma_v = \frac{1}{\sqrt{2}}\left[(\sigma_x - \sigma_y)^2 + (\sigma_y - \sigma_z)^2 + (\sigma_x - \sigma_z)^2 + 6(\tau_{xy}^2 + \tau_{yz}^2 + \tau_{xz}^2)\right]^{1/2} \tag{6.3}$$

$$\sigma_v = \frac{1}{\sqrt{2}}\left[(\sigma_1 - \sigma_2)^2 + (\sigma_2 - \sigma_3)^2 + (\sigma_1 - \sigma_3)^2\right]^{1/2} \tag{6.4}$$

Equation (6.3) and (6.4) are the expression of the six-dimensional stress space and the expression of the three-dimensional principle stress (σ_1, σ_2, σ_3) space, respectively[2].

From the observation of shakedown and elastic limits in Figure 6.1 (in-plane loading), the margins of lamina in the first and the third planes were larger than those in the second and the fourth planes. It can be explained with von Mises stress distribution as follows. Figure 6.16 shows von Mises stress distribution of lamina for the in-plane loading. Here, only the half plane ($\Sigma_y > 0$) was considered because of the symmetry of the yield locus at room temperature (without temperature change). The presented von Mises stress denotes the stress states along the loading directions which were rotated by 45^o about the coordinate axes. Each plane denotes the global biaxial stress states having a specific combination of tension and compression for two directional loading.

[2] It is from the assumption of plastic incompressibility and yield-independence with respect to hydrostatic stress. To understand the detail description of the von Mises criterion and the Tresca criterion, see the references [12, 13].

Figure 6.16 (a) indicates von Mises stress distribution for the second quarter plane ($\Sigma_x = -\Sigma_y$), and (b) indicates von Mises stress distribution for the first quarter plane ($\Sigma_x = \Sigma_y$). The von Mises stress profile was uniformly distributed in the biaxial loading plane (Figure 6.16 (b)). The maximum value of von Mises stress of matrix was about 70 MPa. On the other hand, in the tension-compression combined loading (Figure 6.16 (a)), the maximum value of von Mises stress of the matrix was over 180 MPa and the distribution was highly localized. From the comparison between Figure 6.1 and 6.16, the elastic limits, the shakedown limit and their margins were closely related with the maximum value of von Mises stress and its distribution profile.

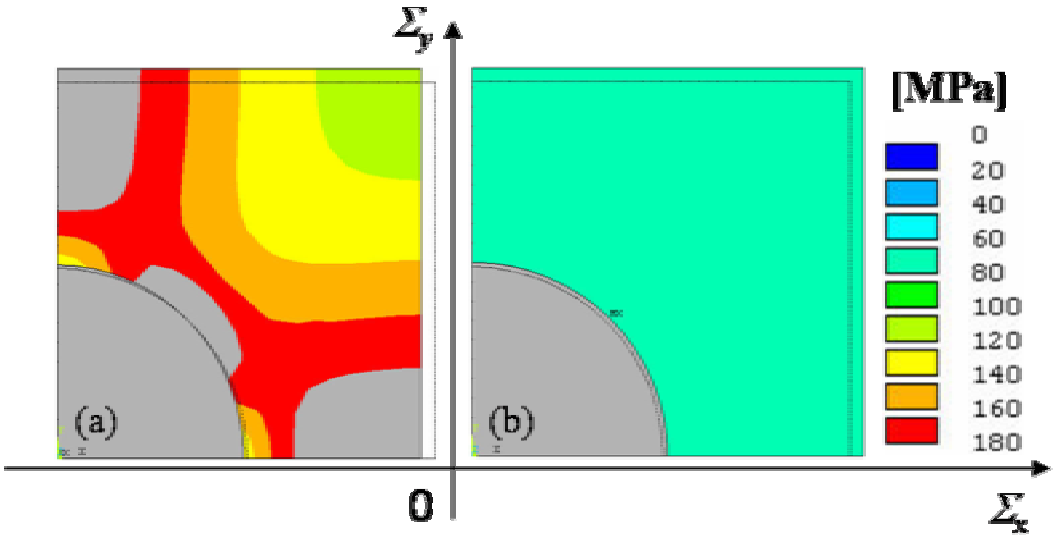

Figure 6.16. Von Mises stress distribution of lamina with 20 % of fiber volume fraction using three-dimensional analysis without considering thermal loading (from Figure 6.1): (a) compression loading to *x*-directional axis and tension loading to *y*-directional axis, and (b) biaxial tension loading to *x*- and *y*-directional axes.

From the observation of the shakedown limits and the elastic limits in Figure 6.3 (out-of-plane loading), the margins of lamina along the axial loading planes (*z*-directional axis) were larger than those in the other loading planes. It can be explained with von Mises stress distribution of lamina in the out-of-plane loading. Figure 6.17 shows von Mises stress distribution of lamina with out-of-plane loading (see Figure 6.3). Figure 6.17 (a) indicates von Mises stress distribution for the second quarter plane ($\Sigma_x = -\Sigma_z$), (b) indicates von Mises stress distribution for the axial direction ($\Sigma_x = 0$, $\Sigma_z = P$), and (c) indicates von Mises stress distribution for the first quarter plane ($\Sigma_x = \Sigma_z$).

In the axial loading, the maximum value of von Mises stress was minimized (about 70 MPa) and its distribution was uniformly shown, as represented in Figure 6.17 (b). However, in other loading planes (Figure 6.17 (a) and (c)), the maximum values of von Mises stress were between 120 MPa and 160 MPa, and the distribution of stress was significantly localized. As shown in the previous results of in-plane loading, the margins of the shakedown limits were increased when the maximum value of von Mises stress profile was minimized and the stress profile was well distributed (Figure 6.17 (b)). The comparison between Figure 6.3 and 6.17 shows that the elastic limits, the shakedown limit, and their margins were influenced by the maximum value of von Mises stress with its distribution trend.

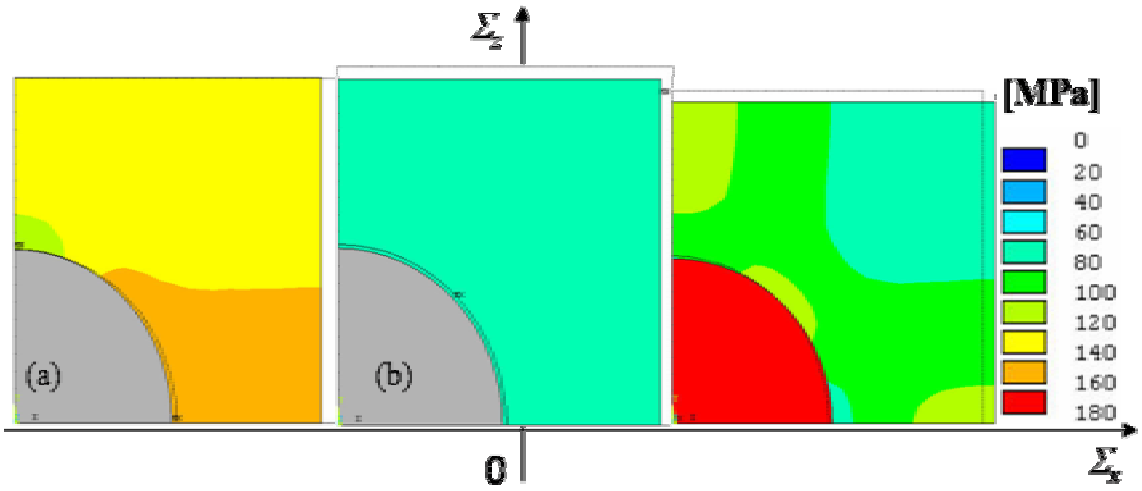

Figure 6.17 Von Mises stress distribution of lamina with 20 % of fiber volume fraction using three-dimensional analysis without considering thermal loading (from Figure 6.3): (a) compression loading to *x*-directional axis and tension loading to *z*-directional axis, (b) tension loading to *z*-directional axis, and (c) biaxial tension loading to *x*- and *z*-directional axes.

From the results of the laminate structure in Figure 6.10 (in-plane loading), the margins between shakedown limits and elastic limits of laminate structure were quite less than those of lamina structure. The longish extent of the shakedown limits of the laminate structure was less than that of the lamina structure. It can be also explained with von Mises stress profile of laminate. Figure 6.18 shows von Mises stress distribution of laminate with in-plane loading. Figure 6.18 (a) indicates von Mises stress distribution for the second quarter plane ($\Sigma_x = -\Sigma_y$), and (b) indicates von Mises stress distribution for the first quarter plane ($\Sigma_x = \Sigma_y$).

In the biaxial tension loading, the maximum value of von Mises stress of matrix was also increased to about 110 MPa (Figure 6.18 (b)) in comparison with lamina in the same loading ($\cong$ 70 MPa). The resulting von Mises stress profile was not uniformly distributed. In tension-compression combined loading (Figure 6.18 (a)), the maximum value of von Mises stress of matrix was about 150 MPa and the distribution was highly localized. From the graphical observation, von Mises stress state of laminate was highly localized under any loading condition and the maximum value of the resulting von Mises stress of the matrix was also increased. This was due to the complex geometry of the laminate structure. Therefore it was explained that the margins between the shakedown limits and the elastic limits of the laminate structure were significantly narrower in all loading combinations (Figure 6.10).

For the investigation for the out-of-plane loading of laminate structure, von Mises stress distribution of laminate is represented in Figure 6.19. Figure 6.19 (a) indicates von Mises stress distribution for the second quarter plane ($\Sigma_x = -\Sigma_z$), and (b) indicates von Mises stress distribution for the first quarter plane ($\Sigma_x = \Sigma_z$). The maximum value of von Mises stress of the matrix was about 110 MPa. In tension-compression combined loading (Figure 6.18 (a)), the maximum value of von Mises stress of matrix was over 180 MPa and the distribution was highly localized. The von-Mises stress of out-of-plane loading was highly localized and the value was increased, as previously mentioned in the in-plane loading.

From the results in this section, the maximum value of von Mises stress and its distribution influenced the tendency of shakedown limits and elastic limits. If the maximum value of von Mises stress is decreased in certain loading conditions and the distribution is uniformly represented, the serviceability of the structure can be increased from an elastic viewpoint as well as a shakedown viewpoint.

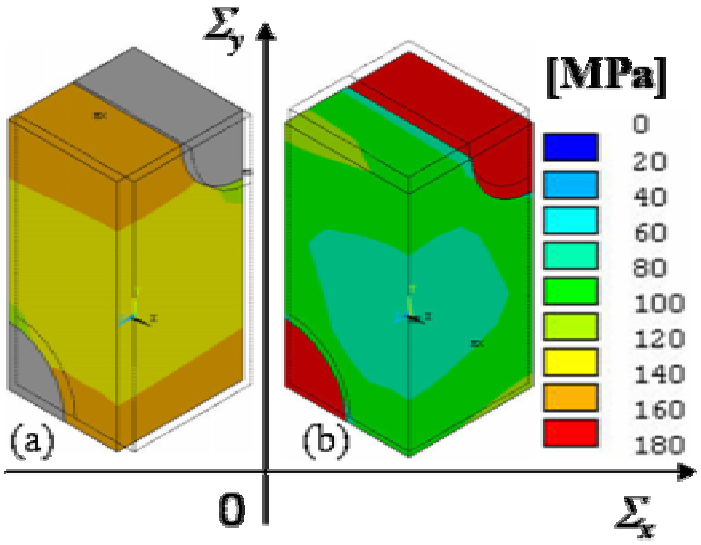

Figure 6.18. Von Mises stress distribution of laminate with 20 % of fiber volume fraction using three-dimensional analysis without considering thermal loading (from Figure 6.11): (a) compression loading to *x*-directional axis and tension loading to *y*-directional axis, and (b) biaxial tension loading to *x*- and *y*-directional axes.

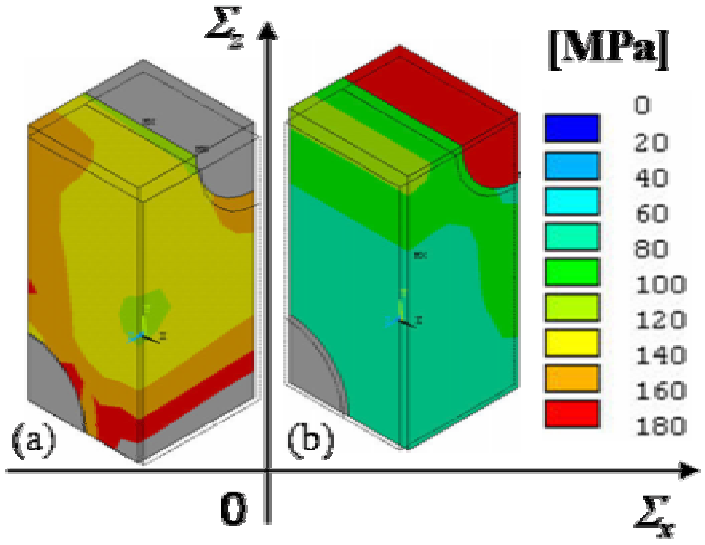

Figure 6.19 Von Mises stress distribution of lamina with 20 % of fiber volume fraction using three-dimensional analysis without considering thermal loading (from Figure 6.12): (a) compression loading to *x*-directional axis and tension loading to *z*-directional axis, and (b) biaxial tension loading to *x*- and *z*-directional axes.

In this work, the heating condition was considered in the results of the shakedown limits, i.e. the reference temperatures were positive value. The FRMMC layer is normally manufactured at higher temperature than its operation temperature. Therefore the shakedown limits with the cooling condition may give a clear insight with regard to the real conditions. Therefore, the shakedown limits were obtained in the cooling condition. The results of shakedown limits for lamina and laminate FRMMCs for cooling are attached in Appendix D. The elastic limits and the shakedown limits in cooling showed mirror images for the line $y = -x$ with respect to heating. These results occurred because the thermal cooling induced the contraction of FRMMC at the same magnitude as its expansion during the heating.

7. Application of Shakedown Analysis

In this chapter, several parametric studies are performed by considering the fusion-relevant loading conditions in the PFC component for the comparison with the results of shakedown analysis. For this, shakedown limits are represented in the three-dimensional loading space. Finally, the loading paths obtained by incremental analysis are compared with the shakedown limits determined for the three-dimensional thermomechanical loading space.

7.1. Loading parameters of PFC

Six sets of loading parameters were chosen to investigate the effect of the loading conditions. The thermal history including the manufacturing procedure was schematically described in the chapter 5. Since the heat flux on the surface of a PFC of a future fusion reactor may reach up to 20 MW/m^2, three different quasi-stationary heat flux conditions (10, 15, 20 MW/m^2) were considered. The joining temperature was fixed to 700 ^{o}C. Water coolant temperatures were assumed to be 250 and 350 ^{o}C. The heat load duration time and cooling duration time were fixed at 30 seconds and 20 seconds, respectively. Therefore, six cases are represented in Table 7.1.

Table 7.1. Loading parameters used for this analysis

Boundary condition	Case 1	Case 2	Case 3	Case 4	Case 5	Case 6
Joining temperature, JT (^{o}C)	700	700	700	700	700	700
Heat flux, HF (MW/m^2)	10	10	15	15	20	20
Heat load duration (sec)	30	30	30	30	30	30
Coolant temperature, CT (^{o}C)	250	350	250	350	250	350
Cooling duration (sec)	20	20	20	20	20	20

7.2. Diagram of thermomechanical loading paths

The thermomechanical loading paths were constructed for the six loading cases. To obtain thermomechanical loading paths, the finite element analysis (FEA) was performed. The detail of procedures was explained in section 5.4.2. The selected material properties used for the FEA were also listed in Table 5.2. The whole loading history used in the computational analysis consists of two main steps: (i) FEA for temperature computation and (ii) FEA for stress computation. Since the materials were assumed to be thermo-elasto-plastic, the thermal-structural coupled analysis was performed using commercial finite element code ANSYS.

Firstly, the thermal-structural analysis for the loading case 1 (Table 7.1) was considered in the different locations of FRMMCs (Figure 5.6). From the FEA analysis, temperature and stress evolutions in four local points of the FRMMC layer were obtained for the considered loading history with two cycles of high heat flux loading, as shown in Figure 7.1. The red line indicates temperature evolution curve, and the black line and the blue line indicate *x*-

directional stress and *y*-directional stress, respectively. In these figures, the starting points of evolution paths were located at the considered manufacturing stage. FRMMCs in the PFC component were assembled at high joining temperature of 700 ^{o}C. The joining state was also assumed to be in stress-free state. Therefore, the components of temperature and stress of the initial point were represented as 700 ^{o}C and 0 MPa. During the cooling step (residual state in Figure 7.1), FRMMCs underwent a biaxial tension loading. In high heat flux loading (1st and 2nd cycles), the temperature evolution induces the mechanical stress states. For other loading cases (cases 2-6), the temperature and stress evolution paths may be easily drawn in the same manner.

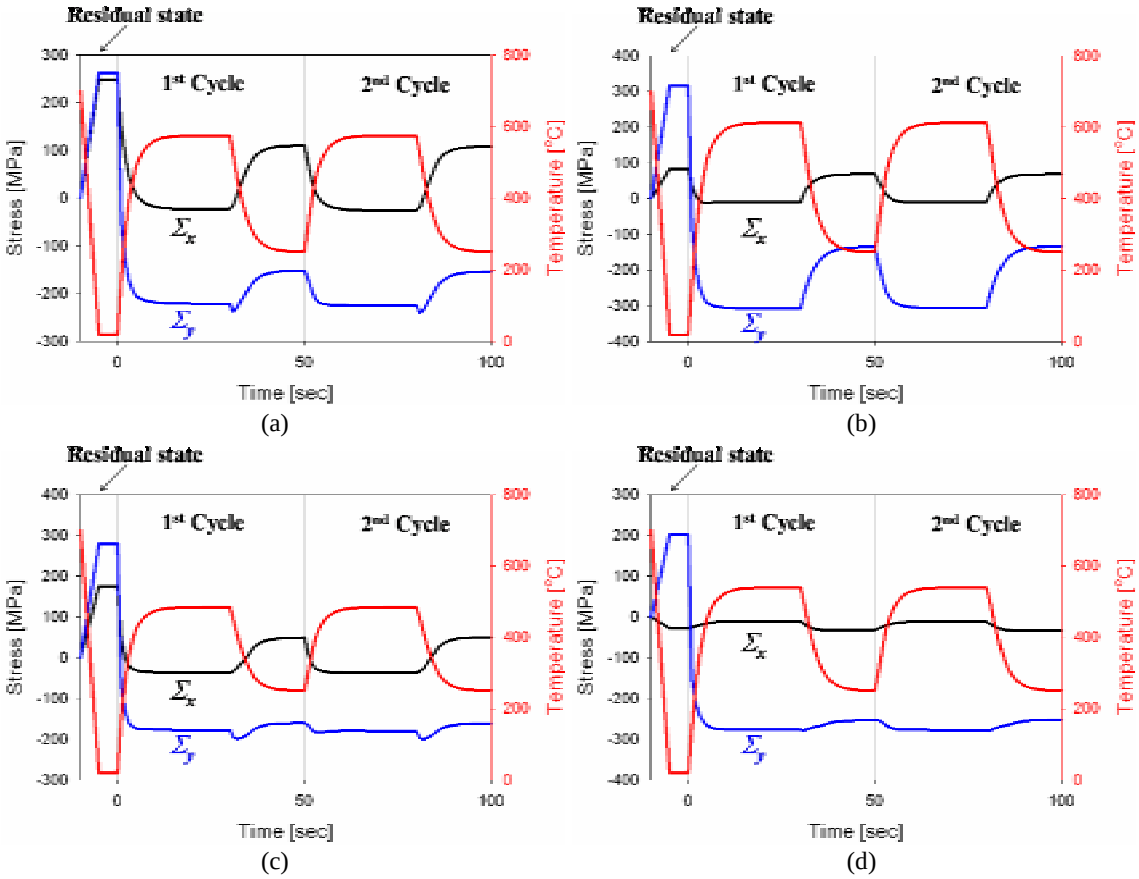

Figure 7.1. Temperature and stress evolution diagram of case 1 in Table 7.1: (a) location L1, (b) location L2, (c) location L3, and (d) location L4 in Figure 5.6. Red line indicates temperature component and black and blue line indicate stress components, respectively.

The components of stress and temperature can be redrawn in a three-dimensional space (Σ_x, Σ_y, T), so called, thermomechanical loading path. The obtained thermomechanical loading paths for all the loading cases are represented in Figure 7.2. For example, the red line in Figure 7.2 (a) indicates a thermomechanical loading path for position L1. It can be drawn from the three evolution lines in Figure 7.1 (a). Like the preceding, thermomechanical loading paths for positions L2 to L4 can be obtained from Figure 7.1 (b) to (d). They are represented as the green line, the yellow line, and the blue line in Figure 7.2 (a). Here, the dotted line at each curve indicates the loading path from the manufacturing step to the first cycle and the solid line indicates the loading path for the second cycle. Likewise, the thermomechanical loading paths can be drawn for the other loading cases (cases 2-6). They are represented in Figure 7.2 (b)-(f). Several dominant effects were observed from theses results.

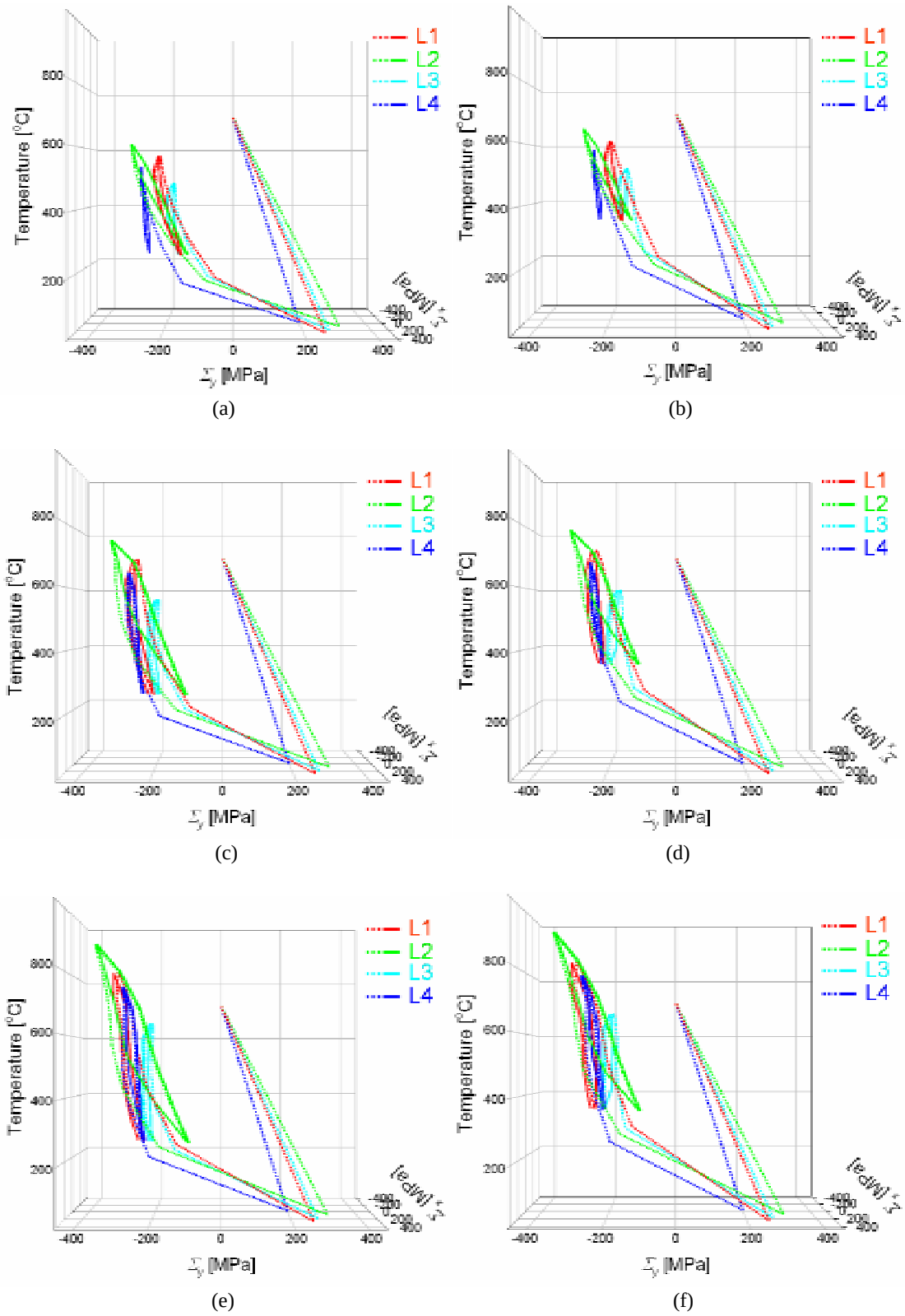

Figure 7.2. Thermomechanical loading paths in three-dimensional loading space: (a) case 1, (b) case 2, (c) case 3, (d) case 4, (e) case5, and (f) case 6. L1, L2, L3, and L4 indicate typical locations of FRMMC layer as shown in Figure 5.6. Dotted line represents loading path of manufacturing process and 1st heat flux loading and solid line shows 2nd heat flux loading.

(i) There was a significant change of the thermomechanical stress state during the initial manufacturing process in all the locations (dotted lines in Figure 7.2).

(ii) Since the nearest position from the cooling channel was the location L3 (yellow line), the range of temperature was not increased. As a result, the stress increase of L3 was relatively lower than other positions during cyclic heat flux loading, i.e. loading path of L3 (yellow line) was located in the right side of the loading paths.

(iii) The width of stress y-directional stress component (Σ_y) between the manufacturing stage and the second loading cycle depends on the coolant temperature. From Figure 6.2 (a) and (b), the width in case 2 was relatively smaller than the width in case 1. Since the stress state at the lower coolant temperature was apart from the stress-free state, the width was increased at the lower coolant temperature.

7.3. Shakedown limits and loading paths

To compare the three-dimensional loading path with the shakedown limits, some graphical modifications of shakedown limits are necessary. In the previous chapter, shakedown limits were represented in the two-dimensional loading space with temperature increases. To reconstruct these shakedown limits in the three-dimensional loading space, z-axis can be chosen as the axis for thermal loading. Then the shakedown limits were possibly redrawn in the three-dimensional loading space. Next, the normalized stress and thermal stress were converted to the realistic stresses and temperatures for the comparison with loading paths. Finally, the resulting loading paths were drawn simultaneously in the three-dimensional loading spaces.

In Figure 7.3, shakedown limits and the loading paths are represented in a three-dimensional loading space (Σ_x, Σ_y, ΔT). The shakedown limits are denoted by the black curves. For the comparison, the shakedown limits considering limited kinematic hardening (LKH) model are represented as grey curves. Shakedown limits with unlimited kinematic hardening (ULKH) model are not represented, since safety limits are significantly overestimated with this material model. The general trend can be observed in Figure 7.3. However, there were some ambiguous regions to compare the shakedown limits and loading paths. The additional figures in two-dimensional graphical projection ((Σ_x, Σ_y), (Σ_x, ΔT), (Σ_y, ΔT)) can be used for clear observation. They are attached in Appendix E.

In these figures, the center of shakedown limits was located in the stress free state of the structure. During the cooling process, from the joining temperature to room temperature, the PFCs undergo the severe change of the stress state (as expected in Figures 1.5). The center of the shakedown space was matched with the stress free state (0 MPa, 0 MPa, 700 ^{o}C) of the thermomechanical loading path. Several dominant facts were observed from these results.

(i) The results show that the loading paths were located partly outside of the shakedown limits.

(ii) The magnitude of the loading paths outside of the shakedown space was varied with the loading cases.

(iii) In high heat flux loading (20 MW/m^2), the loading path in the position L4 penetrates the space of the shakedown limits.

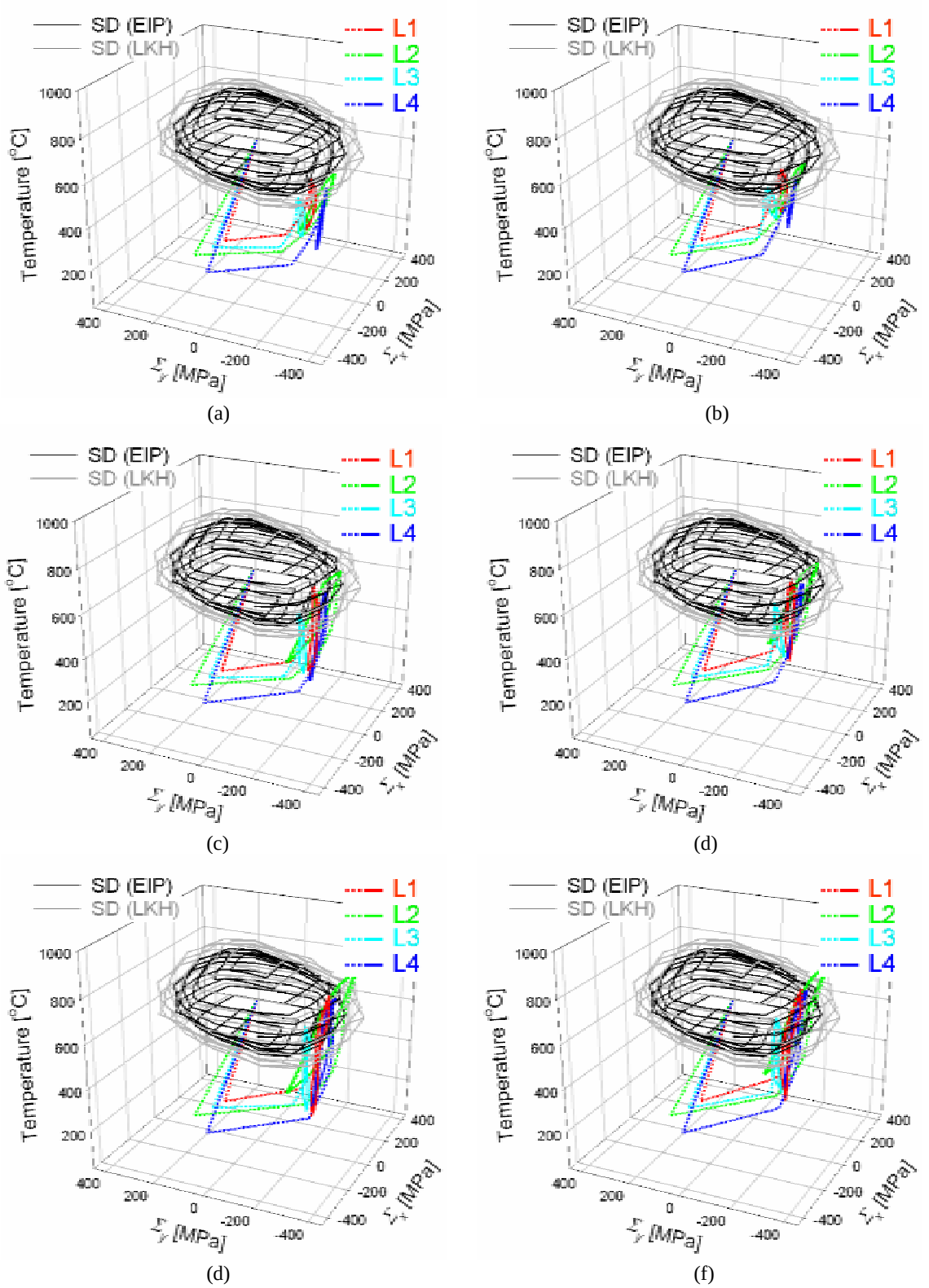

Figure 7.3. Shakedown limits and thermomechanical loading paths in three-dimensional loading space (700 °C of joining temp.): (a) case 1, (b) case 2, (c) case 3, (d) case 4, (e) case 5, and (f) case 6 in Table 7.1. L1, L2, L3, and L4 indicate typical locations of FRMMC layer as shown in Figure 5.6. Dotted line represents loading path of manufacturing process and 1st heat flux loading and solid line shows 2nd heat flux loading. SD (EIP) and SD (LKH) indicate shakedown limits with EIP model and with LKH model, respectively.

The data given in Table 7.2 rives a clearer view of the stress components and temperature at each typical loading state. The loading states considered here are the joining temperature (JT), room temperature (RT), 1st, 2nd heat flux (HF), and 1st, 2nd cooling temperature (CT).

As the temperature was cooled down to RT, the stress was significantly increased to the positive biaxial loading plane. The components of x-directional and y-directional stress (Σ_x, Σ_y) of position L1 were (249, 263), respectively. For position L2, Σ_x was decreased to 83 MPa while Σ_y was increased to 316 MPa in comparison with position L1. Since position L2 was the upper-edge (free surface) part of FRMMC layer (see Figure 5.6), Σ_x was decreased due to free boundary conditions to x-direction. However Σ_y was increased due to constrained boundary conditions combined with high thermal loading due to the long distance from coolant channel in comparison with position L1. In position L3 and L4, the increase of stress was similarly observed. It shows that FRMMC undergoes significant applied tension loading during the first cooling process from manufacturing.

During the cyclic heat flux loading and cooling, the stability (or instability) of loading state might be investigated. For example, case 1 (10 MW/m^2 (HF) and 250 ^{o}C (CT)) was considered. The temperature of position L1 varied between 575 ^{o}C and 250 ^{o}C during the high heat flux loading state and the cooling state. The components of (Σ_x, Σ_y) varied between (-23, -221) and (110, -151) in 1st cycle and between (-26, -225) and (108, -154) in 2nd cycle. The components of temperature and stress in 2nd cycle were not significantly deviated from those in 1st cycle. For the other locations (L2-L4), the magnitude of deviation between two cycles showed similar tendencies with the position L1.

In case 2 (10 MW/m^2 (HF) and 350 ^{o}C (CT)), temperature of position L1 was altered between 611 ^{o}C and 350 ^{o}C. The components of (Σ_x, Σ_y) undergo stress changes between (-17, -198) and (83, -160) in 1st cycle and between (-21, -202) and (80, -163) in 2nd cycle. The ranges of stress and temperature between heat flux state and cooling state were decreased in comparison with case 1. Since the higher coolant temperature (350 ^{o}C) was closer to the stress free state (700 ^{o}C), the stress mismatch was less likely. For the other locations (L2-L4), the tendencies of the loading path were similarly obtained as with position L1.

In case 3 (15 MW/m^2 (HF) and 250 ^{o}C (CT)), the temperature of position L1 differs between 701 ^{o}C and 250 ^{o}C. The components of (Σ_x, Σ_y) varied between (-64, -261) and (32, -208) in 1st cycle and (-105, -276) and (-5, -225) in 2nd cycle. The value of the loading path was significantly increased in comparison with the previous loading cases. The difference of each component of stresses between 1st cycle and 2nd cycle was significantly larger. This was observed in the whole region of FRMMC. It shows the range of the loading paths can be increased from cycle to cycle. The gradual stress evolution might be expected in this loading case. In case 4 (15 MW/m^2 (HF) and 350 ^{o}C (CT)), the general tendency of the loading path was similarly represented in comparison with loading case 3. However, the magnitude of loading path was decreased. This can be explained by the same reason as in case 2.

In case 5 (20 MW/m^2 (HF) and 250 ^{o}C (CT)), the temperature of position L1 differs between 701 ^{o}C and 250 ^{o}C. The components of (Σ_x, Σ_y) varied between (-104, -319) and (-44, -239) in 1st cycle and (-163, -338) and (-82, -253). The magnitude of deviation of stress state between the first cycle and the second cycle was significantly increased. In case 6 (20 MW/m^2 (HF) and 350 ^{o}C (CT)), the loading evolution had a similar trend with loading case 5, even though the range of loading was decreased.

Table 7.2 Stress components and temperature at each loading state (700 °C of joining temp.).

Case	Loading State	L1			L2			L3			L4		
		(Σ_x	Σ_y	T)	(Σ_x	Σ_y	T)	(Σ_x	Σ_y	T)	(Σ_x	Σ_y	T)
1	JT	0	0	700	0	0	700	0	0	700	0	0	700
	RT	248.9	262.5	20	83.4	315.5	20	174.6	279.1	20	-29.0	201.7	20
	1st HF	-23.1	-221.1	575.0	-10.2	-307.5	612.5	-37.1	-177.3	483.6	-11.3	-276.8	539.5
	1st CT	110.0	-151.8	250.5	69.0	-135.2	250.5	48.5	-160.7	250.4	-32.5	-253.8	250.4
	2nd HF	-25.9	-225.1	575.0	-10.7	-306.4	612.5	-37.7	-179.8	483.6	-11.8	-277.1	539.5
	2nd CT	108.2	-154.4	250.5	68.6	-133.7	250.5	49.4	-161.7	250.4	-33.3	-252.7	250.4
2	JT	0	0	700	0	0	700	0	0	700	0	0	700
	RT	248.9	262.5	20	83.4	315.5	20	174.6	279.1	20	-29.0	201.7	20
	1st HF	-17.1	-197.6	611.3	-11.8	-282.3	652.6	-26.3	-148.2	519.6	-10.0	-250.4	581.0
	1st CT	83.2	-159.5	350.1	55.7	-132.9	350.1	23.5	-166.1	350.0	-31.8	-233.5	350.1
	2nd HF	-20.9	-202.3	611.3	-12.6	-281.7	652.6	-27.2	-151.3	519.6	-10.3	-250.8	581.0
	2nd CT	80.2	-163.0	350.1	55.2	-131.8	350.1	24.0	-167.7	350.0	-32.3	-232.8	350.1
3	JT	0	0	700	0	0	700	0	0	700	0	0	700
	RT	248.9	262.5	20	83.4	315.5	20	174.6	279.1	20	-29.0	201.7	20
	1st HF	-63.9	-260.9	701.1	-8.5	-339.0	760.6	-48.8	-195.8	566.5	-3.7	-285.3	654.6
	1st CT	32.3	-207.6	250.7	63.4	-109.5	250.8	21.1	-190.3	250.6	-38.5	-245.2	250.7
	2nd HF	-104.9	-276.3	701.1	-11.4	-336.5	760.6	-66.7	-204.6	566.5	-4.0	-282.0	654.6
	2nd CT	-4.8	-224.5	250.7	60.8	-105.6	250.8	1.8	-199.4	250.6	-38.6	-239.6	250.7
4	JT	0	0	700	0	0	700	0	0	700	0	0	700
	RT	248.9	262.5	20	83.4	315.5	20	174.6	279.1	20	-29.0	201.7	20
	1st HF	-60.1	-246.1	730.8	-8.9	-322.1	793.9	-38.1	-170.5	596.1	-1.9	-262.7	688.6
	1st CT	-10.9	-219.2	350.1	50.2	-114.4	350.1	-9.1	-199.4	350.1	-32.7	-228.2	350.1
	2nd HF	-112.6	-264.3	730.8	-11.9	-319.7	793.9	-61.2	-181.2	596.1	-2.1	-259.5	688.6
	2nd CT	-54.5	-236.7	350.1	47.4	-110.1	350.1	-32.7	-209.9	350.1	-32.2	-221.1	350.1
5	JT	0	0	700	0	0	700	0	0	700	0	0	700
	RT	248.9	262.5	20	83.4	315.5	20	174.6	279.1	20	-29.0	201.7	20
	1st HF	-103.9	-319.2	821.0	-5.4	-382.0	904.2	-49.5	-209.7	643.5	2.4	-300.6	763.4
	1st CT	-43.5	-238.6	250.9	57.3	-99.1	251.0	-26.1	-210.6	250.8	-38.1	-239.4	250.9
	2nd HF	-163.0	-338.1	821.0	-8.4	-376.6	904.2	-75.7	-219.9	643.5	2.1	-295.0	763.4
	2nd CT	-82.4	-253.4	250.9	55.1	-94.6	251.0	-50.9	-220.5	250.8	-38.1	-232.5	250.9
6	JT	0	0	700	0	0	700	0	0	700	0	0	700
	RT	248.9	262.5	20.0	83.4	315.5	20.0	174.6	279.1	20.0	-29.0	201.7	20.0
	1st HF	-100.3	-305.0	847.2	-5.5	-367.4	933.7	-38.8	-188.0	669.1	3.8	-286.2	793.4
	1st CT	-84.1	-247.3	350.2	46.3	-109.2	350.2	-52.4	-218.2	350.1	-31.7	-223.2	350.2
	2nd HF	-167.6	-326.1	847.2	-8.0	-362.4	933.7	-68.3	-199.4	669.1	3.4	-280.0	793.4
	2nd CT	-124.8	-262.1	350.2	44.3	-105.2	350.2	-75.0	-227.1	350.1	-31.1	-215.1	350.2

∗ JT: joining temperature (700 °C), RT: room temperature (20 °C), 1st: first cycle, 2nd: second cycle, HF: heat flux loading state, CT: cooling temperature state.

From the previous results, the loading paths and the shakedown limits were represented on the basis of the joining temperature (700 ^{o}C). The stress relaxation should be considered in the real material, temperature drop in FRMMC induces the difference of effective temperature between the test temperature and that at which the specimen would be free of any deviatoric stress. The effective temperature change occurred, because stress relieving processes can act to reduce its values to substantially below the actual temperature change.

The effectively stress free temperature ΔT_{esf} should be considered to reflect the stress relaxation effect. ΔT_{esf} can be obtained from the values of P, Q and the experimentally observed difference between tensile and compressive yield stresses. Here, P is a dimensionless constant. Q [MPa/K] represents the difference between axial and transverse matrix stresses caused by cooling the composite through 1 ^{o}K [24].

$$\Delta T_{esf} = \frac{P(\sigma^{A}_{Ycompressive} - \sigma^{A}_{Ytensile})}{2Q} \tag{7.1}$$

In aluminum and SiC whisker (15 %) composite, the estimated stress free temperature was obtained as 350 ^{o}C [127]. In this case (CuCrZr-SiC FRMMC), ΔT_{esf} was assumed as 400 ^{o}C since copper alloy has a higher melting temperature than aluminum. When 400 ^{o}C of effectively stress free temperature is considered, shakedown limits and the loading paths can be reconstructed, as represented in Figure 7.4. From the results, some facts were observed as follows.

(i) When the results were compared with Figure 7.3, the loading paths in these figures were mostly inside of the modified shakedown limits considering effectively stress free temperature. Especially the loading path in the relatively low range of heat flux state (10 MW/m^2) was nearly inside the shakedown space.

(ii) In the relatively high heat flux loading state (15, 20 MW/m^2), the loading paths penetrated the shakedown limits.

Components of stress and temperature at typical loading states are represented in Table 7.3 The chosen loading states are effectively stress free temperature (ET, 400 ^{o}C), room temperature (RT), 1st, 2nd heat flux (HF), and 1st, 2nd cooling temperature (CT).

In the manufacturing process (ET $\rightarrow$ RT), the magnitude of each stress component was decreased in comparison with the previous result (JT $\rightarrow$ RT in Table 7.2). (Σ_x, Σ_y) of position L1 at RT from ET were (151, 134) while those were (249, 263) at RT from JT. In other positions (L2-L4), the general tendency was similarly observed.

During cyclic heat flux loading and cooling, the magnitude of each stress component was significantly decreased even though the range of each temperature component was the same with Table 7.2. For example, in case 1 (10 MW/m^2 (HF) and 250 ^{o}C (CT)), the components of (Σ_x, Σ_y) varies between (-56, -155) and (69, -71) in 1st cycle and between (-58, -158) and (69, -72) in 2nd cycle. The difference of each stress component between 1st cycle and 2nd cycle was decreased in contrast to Table 7.2. For the other locations (L2-L4), the magnitude of deviation between two cycles shows similar tendency with position L1.

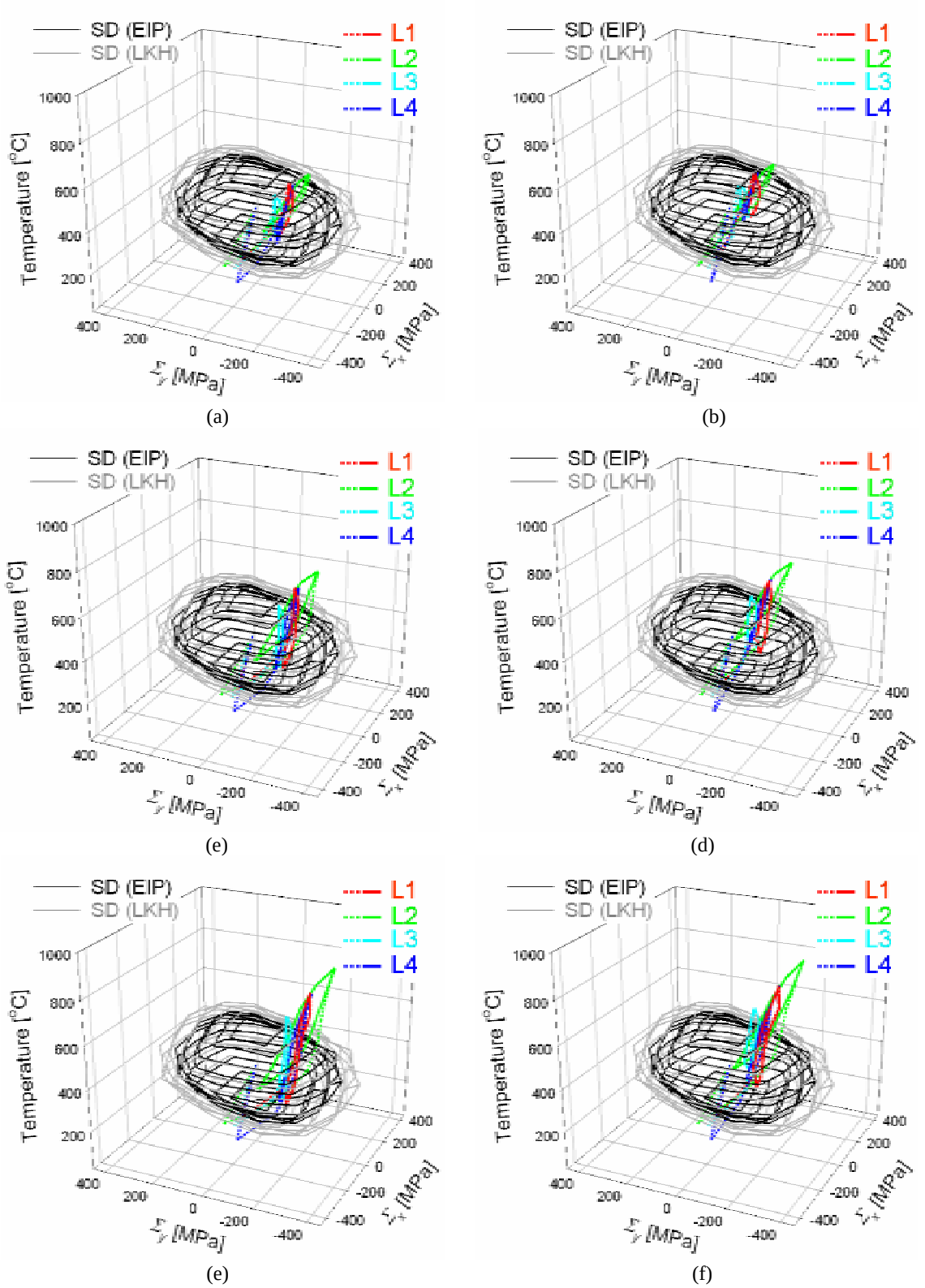

Figure 7.4. Shakedown limits and thermomechanical loading paths in three-dimensional loading space (400 °C of effectively stress free temp.): (a) case 1, (b) case 2, (c) case 3, (d) case 4, (e) case 5, and (f) case 6 in Table 7.1. L1, L2, L3, and L4 indicate typical locations of FRMMC layer as shown in Figure 5.6. Dotted line represents loading path of manufacturing process and 1st heat flux loading and solid line shows 2nd heat flux loading. SD (EIP) and SD (LKH) indicate shakedown limits with EIP model and with LKH model, respectively.

Table 7.3 Stress components and temperature at each loading state (400 ^{o}C of effectively stress free temp.).

Case	Loading State	L1			L2			L3			L4		
		(Σ_x	Σ_y	T)	(Σ_x	Σ_y	T)	(Σ_x	Σ_y	T)	(Σ_x	Σ_y	T)
1	ET	0	0	400	0	0	400	0	0	400	0	0	400
	RT	150.5	134.4	20.0	76.0	177.1	20.0	77.0	129.9	20.0	-25.8	68.7	20.0
	1st HF	-56.0	-155.4	575.0	-22.7	-221.3	612.5	-12.0	-81.5	483.6	10.5	-145.4	539.5
	1st CT	69.4	-71.0	250.6	55.2	-5.4	250.7	34.0	-73.2	250.5	-14.7	-92.5	250.6
	2nd HF	-58.4	-157.9	575.0	-23.2	-218.3	612.5	-11.9	-82.4	483.6	10.5	-143.5	539.5
	2nd CT	68.5	-72.3	250.5	55.2	-3.4	250.5	34.0	-73.9	250.4	-14.6	-91.4	250.4
2	ET	0	0	400	0	0	400	0	0	400	0	0	400
	RT	150.5	134.4	20.0	76.0	177.1	20.0	77.0	129.9	20.0	-25.8	68.7	20.0
	1st HF	-59.0	-125.5	611.3	-24.6	-185.6	652.6	-0.1	-39.1	519.6	14.5	-107.4	581.0
	1st CT	33.3	-71.9	350.1	40.9	2.6	350.1	28.5	-65.0	350.0	-4.5	-58.0	350.1
	2nd HF	-60.9	-127.7	611.3	-25.1	-183.1	652.6	0.2	-40.1	519.6	14.4	-106.3	581.0
	2nd CT	32.4	-73.2	350.1	41.0	3.8	350.1	28.6	-65.7	350.0	-4.4	-57.5	350.1
3	ET	0	0	400	0	0	400	0	0	400	0	0	400
	RT	150.5	134.4	20.0	76.0	177.1	20.0	77.0	129.9	20.0	-25.8	68.7	20.0
	1st HF	-73.8	-197.8	701.1	-19.7	-261.9	760.6	6.0	-100.2	566.5	14.2	-175.3	654.6
	1st CT	44.5	-105.1	250.7	47.1	12.4	250.8	33.7	-95.2	250.6	-13.5	-94.9	250.7
	2nd HF	-84.0	-201.4	701.1	-20.8	-259.2	760.6	2.4	-102.1	566.5	14.1	-173.5	654.6
	2nd CT	34.1	-109.7	250.7	46.8	13.5	250.8	30.4	-97.0	250.6	-13.4	-93.9	250.7
4	ET	0	0	400	0	0	400	0	0	400	0	0	400
	RT	150.5	134.4	20.0	76.0	177.1	20.0	77.0	129.9	20.0	-25.8	68.7	20.0
	1st HF	-78.4	-178.7	730.8	-19.9	-238.8	793.9	18.1	-65.6	596.1	15.8	-144.4	688.6
	1st CT	-0.8	-109.9	350.1	35.4	12.9	350.1	25.4	-90.2	350.1	-3.7	-65.6	350.1
	2nd HF	-93.2	-184.3	730.8	-20.8	-237.2	793.9	12.3	-68.8	596.1	15.7	-143.8	688.6
	2nd CT	-15.3	-115.8	350.1	35.6	13.4	350.1	20.8	-93.0	350.1	-3.6	-65.8	350.1
5	ET	0	0	400	0	0	400	0	0	400	0	0	400
	RT	150.5	134.4	20.0	76.0	177.1	20.0	77.0	129.9	20.0	-25.8	68.7	20.0
	1st HF	-95.0	-248.8	821.0	-13.2	-306.5	904.2	20.3	-112.9	643.5	16.1	-211.3	763.4
	1st CT	-5.6	-126.3	250.9	47.1	12.5	251.0	16.3	-104.2	250.8	-12.9	-99.3	250.9
	2nd HF	-117.9	-257.2	821.0	-12.6	-305.6	904.2	13.0	-116.7	643.5	16.2	-210.3	763.4
	2nd CT	-23.7	-133.7	250.9	48.9	11.0	251.0	10.1	-107.5	250.8	-12.7	-100.8	250.9
6	ET	0	0	400	0	0	400	0	0	400	0	0	400
	RT	150.5	134.4	20.0	76.0	177.1	20.0	77.0	129.9	20.0	-25.8	68.7	20.0
	1st HF	-97.4	-231.5	847.2	-13.1	-286.3	933.7	32.9	-82.7	669.1	17.4	-188.5	793.4
	1st CT	-44.3	-127.1	350.2	37.0	8.5	350.2	10.4	-99.4	350.1	-3.1	-73.0	350.2
	2nd HF	-123.1	-240.8	847.2	-12.2	-286.9	933.7	24.4	-87.4	669.1	17.4	-188.0	793.4
	2nd CT	-62.5	-134.4	350.2	39.1	6.2	350.2	4.1	-102.6	350.1	-2.9	-74.6	350.2

∗ ET: effectively stress free temperature (400 ^{o}C), RT: room temperature (20 ^{o}C), 1st: first cycle, 2nd: second cycle, HF: heat flux loading state, CT: cooling temperature state.

In other cases (case 2-6), the difference of each stress component between 1st cycle and 2nd cycle was significantly decreased in comparison with previous results (Table 7.2). The results were reasonable because the lower stress free temperature (400 ^{o}C of ET) was used and the differences of stress between loading states were decreased in comparison with Table 7.2 (700 ^{o}C of JT). The realistic behavior might be somewhere in between two limit cases, that is, one based on JT and the other based on ET.

7.4. Remarks for fusion application

In the previous results, temperature and stress components were investigated at each loading step. The distance of stress components at two different loading steps might be useful to predict the stability of structural state under the considered loading conditions. Therefore, the distance of applied loading at a certain path between two neighboring loading steps, so-called loading scale, was obtained as follows. Here *i* and *j* denote two neighboring loading stages for the chosen loading paths. The obtained results for all cases are represented in Table 7.4.

$$\sigma^{ij}(Loading\ \ scale) = \sqrt{(\sigma_x^i - \sigma_x^j)^2 + (\sigma_y^i - \sigma_y^j)^2} \tag{7.2}$$

Firstly, the results of the loading scale for JT (700 ^{o}C) were discussed. In the relatively low heat flux loading (case 1 and case 2), the loading scales in the manufacturing step (JT or ET $\rightarrow$ RT) and the first high heat flux loading (RT $\rightarrow$ 1st HF) were higher than the other loading steps, since there was a significant change of thermal history. However, the loading scales in all the positions were nearly stabilized for two heat flux loading cycles.

In case 3 and case 4, the loading scales in the position L1 and L3 were not stabilized. Therefore in this region the structure might have incremental plastic failure due to accumulation of deformation. For the accurate investigation of incremental plastic collapse, however, the cyclic thermo-elastic-plastic incremental analysis should be performed in consideration with nonlinear hardening effect for a number of cycles. In the position L2, loading scale was stabilized but it slightly deviates from two shakedown limits (elastic-ideal plastic (EIP) model and limited kinematic hardening (LKH) model), as shown in Figure 7.4. Therefore the position L2 might have a safety problem from a shakedown viewpoint. In the high heat flux loading (20 MW/m^2), i.e. case 5 and case 6, the loading scales in the position L1 and L3 were not stabilized. In the position L2, loading scale was stabilized but it slightly deviates from two shakedown limits (EIP model and LKH model).

Throughout all the loading cases, loading scales of position L3 were decreased with an increase of heat flux loading while loading scales of position L2 and L4 were increased. In position L1, loading scales were decreased with increase of heat flux loading between 10 and 15 MW/m^2, while they were slightly increased with an increase of heat flux loading between 15 and 20 MW/m^2. These tendencies can be explained by the relationship between the distance from coolant channel and heat flux loading surface. Since the position L3 was located in the nearest region with coolant, there was no significant stress change during cyclic heat flux loading. Since the positions L2 and L4 were located far from the coolant channel, the stress state was mainly determined by the extent of heat flux loading.

Table 7.4. Loading scales between two neighboring loading states.

Case	Position	L1		L2		L3		L4	
	Stress free temperature	700 °C	400 °C	700 °C	400 °C	700 °C	400 °C	700 °C	400 °C
1	JT, ET→RT	361.7	201.8	326.3	192.7	329.2	151.0	203.8	73.4
	RT→1st HF	554.8	355.8	630.0	410.4	503.1	229.4	478.9	217.2
	1st HF→1st CT	150.0	151.2	189.6	229.5	87.2	46.7	31.3	58.6
	1st CT→2nd HF	154.4	154.5	188.8	226.9	88.2	46.8	31.2	56.9
	2nd HF→2nd CT	151.6	153.1	190.1	228.8	89.0	46.7	32.5	57.8
2	JT, ET →RT	361.7	201.8	326.3	192.7	329.2	151.0	203.8	73.4
	RT→1st HF	531.5	333.8	605.3	376.4	472.2	185.8	452.6	180.7
	1st HF→1st CT	107.2	106.7	163.9	199.3	52.9	38.6	27.6	52.9
	1st CT→2nd HF	112.5	109.5	163.7	197.1	52.8	37.7	27.7	51.9
	2nd HF→2nd CT	108.5	108.1	164.5	198.2	53.8	38.2	28.4	52.3
3	JT, ET →RT	361.7	201.8	326.3	192.7	329.2	151.0	203.8	73.4
	RT→1st HF	609.8	400.8	661.0	449.3	524.9	240.8	487.6	247.3
	1st HF→1st CT	110.0	150.3	240.5	282.3	70.1	28.1	53.1	85.0
	1st CT→2nd HF	153.4	160.6	239.0	280.0	88.9	32.1	50.5	83.3
	2nd HF→2nd CT	112.7	149.5	241.9	281.0	68.7	28.5	54.7	84.2
4	JT, ET →RT	361.7	201.8	326.3	192.7	329.2	151.0	203.8	73.4
	RT→1st HF	595.1	387.8	644.2	426.8	497.4	204.2	465.2	217.1
	1st HF→1st CT	56.1	103.7	216.0	257.7	40.9	25.7	46.3	81.2
	1st CT→2nd HF	111.2	118.6	214.6	256.3	55.2	25.1	43.8	80.6
	2nd HF→2nd CT	64.3	103.7	217.9	256.9	40.4	25.6	48.8	80.4
5	JT, ET →RT	361.7	201.8	326.3	192.7	329.2	151.0	203.8	73.4
	RT→1st HF	680.3	455.1	703.1	491.8	537.8	249.3	503.3	283.1
	1st HF→1st CT	100.6	151.7	289.7	324.6	23.4	9.6	73.4	115.7
	1st CT→2nd HF	155.5	172.5	285.1	323.7	50.4	12.9	68.6	114.8
	2nd HF→2nd CT	116.9	155.3	289.0	322.5	24.8	9.6	74.3	113.2
6	JT, ET →RT	361.7	201.8	326.3	192.7	329.2	151.0	203.8	73.4
	RT→1st HF	666.4	442.0	688.7	471.9	513.6	217.1	489.0	260.8
	1st HF→1st CT	60.0	117.1	263.4	299.0	33.1	28.0	72.3	117.3
	1st CT→2nd HF	114.9	138.3	259.0	299.5	24.6	18.4	66.8	116.8
	2nd HF→2nd CT	77.1	122.4	262.4	297.6	28.5	25.4	73.5	115.2

∗ JT: joining temperature (700 °C), ET: effectively stress free temperature (400 °C), RT: room temperature (20 °C), 1st: first cycle, 2nd: second cycle, HF: heat flux loading state, CT: cooling temperature state

The loading case 2 induced less thermal stress mismatch due to the combination of relatively low heat flux (10 MW/m^2) and high coolant temperature (350 ^{o}C). Since the resulting loading scale of the loading case 2 was relatively low, FRMMC-layered PFCs might be in the safe state from a shakedown viewpoint. However, in other loading cases, some parts of FRMMC might have structural problems due to strain accumulation (incremental plastic collapse) after some loading cycles.

Secondly, the loading scale for ET (400 ^{o}C) were investigated. In the low heat flux (case 1 and case 2), the loading scales in the manufacturing step (JT or ET $\rightarrow$ RT) and the first high heat flux loading (RT$\rightarrow$1st HF) were higher than the other loading steps, since there was a significant change of thermal history. Loading scales of ET in the first two steps (ET $\rightarrow$ RT $\rightarrow$ 1st HF) were decreased in comparison with those of JT, while the scales of ET in the heat flux state (1st HF$\rightarrow$ 2nd CT) were instead increased at the edge region of FRMMC layer (L2 and L4). However, the loading scales of both approaches (JT and ET) were nearly stabilized for heat flux loading cycles.

In case 3 and case 4, the loading scale in the position L1 were not stabilized like those of JT, while that in L3 was stabilized. The magnitude of deviation of loading scale of L1 was also decreased. In position L2 and L4, loading scales were increased in comparison with those of JT. In the high heat flux loading (case 5 and case 6), the loading scales in position L1 and L3 were not stabilized as in the case of JT. In position L2 and L4, loading scales were significantly increased in comparison with those of ET like the preceding cases (case 3 and case 4).

The results of loading scales of JT and ET showed some opposite trends with chosen region of FRMMC layer. Especially, the loading scales of ET (400 ^{o}C) were significantly increased in comparison with those of JT (700 ^{o}C) at the edge region. In heat flux state, the temperature of FRMMC layer (L2) was elevated to between 613 ^{o}C (10 MW/m^2) and 934 ^{o}C (20 MW/m^2). This high operation temperature induced larger loading scales of ET than those of JT due to a larger difference between ET and the operation temperature.

In this chapter, the application of shakedown analysis was investigated to the fusion system from the comparative study between shakedown limits and the loading path of the fusion system. For this, several parametric studies with different loading conditions were performed by considering the fusion-relevant loading conditions in the PFCs. The loadings were mainly determined from the relationship between heat flux and coolant temperature. The represented loading paths by thermo-elasto-plastic FEM analyses were compared with the shakedown limits in the three-dimensional loading space and the loading scales were obtained between two neighboring states. From these results, the optimal design concept of PFC component can be suggested and is discussed for fusion application.

The elastic limit could estimate the strict safety criterion of structure under cyclic loads. FRMMCs will be exposed to significant cyclic heat flux loading in the fusion device, and the resulting stress fields of the matrix at a mesoscopic level would be highly heterogeneous and often exceed the yield limits. The elastic limits cannot be used in this case. Therefore, the shakedown limits were chosen as the safety criterion in this work. It was observed that the shakedown limits were less stringent criterion than the elastic limits without incurring progressive plastic failure (low cycle fatigue).

For structural safety of the PFC, the loading path of the FRMMC has to be located inside the shakedown limits. However, the results in this chapter show that the loading paths were partly outside of the shakedown limits. It was interpreted that the FRMMC layers will eventually fail in the matrix region or interface due to low cycle fatigue. Therefore, the failure control should be investigated with the shakedown analysis for structural safety assessment in the fusion operation.

8. Summary

Shakedown analysis tool was developed with finite element method (FEM) and nonlinear optimization program. It was extended to three-dimensional models. Then shakedown analysis was performed for the complex three-dimensional fiber-reinforced metal matrix composites (FRMMCs) considering thermomechanical loading. Finally, for the comparison with the results of the shakedown analysis, thermomechanical loading paths were obtained using incremental analysis in fusion-relevant loading.

Development of shakedown algorithm

In this study, the behaviors of the structure subjected to cyclic loading were discussed to find the relevant safety criterion. Shakedown theorem was formulated using Melan's static approach. The proof of static shakedown theorem was given. Static shakedown theorem was extended to the thermal loading case and hardening models. The numerical formulation of shakedown theory was carried out for three-dimensional models. The details of shakedown formulation were described by finite element discretization with the nonlinear large-scale mathematical optimization program (LANCELOT). The developed computational tool for shakedown analysis was verified with several literature examples.

Remarks on results of shakedown analysis

FRMMCs of lamina and laminate were investigated to obtain their shakedown limits in three-dimensional loading space. The obtained shakedown limits were significantly dependent on the geometrical factors (fiber volume fraction and fiber array), and the loading combinations. Both shakedown spaces and elastic spaces had longish shapes along the first quarter plane and the third quarter plane. In the lamina structure, the margins from shakedown limits in the first quarter plane and the third quarter plane were bigger than those in the second quarter plane and the fourth quarter plane. However, the margins along the first quarter plane and the third quarter plane of the laminate structure were significantly less than those of the lamina structure. For the second quarter plane and the fourth quarter plane, shakedown limits and their margins of lamina and laminate have similar tendencies. Shakedown limits were obtained with two different hardening states, i.e. unlimited kinematic hardening (ULKH) model and limited kinematic hardening (LKH) model. Shakedown limits of ULKH model increased significantly, while shakedown limits of LKH model did not significantly increase.

The results of the shakedown limits and the elastic limits were investigated from von Mises stress distribution. Von Mises stress distribution profiles were represented to explain the shape of the elastic space and the shakedown space. When the von Mises stress profile was well distributed and its magnitude was decreased, the margins of the shakedown limits were increased to the same loading condition. To the contrary, the margins of the shakedown limits were decreased when von Mises stress profile was highly localized and its magnitude was greatly increased.

It was observed that the shakedown limits were larger than elastic limits. This means that the gap between shakedown limits and elastic limits could be still viable from a shakedown viewpoint. Therefore, the shakedown limits could give a more economic margin for safety criterion as they can be practically used for the application in the highly loaded area.

Remarks on fusion application

The application of shakedown analysis to the real system was made to investigate a design concept of plasma facing component (PFC) for fusion application. The loading paths were obtained using incremental analyses and illustrated with shakedown limits in three-dimensional loading space. Several parametric studies were performed by considering the fusion-relevant loading conditions in the PFC component.

FRMMCs will be exposed to significant cyclic heat flux loading in the fusion application, and the resulting stress fields of the matrix in a mesoscopic level were highly heterogeneous and exceeded yield limits. In this case, the elastic limits are not relevant for structural analysis. The shakedown limits were used as the safety criterion of FRMMC layer in relation to the fusion application. For structural safety of the FRMMC, the loading paths of the FRMMC should be located within the shakedown limits. The comparative results showed that the loading paths under cyclic heat flux loading were partly outside of the shakedown limits. It is interpreted that the FRMMC layers will eventually fail in the matrix region or interface due to low cycle fatigue.

The failure potential of the component could be qualitatively estimated from the relative position of loading path in comparison with shakedown limits. In the case of the low heat flux loading (10 MW/m^2), shakedown limits of FRMMC covered nearly all the loading paths except the first cooling process. With increases of the heat flux loading, the loading paths had deviated significantly from the shakedown limits (Figure 7.4). As the magnitude of deviation of loading paths from shakedown limits is increased, the possibility of structure failure might be extremely high. Therefore, the shakedown limits can be used for the structural safety assessment of FRMMCs without incurring failure for fusion-relevant loading.

Appendix A. Thermonuclear Fusion

A.1 Nuclear fusion

Nuclear fusion is the nuclear reaction between nuclei of light elements that fuse together to form a heavier element releasing large amounts of energy. This process takes place continuously in the core of the sun where, at temperatures of 10-15 million ^{o}C, hydrogen (H) is converted to helium (He) providing enough energy to sustain life on Earth.

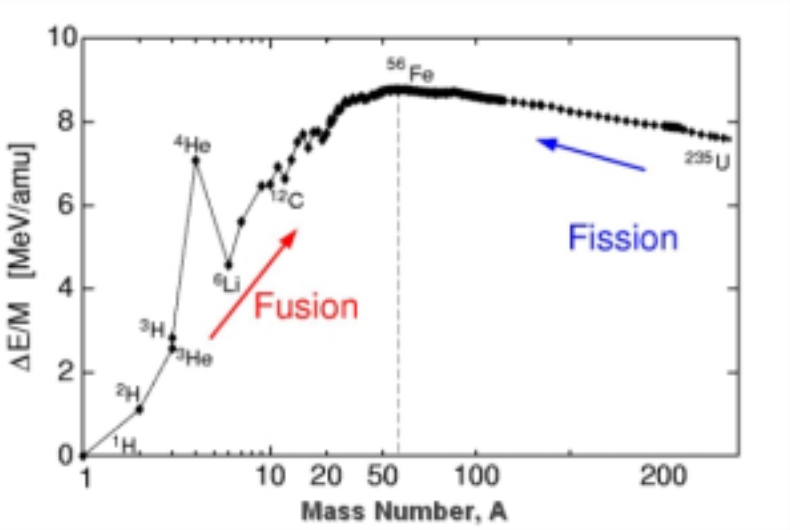

Figure A.1. Binding energy per nuclear particle (nucleon) in MeV as a function of the Mass Number, A [127].

Figure A.1 shows the binding energy per nucleon as a function of the Mass Number, A. It has a maximum around 9 MeV for nuclei closed to the iron (Fe), which is the most stable nucleus. For light elements, the larger A is, the stronger is the binding energy per nucleon (see Figure A.1), i.e. the nucleons are lighter and the nucleus more stable. Therefore, in a fusion reaction between light nuclei, the total mass of the resultant nuclei is slightly less than the total mass of the original particles; this mass difference is converted into kinetic energy of the resultant fusion products, as described by Einstein's famous equation:

$$E = mc^2 \tag{A.1}$$

where E is the released energy, which is equal to the mass difference, m, multiplied by the squared velocity of the light, c.

There are several fusion reactions involving light isotopes, but the reaction between the nuclei of the two heavy isotopes of H -deuterium (D) and tritium (T)- is the most suitable one (Figure A.2); this reaction proceeds as following:

$$D + T \rightarrow {}^{4}He\ (3.517\ MeV) + n\ (14.069\ MeV) \tag{A.2}$$

where the energies given are the kinetic energies of the reaction products: ^{4}He and a neutron (n). D is a plentiful resource: it is naturally found in sea water with a density of 30 g/m^3. T is a

weak radioactive element, and it transforms spontaneously into non-radioactive He, emitting an electron (e^-) and causing energy to be released in the form of beta radiation (β) with a half-life of 12.43 years. This low-energy β cannot penetrate human skin, so that only consuming large amounts of T could be dangerous. In a fusion reactor, T can be produced from the reaction of lithium (Li), which will cover the central part of the reactor, with the neutrons released from the fusion reactions:

$$^6\text{Li} + \text{n} \rightarrow {}^4\text{He} + \text{T} + 4.86\ \text{MeV} \quad \text{(A.3)}$$

$$^7\text{Li} + \text{n} \rightarrow {}^4\text{He} + \text{T} + \text{n} - 2.5\ \text{MeV} \quad \text{(A.4)}$$

There are large reserves of Li in the Earth's crust. Eventually, reactions involving just D-D or D-He (^{3}He) may be also used, but they are not as favorable as the D-T reaction, which has by far the largest cross section for relatively low temperatures [128].

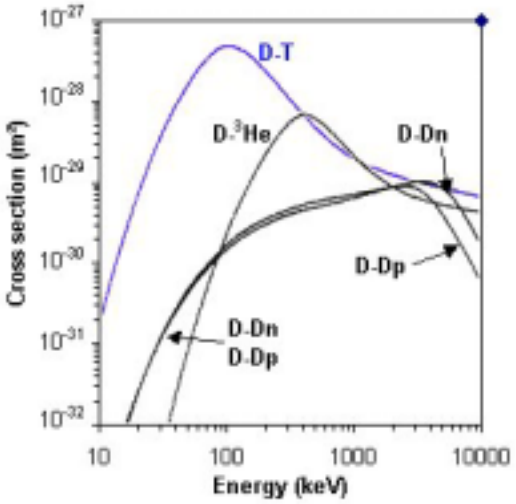

Figure A.2. Cross-sections of different fusion reactions as a function of the required energy [129].

The development of nuclear fusion as an energy source is one of the most complex scientific and technical tasks ever undertaken for non-military purposes and it will still span several human generations. In order to induce the fusion of nuclei of D and T it is necessary to surmount the Coulomb repelling force so that the attractive nuclear forces come into play. To achieve this, the particles must retain their energy and remain in the reacting region for a sufficient time. At these required temperatures (around 10 keV, that is, about 100 Mills. ºC[1]) the fuel is completely ionized; the resulting gas is an electrically neutral mixture of nuclear ions (positive) and electrons (negative) with very high thermal kinetic energies, called plasma. There are currently known three methods to confine the plasma in order to generate nuclear fusion: gravitational, inertial and magnetic confinement (Figure A.3). But only the two last methods are possible for producing nuclear fusion on Earth.

Inertial fusion consists of micro-explosions of small fuel pellets by means of powerful lasers or particle beams. Confinement of the fuel is based on the inertia of the pellet fuel mass,

[1] The temperature is lower than that corresponding to the energy of maximum cross-section (Figure A.2) because the required reactions occur in the high-energy tail of the Maxwellian distribution of heated particles.

which resists the natural expansion when it is heated to thermonuclear fusion temperatures. Additional information about inertial fusion can be found in [130]. Magnetic fusion heats and confines hot plasma within closed nested magnetic surfaces in a toroidal vacuum vessel. The European fusion effort is concentrated on the latter and only this method will be briefly reviewed here.

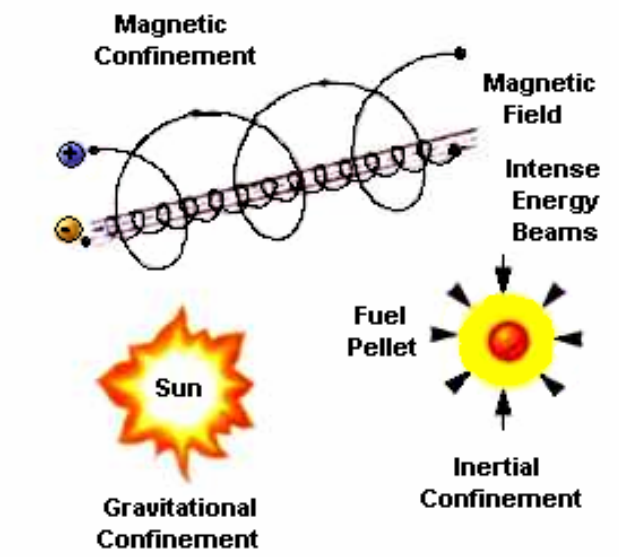

Figure A.3. Three types of plasma confinement methods.

A.2 Magnetic plasma confinement

In a fusion reactor, the magnetic plasma confinement can basically be performed with two different approaches: tokamak and stellarator (Figure A.4).

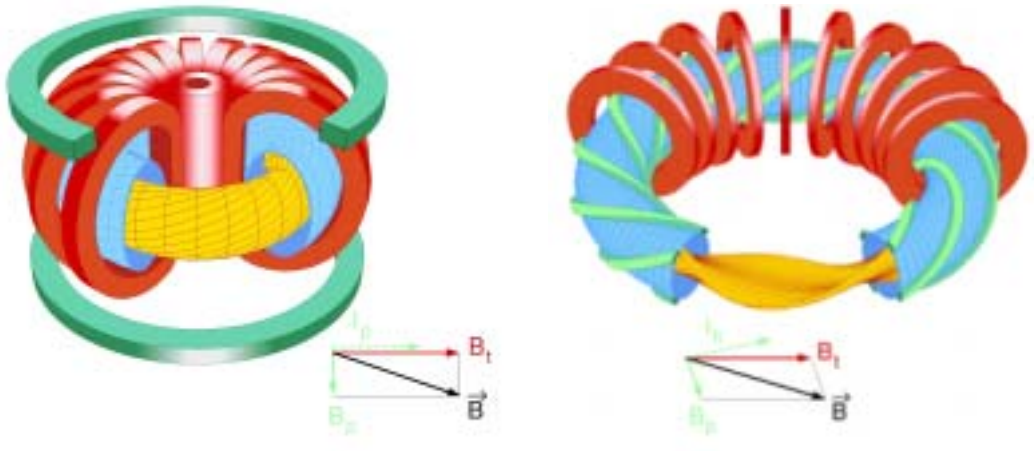

(a) (b)

Figure A.4. Schematics of the magnetic plasma confinement approaches tokamak (a) and stellarator (b).

Tokamak means in Russian "toroidal chamber" (toroidalnaya kamera magnitnoi katushki); the Russians L. Artsimovich and A. Sakharov invented it in 1952. The realization of the closed nested magnetic surfaces for plasma confinement is obtained by superposition of a strong toroidal field of the order of several Tesla with a poloidal field from an internal toroidal current flowing in the plasma (see Figure A.4 a) [128]. The toroidal field is produced by a set of external discrete coils equally spaced around the vacuum vessel; this field keeps the plasma away from the walls but, however, it is not enough to confine the plasma by itself. For that reason, a second poloidal field is necessary to cancel out the natural pressure inside the plasma, which tries to make it expand. Transformer coupling of the currents in toroidal ring coils induces the toroidal plasma current, which produces the necessary poloidal magnetic field component and, in addition, heats the plasma by ohmic heating. As a result of the superposition of both magnetic field components, nested magnetic surfaces are formed, which effectively confine the charged particles of the plasma. Further toroidal coils are installed for plasma positioning, shape control and for diverting the magnetic field lines at the plasma boundary away from the plasma core, in order to enable magnetic plasma limitation and to solve the particle and energy exhaust problem; this device is called divertor.

In the stellarator configuration as shown in Figure A.4 (b), closed nested magnetic surfaces are entirely created by specially shaped external superconducting coils. The stellarator thus explicitly allows stationary plasma confinement. There is no net current flowing within the plasma. This implies, however, that magnetic surfaces can be established only if the plasma has a toroidally periodic (i.e. not axially symmetric) form. The stellarator concept became even more attractive after the development of optimized confinement configurations and of the modular coil arrangement, and particularly after the discovery of quasi-dynamic and quasi-helically symmetric configurations, which main attain very favorable intrinsic confinement properties.

In view of the fact that the tokamak concept has been brought to a high level of development in all the major fusion programs of the world, the following information will be focused on it. To obtain in a tokamak a net positive energy output, i.e. to reach the so-called ignition condition, D-T plasma has to be heated to temperatures up to very high temperatures (at least 12 keV, ~140 millions ºC) and a good confinement is necessary. Several criteria have been developed in order to quantify the required confinement in a tokamak. Generally such criteria arise from the balance of the energy given up by the He in heating the plasma against the many mechanisms of energy loss (conduction, diffusion and radiation). Normally, the plasma density (n), the plasma temperature (T) and the energy confinement time (τ_E) are used to quantify the result and the balance equation results in the following triple product, or criteria for ignition:

$$n \cdot T \cdot \tau_E \cong 6 \times 10^{21}\ \mathrm{m^{-3}\ keV\ s} \qquad \textbf{(A.5)}$$

Here, n must be sufficiently large for fusion reactions to take place at the required rate ($>10^{20}$ m^{-3}). The fusion power generated will be reduced if impurity atoms released from the fusion reaction dilute the fuel; consequently, He ash must be removed. τ_E measures the efficiency of the magnetic insulation; it is the characteristic time-scale for plasma cooling when the source of heat is removed, and it has to be in the order of seconds. T must be high enough to prevail the repulsive Coulomb's force and to produce an adequate amount of fusion reactions.

In Figure A.5 it is shown the fantastic progress obtained in magnetic fusion in the last 30 years. Three generations of tokamaks with doubling of characteristic dimensions at each step led to a 10000 times higher value of the fusion triple product. Alternative, non-tokamak magnetic fusion approaches (stellarators, reversed field pinches) may offer economic and operational benefits. However, these approaches are more than one generation behind the tokamak line.

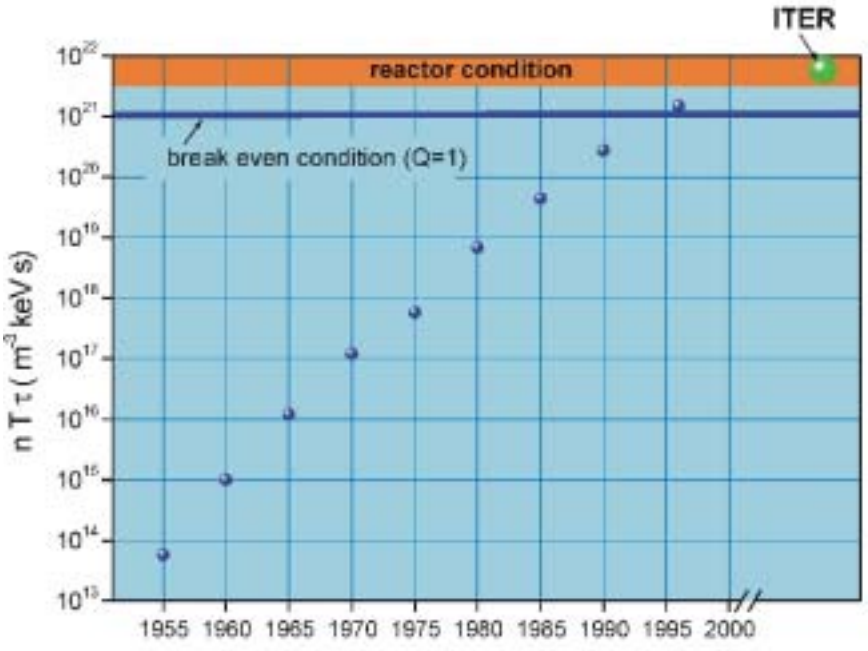

Figure A.5. Progress on fusion.

A.3 International Thermonuclear Experimental Reactor (ITER)

The International Thermonuclear Experimental Reactor (ITER) is the next major step for the development of fusion (Figure A.5). Scientists and engineers from Europe, Canada, Japan, Russia, Korea, China and USA are working in an unprecedented international collaboration on this reactor, which is the second world's largest international co-operative research and development project after the International Space Station (ISS).

With the impending construction and operation of ITER, fusion research is at the dawn of a new era. ITER will be the first machine based on the tokamak configuration to provide plasma dominated by α-particle heating, combining the plasma physics with the key reactor technologies of high heat flux components and long-term superconducting magnet technology necessary for power production.

One of the main ITER goals is to demonstrate the safety and environmental potential of fusion power for its essential characteristics: low fuel inventory, ease of burn termination, low power and energy densities, large heat transfer surfaces and the fact that confinement barriers exist and must anyway be leak-tight for successful operation.

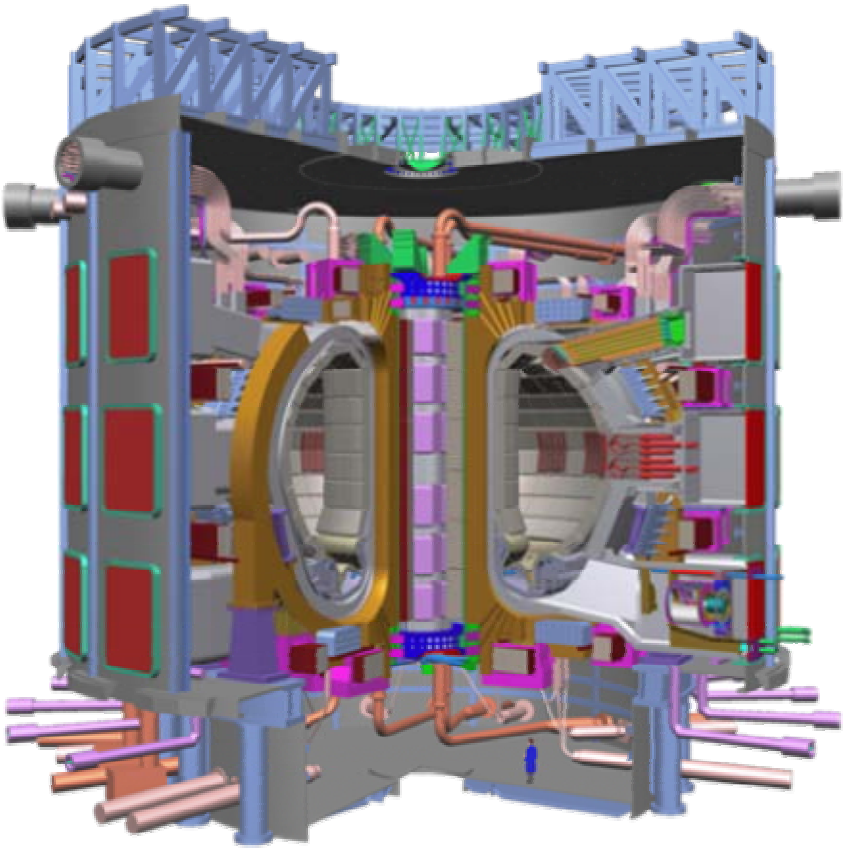

Figure A.6. A cut-away view of the ITER tokamak

A cutaway of the ITER tokamak is shown in Figure A.6. The magnet system consists of 18 Nb_3Sn toroidal field (TF) coils, a central solenoid (CS) of six modules, which can be powered separately, six NbTi poloidal field (PF) coils, and 18 NbTi saddle-shaped coils. ITER will be the first device to use Nb_3Sn superconductors on a large scale. It adopts a new design of superconducting cables in a conduit of steel [131]. The major parameters and dimensions of ITER are shown in Table A.1.

Table A.1. Main parameters and dimensions of ITER.

Total Fusion Power (MW)	500 (700)
Plasma major radius (R,m)	6,2
Plasma minor radius (a,m)	2,0
Plasma current (I_p,MA)	15
Plasma volume (m^3)	837
Plasma surface (m^2)	678
Current drive power (MW)	73

ITER's goal is to demonstrate the scientific and technical feasibility of fusion energy for peaceful purposes, which means to demonstrate moderate power amplification and extended burn of D-T plasmas, with steady-state as an ultimate goal and to perform testing of high heat flux and nuclear components [132].

A.4 PFC and related material questions

Structural materials of plasma facing components (PFCs) for future fusion reactors should withstand high heat flux (HHF) loads and energetic neutron irradiation. The ability to remove incident stationary heat fluxes of 10-20 MW/m^2 is the prime objective for the divertor component whereas reduced activation and mechanical stability under irradiation and high operation temperatures are the important concerns for the PFCs in general. It is obvious that the mechanical strength at elevated temperatures is one of the crucial criteria for the structural materials, as the PFCs will be subjected to considerable thermal stresses [2,3].

The heat sink materials have to exhibit a high thermal conductivity, needed for achieving an efficient heat transfer into the cooling system. In addition to thermal conductivity, other properties as tensile strength and ductility, fracture toughness, fatigue at high temperature and irradiation resistance have to be taken into consideration. Owing to its excellent thermal conductivity strengthened copper is a viable candidate for heat sink applications in the divertor of ITER. A selected number of precipitation hardened (PH) and dispersion strengthened (DS) copper alloys, which possess good thermal conductivity, stable elevated temperature strength and adequate resistance to irradiation damage are the choice for the heat sink of the high heat flux components in ITER.

As divertor heat sink material until now both the dispersion strengthened (DS) and the precipitation hardened (PH) Cu-alloys have been investigated to suppress the loss of strength at elevated temperatures [2,133-135]. According to the estimation in [122] based on the RCC-MR code, the PH copper alloys could be used for the PFCs up to 350 ^oC under the applied stress intensity of 100 MPa (however, PH Cu is not code qualified yet). On the other hand, the large coefficient of thermal expansion (CTE) of these alloys is detrimental to the strength of a joint component consisting of two or three materials bonded each other.

For the first wall and blanket structures of future reactors, so called reduced activation martensitic steels (RAMS) have been intensively developed in the last decade [3,136]. The service temperature of such steels like Eurofer is normally limited to 550 ^oC. Recently, there has been a research effort to develop the oxide dispersion strengthened (ODS) RAMS to improve the high-temperature strength [137]. It is expected that an increase of the service temperature by more than 100 ^oC can be achieved with the ODS RAMS compared to the plain RAMS. The higher service temperature of the first wall and blanket components will lead to an increased energy efficiency of a fusion power plant.

Compared to these candidate materials the fiber-reinforced metal matrix composites (FRMMCs) could become potential candidate materials for the PFC application, since the combination of different properties of fiber and matrix can lead to versatile performances of these materials. The can possess much higher ultimate strength, work hardening rate and creep resistance than the conventional PH or ODS alloys in a wide temperature range. The global yielding is usually increased by the fiber reinforcement. But the yield stress of a FRMMCs can be influenced by residual stresses. The ultimate load carrying capacity of such composites will depend either on the onset of unconstrained plastic flow of the matrix or on the overall fiber fracture. The elastic stiffness as well as the CTE can be tailored to some extent. This feature may be advantageous for a bond joint PFC, which consists of the plasma facing material being bonded to the heat sink, since the thermal mismatch stresses resulting from this material joining can be reduced. Permanent dimensional change by plastic ratcheting can be effectively suppressed. In addition, the FRMMCs can be introduced locally into the highly loaded regions of the PFCs.

A three dimensional model of the divertor is shown in Figure A.7. Due to erosion of the vertical target in the strike point region the divertor is considered a consumable. The divertor must therefore be possible to be replaced and upgraded in a relatively short time frame during the life of thermonuclear reactors. For this reason the ITER divertor is segmented into 60 cassettes which are introduced into the vessel through four remote maintenance posts [6]. The main parts of divertor is composed of cassettes bodies (CBs), inboard vertical target (IVT), outboard vertical target (OVT), dome, and liner.

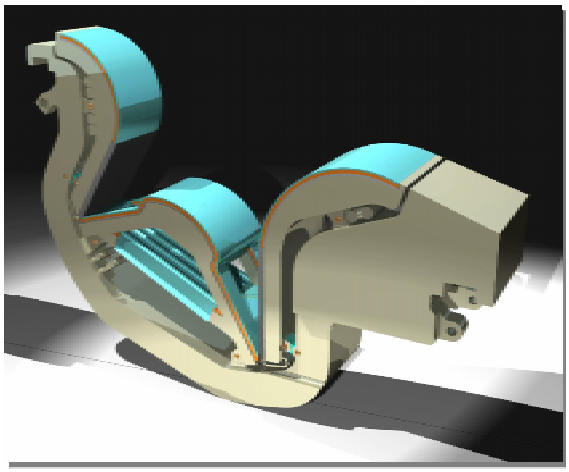

Figure A.7. Picture of the divertor of three dimensional model: the PFCs attachments and the cooling manifolds.

Figure A.8 shows a 600 mm medium scale vertical target prototype produced as part of the divertor large project. Tungsten tiles are mounted on the curved part whereas carbon is used on the flat region which would receive the higher heat flux. The material of heat sink was DS-Cu. This prototype was tested in the range of 10-20 MW/m^2 for more than 2000 cycles [5,138].

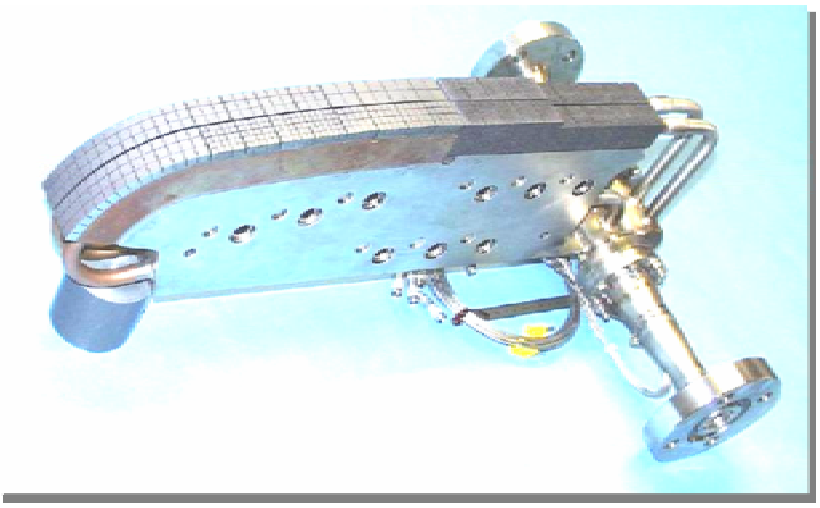

Figure A.8. CfC monoblock and W brush armored vertical target medium scale prototype manufactured by Plansee GmbH (EU).

Appendix B. CMat3D: Fortran Code for C-Matrix

```
C=======================================================================
C     PROGRAM : CMat3D
C=======================================================================

      IMPLICIT REAL*8(A-H,O-Z)
      DIMENSION X(2547),Y(2547),Z(2547),IJK(10000),
     1          NDFIX(2,1500)
      DATA LR,LL,LW,NDF,NODE,INTXY/123,124,125,3,8,8/
      OPEN(UNIT=LR,FILE='input-la20.dat',STATUS='OLD')
      OPEN(UNIT=LL,FILE='CMATRIX-la20.dat',status='unknown')
      OPEN(UNIT=LW,FILE='OUTPUT-la20.dat',status='unknown')
C     (READ THE FINITE ELEMENT MESH)
      NX=0
      NELX=0
      CALL HRMESH(NX,NELX,NODE,X,Y,Z,IJK,LR,LW)
C     (SET THE TOTAL NUMBER OF DEGREES OF FREEDOM)
      NEQ=NDF*NX
      CALL RBOUN1(NDFIX,VFIXED,SPRIN1,NDF,LFIX,LR,LW)
      CALL ASSEMC(IJK,X,Y,Z,NX,NELX,NEQ,NODE,NDF,LR,NDFIX,LFIX,LL,LW)
      STOP
      END

C-----------------------------------------------------------------------
      SUBROUTINE HRMESH(NX,NELX,NODE,X,Y,Z,IJK,LR,LW)
C-----------------------------------------------------------------------

      IMPLICIT REAL*8(A-H,O-Z)
      DIMENSION X(1),Y(1),Z(1),IJK(1),FLAG(10),IJKD(8)
      WRITE(LW,606)
  606 FORMAT(//10X,'----------- MODIFICATION/ADDITION OF NODES',
     1       ' AND ELEMENT CONNECTIVITIES -----------',//,10X,
     2       '< COORDINATES OF NODES >',/)
  598 FORMAT(10A8)
      READ(LR,*) NODADD,NELADD
  500 FORMAT(16I5)
      DO 106 I=1,NODADD
        READ(LR,*) N,X(N),Y(N),Z(N)
  502    FORMAT(I5,2F10.4)
         IF(N.GT.NX) NX=NX+1
        WRITE(LW,600) N,X(N),Y(N),Z(N),NX
  600    FORMAT(15X,'NODE ',I4,5X,'(  ',3F12.4,' )',5X,'NEW NX = ',I5)
  106 CONTINUE
      WRITE(LW,604)
  604 FORMAT(//10X,'< ELEMENT CONNECTIVITIES >',/)
      DO 100 I=1,NELADD
        READ(LR,*) NEL,MPE,(IJKD(J),J=1,NODE)    !!!!!!!!!!
        DO 102 J=1,NODE
  102    IJK(NODE*(NEL-1)+J)=IJKD(J)
  504    FORMAT(16I5)
         IF(NEL.GT.NELX) NELX=NELX+1
        WRITE(LW,602) NEL,(IJKD(J),J=1,NODE)
  602    FORMAT(15X,'NEL ',I5,5X,'<IJK>',20I5)
  100 CONTINUE
      RETURN
      END

C-----------------------------------------------------------------------
      SUBROUTINE RBOUN1(NDFIX,VFIXED,SPRING,NDF,LFIX,LR,LW)
C-----------------------------------------------------------------------

      IMPLICIT REAL*8(A-H,O-Z)
      DIMENSION FLAG(10),NDFIX(2,1),VFIXED(3,1)
      READ(LR,500) (FLAG(I),I=1,10)
  500 FORMAT(10A8)
      READ(LR,*) LFIX,SPRING
  502 FORMAT(I5,F20.5)
```

```
      DO 100 I=1,LFIX
        READ(LR,*) (NDFIX(J,I),J=1,2)
  100 CONTINUE
      WRITE(LW,600) SPRING
  600 FORMAT(/////10X,'-------- 1-ST BOUNDARY CONDITION --------',//
     1       15X,'SPRING CONSTANT = ',E10.3,//10X,50('-'),/10X,
     2       ' NODE I  KIND I         VALUE',/10X,50('-'))
      DO 102 I=1,LFIX
  102 WRITE(LW,602) (NDFIX(J,I),J=1,2)
  602 FORMAT(10X,I5,' I ',I5,' I ',3E10.3)
      WRITE(LW,604)
  604 FORMAT(10X,50('-'))
      RETURN
      END

C-----------------------------------------------------------------------
      SUBROUTINE ASSEMC(IJK,X,Y,Z,NX,NELX,NEQ,NODE,NDF,LR,NDFIX,
     1                  LFIX,LL,LW)
C-----------------------------------------------------------------------

      IMPLICIT REAL*8(A-H,O-Z)
      DIMENSION SC(10000,5000),NDFIX(2,1),X(1),Y(1),Z(1),IJK(1),SCE(8,24,6)
C     (CONSTUCT THE GLOBAL C MATRIX)
      DO 100 NEL=1,NELX
         CALL ESTIFC(NEL,SCE,IJK,X,Y,Z,NODE,NDF,LW)
         DO 200 IAA=1,8   ! NO. OF GAUSS POINT
           DO IA=1,NODE    ! NODE=8
              IJKIA=IJK(NODE*(NEL-1)+IA)
              DO I=1,NDF   ! NDF=3
                 NIAI=NDF*(IJKIA-1)+I
                 SC(NIAI,6*NEL-5)=SCE(IAA,NDF*(IA-1)+I,1)
                 SC(NIAI,6*NEL-4)=SCE(IAA,NDF*(IA-1)+I,2)
                 SC(NIAI,6*NEL-3)=SCE(IAA,NDF*(IA-1)+I,3)
                 SC(NIAI,6*NEL-2)=SCE(IAA,NDF*(IA-1)+I,4)
                 SC(NIAI,6*NEL-1)=SCE(IAA,NDF*(IA-1)+I,5)
                 SC(NIAI,6*NEL)  =SCE(IAA,NDF*(IA-1)+I,6)
               ENDDO
           ENDDO

C     APPLY KINEMATIC BOUNDARY CONDITION
             DO 1100 KJI=1,LFIX
                NNODE=NDFIX(1,KJI)
                NFIX2=NDFIX(2,KJI)
                DO 1100 JJ=1,NDF
                   IF(NFIX2.LT.10**(NDF-JJ)) GOTO 1100
                     NC=NDF*(NNODE-1)+JJ
                   DO KEL=1,6*NELX
                      SC(NC,KEL)=0.
                   ENDDO
              NFIX2=NFIX2-10**(NDF-JJ)
 1100         CONTINUE
      DO JJJ=1,NDF*NX    ! TOTAL NODE * NDF(3)
         DO KKK=1,6*NELX ! TOTAL ELEM * STRESS DIM.(X-,Y-,Z-,XY-,YZ-,ZX-)
            IF(SC(JJJ,KKK)) 1101,1102,1101
 1101         KKKK=(6*NELX)*(IAA-1)+KKK
      IF(JJJ.LT.10) THEN
        IF(KKKK.LT.10) THEN
           WRITE(LL,211) JJJ,KKKK,SC(JJJ,KKK)
        ELSEIF(KKKK.LT.100) THEN
           WRITE(LL,212) JJJ,KKKK,SC(JJJ,KKK)
        ELSEIF(KKKK.LT.1000) THEN
           WRITE(LL,213) JJJ,KKKK,SC(JJJ,KKK)
        ELSEIF(KKKK.LT.10000) THEN
           WRITE(LL,214) JJJ,KKKK,SC(JJJ,KKK)
        ELSE
           WRITE(LL,215) JJJ,KKKK,SC(JJJ,KKK)
        ENDIF
      GOTO 1102

      ELSEIF(JJJ.LT.100) THEN
        IF(KKKK.LT.10) THEN
```

```
         WRITE(LL,221) JJJ,KKKK,SC(JJJ,KKK)
       ELSEIF(KKKK.LT.100) THEN
         WRITE(LL,222) JJJ,KKKK,SC(JJJ,KKK)
       ELSEIF(KKKK.LT.1000) THEN
         WRITE(LL,223) JJJ,KKKK,SC(JJJ,KKK)
       ELSEIF(KKKK.LT.10000) THEN
         WRITE(LL,224) JJJ,KKKK,SC(JJJ,KKK)
       ELSE
         WRITE(LL,225) JJJ,KKKK,SC(JJJ,KKK)
       ENDIF
     GOTO 1102

     ELSEIF(JJJ.LT.1000) THEN
       IF(KKKK.LT.10) THEN
         WRITE(LL,231) JJJ,KKKK,SC(JJJ,KKK)
       ELSEIF(KKKK.LT.100) THEN
         WRITE(LL,232) JJJ,KKKK,SC(JJJ,KKK)
       ELSEIF(KKKK.LT.1000) THEN
         WRITE(LL,233) JJJ,KKKK,SC(JJJ,KKK)
       ELSEIF(KKKK.LT.10000) THEN
         WRITE(LL,234) JJJ,KKKK,SC(JJJ,KKK)
       ELSE
         WRITE(LL,235) JJJ,KKKK,SC(JJJ,KKK)
       ENDIF
     GOTO 1102

     ELSE
       IF(KKKK.LT.10) THEN
         WRITE(LL,241) JJJ,KKKK,SC(JJJ,KKK)
       ELSEIF(KKKK.LT.100) THEN
         WRITE(LL,242) JJJ,KKKK,SC(JJJ,KKK)
       ELSEIF(KKKK.LT.1000) THEN
         WRITE(LL,243) JJJ,KKKK,SC(JJJ,KKK)
       ELSEIF(KKKK.LT.10000) THEN
         WRITE(LL,244) JJJ,KKKK,SC(JJJ,KKK)
       ELSE
         WRITE(LL,245) JJJ,KKKK,SC(JJJ,KKK)
       ENDIF
     ENDIF
1102          CONTINUE
           ENDDO
        ENDDO
 200 CONTINUE
     DO IQ=1,NDF*NX
        DO IEQ=1,6*NEL
           SC(IQ,IEQ)=0.
        ENDDO
     ENDDO

 100 CONTINUE
 211 FORMAT(1X,'XE',1X,'z',I1,8X,'r',I1,8X,1X,E11.5)
 212 FORMAT(1X,'XE',1X,'z',I1,8X,'r',I2,7X,1X,E11.5)
 213 FORMAT(1X,'XE',1X,'z',I1,8X,'r',I3,6X,1X,E11.5)
 214 FORMAT(1X,'XE',1X,'z',I1,8X,'r',I4,5X,1X,E11.5)
 215 FORMAT(1X,'XE',1X,'z',I1,8X,'r',I5,4X,1X,E11.5)
 221 FORMAT(1X,'XE',1X,'z',I2,7X,'r',I1,8X,1X,E11.5)
 222 FORMAT(1X,'XE',1X,'z',I2,7X,'r',I2,7X,1X,E11.5)
 223 FORMAT(1X,'XE',1X,'z',I2,7X,'r',I3,6X,1X,E11.5)
 224 FORMAT(1X,'XE',1X,'z',I2,7X,'r',I4,5X,1X,E11.5)
 225 FORMAT(1X,'XE',1X,'z',I2,7X,'r',I5,4X,1X,E11.5)
 231 FORMAT(1X,'XE',1X,'z',I3,6X,'r',I1,8X,1X,E11.5)
 232 FORMAT(1X,'XE',1X,'z',I3,6X,'r',I2,7X,1X,E11.5)
 233 FORMAT(1X,'XE',1X,'z',I3,6X,'r',I3,6X,1X,E11.5)
 234 FORMAT(1X,'XE',1X,'z',I3,6X,'r',I4,5X,1X,E11.5)
 235 FORMAT(1X,'XE',1X,'z',I3,6X,'r',I5,4X,1X,E11.5)
 241 FORMAT(1X,'XE',1X,'z',I4,5X,'r',I1,8X,1X,E11.5)
 242 FORMAT(1X,'XE',1X,'z',I4,5X,'r',I2,7X,1X,E11.5)
 243 FORMAT(1X,'XE',1X,'z',I4,5X,'r',I3,6X,1X,E11.5)
 244 FORMAT(1X,'XE',1X,'z',I4,5X,'r',I4,5X,1X,E11.5)
 245 FORMAT(1X,'XE',1X,'z',I4,5X,'r',I5,4X,1X,E11.5)
     RETURN
```

```
      END

C-----------------------------------------------------------------------
      SUBROUTINE ESTIFC(NEL,SCE,IJK,X,Y,Z,NODE,NDF,LW)
C-----------------------------------------------------------------------

      IMPLICIT REAL*8(A-H,O-Z)
C     SCE(I,J,K) : TRANSPOSE SHAPE OF [B]*WX*WY*DET
C                  I : GAUSS POINT
C                  J : X-,Y- DIRECTION AT EACH NODE AT ELEMENT
C                  K : NO. OF STRESS DIRECTION (X-,Y-,XY-)

      DIMENSION SCE(8,24,6),XE(8,NDF),D(3,3,3,3),SH(8),GDN(8,NDF)
      DIMENSION X(1),Y(1),Z(1),IJK(1)
      DIMENSION GX(8),GY(8),GZ(8)

C     (SET THE INTEGRATION POINTS AND WEIGHTS)
      DATA GX/-0.577350269189626, 0.577350269189626,
     1         0.577350269189626,-0.577350269189626,
     2        -0.577350269189626, 0.577350269189626,
     3         0.577350269189626,-0.577350269189626/
      DATA GY/-0.577350269189626,-0.577350269189626,
     1         0.577350269189626, 0.577350269189626,
     2        -0.577350269189626,-0.577350269189626,
     3         0.577350269189626, 0.577350269189626/
      DATA GZ/-0.577350269189626,-0.577350269189626,
     1        -0.577350269189626,-0.577350269189626,
     2         0.577350269189626, 0.577350269189626,
     3         0.577350269189626, 0.577350269189626/
      DATA GW/1./
      DATA ITX,ITY,ITZ/2,2,2/

C     (COORDINATES)
      DO 102 I=1,NODE
         II=IJK(NODE*(NEL-1)+I)
      WRITE(LW,*) NEL,I,II,X(II),Y(II),Z(II)
         XE(I,1)=X(II)
         XE(I,2)=Y(II)
  102    XE(I,3)=Z(II)
      NODNDF=NDF*NODE
      DO 100 KKK=1,NODE
         XL=GX(KKK)
         WX=GW
         YL=GY(KKK)
         WY=GW
         ZL=GZ(KKK)
         WZ=GW

            CALL GGRAD8(NEL,XL,YL,ZL,SH,DET,GDN,XE,LW)
C     (COORDINATES OF THE INTEGRATION POINT)
            XIT=0.
           YIT=0.
           ZIT=0.
           DO 230 I=1,NODE
              XIT=XIT+XE(I,1)*SH(I)
               YIT=YIT+XE(I,2)*SH(I)
  230          ZIT=ZIT+XE(I,3)*SH(I)
      WRITE(LW,119)NEL,KKK,XIT,YIT,ZIT
  119 FORMAT(2I5,3F11.4)

C     (RESDUAL STRESS - C ELEMENT MATRIX)
      DO 108 IA=1,NODE
      GDN(IA,1)=GDN(IA,1)*WX*WY*WZ*DET
      GDN(IA,2)=GDN(IA,2)*WX*WY*WZ*DET
      GDN(IA,3)=GDN(IA,3)*WX*WY*WZ*DET
      SCE(KKK,3*IA-2,1)=GDN(IA,1)
      SCE(KKK,3*IA-2,2)=0.
      SCE(KKK,3*IA-2,3)=0.
      SCE(KKK,3*IA-2,4)=GDN(IA,2)
      SCE(KKK,3*IA-2,5)=0.
      SCE(KKK,3*IA-2,6)=GDN(IA,3)
```

```
      SCE(KKK,3*IA-1,1)=0.
      SCE(KKK,3*IA-1,2)=GDN(IA,2)
      SCE(KKK,3*IA-1,3)=0.
      SCE(KKK,3*IA-1,4)=GDN(IA,1)
      SCE(KKK,3*IA-1,5)=GDN(IA,3)
      SCE(KKK,3*IA-1,6)=0.
      SCE(KKK,3*IA,1)  =0.
      SCE(KKK,3*IA,2)  =0.
      SCE(KKK,3*IA,3)  =GDN(IA,3)
      SCE(KKK,3*IA,4)  =0.
      SCE(KKK,3*IA,5)  =GDN(IA,2)
      SCE(KKK,3*IA,6)  =GDN(IA,1)
  108 CONTINUE
  100 CONTINUE
      RETURN
      END

C-----------------------------------------------------------------------
      SUBROUTINE GGRAD8(NEL,XL,YL,ZL,SH,DET,GDN,XE,LW)
C-----------------------------------------------------------------------

      IMPLICIT REAL*8(A-H,O-Z)
      DIMENSION SH(8),GDN(8,3),DN(8,3),DJ(3,3),XE(8,3)
C     (SET THE SHAPE FUNCTIONS FOR THE 20-NODE ELEMENT)
      SH(1)=0.125*(1.-XL)*(1.-YL)*(1.-ZL)
      SH(5)=0.125*(1.-XL)*(1.-YL)*(1.+ZL)
      SH(4)=0.125*(1.-XL)*(1.+YL)*(1.-ZL)
      SH(8)=0.125*(1.-XL)*(1.+YL)*(1.+ZL)
      SH(2)=0.125*(1.+XL)*(1.-YL)*(1.-ZL)
      SH(6)=0.125*(1.+XL)*(1.-YL)*(1.+ZL)
      SH(3)=0.125*(1.+XL)*(1.+YL)*(1.-ZL)
      SH(7)=0.125*(1.+XL)*(1.+YL)*(1.+ZL)

      DN(1,1)=-0.125*(1.-YL)*(1.-ZL)
      DN(5,1)=-0.125*(1.-YL)*(1.+ZL)
      DN(4,1)=-0.125*(1.+YL)*(1.-ZL)
      DN(8,1)=-0.125*(1.+YL)*(1.+ZL)
      DN(2,1)= 0.125*(1.-YL)*(1.-ZL)
      DN(6,1)= 0.125*(1.-YL)*(1.+ZL)
      DN(3,1)= 0.125*(1.+YL)*(1.-ZL)
      DN(7,1)= 0.125*(1.+YL)*(1.+ZL)

      DN(1,2)=-0.125*(1.-XL)*(1.-ZL)
      DN(5,2)=-0.125*(1.-XL)*(1.+ZL)
      DN(4,2)= 0.125*(1.-XL)*(1.-ZL)
      DN(8,2)= 0.125*(1.-XL)*(1.+ZL)
      DN(2,2)=-0.125*(1.+XL)*(1.-ZL)
      DN(6,2)=-0.125*(1.+XL)*(1.+ZL)
      DN(3,2)= 0.125*(1.+XL)*(1.-ZL)
      DN(7,2)= 0.125*(1.+XL)*(1.+ZL)

      DN(1,3)=-0.125*(1.-XL)*(1.-YL)
      DN(5,3)= 0.125*(1.-XL)*(1.-YL)
      DN(4,3)=-0.125*(1.-XL)*(1.+YL)
      DN(8,3)= 0.125*(1.-XL)*(1.+YL)
      DN(2,3)=-0.125*(1.+XL)*(1.-YL)
      DN(6,3)= 0.125*(1.+XL)*(1.-YL)
      DN(3,3)=-0.125*(1.+XL)*(1.+YL)
      DN(7,3)= 0.125*(1.+XL)*(1.+YL)

C     (COMPUTE THE JACBIAN MATRIX)
      DO 200 I=1,3
         DO 200 J=1,3
            DJIJ=0.
            DO 202 IA=1,8
  202       DJIJ=DJIJ+XE(IA,J)*DN(IA,I)
  200          DJ(I,J)=DJIJ

C     DETERMINANT OF DJ(I,J)
      DET=DJ(1,1)*DJ(2,2)*DJ(3,3)+DJ(1,2)*DJ(2,3)*DJ(3,1)
     1   +DJ(1,3)*DJ(2,1)*DJ(3,2)-DJ(1,1)*DJ(2,3)*DJ(3,2)
```

```
     2   -DJ(1,2)*DJ(2,1)*DJ(3,3)-DJ(1,3)*DJ(2,2)*DJ(3,1)
      WRITE(125,*) 'DET',DET
      IF(DET.LE.0.) GOTO 110

C     INVERSE MATRIX OF DJ(I,J)
      CALL INVERSE(DJ)
C     (GLOBAL GRADIENT OF THE SHAPE FUNCTIONS)
      DO 204 IA=1,8
      GDN(IA,1)=DJ(1,1)*DN(IA,1)+DJ(1,2)*DN(IA,2)+DJ(1,3)*DN(IA,3)
      GDN(IA,2)=DJ(2,1)*DN(IA,1)+DJ(2,2)*DN(IA,2)+DJ(2,3)*DN(IA,3)
  204 GDN(IA,3)=DJ(3,1)*DN(IA,1)+DJ(3,2)*DN(IA,2)+DJ(3,3)*DN(IA,3)
      RETURN
  110 WRITE(LW,600) NEL,XL,YL,ZL
  600 FORMAT(/////2X,'STOP STOP ! THE DETERMINANT BECOMES ZERO',/
     1       /10X,'ELEMENT  ',I4,5X,'(',3F10.4,')')
      STOP
      END

C-----------------------------------------------------------------------
      SUBROUTINE INVERSE(DJ)
C-----------------------------------------------------------------------

      IMPLICIT REAL*8(A-H,O-Z)
      DIMENSION DJ(3,3),Y(3,3),INDX(3)
      DO I=1,3
         DO J=1,3
            Y(I,J)=0.
         ENDDO
         Y(I,I)=1.
      ENDDO

      CALL LUDCMP(DJ,3,3,INDX,D)
      DO J=1,3
         CALL LUBKSB(DJ,3,3,INDX,Y(1,J))
      ENDDO
      DO I=1,3
         DO J=1,3
            DJ(I,J)=Y(I,J)
         ENDDO
      ENDDO
      RETURN
      END

C-----------------------------------------------------------------------
      SUBROUTINE LUDCMP(A,N,NP,INDX,D)
C-----------------------------------------------------------------------

      IMPLICIT REAL*8(A-H,O-Z)
      DIMENSION A(3,3),INDX(3),VV(3)
      PARAMETER (NMAX=500, TINY=1.0E-20)
      D=1.
      DO I=1,N
         AAMAX=0.
         DO J=1,N
            IF(ABS(A(I,J)).GT.AAMAX) AAMAX=ABS(A(I,J))
         ENDDO
         VV(I)=1./AAMAX
      ENDDO

      DO J=1,N
         DO I=1,J-1
            SUM=A(I,J)
            DO K=1,I-1
               SUM=SUM-A(I,K)*A(K,J)
            ENDDO
            A(I,J)=SUM
         ENDDO
         AAMAX=0.
         DO I=J,N
            SUM=A(I,J)
            DO K=1,J-1
```

```
               SUM=SUM-A(I,K)*A(K,J)
             ENDDO
             A(I,J)=SUM
             DUM=VV(I)*ABS(SUM)
             IF (DUM.GE.AAMAX) THEN
                IMAX=I
                AAMAX=DUM
             ENDIF
          ENDDO
          IF(J.NE.IMAX) THEN
            DO K=1,N
               DUM=A(IMAX,K)
               A(IMAX,K)=A(J,K)
               A(J,K)=DUM
            ENDDO
            D=-D
            VV(IMAX)=VV(J)
          ENDIF
          INDX(J)=IMAX
          IF(A(J,J).EQ.0.) A(J,J)=TINY
          IF(J.NE.N) THEN
            DUM=1./A(J,J)
            DO I=J+1,N
               A(I,J)=A(I,J)*DUM
            ENDDO
          ENDIF
       ENDDO
       RETURN
       END

C-----------------------------------------------------------------------
       SUBROUTINE LUBKSB(A,N,NP,INDX,B)
C-----------------------------------------------------------------------

       IMPLICIT REAL*8(A-H,O-Z)
       DIMENSION A(3,3),B(3),INDX(3)
       II=0
       DO I=1,N
          LL=INDX(I)
          SUM=B(LL)
          B(LL)=B(I)
          IF(II.NE.0) THEN
            DO J=II,I-1
               SUM=SUM-A(I,J)*B(J)
            ENDDO
          ELSEIF(SUM.NE.0) THEN
            II=I
          ENDIF
          B(I)=SUM
       ENDDO
       DO I=N,1,-1
          SUM=B(I)
          DO J=I+1,N
             SUM=SUM-A(I,J)*B(J)
          ENDDO
          B(I)=SUM/A(I,I)
       ENDDO
       RETURN
       END
```

Appendix C. An Example of Standard Input File (SIF)

```
* model with two quadrilateral elements (six nodes)
* two-independent loading > four loading corners (s,x,y,j)

* code explanation
* DO: Do command (same with Fotran)
* EV: Elemental Variable
* EP: Elemental Parameter
* FR: Bounds section
* IA: Integer type and + operator
* IE: Integer type and = operator
* IM: Integer type and × operator
* I-: Integer type and - operator
* OD: Termination of Do command (same with enddo in Fortran)
* RD: Real type and / operator
* RE: Real type and = operator
* RM: Real type and × operator
* R-: Real type and - operator
* X : Code for definition of parameter
* XE: Constraint (≤ constant)
* XL: Bounded below by the value (Lower)
* XN: Objective function
* XP: Unbounded above (Plus infinity)
* XT: an Array of group and
* XV: an Array of group and Variable
* ZE: an Array of group and = opertor
* ZP: an Array of group and Paramater
* ZV: an Array of group and Variable


NAME          shake

* main variables

 IE NGAUSS              8
 IM NG*3      NGAUSS    3
 IE 1                   1
 RE Null                0.0d0

* ELASTIC STRESSES   STEP 1 (SigX=100, SigY=100)

 RE s1                   0.10000E+03
 RE s2                   0.10000E+03
 RE s3                   0.00000E+00
 RE s7                   0.10000E+03
 RE s8                   0.10000E+03
 RE s9                   0.00000E+00
 RE s13                  0.10000E+03
 RE s14                  0.10000E+03
 RE s15                  0.00000E+00
 RE s19                  0.10000E+03
 RE s20                  0.10000E+03
 RE s21                  0.00000E+00
 RE s4                   0.10000E+03
 RE s5                   0.10000E+03
 RE s6                   0.00000E+00
 RE s10                  0.10000E+03
 RE s11                  0.10000E+03
 RE s12                  0.00000E+00
 RE s16                  0.10000E+03
 RE s17                  0.10000E+03
 RE s18                  0.00000E+00
 RE s22                  0.10000E+03
 RE s23                  0.10000E+03
 RE s24                  0.00000E+00
```

```
* ELASTIC STRESSES   STEP 2 (SigX=100, SigY=0)

 RE x1                    0.10000E+03
 RE x2                    0.00000E+00
 RE x3                    0.00000E+00
 RE x7                    0.10000E+03
 RE x8                    0.00000E+00
 RE x9                    0.00000E+00
 RE x13                   0.10000E+03
 RE x14                   0.00000E+00
 RE x15                   0.00000E+00
 RE x19                   0.10000E+03
 RE x20                   0.00000E+00
 RE x21                   0.00000E+00
 RE x4                    0.10000E+03
 RE x5                    0.00000E+00
 RE x6                    0.00000E+00
 RE x10                   0.10000E+03
 RE x11                   0.00000E+00
 RE x12                   0.00000E+00
 RE x16                   0.10000E+03
 RE x17                   0.00000E+00
 RE x18                   0.00000E+00
 RE x22                   0.10000E+03
 RE x23                   0.00000E+00
 RE x24                   0.00000E+00

* ELASTIC STRESSES   STEP 3 (SigX=0, SigY=100)

 RE y1                    0.00000E+00
 RE y2                    0.10000E+03
 RE y3                    0.00000E+00
 RE y7                    0.00000E+00
 RE y8                    0.10000E+03
 RE y9                    0.00000E+00
 RE y13                   0.00000E+00
 RE y14                   0.10000E+03
 RE y15                   0.00000E+00
 RE y19                   0.00000E+00
 RE y20                   0.10000E+03
 RE y21                   0.00000E+00
 RE y4                    0.00000E+00
 RE y5                    0.10000E+03
 RE y6                    0.00000E+00
 RE y10                   0.00000E+00
 RE y11                   0.10000E+03
 RE y12                   0.00000E+00
 RE y16                   0.00000E+00
 RE y17                   0.10000E+03
 RE y18                   0.00000E+00
 RE y22                   0.00000E+00
 RE y23                   0.10000E+03
 RE y24                   0.00000E+00

* ELASTIC STRESSES   STEP 4 (SigX=0, SigY=0)

 RE j1                    0.00000E+00
 RE j2                    0.00000E+00
 RE j3                    0.00000E+00
 RE j7                    0.00000E+00
 RE j8                    0.00000E+00
 RE j9                    0.00000E+00
 RE j13                   0.00000E+00
 RE j14                   0.00000E+00
 RE j15                   0.00000E+00
 RE j19                   0.00000E+00
 RE j20                   0.00000E+00
 RE j21                   0.00000E+00
 RE j4                    0.00000E+00
 RE j5                    0.00000E+00
```

```
 RE j6                  0.00000E+00
 RE j10                 0.00000E+00
 RE j11                 0.00000E+00
 RE j12                 0.00000E+00
 RE j16                 0.00000E+00
 RE j17                 0.00000E+00
 RE j18                 0.00000E+00
 RE j22                 0.00000E+00
 RE j23                 0.00000E+00
 RE j24                 0.00000E+00

* YIELD STRESS

 RE SY                  280
 R* SYQ       SY                        SY
 RD 1/SYQ     SYQ       1.0
 RM 3/SYQ     1/SYQ     3.0
 RM M/SYQ     1/SYQ     -1.0

VARIABLES

    alpha
 DO i         1                         NG*3
 X  r(i)
 OD i

GROUPS

* Object function: F = alpha
 XN max       alpha     -1.0

* Inequalities by yield-functions

 DO i         1                         NGAUSS
 XL a(i)
 OD i
 DO i         1                         NGAUSS
 XL c(i)
 OD i
 DO i         1                         NGAUSS
 XL d(i)
 OD i
 DO i         1                         NGAUSS
 XL e(i)
 OD i

* CONTRAINTS BY THE C-MATRIX

 XE z3        r1        0.19717E+00
 XE z3        r3        -.52831E-01
 XE z3        r4        -.19717E+00
 XE z3        r6        -.19717E+00
 XE z3        r7        0.52831E-01
 XE z3        r9        -.52831E-01
 XE z3        r10       -.52831E-01
 XE z3        r12       -.19717E+00
 XE z3        r13       0.19717E+00
 XE z3        r15       -.19717E+00
 XE z3        r16       -.19717E+00
 XE z3        r18       -.52831E-01
 XE z3        r19       0.52831E-01
 XE z3        r21       -.19717E+00
 XE z3        r22       -.52831E-01
 XE z3        r24       -.52831E-01
 XE z5        r4        0.19717E+00
 XE z5        r6        -.52831E-01
 XE z5        r10       0.52831E-01
 XE z5        r12       -.52831E-01
 XE z5        r16       0.19717E+00
 XE z5        r18       -.19717E+00
 XE z5        r22       0.52831E-01
```

```
 XE z5        r24        -.19717E+00
 XE z8        r2         0.19717E+00
 XE z8        r3         -.52831E-01
 XE z8        r8         0.19717E+00
 XE z8        r9         -.19717E+00
 XE z8        r14        0.52831E-01
 XE z8        r15        -.52831E-01
 XE z8        r20        0.52831E-01
 XE z8        r21        -.19717E+00
 XE z9        r1         0.52831E-01
 XE z9        r3         0.52831E-01
 XE z9        r4         -.52831E-01
 XE z9        r6         0.19717E+00
 XE z9        r7         0.19717E+00
 XE z9        r9         0.52831E-01
 XE z9        r10        -.19717E+00
 XE z9        r12        0.19717E+00
 XE z9        r13        0.52831E-01
 XE z9        r15        0.19717E+00
 XE z9        r16        -.52831E-01
 XE z9        r18        0.52831E-01
 XE z9        r19        0.19717E+00
 XE z9        r21        0.19717E+00
 XE z9        r22        -.19717E+00
 XE z9        r24        0.52831E-01
 XE z10       r2         0.52831E-01
 XE z10       r3         0.52831E-01
 XE z10       r5         0.19717E+00
 XE z10       r6         -.52831E-01
 XE z10       r8         0.52831E-01
 XE z10       r9         0.19717E+00
 XE z10       r11        0.19717E+00
 XE z10       r12        -.19717E+00
 XE z10       r14        0.19717E+00
 XE z10       r15        0.52831E-01
 XE z10       r17        0.52831E-01
 XE z10       r18        -.52831E-01
 XE z10       r20        0.19717E+00
 XE z10       r21        0.19717E+00
 XE z10       r23        0.52831E-01
 XE z10       r24        -.19717E+00
 XE z11       r4         0.52831E-01
 XE z11       r6         0.52831E-01
 XE z11       r10        0.19717E+00
 XE z11       r12        0.52831E-01
 XE z11       r16        0.52831E-01
 XE z11       r18        0.19717E+00
 XE z11       r22        0.19717E+00
 XE z11       r24        0.19717E+00
 XE z12       r5         0.52831E-01
 XE z12       r6         0.52831E-01
 XE z12       r11        0.52831E-01
 XE z12       r12        0.19717E+00
 XE z12       r17        0.19717E+00
 XE z12       r18        0.52831E-01
 XE z12       r23        0.19717E+00
 XE z12       r24        0.19717E+00

CONSTANTS

* Right hand side of the inequalities
 DO i         1                        NGAUSS
 X  shake     a(i)       1.
 OD i
 DO i         1                        NGAUSS
 X  shake     c(i)       1.
 OD i
 DO i         1                        NGAUSS
 X  shake     d(i)       1.
 OD i
 DO i         1                        NGAUSS
```

```
 X  shake     e(i)       1.
 OD i

BOUNDS

* The residual stresses are free while alpha is limited with alpha > 0
 FR shake     'DEFAULT'
 XL shake     alpha     0.0

START POINT

* Initial estimation, Give elastic solution at the beginning
 XV shake     alpha       .48342E+00

ELEMENT TYPE

 EV GSQ       al
 EV GSQ       rho1
 EV GSQ       rho2
 EP GSQ       sig1
 EP GSQ       sig2
 EV HSQ       al
 EV HSQ       rho1
 EV HSQ       rho2
 EP HSQ       sig1
 EP HSQ       sig2

* Non linear element containing shear stresses

 EV SSQ       al
 EV SSQ       rho
 EP SSQ       a
 EP SSQ       b
 EP SSQ       tau

ELEMENT USES

* Define for each Gaussian-Point three nonlinear  elements

 DO i         1                         NGAUSS

 I- i-1       i                         1
 IM 3[i-1]    i-1       3
 IA pos1      3[i-1]    1
 IA pos2      3[i-1]    2
 IA pos3      3[i-1]    3

 XT t(pos1)   HSQ
 ZV t(pos1)   al                        alpha
 ZV t(pos1)   rho1                      r(pos1)
 ZV t(pos1)   rho2                      r(pos2)
 ZP t(pos1)   sig1                      s(pos1)
 ZP t(pos1)   sig2                      s(pos2)

 XT t(pos2)   GSQ
 ZV t(pos2)   al                        alpha
 ZV t(pos2)   rho1                      r(pos1)
 ZV t(pos2)   rho2                      r(pos2)
 ZP t(pos2)   sig1                      s(pos1)
 ZP t(pos2)   sig2                      s(pos2)

 XT t(pos3)   SSQ
 ZV t(pos3)   al                        alpha
 ZV t(pos3)   rho                       r(pos3)
 ZP t(pos3)   tau                       s(pos3)
 XP t(pos3)   a          0.
 XP t(pos3)   b          0.

 XT v(pos1)   HSQ
 ZV v(pos1)   al                        alpha
 ZV v(pos1)   rho1                      r(pos1)
```

```
 ZV v(pos1)   rho2                      r(pos2)
 ZP v(pos1)   sig1                      x(pos1)
 ZP v(pos1)   sig2                      x(pos2)

 XT v(pos2)   GSQ
 ZV v(pos2)   al                        alpha
 ZV v(pos2)   rho1                      r(pos1)
 ZV v(pos2)   rho2                      r(pos2)
 ZP v(pos2)   sig1                      x(pos1)
 ZP v(pos2)   sig2                      x(pos2)

 XT v(pos3)   SSQ
 ZV v(pos3)   al                        alpha
 ZV v(pos3)   rho                       r(pos3)
 ZP v(pos3)   tau                       x(pos3)
 XP v(pos3)   a          0.0
 XP v(pos3)   b          0.0

 XT w(pos1)   HSQ
 ZV w(pos1)   al                        alpha
 ZV w(pos1)   rho1                      r(pos1)
 ZV w(pos1)   rho2                      r(pos2)
 ZP w(pos1)   sig1                      y(pos1)
 ZP w(pos1)   sig2                      y(pos2)

 XT w(pos2)   GSQ
 ZV w(pos2)   al                        alpha
 ZV w(pos2)   rho1                      r(pos1)
 ZV w(pos2)   rho2                      r(pos2)
 ZP w(pos2)   sig1                      y(pos1)
 ZP w(pos2)   sig2                      y(pos2)

 XT w(pos3)   SSQ
 ZV w(pos3)   al                        alpha
 ZV w(pos3)   rho                       r(pos3)
 ZP w(pos3)   tau                       y(pos3)
 XP w(pos3)   a          0.0
 XP w(pos3)   b          0.0

 XT n(pos1)   HSQ
 ZV n(pos1)   al                        alpha
 ZV n(pos1)   rho1                      r(pos1)
 ZV n(pos1)   rho2                      r(pos2)
 ZP n(pos1)   sig1                      j(pos1)
 ZP n(pos1)   sig2                      j(pos2)

 XT n(pos2)   GSQ
 ZV n(pos2)   al                        alpha
 ZV n(pos2)   rho1                      r(pos1)
 ZV n(pos2)   rho2                      r(pos2)
 ZP n(pos2)   sig1                      j(pos1)
 ZP n(pos2)   sig2                      j(pos2)

 XT n(pos3)   SSQ
 ZV n(pos3)   al                        alpha
 ZV n(pos3)   rho                       r(pos3)
 ZP n(pos3)   tau                       j(pos3)
 XP n(pos3)   a          0.0
 XP n(pos3)   b          0.0

 OD i

GROUP USES

* Combine the nonlinear elements to inequalities

 DO i         1                         NGAUSS
 I- i-1       i                         1
 IM 3[i-1]    i-1        3
 IA pos1      3[i-1]     1
 IA pos2      3[i-1]     2
```

```
 IA pos3      3[i-1]    3

 ZE a(i)      t(pos1)                 1/SYQ
 ZE a(i)      t(pos2)                 M/SYQ
 ZE a(i)      t(pos3)                 3/SYQ
 ZE c(i)      v(pos1)                 1/SYQ
 ZE c(i)      v(pos2)                 M/SYQ
 ZE c(i)      v(pos3)                 3/SYQ
 ZE d(i)      w(pos1)                 1/SYQ
 ZE d(i)      w(pos2)                 M/SYQ
 ZE d(i)      w(pos3)                 3/SYQ
 ZE e(i)      n(pos1)                 1/SYQ
 ZE e(i)      n(pos2)                 M/SYQ
 ZE e(i)      n(pos3)                 3/SYQ
 OD i

ENDATA


ELEMENTS      shake

* code definition
* A: the name of Auxiliary parameter
* F: nonlinear element Function
* G: Gradient of nonlinear element
* H: Hessian matrix of the nonlinear element
* R: Transformation between the elemental and internal variables
* T: new element Type


TEMPORARIES
 R  Term1
 R  Term2
 R  Term3
 R  Term4
 R  Term5
 R  Term6

INDIVIDUALS
 T  SSQ
 A  Term1              tau*al+rho
 A  Term2              Term1+Term1
 A  Term3              2.0d0*tau
 A  Term4              a+b*al

 F                     Term1*Term1-Term4*Term4/3.0d0
 G  al                 Term2*tau-2.0d0/3.0d0*b*Term4
 G  rho                Term2
 H  al        al       Term3*tau-2.0d0/3.0d0*b*b
 H  al        rho      Term3
 H  rho       rho      2.0d0
 T  GSQ
 A  Term1              al*sig1+rho1
 A  Term2              al*sig2+rho2

 F                     Term1*Term2
 G  al                 sig1*Term2+sig2*Term1
 G  rho1               Term2
 G  rho2               Term1
 H  al        al       2.0d0*sig1*sig2
 H  al        rho1     sig2
 H  al        rho2     sig1
 H  rho1      rho1     0.0d0
 H  rho1      rho2     1.0d0
 H  rho2      rho2     0.0d0
 T  HSQ
 A  Term1              al*sig1+rho1
 A  Term2              al*sig2+rho2

 F                     Term1*Term1+Term2*Term2
 G  al                 2.0d0*Term1*sig1+2.0d0*Term2*sig2
```

```
 G  rho1                2.0d0*Term1
 G  rho2                2.0d0*Term2
 H  al         al       2.0d0*(sig1*sig1+sig2*sig2)
 H  al         rho1     2.0d0*sig1
 H  al         rho2     2.0d0*sig2
 H  rho1       rho1     2.0d0
 H  rho1       rho2     0.0d0
 H  rho2       rho2     2.0d0

ENDATA
```

Appendix D. Shakedown Limits in Cooling

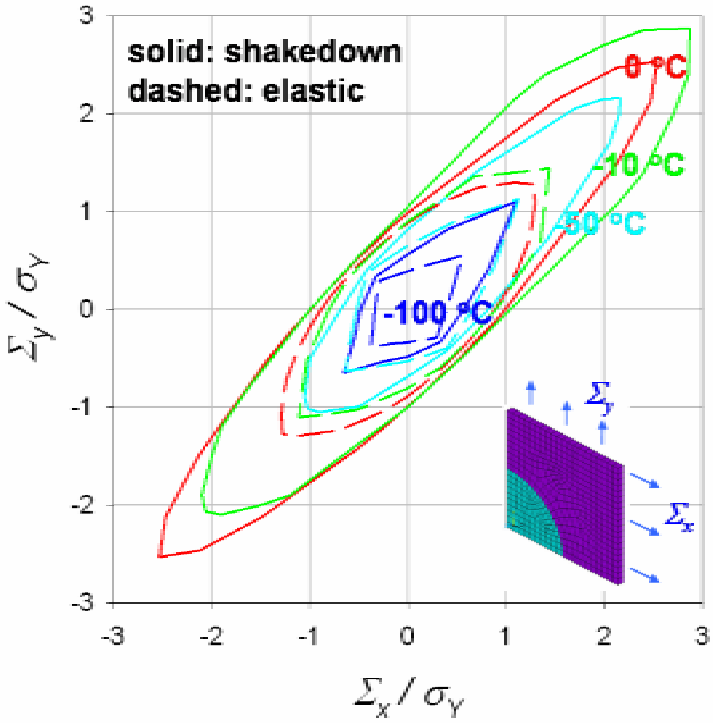

Figure D.1. Elastic limits and shakedown limits of lamina with 20 % of fiber volume fraction in in-plane biaxial loading space (3D analysis): -10, -50, and -100 °C indicate the temperature decrease (cooling).

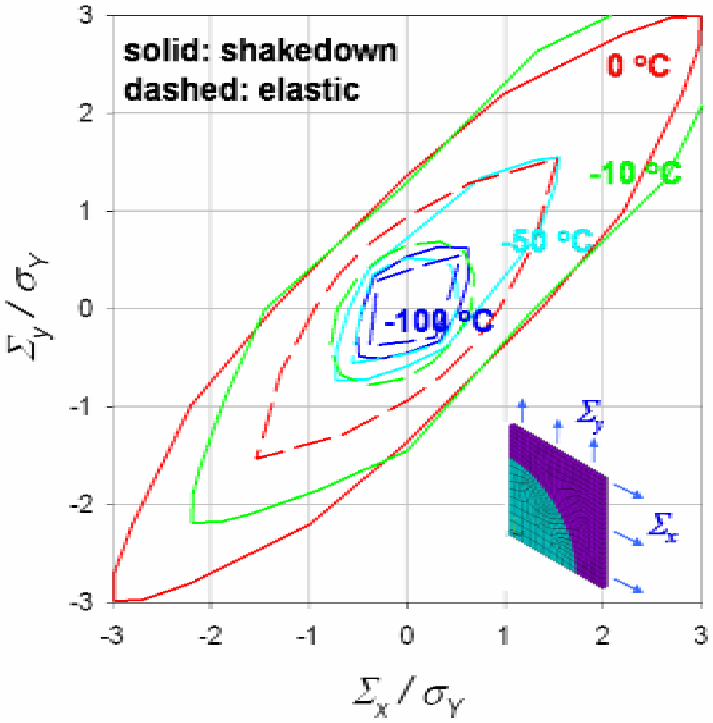

Figure D.2. Elastic limits and shakedown limits of lamina with 40 % of fiber volume fraction in in-plane biaxial loading space (3D analysis): 10, -50, and -100 °C indicate the temperature decrease (cooling).

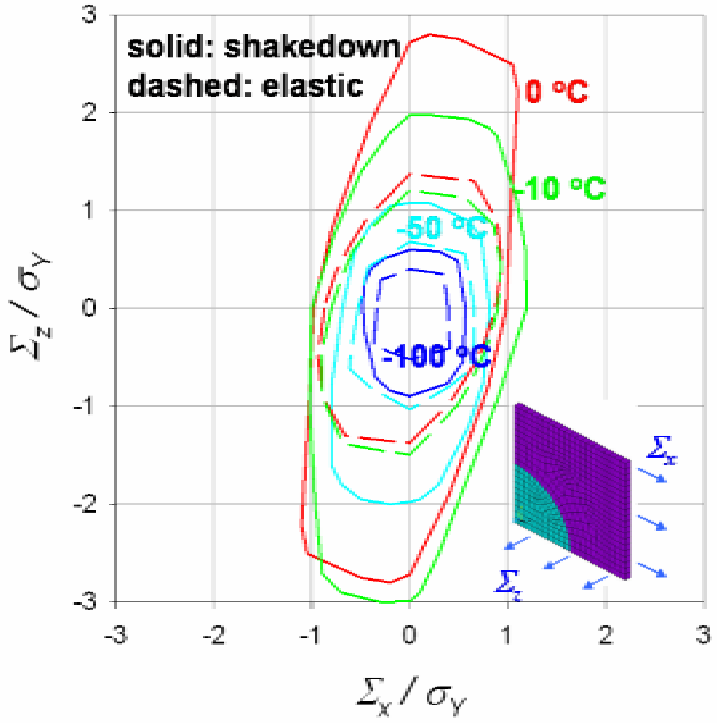

Figure D.3. Elastic limits and shakedown limits of lamina with 20 % of fiber volume fraction in out-of-plane biaxial loading space (3D analysis): 10, -50, and -100 ^{o}C indicate the temperature decrease (cooling).

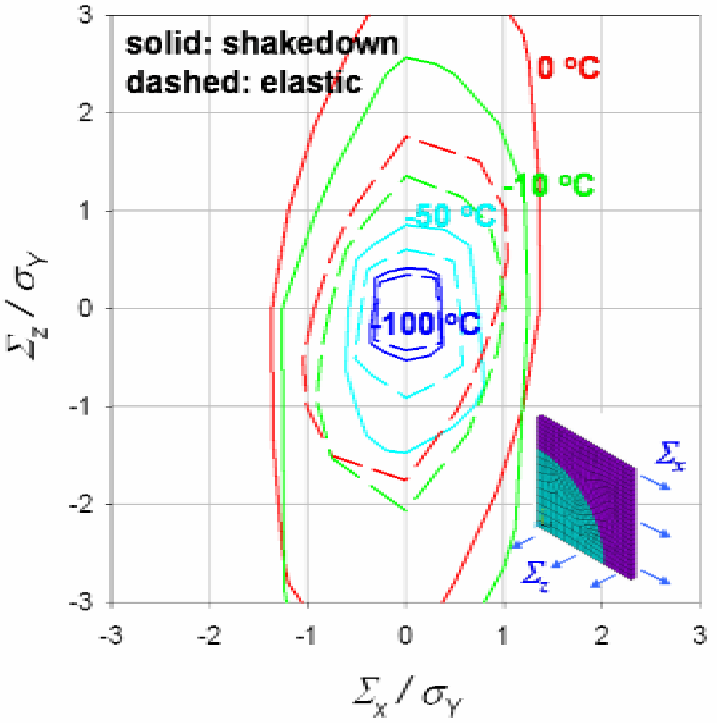

Figure D.4. Elastic limits and shakedown limits of lamina with 40 % of fiber volume fraction in out-of-plane biaxial loading space (3D analysis): 10, -50, and -100 ^{o}C indicate the temperature decrease (cooling).

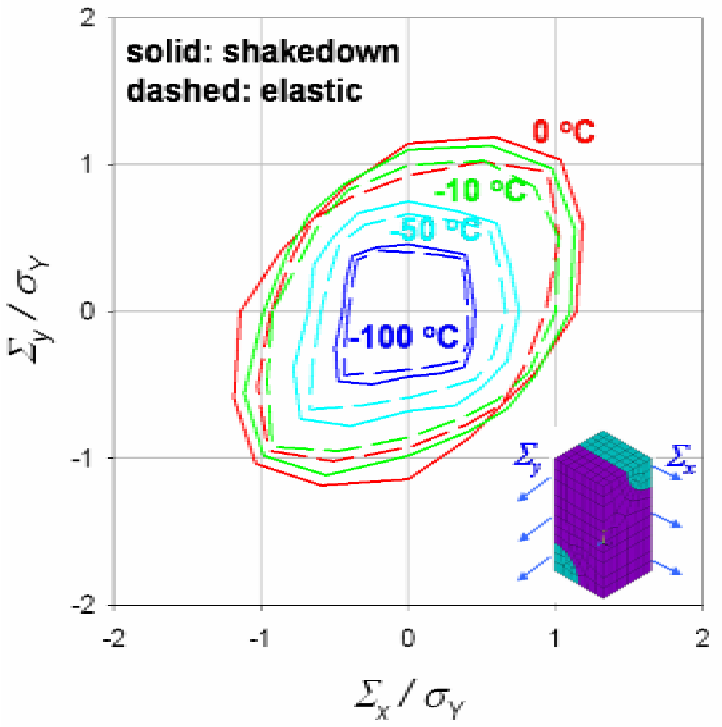

Figure D.5. Elastic limits and shakedown limits of laminate with 20 % of fiber volume fraction in in-plane biaxial loading space (3D analysis): 10, -50, and -100 ^{o}C indicate the temperature decrease (cooling).

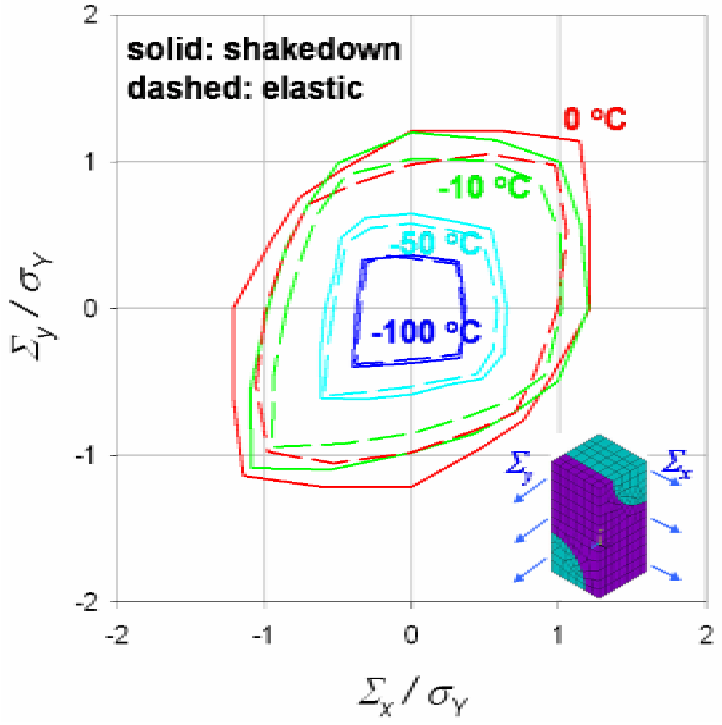

Figure D.6. Elastic limits and shakedown limits of laminate with 40 % of fiber volume fraction in in-plane biaxial loading space (3D analysis): 10, -50, and -100 ^{o}C indicate the temperature decrease (cooling).

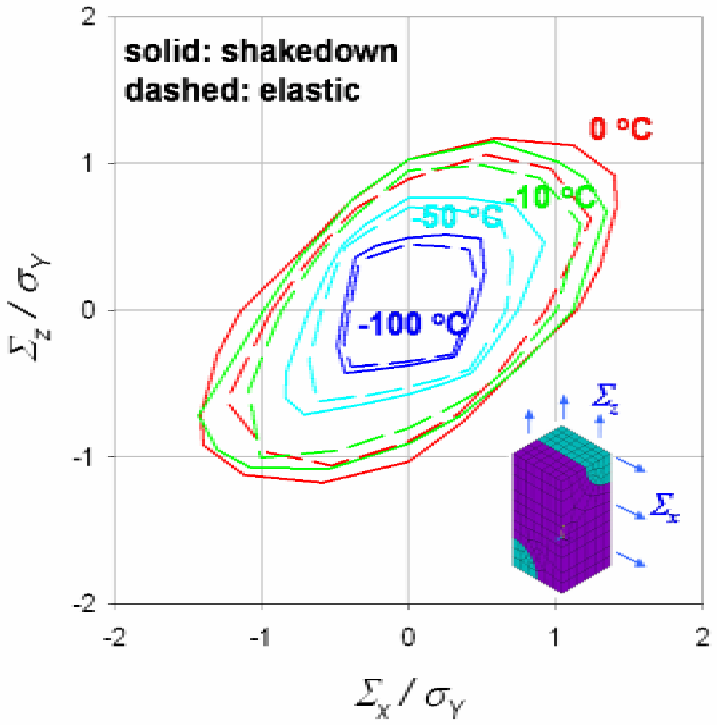

Figure D.7. Elastic limits and shakedown limits of laminate with 20 % of fiber volume fraction in out-of-plane biaxial loading space (3D analysis): 10, -50, and -100 ^{o}C indicate the temperature decrease (cooling).

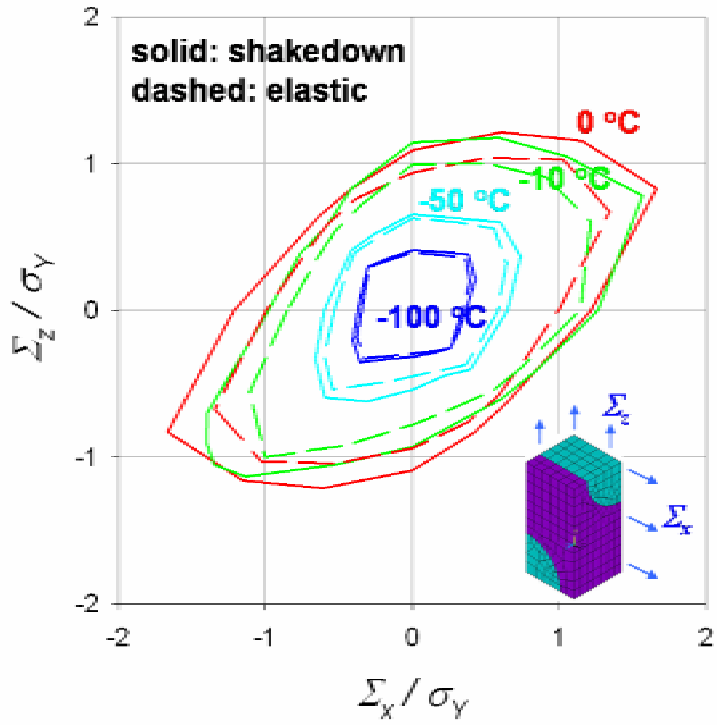

Figure D.8. Elastic limits and shakedown limits of laminate with 40 % of fiber volume fraction in out-of-plane biaxial loading space (3D analysis): 10, -50, and -100 ^{o}C indicate the temperature decrease (cooling).

Appendix E. Shakedown Limits and Loading Paths

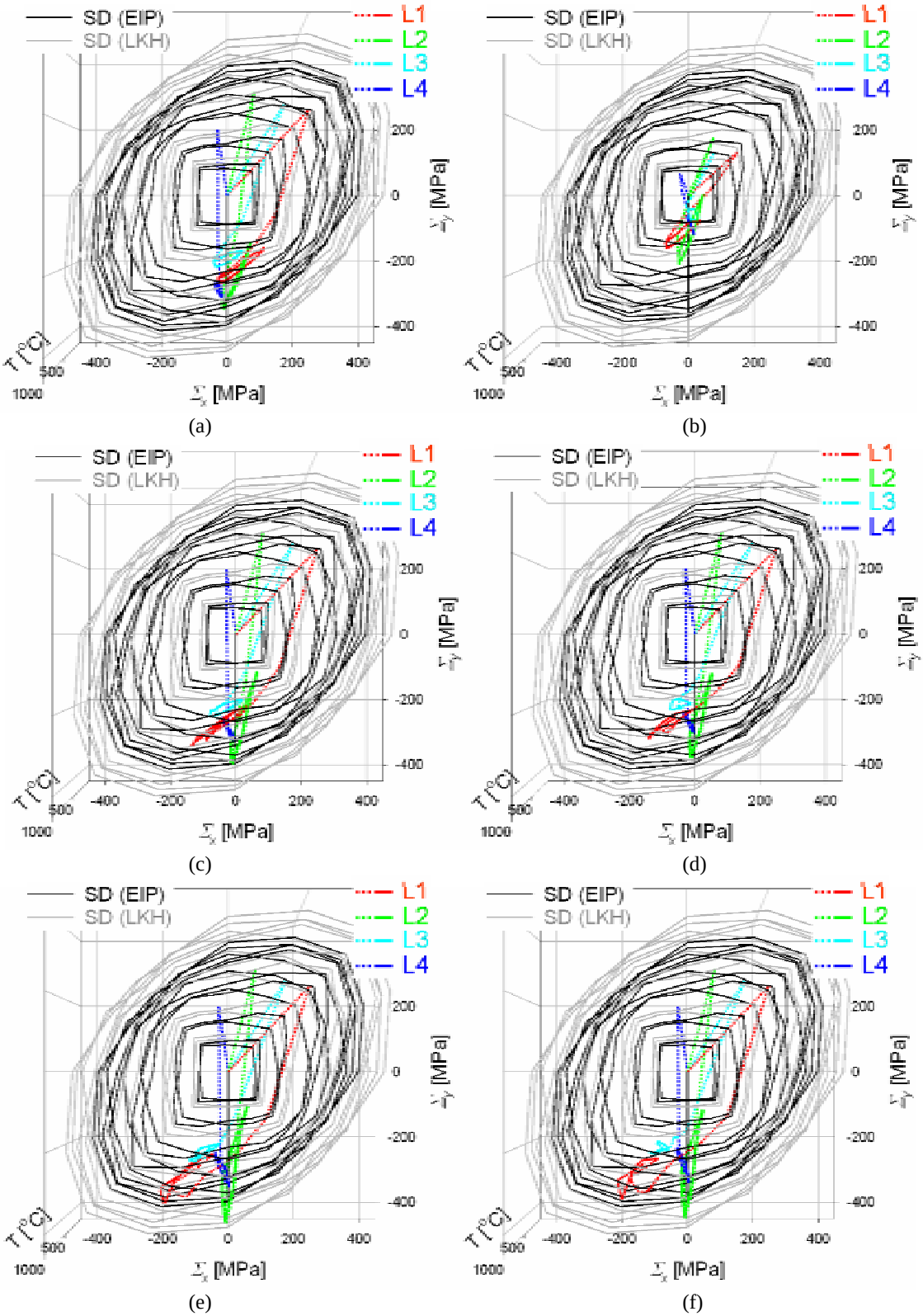

Figure E.1. Shakedown limits and thermomechanical loading paths in two-dimensional loading space (Σ_x, Σ_y): Additional view from Figure 7.3.

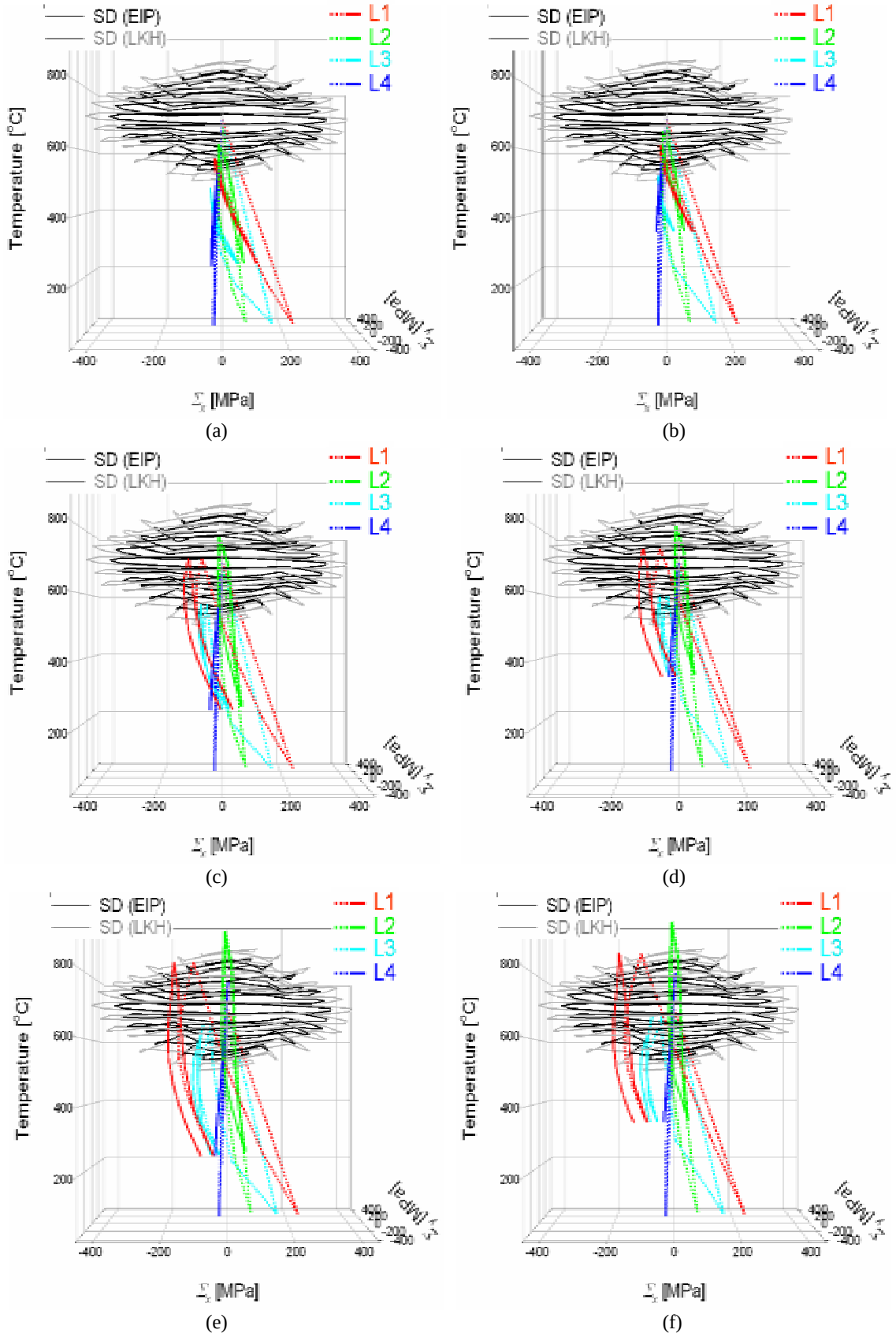

Figure E.2. Shakedown limits and thermomechanical loading paths in two-dimensional loading space (Σ_x, ΔT): Additional view from Figure 7.3.

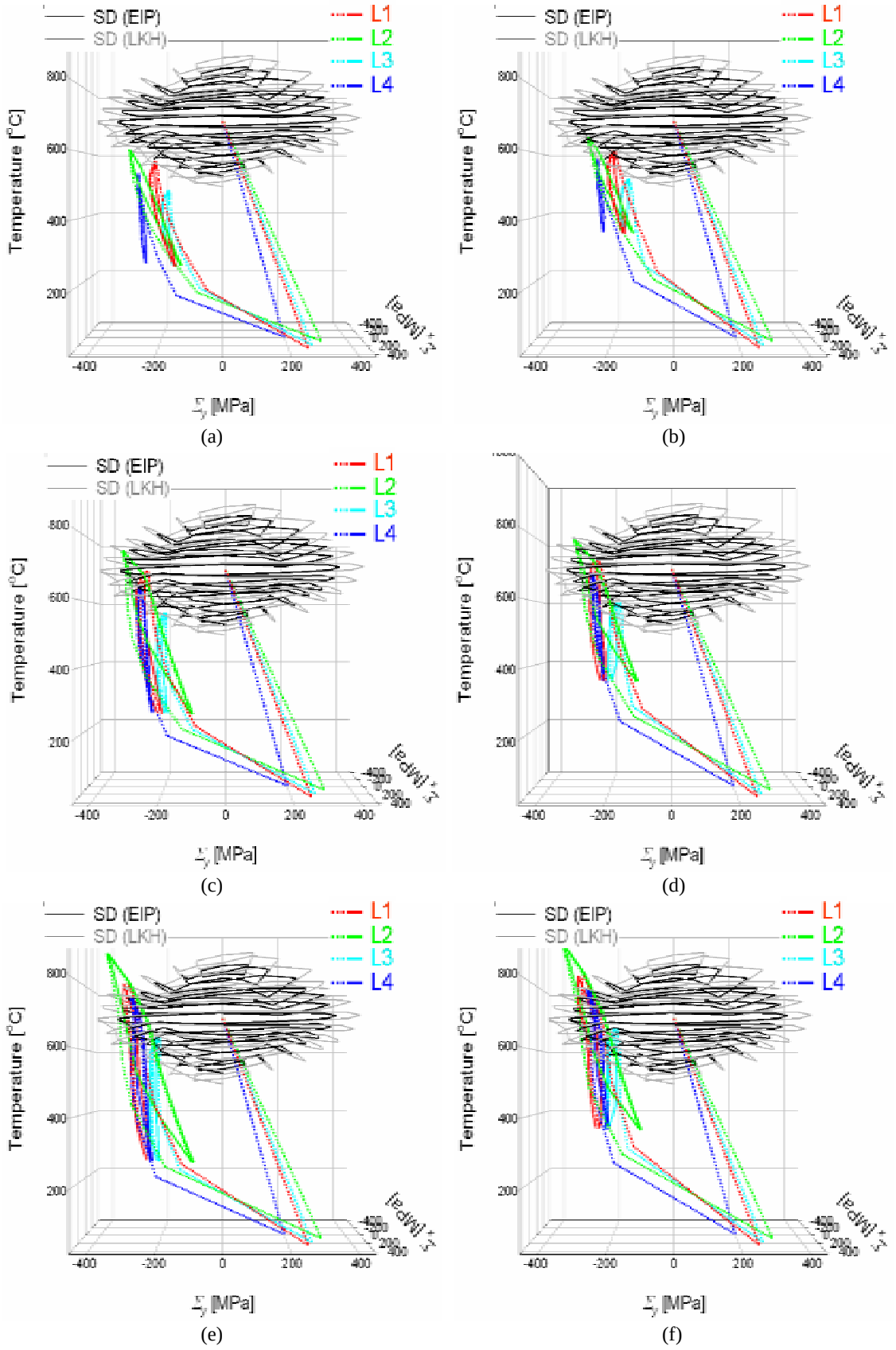

Figure E.3. Shakedown limits and thermomechanical loading paths in two-dimensional loading space (Σ_y, ΔT): Additional view from Figure 7.3.

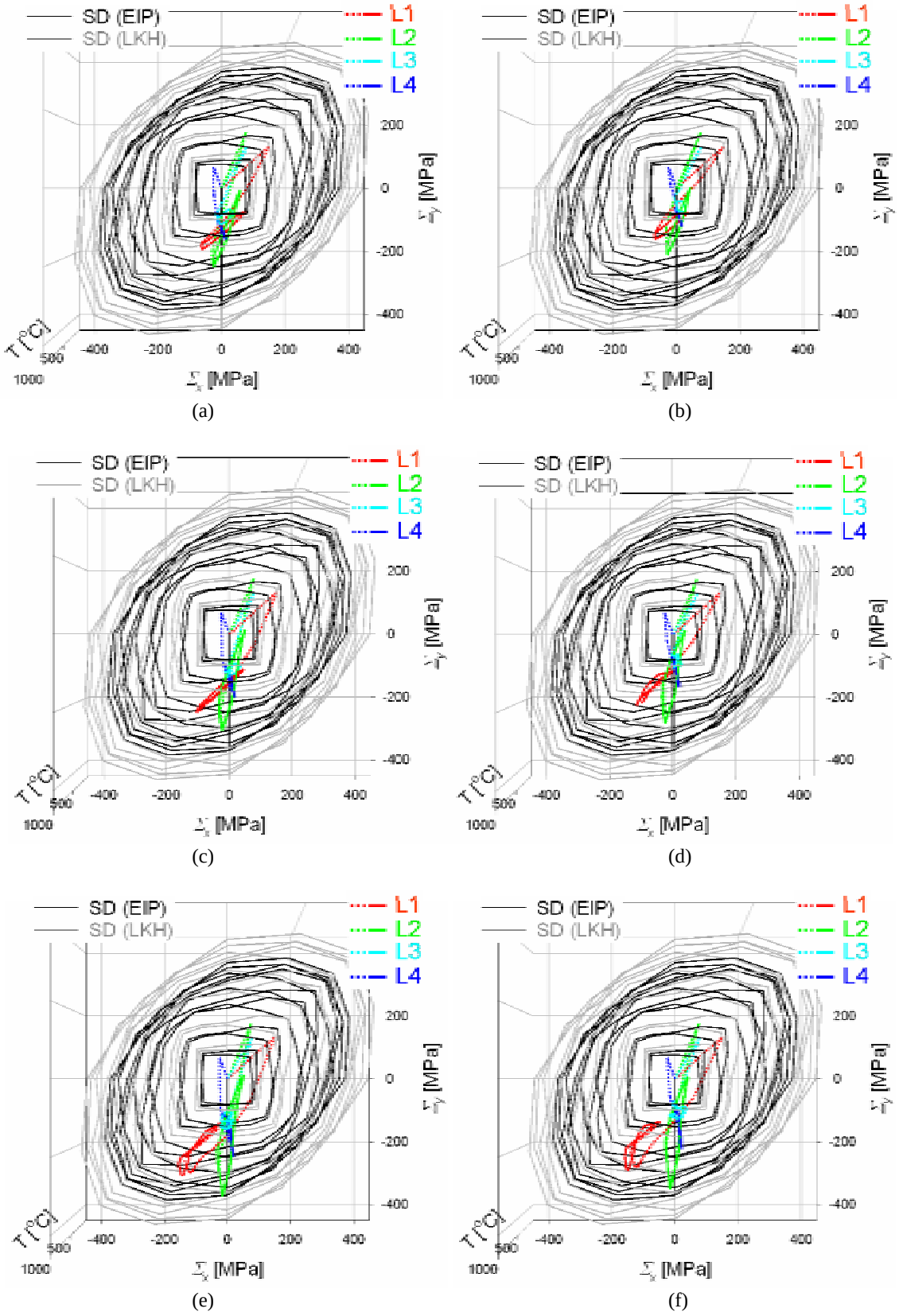

Figure E.4. Shakedown limits and thermomechanical loading paths in two-dimensional loading space (Σ_x, Σ_y): Additional view from Figure 7.4.

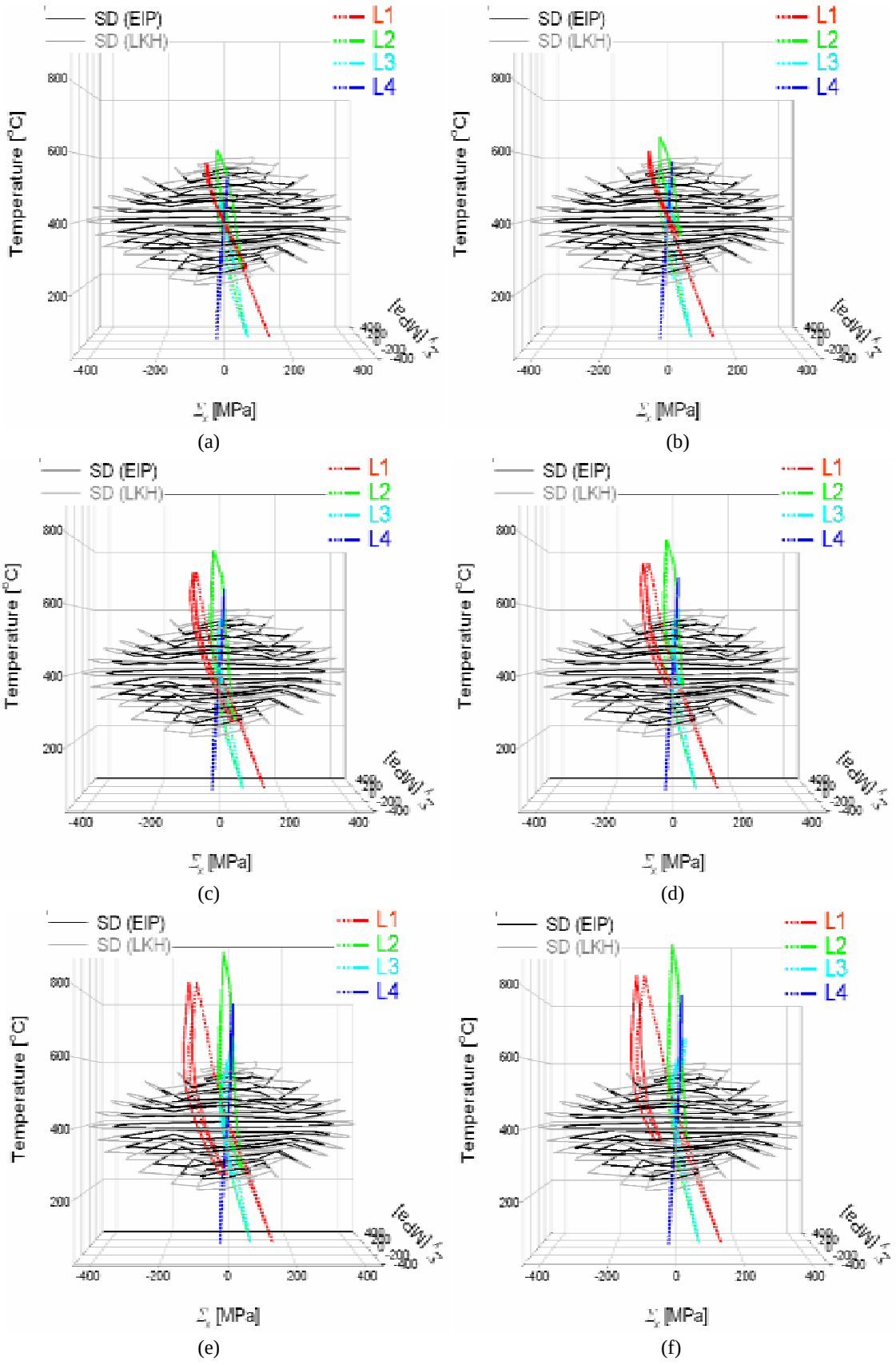

Figure E.5. Shakedown limits and thermomechanical loading paths in two-dimensional loading space (Σ_x, ΔT): Additional view from Figure 7.4.

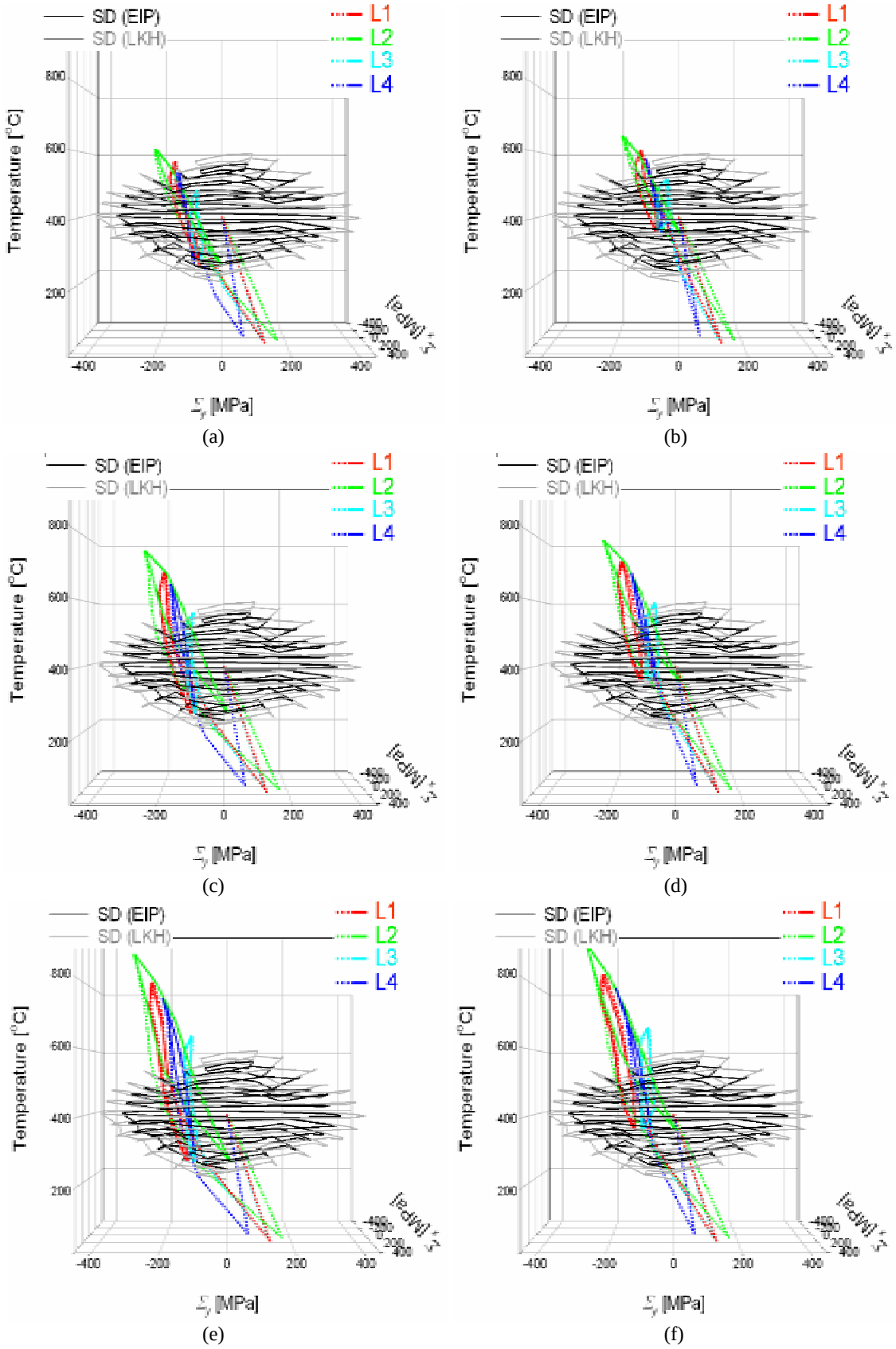

Figure A.6 Shakedown limits and thermomechanical loading paths in two-dimensional loading space (Σ_y, ΔT): Additional view from Figure 7.4.

References

[1] K. Ioki, V. Barabash, A. Cardella, F. Elio, Y. Gohar, G. Janeschitz, G. Johnson, G. Kalinin, D. Lousteau, M. Onozuka, R. Parker, G. Sannazzaro, R. Tivey, *J. Nucl. Mater.* **258-263** (1998) 74.

[2] G. Kalinin, W. Gauster, R. Matera, A.F. Tavassoli, A. Rowcliffe, S. Fabritsiev, H. Kawamura, *J. Nucl. Mater.* **233-237** (1996) 9.

[3] K. Ehrlich, *Fus. Eng. Des.* **56-57** (2001) 71.

[4] H. Bolt, V. Barabash, G. Federici, J. Linke, A. Loarte, J. Roth, K. Sato, *J. Nucl. Mater.* **307-311** (2002) 43.

[5] R. Aymar, International team, *J. Nucl. Mater.* **307-311** (2002) 1.

[6] G. Mazzone, G. Brolatti, E. D'Agata, A. Iorizzo, F. Lucca, A. Marin, M. Merola, L. Petrizzi, A. Pizzuto, M. Roccella, L. Semeraro, G. Zanotelli, *Fus. Eng. Des.* **61-62** (2002) 153.

[7] *ITER Materials Assessment Report*, ITER Doc. G74 MA 1001-07011 W0.2 (2000).

[8] S.T. Peters, *Handbook of Composites*, 2nd ed., Champion & Hall, London, UK (1998).

[9] K.K. Chawla, *Composite Materials: Science and Engineering*, 2nd ed., Springer, New York, USA (1998).

[10] P.K. Mallick, *Composite Engineering Handbook*, Marcel Dekker, Inc., New York, USA (1997).

[11] B. Terry, G. Jones, *Metal matrix composites*, Elsevier Advanced Technology, Mayfield House, Oxford, UK (1990) 3-11.

[12] M.C.Y. Niu, *Composite Airframe Structures: Practical Design Information and Data*, Conmilit Press Ltd., Hong Kong (1992).

[13] S. Suresh, A. Mortensen, A. Needleman (Eds.), *Fundamentals of metal matrix composites*, Butterworth-Heinemann, Stoneham, (1993) 297.

[14] W. D. Calliseter, *Materilas Science and Engineering: An Introduction*, 6th ed., John Wiley & Sons, Inc., NY, USA (2003) 527-530.

[15] T.W. Clyne, *Metal Matrix Composites*, in *Comprehensive Composite Materials*, vol. **3**, A. Kelly, C. Zweben, eds., Elsevier, Dundee, UK (2000) 717-740.

[16] R. Warren, *Polymer Matrix Composites*, in *Comprehensive Composite Materials*, vol. 2, A. Kelly, C. Zweben, eds., Elsevier, Dundee, UK (2000).

[17] R. Warren, *Carbon/Carbon, Cement, and Ceramic Matrix Composites*, in

Comprehensive Composite Materials, vol. **4**, A. Kelly, C. Zweben, eds., Elsevier, Dundee, UK (2000).

[18] J.H. You, H. Bolt, *J. Nucl. Mater.* **305** (2002) 14.

[19] J.H. You, H. Bolt, *J. Nucl. Mater.* **307-311** (2002) 74.

[20] M.W. Hyer, *Stress Analysis of Fiber-Reinforced Composite Materials*, WCB/McGraw-Hill, Singapore (1997).

[21] A. Savaidis, G. savaidis, Ch. Zhang, *Inter. J. Fatigue* **23** (2001) 303.

[22] L. Bocher, P. Delobelle, P. Robinet, X. Feaugas, *Inter. J. Plasticity* **17** (2001) 1491.

[23] T. Inoue, N. Ohno, A. Suzuki, T. Igari, *Nucl. Eng. Des.* **114** (1989) 295.

[24] T.W. Clyne, P.J. Withers, *An introduction to metal matrix composites*, Cambridge University Press, Cambridge, UK (1993).

[25] J. Lemaitre, J.-L. Chaboche, *Mechanics of solid materials*, Cambridge University Press, Cambridge, UK (1987) 178-180.

[26] A. S. Khan, S. Huang, *Continuum Theory of Plasticity*, John Wiley & Sons, Inc., NY, USA (1995) 82-103.

[27] H. Bolt, V. Barabash, W. Krauss, J. Linke, R. Neu, S. Suzuki, N. Yoshida, ASDEX Upgrade Team, *J. Nucl. Mater.* **329-333** (2004) 66.

[28] J.H. You, H. Bolt, *J. Nucl Mater.* **299** (2001) 1.

[29] S. Suresh, *Fatigue of materials*, Cambridge University Press, Cambridge, UK (1991).

[30] L. Taleb, M. Cousin, J. F. Jullien, *Inter. J. Pressure Vessels Piping* **75** (1998) 173.

[31] M.V. Borodii, V.A. Strizhalo, *Inter. J. Fatigue* **22** (2000) 275.

[32] A.R.S. Ponter, *Shakedown and ratchetting below the creep range*, CEC Report EUR8702 EN, Brussels (1983).

[33] M. Heitzer, M. Staat, H. Reiners, F. Schbert, *Nucl. Eng. Des.* **225** (2003) 11.

[34] H. Lang, K. Wirtz, M. Heitzer, M. Staat, R. Oettel, *Nucl. Eng. Des.* **206** (2001) 235.

[35] G.J. Dvorak, Y.A. Bahei-El-Din, Y. Macheret, G.H. Liu, *J. Mech. Phys. Solids* **36** (1988) 655.

[36] S. Jansson, F.A. Leckie, *J. Mech. Phys. Solids* **40** (1992) 593.

[37] S. Jansson, F.A. Leckie, *Mech. Mater.* **18** (1994) 205.

[38] S.R. Gunawardena, S. Jasson, F.A. Leckie, *Acta Metall. Mater.* **41** (1993) 3147.

[39] D.B. Zahl, S. Schmauder, R.M. McMeeking, *Acta Metall. Mater.* **42** (1994) 2983.

[40] Z.-Z. Du, R.M. McMeeking, *J. Computer-Aided Mater. Des.* **1** (1994) 243.

[41] C.A. Bigelow, *NASA Technical Memorandum* **107649** (1992).

[42] T. Nicholas, J.L. Kroupa, R.W. Neu, *Compos. Eng.* **3** (1993) 675.

[43] J.A. Sherwood, H.M. Quimby, *Computer Struct.* **56** (1995) 505.

[44] H. Ismar, F. Schröter, *Mech. Mater.* **32** (2000) 329.

[45] H. Ismar, F. Schröter, F. Streicher, *Int. J. Solids Struc.* **38** (2001) 127.

[46] E. Melan, *Ing. Arch.* **8** (1938) 116.

[47] W.T. Koiter, *General theorems for elastic-plastic solids*, in *Progress in Solid Mechanics*, I.N. Sneddon, R. Hill eds., Amsterdam, North-Holland (1960) 165.

[48] D.A. Gokhfeld and O.F. Cherniavsky, *Limit analysis of structures at thermal cycling*, Sijthoff and Noordhoff, Leyden (1980).

[49] J.A. König, *Shakedown of elastic-plastic structures*, Elsevier, Amsterdam (1987).

[50] Z. Mróz, D. Weichert, S. Dorosz, *Inelastic Behaviour of Structures under Variable Loads*, Jan Andrezej König Memorial Volume, Kulwer Academic Publishers, Dordrecht, Netherlands (1995).

[51] D. Weichert, G. Maier, *Inelastic Analysis of Structures under Variable Loads: Theory and Engineering Applications*, Kluwer Academic Publishers, Dordrecht, Netherlands (2000).

[52] M. Staat, M. Heitzer, eds., *Numerical Methods for Limit and Shakedown Analysis: Deterministic and Probabilistic Problems*, NIC Series Volume **15**, Central Institute for Applied Mathematics, Research Center Jülich, Germany (2002).

[53] E. Melan, *Sitber. Akad. Wiss.*, Abt. IIA 145, Wien, Austria (1936) 195.

[54] B.G. Neal, *J. Aeronaut. Sci.* **17** (1950) 297.

[55] A.R.S. Ponter, *Proc. SMiRT-3*, paper L5/2, London, UK (1975).

[56] J. Zarka, J. Casier, *Elastic-plastic response of a structure to cyclic loading: practical rules*, in *Mechanics Today*, S. Nemat-Nasser, ed., Vol. 6, Pergamon, Oxford, UK (1981) 93-198.

[57] G. Maier, *Proc. ASCE, J. Eng. Mech.*, Div. 98, N. EM5, (1972) 1322.

[58] J.A. König, A. Siemaszko, *Ing. Arch.* **58** (1988) 58.

[59] B. Halphen, Q.S. Nguyen, *J. Mech.* **14** (1975) 39.

[60] J. Mandel, *Mech. Res. Comm.* **3** (1976) 483.

[61] D. Weichert, J. Gross-Weege, *Int. J. Mech.* **30** (1988) 757.

[62] C. Comi, A. Corigliano, *Int. J. Plasiticy* **7** (1991) 679.

[63] C. Polizzotto, G. Borino, P. Fuschi, *Eur. J. Mech. A/ Solids* **15** (1996) 825.

[64] G. Maier, *Meccanica* **4** (1969) 250.

[65] E. Stein, G. Zhang, Y. Huang, *Comput. Methods Appl. Mech. Eng.* **103** (1993) 247.

[66] A. Corigliano, G. Maier, S. Pycko, *Int. J. Solids Struct.* **32** (1995) 3145.

[67] S. Pycko, G. Maier, *Int. J. Plasticity* **11** (1995) 367.

[68] G. Maier, In *Foundations in Plasticity*, ed. A. Sawczuk, Noordoff, Leyden, Netherlands (1973) 417.

[69] A. Siemaszko, J,A, König, *J. Struct. Mech.* **13** (1985) 301.

[70] D. Weichert, *Mech. Res. Comm.* **11** (1983) 127.

[71] D. Weichert, *Int. J. Plasticity* **2** (1986) 135.

[72] D. Weichert, *Arch. Mech.* **41** (1989) 61.

[73] J. Gross-Weege, *Int. J. Plasticity* **6** (1990) 433.

[74] S. Pycko, J.A. König, *Eur. J. Mech. A/ Solids* **10** (1991) 563.

[75] C. Polizzotto, G. Borino, *Int. J. Solids Struct.* **33** (1996) 3415.

[76] J. Saczuk, H. Stumpf, IFM-Report, no. **74**, Ruhr University, Bochum, Germany (1990).

[77] J.B. Tritsch, D. Weichert, in *Inelastic Behavior of Structures under Variable Loads*, A. Mróz, D. Weichert, S. Dorosz, eds., Kulwer Academic, Dordrecht, Netherlands (1995) 309.

[78] H. Stumpf, *J. Plasticity* **9** (1993) 583.

[79] J. Saczuk, *Arch. Mech.* **49** (1997) 525.

[80] X.Q. Feng, X.S. Liu, *Int. J. Plasticity* **12** (1996) 1241.

[81] H.F. Chen, F.A. Leckie, *Int. J. Pressures Vessels Piping* **78** (2001) 443.

[82] L. Khalij, S. Hariri, R. Vaucher, *Comp. Mater. Sci.* **24** (2002) 393.

[83] J.Q. Tarn, G.J. Dvorak, M.S.M. Rao, *Int. J. solids Struct.* **11** (1975) 751.

[84] A.R.S. Ponter, F.A. Leckie, *J. Mech. Phys. Solids* **46** (1998) 697.

[85] V. Carvelli, G. Maier, A. Taliefcio, *J. Mech. Eng.* **50** (1999) 229.

[86] D. Weichert, A. Hachemi, F. Schwabe, *Mech. Res. Comm.* **26** (1999) 309.

[87] D. Weichert, A. Hachemi, F. Schwabe, *Arch. Appl. Mech.* **69** (1999) 623.

[88] G. Maier, V. Carvelli, G. Cocchetti, *Eur. J. Mech. A/Solids* **19** (2000) 79.

[89] G.J. Dvorak, D.C. Lagoudas, C.-M. Huang, in *Inelastic Analysis of Structures under Variable Loads*, D. Weichert, G. Maier, eds., Kluwer Academic Publishers, Dordrecht, Netherlands (2000) 183.

[90] D. Weichert, A. Hachemi, *J. Theoretical Appl. Mech.* **1** (2002) 40.

[91] F. Schwabe, *Einspieluntersuchungen von Verbundwerkstoffen mit periodischer Mikrostruktur*, Ph.D. Dissertation, RWTH University, Aachen, Germany (2000).

[92] H. Kordisch, G. Nagel, J.-G. Blauel, H. Stöckl, M. Sester, *Nucl. Eng. Des.* **151** (1994) 321.

[93] M. Heitzer, M. Staat, *Nucl. Eng. Des.* **193** (1999) 349.

[94] M. Staat, M. Heitzer, *Nucl. Eng. Des.* **206** (2001) 151.

[95] Y. Yao, M.-W. Lu, X. Zhang, *Nucl. Eng. Des.* **229** (2004) 189.

[96] M. Heitzer, M. Staat, H. Reiners, F. Schubert, *Nucl. Eng. Des.* **225** (2003) 11.

[97] A. S. Khan, S. Huang, *Continuum Theory of Plasticity*, John Wiley & Sons, Inc., NY, USA (1995) 146-156.

[98] D.C. Drucker, *J. Appl. Mech.* **26** (1959) 101.

[99] W.M. Lai, D. Rubin, E. Krempl, *Introduction to Continuum Mechanics*, 3rd ed., Pergamon Press Ltd., Seoul, Korea (1993) 431.

[100] D.L. Logan, A *First Course in the Finite Element Method*, 2nd ed., PWS Publishing Company, Boston, USA (1992).

[101] J.N. Reddy, *An Introduction to the Finite Element Method*, 2nd ed., McGraw-Hill, Inc., Singapore (1993).

[102] O.C. Zienkiewicz, R.L. Taylor, *The Finite Element Method*, 4th ed., McGraw-Hill, Inc., Singapore (1989).

[103] I.M. Smith, D.V. Griffiths, *Programming the Finite Element Method*, 2nd ed., John Wiley & Sons, Singapore (1988).

[104] R.D. Cook, *Finite Element Modeling for Stress Analysis*, John Wiley& Sons, Inc., New York, USA (1994).

[105] K.-J. Bathe, *Finite Element Procedures*, Prentice Hall, Englewood Cliffs, New Jersey, USA (1966).

[106] N. Kikuchi, *Finite Element Methods in Mechanics*, Cambridge University Press, Cambridge, UK (1986).

[107] B.Y. Kim, *Computation Implementation of Three-Dimensional Shakedown Formulation*, IPP-Report, unpublished, Garching, Germany (2004).

[108] J.A. König, M. Klever, *Bull. Acad. Polon. Sci.* **26** (1978) 165.

[109] G. Zhang, *Einspielen und dessen numerische Behandlung von Flächentragwerken aus ideal plastischem bzw. kinematisch verfestigendem Material*, Ph.D. Dissertation, University Hannover (1991).

[110] J. Gross-Weege, *Int. J. Mech. Sci.* **39** (1997) 417.

[111] A.R. Conn, N.I.M. Gould, Ph.L. Toint, *LANCELOT: A fortran package for large-scale nonlinear optimization (Release A)*, Springer-Verlag, Berlin, Germany (1992).

[112] P.E. Gill, W. Murray, M.H. Wright, *Practical Optimization*, Academic press, London and New York (1981).

[113] E. Stiefel, *Numer. Math.* **2** (1960) 1.

[114] T. Belytschko, *Int. J. Mech. Sci.* **14** (1972) 619.

[115] Nguyen Dang Hung, L. Palgen, *Proc. SMiRT-5*, paper **L3/3**, Berlin, Germany (1979).

[116] L. Corradi, A. Zavelani, *Comp. Meth. Appl. Mech. Eng.* **3** (1974) 37.

[117] F. Genna, *Int. J. Mech. Sci.* **30** (1988) 769.

[118] S.P. Timoshenko, J.N. Goodier, *Theory of Elasticity*, 3rd ed., McGraw-Hill, Singapore (1982) 15-18.

[119] S. Suresh, A. Mortensen, A. Needleman, eds., *Fundamentals of metal matrix composites*, Butterworth-Heinemann, Stoneham, (1993) 179-182.

[120] Z.-Z. Du, R.M. McMeeking, S. Schmauder, *Mech. Comp. mat. Struc.* **1** (1994) 171.

[121] A.R.S. Ponter, K.F. Carter, J.M. Duggan, *Shakedown limits for a metal matrix composite*, unpublished (1998).

[122] A.F. Tavassoli, *J. Nucl. Mater.* **258-263** (1998) 85.

[123] *ITER Material Properties Handbook*, ITER Document No. S74RE1 (1997).

[124] H. Bolt, V. Barabash, G. Federici, J. Linke, A. Loarte, J. Roth, K. Sato, *J. Nucl. Mater.* **307-311** (2002) 43.

[125] J.H. You, H. Bolt, *J. Nucl. Mater.* **299** (2001) 9.

[126] J.H. You, H. Bolt, *J. Nucl. Mater.* **329-333** (2004) 702.

[127] U. Schumacher, *Wissenschaftliche Buchgesellschaft*, Darmstadt, (1993) 3.

[128] J. Wesson, *Tokamaks*, Oxford Engineering Science Series **48**, 2nd ed., Clarendon Press, Oxford, UK (1997).

[129] F. Engelmann, in *Physics of Plasma Wall Interaction in Controlled Fusion*, D.E. Post and R. Behrisch, eds., NATO ISI Series B Physics Vol. **131**, Plenum Press, New York, London (1986).

[130] W.J. Hogan, ed., *Energy from Inertial Fusion*, International Atomic Energy Agency, Vienna, Austria (1995).

[131] *Technical Basis for the ITER Final design*, EDA Documentation Series No.**22**, IAEA, Vienna (2001).

[132] R. Aymar, Y. Shimomura, M. Huguet, V. Chuyanov and ITER teams, *19th IAEA Fusion Energy Conference*, Lyon, France, Oct. (2002).

[133] K. Ioki, V. Barabash, A. Cardella, F. Elio, G. Kalinin, N. Miki, M. Onozuka, T. Okasi, V. Rozov, G. Sannazzaro, Y. Utin, M. Yamada, H. Yoshimura, *Fus. Eng. Des.* **58&59** (2001) 573.

[134] M. Merola, G. Vieider, M. Bet, I. Bobin Vastra, L. Briottet, P. Chappuis, K. Cheyne, G. Dell'Orco, D. Duglué, R. Duwe, S. Erskine, F. Escourbiac, M. Fèbvre, M. Grattarola, F. Moreschi, A. Orsini, R. Pamato, L. Petrizzi, L. Plöchl, B. Riccardi, E. Rigal, M. Rödig, J.F. Salavy, B. Schedler, J. Schlosser, S. Tähtinen, R. Vesprini, E. Visca, C.H. Wu, *Fus. Eng. Des.* **56&57** (2001) 173.

[135] S.A. Fabritsiev, S.J. Zinkle, B.N. Smith, *J. Nucl. Mater.* **233-237** (1996) 127.

[136] R. Lindau, M. Schirra, *Fus. Eng. Des.* **58&59** (2001) 781.

[137] R. Lindau, A. Moeslang, M. Schirra, P. Schlossmacher, M. Klimenkov, *Proceedings of the 10th International Conference on Fusion Reactor Materials*, Baden-Baden, Germany, October 14-19, 2001, Elsevier, J. Nucl. Mater. (2002).

[138] R.N. Giniyatulin, V.L. Komarov, E.G. Kuzmin, A.N. Makhankov, I.V. Mazul, N.A. Yablokov, A.N. Zhuk, *Fus. Eng. Des.* **61-62** (2002) 185.